The University Of Sheffield.

AN *EX VIVO* MODEL OF PERIPHERAL NERVE REGENERATION

Mehri Behbehani

A thesis submitted in partial fulfilment of the requirements for the degree of Doctor of Philosophy

The University of Sheffield

Faculty of Engineering

Department of Materials Science and Engineering

January 2019

Abstract

Nerve guidance conduits (NGCs) fail to promote peripheral nerve regeneration at gap lengths >3 cm in humans. Internal NGC scaffolds through microfibres could provide additional outgrowth guidance to enhance regeneration outcome. No ideal NGC scaffold has yet been identified, and no study has systematically attempted to evaluate different scaffold variables (such as fibre diameter, fibre density, or surface modification) directly inside an NGC. Therefore, this thesis reports on a study to develop a 3D *ex vivo* model of peripheral nerve regeneration. The overall goal was a platform that permitted the reproducible and reliable comparison of NGC scaffolds made directly inside an NGC using a single setup, that also enables the reduction of more traditional *in vivo* nerve injury models.

The response of NG108-15 neuronal cells and primary rat Schwann cells to polycaprolactone (PCL) fibres with 1, 5, 8, 10 and 13 µm diameter was explored, finding that fibre diameter and fibre surface topography influenced axon and Schwann cell growth. Fibres with 8 and 10 µm diameter supported optimal neurite alignment, incidence and length. In contrast, Schwann cell metabolic activity and attachment was limited on 1 µm fibres. Topographies on fibre surface were deep and elongated on fibres 5 – 13 µm and shallow, round-shaped and more frequent on 1 µm fibres.

A method based on calculated fibre weight was developed to reproducibly fill NGCs with different fibre densities. From this, a 3D *ex vivo* model was developed placing dorsal root ganglia (DRGs) on scaffold-filled NGCs to mirror the proximal nerve stump after injury. Chick embryo DRGs and light-sheet microscopy imaging were of particular value and enhanced model reliability, accuracy and ethical acceptance. DRG outgrowth incidence and length was initially poor on PCL fibre scaffolds, but improved significantly (by more than five-fold) after air plasma modification.

XPS confirmed that a 60 second air plasma treatment was sufficient to increase the surface polarity of fibre scaffolds inside conduits along their entire length. The model proved valuable for evaluating and comparing scaffolds with different fibre diameters, densities (10, 20 and 40 %), fibre materials, and for studying potential cell therapy

approaches to aid peripheral nerve repair. For this, Schwann cells from chick embryo sciatic nerves were successfully isolated, purified and cultured inside NGCs using a selective DMEM D-valine method.

Finally, across all variables investigated, it was concluded that conduits containing a 20 % density of air plasma-modified 10 µm diameter fibres supported optimal chick DRG outgrowth, regenerating more than 85 % of the conduits in 21 days.

Acknowledgements

First and foremost, I would like to thank my supervisory team Professor John Haycock and Dr. Frederik Claeyssens for their guidance and support throughout my PhD. I am grateful for the freedom you both gave me and the confidence you had in me to guide my own project. I would like to thank John in particular as he gave me the chance to start my PhD directly after my bachelor studies and always believed in me. I never heard John say no to all the expensive reagents or equipment that I wanted to use. This allowed me to pursue all kinds of project ideas, even if sometimes not successful but I believe this contributed to me becoming a more creative and knowledgeable researcher. Fred, I'm particularly grateful for all your motivating words and enthusiasm that encouraged me to always believe in my project and in myself.

Great thanks also goes to the EPSRC who's financial support was received most gratefully.

To all my friends and colleagues, in particular Betül Aldemir Dikici, Serkan Dikici, George Bullock, Ana Maria Sandoval Castellanos, Dr. Robert Owen and Jonathan Field, I would like to thank you all for your help, advice and motivating words. Especially Dr. Adam Glen and Dr. Caroline Taylor, who contributed to the success of my project particularly at the start. Adam, I thank you for all your wise words, advise and help to make me see things that were not as obvious at first. You always encouraged me to think "outside the box" which I am most grateful for. Caroline, you have always been a great help in the lab and I particularly enjoyed our little and sometimes long chats early in the morning which made me forget about thesis writing and all sorts of other stress.

To Dr. Victoria Workman and Dr. Kathryn Murray, I would like to thank you both for taking the time and patience to proof-read my entire thesis and your brilliant and always helpful feedback. I don't know what I would have done without you. I would also like to thank my PhD thesis mentor Dr. Nicola Galley for letting me talk her ear off with everything relating to my PhD. I am very grateful for all your advice and continued motivation.

To Liam Boyle, my partner and rock, I could have never done it without you. I am so grateful for everything you have done for me, for your help in the lab, with writing and proof-reading all kinds of documents and your critical but most helpful feedback to my work. Your kindness, optimism and humour always made me smile even in stressful and sometimes hard times.

To my parents Anja and Masoud, my Aunt Gesa, my uncle Claus and my sisters, I am grateful for everything you have done for me, your never-ending confidence in my success, your advice and your shoulders to cry on when everything went wrong. I don't know what I would have done without the long phone calls to my mum, dad and sister, Laleh. This thesis is dedicated to my beloved grandparents Irene and Günther Labenski for which support I am so grateful for. Thank you for all your love.

Outputs

Publications

1. **M. Behbehani**, A. Glen, C. S. Taylor, A. Schuhmacher, F. Claeyssens, and J. W. Haycock, "Pre-clinical evaluation of advanced nerve guide conduits using a novel 3D *in vitro* testing model," *International Journal of Bioprinting*, vol. 4, 2018.

Publications in Preparation

1. **M. Behbehani**, F. Claeyssens and J. W. Haycock, "Fibre diameter and surface topography influence performance of scaffolds in peripheral nerve regeneration*", To be submitted to Biotechnology and Bioengineering*
2. **M. Behbehani**, F. Claeyssens and J. W. Haycock, "An *ex vivo* model of peripheral nerve regeneration", *To be submitted to Biomaterials*
3. P. Basnett, U. Illangakoon, J. Dawson, J. Wells, J.M. Kanczler, C. Taylor, **M. Behbehani**, E. Humphrey, Q. Majid, B. Lukasiewicz, R.K. Matharu, R. Oreffo, J Haycock, Cesare Terracciano, S. Harding, M. Edirisinghe, I. Roy, "Polyhydroxyalkanaotes, a family of highly biocompatible natural polymers combined with gyrospinning, a scalable processing method: a tool box par excellence for hard and soft tissue engineering", *To be submitted to Nature Materials*
4. C. S. Taylor, **M. Behbehani**, A. Glen, R. Nigmatulin, P. Basnett, F. Claeyssens, I. Roy, J. W. Haycock, "Evaluation of aligned polyhydroxyalkanoate blend intraluminal guidance scaffolds for peripheral nerve repair using organotypic DRG explant culture"

Oral Presentations

1. "Polycaprolactone microfibres for peripheral nerve repair in a novel 3D nerve model", Young researchers meeting, Macro Group UK, Dublin (Ireland), July 2018
2. "A 3D *ex vivo* model for testing nerve guidance conduits using high throughput light-sheet microscopy", Tissue and Cell Engineering Society Annual Conference, Keele (UK), July 2018
3. "Bioengineering approaches for peripheral nerve repair", invited speaker at the UK Nerve Engineering Network Meeting, London (UK), November 2018

Poster Presentations

1. "Development of a 3D neuronal-culture model for peripheral nerve studies", Tissue and Cell Engineering Society Annual Conference, London (UK), *July 2016*
2. "Development of a 3D neuronal-culture model for peripheral nerve studies", Biomaterials & Tissue Engineering Group, 18th Annual White Rose Work in Progress Meeting, Durham (UK), *December 2016* **+ 90 seconds flash poster presentation**
3. "3D *in vitro* evaluation of electrospun polycaprolactone microfibres as an internal scaffold in nerve guidance conduits", Tissue and Cell Engineering Society Annual Conference, Manchester (UK), *July 2017*
4. "3D *in vitro* evaluation of electrospun polycaprolactone microfibres as an internal scaffold in nerve guidance conduits", 28th European Conference on Biomaterials, Athens (Greece), *September 2017*
5. "Polycaprolactone microfibres for peripheral nerve repair – The influence of fibre diameter and air plasma deposition", Biomaterials & Tissue Engineering Group, 19th Annual White Rose Work in Progress Meeting, Leeds (UK), *December 2017* **+ 90 seconds flash poster presentation**
6. "A pre-clinical 3D model for testing nerve guidance conduits using high throughput light-sheet microscopy", 29th European Conference on Biomaterials, Maastricht (Netherlands), *September 2018*

7. "An *in vitro* model of peripheral nerve injury regeneration", Biomaterials & Tissue Engineering Group, 19th Annual White Rose Work in Progress Meeting, Sheffield (UK), *December 2018* **+ 90 seconds flash poster presentation**

Awards

1. Best flash poster presentation

   Biomaterials & Tissue Engineering Group, 19th Annual White Rose Work in Progress Meeting, Sheffield (UK), *December 2018*

2. 2nd place Image Competition

   Imaging Life Symposium, Sheffield (UK), *September 2018*

3. Best oral presentation

   Young researchers meeting, Macro Group UK, Dublin (Ireland), *July 2018*

4. Best oral presentation

   Tissue and Cell Engineering Society Annual Conference, Keele (UK), *July 2018*

5. 1st place Image Competition

   Tissue and Cell Engineering Society Annual Conference, Keele (UK), *July 2018*

6. 1st place Image Competition

   Department of Materials Science & Engineering, The University of Sheffield (UK), *May 2018*

7. Best poster presentation

   Biomaterials & Tissue Engineering Group, 19th Annual White Rose Work in Progress Meeting, Leeds (UK), *December 2017*

8. 2nd place Poster Presentation

   Tissue and Cell Engineering Society Annual Conference, Manchester (UK), *July 2017*

Contents

List of Figures

List of Tables

List of Equations

Abbreviations

2D	Two dimensions or two-dimensional
3D	Three dimensions or three-dimensional
3Rs	Reduction, Replacement and Refinement
AFM	Atomic force microscopy
ANOVA	Analysis of variance
ATR-FTIR	Attenuated total reflectance Fourier transform spectroscopy
BDGF	Brain-derived growth factor
BSA	Bovine serum albumin
CE	Conformité Européenne
CNF	Ciliary neurotrophic factor
CNS	Central nervous system
DAAO	D-amino acid oxidase
DAPI	4',6-Diamidino-2-phenylindole
DCM	Dichloromethane
dH_2O	Deionised water
DMD	Digital micromirror device
DMEM	Dulbecco's Modified Eagle Medium
DMSO	Dimethyl sulfoxide
DRG (DRGs)	Dorsal root ganglion (dorsal root ganglia)
ECM	Extracellular matrix
EDAC	1-Ethyl-3-(3- dimethylaminopropyl)-carbodiimide
EDD	Embryonic development day
EDTA	Ethylenediaminetetraacetic acid
FAK	Focal adhesion kinase
FBS	Foetal bovine serum
FDA	Food and Drug Administration
FITC	Fluorescein isothiocyanate
FWHM	Full width at half maximum
GDNF	Glial cell line-derived neurotrophic factor
GFAP	Glial fibrillary acidic protein

GIMP	GNU Image Manipulation Program
HIV	Human immunodeficiency virus
HMDS	Hexamethyldisilazane
HUVECs	Human umbilical vein endothelial cells
IL	Interleukin
IPA	Isopropyl alcohol
LIF	Leukemia inhibitory factor
LSM	Light-sheet microscopy
Micro-CT	Micro-computed tomography
N	Experimental repeats
n	Experimental replica within one experiment
NA	Numerical aperture
NaOH	Sodium hydroxide
NC3Rs	National Centre for the Replacement, Refinement and Reduction of Animals in Research
NGC	Nerve guidance conduit
NGF	Nerve growth factor
NHS	N-hydroxysuccinimide
NT	Neurotrophin
P3HB	Poly-3-hydroxybutyrate
P3HO-*co*-3HD	Poly-3-hydroxyoctanoate-*co*-3-hydroxydecanoate
PBS	Phosphate-buffered saline
PCL	Polycaprolactone
pcSCs	Primary chick Schwann cells
PDMS	Polydimethylsiloxane
PEG	Polyethylene glycol
PFA	*Para*-formaldehyde
PGA	Polyglycolic acid
PHA	Polyhydroxyalkanoates
PHSRN	Proline-histidine-serine-arginine-asparagine
PLA	Polylactic acid
PLCL	Poly-L-lactide-co-ε-caprolactone

PLGA	Polylactic-*co*-gycolic acid
PNI	Peripheral nerve injury
PNS	Peripheral nervous system
PVA	Polyvinyl alcohol
RGD	Arginine-glycine-aspartate
SD	Standard deviation
SEM	Scanning electron microscopy
SIS	Small intestinal submucosa
TCP	Tissue culture polystyrene
TIPS	Thermally-induced phase separation
TOF-SIMS	Time-of-flight secondary ion mass spectroscopy
TRITC	Tetramethylrhodamine B isothiocyanate
VIPS	Vapour-induced phase separation
WD	Wallerian degeneration
XPS	X-ray photoelectron spectroscopy
YFP	Yellow fluorescent protein

Chapter 1 Background

1.1 Anatomy of the peripheral nerve

The human nervous system comprises of two systems, the central nervous system (CNS) and the peripheral nervous system (PNS). The CNS is simply summarised as the brain and the spinal cord, where the PNS is formed of nerves which lie in the periphery of these two organs. Simply speaking there are two types of nerves in the PNS, the sensory and motor nerves. Sensory neurons are located in dorsal root ganglia (DRGs), where one axon branch innervates the periphery, e.g. the arms or legs and the other one the dorsal horn in the spinal cord. Motor neurons are located in the ventral horns of the spinal cord, where axon branches innervate muscles in the periphery through neuromuscular junctions. Signals from sensory receptors in the periphery, e.g. in skin are sent through DRGs to the spinal cord, where interneurons connect sensory neurons with motor neurons (Figure 1) [1].

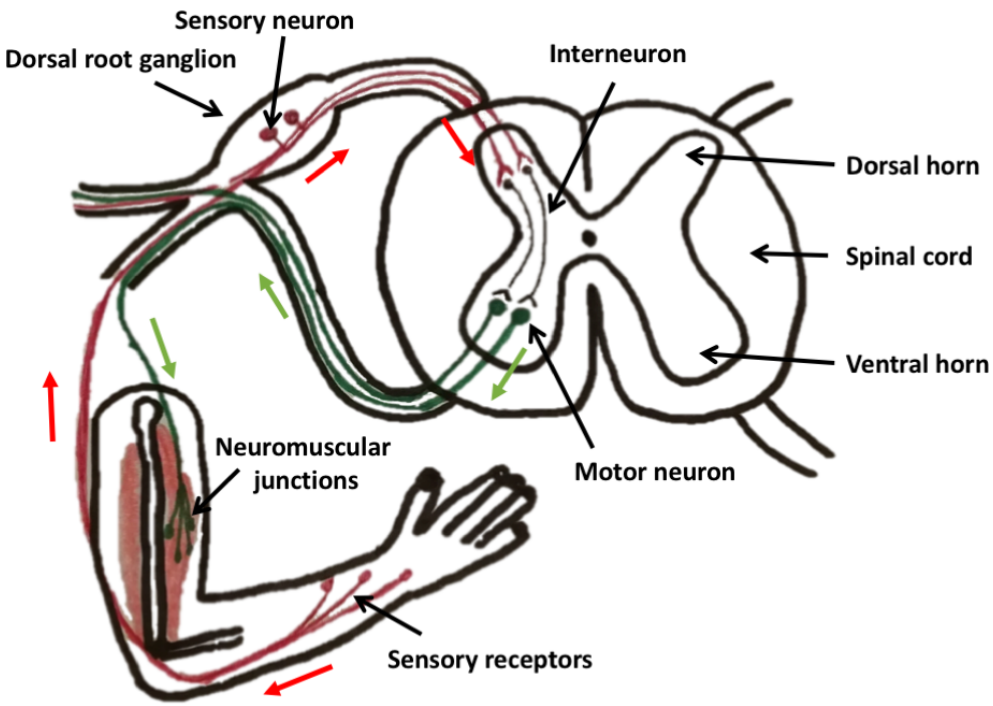

Figure 1 Sensory and motor neurons

Simplified graphical illustration of the location of sensory and motor neurons. Sensory neurons (red) are located in dorsal root ganglia outside of the spinal cord. Neurons are pseudounipolar with one axon branch extending to the periphery and one branch innervating the dorsal horn of the spinal cord. Sensory signals are sent through sensory receptors in the periphery (red arrows) through dorsal root ganglia to the dorsal horn. Interneurons connect sensory and motor neurons. Muscles are controlled through motor neurons which are located in the ventral horn of the spinal cord (green arrows).

Peripheral nerves consist of thousands of axons, where axon number is depending on nerve thickness [2, 3]. Three main connective tissues, the epineurium, the perineurium and the endoneurium, build up the peripheral nerve (Figure 2). The whole nerve and individual nerve fascicles are protected by a collagen-rich layer, the epineurium, which predominantly consists of collagen type I and III. Depending on the tissue it surrounds, there are differences in the nomenclature, where the epifascicular epineurium coats the entire nerve and the interfascicular epineurium surrounds single nerve fascicles. Besides fibroblasts, the epineurium additionally accommodates mast cells and fat cells [4]. Several nerve fascicles include bundles of axons and are arranged within the nerve. The number of fascicles can vary from nerve to nerve depending on the nerve diameter.

Due to the interfascicular epineurium which is loosely attached to the underlying perineurium in fascicles, axons can run through different fascicles in one nerve when they are adjacent to each other [4]. Axon bundles in the fascicles are held together by the perineurium, a multiplex cell layer connective tissue made up of perineurial cells. The perineurium is typically 7 – 20 µm thick and can be assembled from up to 15 layers of perineurial cells [5]. Each cell layer comprises of a basal lamina of laminin, fibronectin and heparan sulfate proteoglycan [4]. Besides perineurial cells, collagen type I and II fibres are present for structural support. In the fascicles, the endoneurium is keeping single axons insulated. Like the perineurium, the endoneurium predominantly contains of collagen type I and II as well as fibroblasts, macrophages, mast cells and endoneurial fluid. The endoneurial fluid gives stability to the nerve due to its slow movement, which is caused by missing lymphatic channels, which additionally provides the perineurium with elasticity [6]. Furthermore, blood vessels run through the entire nerve, the epineurium, perineurium and through the endoneurium. The blood-nerve barrier, which is built up by the inner layer of the perineurium and the endoneurium, protects axons from harmful plasma compounds of the blood [7].

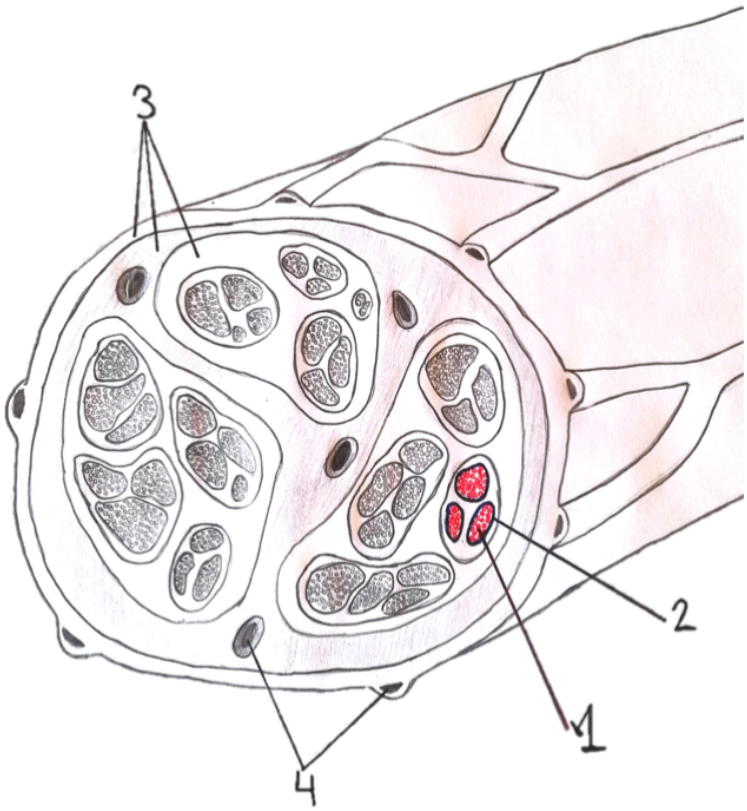

Figure 2 Peripheral nerve cross section

Illustration of a peripheral nerve cross section. The nerve is formed of multiple axons that are arranged into bundles (fascicles). Each axon is surrounded by the endoneurium (1) (red). Whole axon bundles are held together by the perineurium (2) (blue). The epineurium organises groups of nerve fascicles and surrounds the entire nerve (3). Blood vessels (4) run through the lumen as well as the surface of the nerve. Image used with the kind permission of Laleh Louise Behbehani.

1.2 Cellular components in the peripheral nerve – Neurons and Schwann cells

The neuronal phenotype is organised as a cell body, an axon and dendrites. Neuronal cell bodies are in general embedded in DRGs (sensory neurons), the spinal cord (motor neurons) and the brain. The neuronal cell body, called the perikaryon, contains the nucleus and other cell organelles. Characteristic for neurons is the presence of Nissl bodies, which are aggregations of rough endoplasmic reticulum and free ribosomes. Another major characteristic is the absence of centrioles which restricts neurons to undergo mitosis in adults [8, 9]. Axons and dendrites extend from the perikarya, where

axons are unipolar, bipolar, pseudounipolar or multipolar (Figure 3). Unipolar neurons have one axon terminal extending from the axon hillock and dendrites at the end of the axon (Figure 3 A). Bipolar neurons have two axons and two axon hillocks on opposite sides of the perikaryon, which extend in opposite directions with dendrites at one axon end and sensory receptors on the other (Figure 3 B). Sensory neurons are mainly pseudounipolar which describes a neuron with one axon terminal but which splits into two branches with sensory receptors at one axon end and dendrites at the other (Figure 3 C). Motor neurons and interneurons (connect spinal motor and sensory neurons), are mainly multipolar with one axon hillock and axon but several dendrites emerging from the perikaryon and synaptic terminals at the axon end (Figure 3 D) [8].

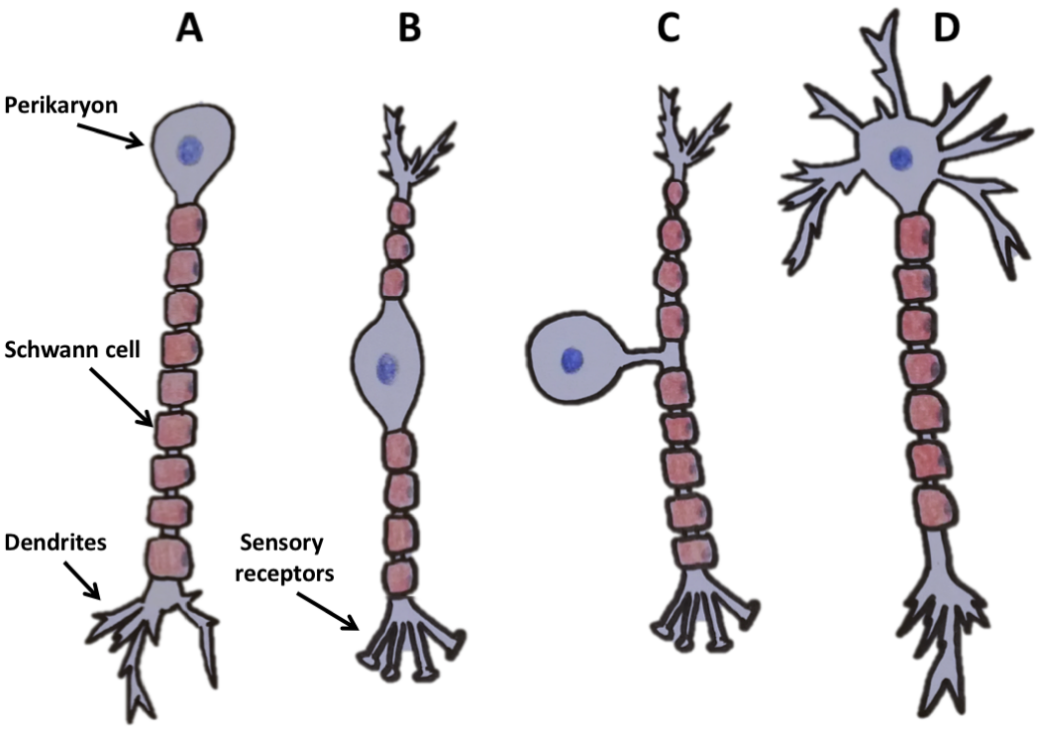

Figure 3 Different types of neurons

Graphical illustration of the four main nerve types: A) unipolar, B) bipolar, C) pseudounipolar and D) multipolar neurons. The neuron is comprised of the perikaryon (neuronal cell body), the axon hillock with emerging axon and dendrites and/or sensory receptors. Schwann cells wrapping around axons are presented in red.

The axon in general transmits action potentials from the perikaryon to the telodendria, the branches present at the end of the axon containing synaptic terminals. Neurotransmitters diffuse from the presynaptic cell into the synaptic cleft, where the

postsynaptic cell receives signals via neurotransmitter receptors [10]. There are either synapses between neurons, where the electrical signal travels along the axon of the presynaptic neuronal cell to another neuronal cell or there are neuromuscular junctions and neuroglandular synapses, on the other hand, describing the signal transmission from the presynaptic cell to either skeletal muscle fibres or to gland cells [10]. The neurotransmitters, which are released can be excitatory, (e.g. acetylcholine) or inhibitory, (e.g. gamma-aminobutyric acid). In a resting state, the neuron has more potassium ions inside and more sodium ions outside the cell [10]. This disequilibrium causes sodium ions to move into the cell and potassium ions out of the cell through leaking channels. However, to maintain the ions at a disequilibrium and a resting state, the sodium-potassium ATPase pump actively pumps sodium ions out and potassium ions in the cell. If excitatory transmitters are released, an action potential in the postsynaptic cell will trigger an influx of positive charged sodium ions into the cell. This increase will trigger the depolarisation of the cell by rising the transmembrane potential from about -70 mV to + 30 mV [11]. The closing of sodium channels and the opening of potassium channels repolarises the cell and the transmembrane potential returns to its original state. During the repolarisation process, adjacent sodium channels on the axon will open to carry the action potential further along the axon. The signal transmission is highly accelerated when axons are myelinated.

Particular concentrated myelinated axons can be found in the white matter of the brain, the spinal cord and motor fibres in the PNS [12]. Myelin is derived from plasma membranes of Schwann cells in the PNS and by oligodendrocytes in the CNS [13]. Schwann cells make up 90 % of all nucleated cells in the peripheral nerve [14], where myelinated axons in the PNS are estimated to be 75 % [13].

The area where Schwann cells encounter on the axon is called “node of Ranvier”. At these nodes no myelin is present, no insulation exists and sodium channels are concentrated. This causes a rapid saltatory conduction (Latin saltare = to jump) through the axon by a signal “jumping” from unmyelinated node to node [15]. How fast the electrical signal can travel through the myelinated axon is depending on the nerve diameter. With decreasing diameter, there is an acceleration in conduction velocity. Additionally, the axon diameter determines myelination. Axons with diameter ≥ 1 µm are

generally myelinated, where smaller axons are ensheathed, a process describing a single Schwann cell wrapped around multiple small axons to keep axons separated by cytoplasm but not myelin [16]. It has been documented that the ratio between axon diameter and the myelinated nerve fibre maintains with a ratio of 0.6 – 0.7 disregarding the axon diameter, where bigger axons can be wrapped up to 300 times [17]. Myelin contains *in situ* 40 % water, 42 – 51 % lipids and 9 – 18 % proteins. As a membrane, myelin differs from other biological membranes, which are viewed as lipid-protein bilayers with an equal lipid-protein ratio [18]. About 70 % of the myelin protein in peripheral nerves consist of glycoprotein P0 [19]. Besides the myelin insulation, Schwann cells secrete trophic factors like nerve growth factor (NGF), brain-derived growth factor (BDGF), glial cell line-derived neurotrophic factor (GDNF), neurotrophin-3 (NT) and ciliary neurotrophic factor (CNF), and adhesion molecules, which support axon growth and attachment to the Schwann cell surface [16, 20]. Additionally, Schwann cells secret Desert Hedgehog protein which contributes to the formation of the protective perineurial sheath in nerves [16].

1.3 Common causes and symptoms of peripheral nerve injuries

Nerve injuries to the PNS are not given such high-profile consideration compared to the CNS, but the consequences arising from damage to the major peripheral nerves can often be life changing. In a ten year study of 5777 trauma patients, 2.8 % had an injury to at least one peripheral nerve [21]. As peripheral nerve injuries (PNIs) mainly affect the limbs (arms, hands, legs and feet), the effects on patient's life quality and daily routine can be severe. This does include physical pain, discomfort and functional defects over a period of years or even the whole life. The impact of such injuries psychologically is often underestimated as not measurable but showed to be dominantly present in patients after nerve repair [22]. Psychological consequences include depression and post-traumatic stress disorder often resulting from a range of different factors such as lifelong changes in cosmetic appearance of the limb or functional deficits making patients' feel worthless [23]. Additionally, PNIs have economic consequences. The costs for health care and loss of production for each patient with traumatic upper limb PNI alone was estimated to be 29,000 € and 75,000 €, respectively as recently revealed by a Swedish study [24].

PNIs are most often sustained in domestic, industrial and traffic accidents in which all age groups and health status can be affected [25]. Most PNIs occur during polytrauma where several body regions are injured, most likely through vehicle accidents. Severe motorcycle crashes often show the highest grade of PNI, for example crush injuries to peripheral nerves, as arising from undamped collisions and high driving speeds [26]. Physical reasons for peripheral nerve lesions are mostly based on laceration, stretch, traction, compression, injection, electricity or temperature. Injuries caused by lacerations can arise from for example glass shards, knives, gunshots or explosions. Although, nerve transections by glass or knives occur more likely in everyday life through, e.g. domestic or car accidents, combat injuries to peripheral nerves are of great concern nowadays due to the global war on terrorism, e.g. in Afghanistan and Syria. A previous study on combat wounds reported that the most common cause of permanent disability was injuries to the limb [27]. Furthermore, explosions caused higher grade disabilities to peripheral nerves than gunshots [27] which is of particular concern as blasts were the most frequent cause of injury [28]. A recent examination of Pakistani soldiers further revealed that the ulnar nerve was the most frequently injured nerve in combat followed by the sciatic nerve [28].

Stretch and traction nerve injuries appear when the peripheral nerve is placed under high stress for a prolonged time or if rapid nerve elongation occurs. It was found that the quicker the nerve was elongated, the more the elongation tolerance decreased. This fact was shown by Haftek (1970) and Rydevick (1990), who elongated rabbit tibial nerves at different velocities. Haftek stretched the nerves 0.5 mm per minute and measured an average ultimate strain of 55.7 % [29]. In comparison, Rydevick elongated the nerves twice as much within the same time (1 mm/min) and noted a lower ultimate elongation of 38.5 % [30]. If peripheral nerves are elongated at their failure points, the nerve can be torn apart, which would indicate the most severe grade of nerve injury. However, clinical prognoses of stretch and traction PNIs are satisfying with spontaneous recovery rates of 65 to 85 % [31]. Besides stretch caused peripheral nerve lesions, compression injuries have severe effects on nerve health. Compressions generally affect the blood-nerve barrier, which makes the nerve vulnerable due to the lack of sufficient protection. Typically, fluid is accumulated in the injured nerve causing swelling and pressure within the nerve [32]. One of the most common examples of peripheral nerve compression is

carpal tunnel syndrome followed by cubital tunnel syndrome, which mostly affect people conducting repeating motions of the hand as for example carpenters or musicians [33, 34]. Common clinical treatments for nerve compressions comprise the reduction of pressure within the nerve whereupon nerve self-recovery can take place.

In industry and households, PNIs often occur through electricity and heat. The severity of electrical nerve injuries depends on the type and density of the current, exposure time and contact area [35]. Furthermore, electrical shocks are often followed by thermal tissue and nerve damage that can be deep on the skin surface occurring at skin contact points [36]. Thermal nerve injuries alone can be caused by a range of hot elements like fluids, steam or flames. Again, the severity of injury can differ from temporary damage with natural occurring self-regeneration to complete functional loss caused by complete tissue destruction, (e.g. through flames) [31].

Injections can additionally cause PNIs as a complication of intramuscular drug administration [25]. PNIs caused by injection were estimated at 0.03 to 1.4 %, where the ulnar, brachial plexus, radial and sciatic were the most commonly affected nerves [25, 37]. Anaesthetics, which are applied locally near the nerve, which innervates the target surgical area and numbs it, can damage peripheral nerves especially when applied in high doses and over prolonged exposure. In 2013, Farber et. al demonstrated the severity of PNIs caused by local anaesthetics in rats. Three different local anaesthetics were injected intravascular into the sciatic nerve and pure saline injection was used as the control. The study showed that drug injection resulted in much more severe PNIs (Sunderland grade 6) compared to the saline control (Sunderland grade 3) [38].

Besides accidents and trauma, diseases affecting nerve health are of high clinical importance in nerve regeneration. The nerve can be affected in different ways and severities depending on disease pathogenesis. Peripheral neuropathies can be caused by diabetes, infections like human immunodeficiency virus (HIV) or leprosy, can be induced through toxins including chemotherapeutic drugs or can be damaged through autoimmune disorders [39]. Neuropathies in general are of high profile concern as a large number of patients are affected. It has been reported that 60 % of diabetic patients suffer from diabetic-associated neuropathies [40]. Additionally, neuropathies affecting sensory nerves are the most common neurological conditions in HIV infections having an

impact on one-third of patients [41]. Primarily, the symptoms of neuropathies are treated instead of the underlying degeneration of axons due to the missing knowledge on pathway mechanisms involved in this process [39]. Protective treatments for neuropathies arising from the application of chemotherapeutic drugs are additionally missing. Such treatment would be of special importance to protect sensory neurons in dorsal root ganglia which are particularly vulnerable to toxic agents as they lack the protection from the blood-brain barrier. As DRGs are connected to capillaries with fenestrated walls, toxic compounds can easily passage and damage neurons [42].

Furthermore, autoimmune disorders that cause peripheral nerve damage and myelin degradation like Guillain-Barré syndrome are one of the most common paralytic neuropathies. It has been reported that approximately 100,000 people worldwide are affected by this disease which has severe consequences such as paralysis that in 20 – 30 % of all cases results in respiratory failure [43]. Although a number of treatments for Guillain-Barré syndrome have been developed (reviewed in [43]), they were not efficient in a wide population of patients. The urge to understand disease development to develop selective treatments has become rather pressing as has been highlighted recently by the association of Zika virus infection in Latin America with Guillain-Barré syndrome [44]. Additionally, neuropathies are frequently seen in cancer patients and the related pain is a leading cause of pain associated to cancer [45].

1.4 Wallerian degeneration and nerve recovery

Wallerian degeneration (WD) is named after Augustus Waller, a British neurologist, who described the process of glossopharyngeal and hypoglossal nerve degeneration after the nerves were separated from the brain and spinal cord in the frog [46]. Waller was the first in his field who described a degeneration process distal to the injury site and from this time on, several scientists further described WD in more detail. In summary, WD describes the die back of axons, which are separated from its cell bodies, the clearance of cell debris in the nerve and the support of axonal regrowth by regeneration promoting factors (Figure 4). In many cases, complete axon regrowth stays incomplete due to long reinnervation distances and complications with maintaining the growth promoting environment. In PNIs classified with Sunderland grade 2 to 5, WD will take place. After injury, the axons do not regenerate immediately. A delayed axon degeneration of the rat

phrenic nerve was reported after 24 to 45 hours [47]. It is assumed that this process is further delayed in humans as suggested by Chaudhry and Cornblath (1992) who examined five patients and reported a complete motor and sensory loss on distal site after 10 to 14 days. It was also mentioned that WD occurred earlier with shorter distal stump and that nerve conduction was reduced earlier in motor nerve injuries than sensory [48].

After injury, the disconnected axons increase in size, swell, and cytoskeletons start to deform. Rising calcium levels in the neuron activate calpain, an enzyme responsible for the degeneration of axon and cytoskeleton [49]. As soon as distal axons degrade and the close contact between Schwann cells and axons becomes lost, Schwann cells will stop the production of myelin and upregulate genes responsible for cell proliferation [50, 51]. This effect has been associated with the transcription factor c-Jun, expression of which has long been known to be low or even absent in myelin cells [52, 53] but is strongly upregulated after peripheral nerve injury [54, 55]. C-Jun is now known to promote the downregulation of genes responsible for myelin-production such as Protein Zero and Myelin Basic Protein as well as myelin transcription factor Egr2 (Krox20) [56]. During the de-differentiation process, Schwann cells shed and start clearing up their own abundant myelin debris. This process is of particular importance as myelin debris contains proteins, in particular myelin-associated glycoprotein, that are inhibitory to axon regeneration [57]. In the first phase of myelin breakdown, Schwann cells themselves remove about 50 % of myelin in the first 5 – 7 days after injury [56]. In the second phase, macrophages phagocyte the remaining myelin debris [58].

Thereafter, Schwann cells start proliferating and reach a peak 3 to 4 days post-injury [59]. Schwann cells proliferate and migrate from both, the proximal and the distal stump, into the nerve lesion and align in their basal lamina tubes [60]. Together with the proliferation and alignment of fibroblasts, they form the so called “bands of Büngner”, which act like an aligned guidance substrate for regenerating axons [61]. In complete but small gap nerve transection injuries, it was shown that a cable from fibrin is formed between the proximal and distal nerve stump. This cable then acts as a guidance substrate to align fibroblasts and Schwann cells to form bands of Büngner [62, 63]. Although often forgotten in review articles on WD [57, 64], regenerating blood vessels

from the proximal nerve stump have been shown to play a major role in directing outgrowing Schwann cells to aligned bands between the proximal and distal nerve stump [65]. It has been highlighted that the hypoxic environment around the nerve lesion from disruptive blood vessels triggered a macrophage response by secreting vascular endothelial growth factor A. After two days of injury, macrophages were predominantly present in the nerve lesion (50 % of total observed cell number), followed by neutrophils (24 %). Only 5 % of cells present at the lesion were endothelial cells at this time point. However, on day 3, a significant increase in endothelial cells was found which had formed new blood vessels [65].

The main contribution to axon regrowth by Schwann cells is given by the expression of extracellular matrix (ECM) molecules, like laminin, and neurotrophic factors, which promote and support axon regeneration. Laminin is, after collagen, the most prominent ECM molecule in the peripheral nerve which expresses two of the 15 laminin trimers (laminin-211 and laminin-411) which expression is upregulated in Schwann cells after nerve injury. Laminin plays a direct role in neurite outgrowth and Schwann cell remyelination after degeneration by binding integrin and dystroglycan receptors that promote cell adhesion and establish a bond between cell's cytoskeleton and the ECM [66-68]. Schwann cells additionally secret trophic factors that help with axon survival and regeneration. This includes interleukin-6 expression of which is upregulated in neurons themselves but also in Schwann cells and other non-neuronal cells after injury. This indirectly triggers the regrowth of axons by causing the upregulation of regeneration associated genes in neurons [69]. Additionally, neurotrophic factors like NGF, BDGF and NT-4 are increasingly expressed after nerve injury [70]. mRNA expression of NGF is upregulated at the site of injury but also in the distal nerve stump, promoting neuron survival as well as axon regrowth [70]. After injury, NGF is upregulated in both fibroblasts and Schwann cells. Furthermore, WD causes an upregulated production of interleukin-6 (IL) in resident fibroblasts and enlisted macrophages, where leukemia inhibitory factor (LIF) is increasingly secreted in both fibroblasts and Schwann cells [69]. Apart from their immune functions, LIF and IL-6 promote neuron survival and axon regrowth. LIF has been additionally found to act as a growth factor for Schwann cells [71]. Although Schwann cells are one major promoter of axon regeneration, their activity and survival rate

declines within two months of WD, this absence is one contributor for failing long-gap nerve regeneration [64].

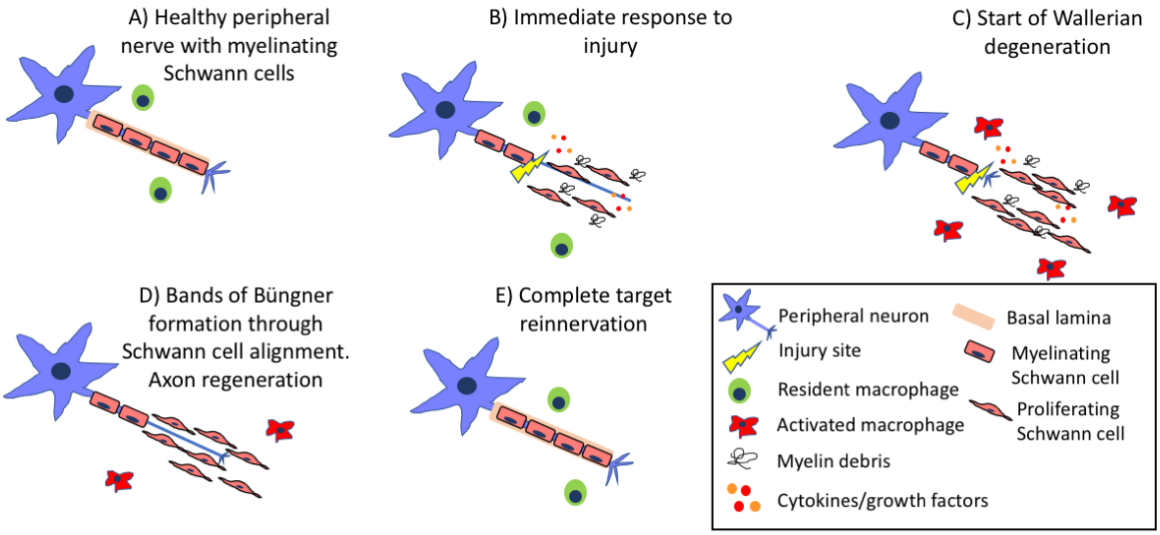

Figure 4 Basic illustration of Wallerian degeneration and axon regeneration

A) shows a healthy peripheral nerve with an intact myelinated axon. B) After injury, Schwann cells start to shed and myelin debris is present at the injury site. Schwann cells secrete neurotrophic factors and cytokines. C) Start of Wallerian degeneration. Clearance of myelin and axon debris with the help of activated macrophages. D) Schwann cells align to Bands of Büngner and axons start to regenerate. E) With sufficient environmental support, axons can regrow the entire distal stump and can achieve complete target reinnervation. Image layout inspired by Gaudet *et al.* [64].

Additionally, the blood-nerve barrier is affected after PNI for a period of about four weeks. Damages to the barrier are first only present directly at the injury site but will further extend to the whole axon when degeneration occurs. The barrier shows increased permeability and reaches peak values, where permeability is twice as high, after four to seven days [72]. Simultaneously, inflammatory responses reach their maximum. The increased permeability of the blood-nerve barrier causes the influx of repair mediating factors and cells. One task of these factors is the recruitment of macrophages to the distal injury site.

The immune cell response after PNI plays a crucial role in the regeneration process. Immune cells will eliminate remaining cell debris and myelin and promote axon regrowth. Neutrophils and macrophages arrive soon after injury, where lymphocytes

need 14 – 28 days to reach peak values [64]. The arrival of immune cells at different time points to the injury site contributes to the maintenance of an inflammatory response over months. Neutrophils infiltrate the distal stump after 8 hours and reach the maximum density after 24 hours. The neutrophils phagocytose cell debris and recruit monocytes, which further differentiate to macrophages. Macrophages pursue the same objectives as neutrophils and additionally clear damaged ECM and contribute to ECM remodelling. By inducing Schwann cell proliferation and the secretion of neurotrophic factors, they indirectly support a robust neurite outgrowth [73]. Furthermore, successful nerve regeneration is believed to depend on a rapid and effective macrophage response [64]. Lastly, T-lymphocytes infiltrate the injury site to promote cellular immunity by producing pro- or anti-inflammatory cytokines. Furthermore, it has been found that Schwann cells in the distal nerve secrete cytokines such as TNFα and interleukin-1α to further amplify the inflammatory response after injury [74].

1.5 Different classes of peripheral nerve injuries

Sir Herbert Seddon (1903-1977), a former professor for orthopaedic surgery at Oxford University, was the first in his field to shape the understanding of PNIs in 1941. He identified three categories to characterise and distinguish grades of PNIs. Neurapraxia, axonotmesis and neurotmesis differ in the number and severity of affected nerve parts [75]. Based on the classification system of Seddon, an improvement of this system was developed by Sydney Sunderland in 1951 [76]. He expanded the system by both concentrating on the nerve damage in general and by also involving the damage of the surrounding connective tissue. With increasing classification grades, there is an increase in severity of nerve damage and the surrounding tissue. Sunderland's classification system is still in clinical use nowadays. The following table presents an overview of the five grades of injury after Sunderland (Table 1), which will be described in more detail in the following paragraph.

Table 1 Summary of the five different grades of peripheral nerve injury according to Sydney Sunderland [76]

	Sunderland	Seddon	Damaged tissue	Wallerian degeneration	Recovery
Increase in severity ↓ Decreased chance of recovery	Grade 1	Neurapraxia	Axon	No	Full, rapid
	Grade 2	Axonotmesis	Axon	Yes	1 mm/day, depending on distal length
	Grade 3	Axonotmesis	Axon Endoneurium	Yes	1 mm/day, disturbed by scarring, axon misguidance
	Grade 4	Axonotmesis	Axon Endoneurium Perineurium	Yes	1 mm/day, disturbed by scarring, axon misguidance
	Grade 5	Neurotmesis	Axon Endoneurium Perineurium Epineurium	Yes	1 mm/day, disturbed by scarring, incomplete

1.5.1 Sunderland grade 1 – Neurapraxia

Sunderland grade 1, (described by Seddon as neurapraxia [76]) is the most harmless but also the least understood grade of PNI (Figure 5 B). All three protecting tissue layers are still intact in the nerve and only the axon is damaged while continuity is still preserved. Signal conduction on the injury side of the axon is disturbed due to partially damaged myelin or nerve compression. Interestingly, axon regeneration is so rapid that the

process cannot be described by WD, the degeneration process, which is taking place after PNI (see section 1.4, Chapter 1) [76]. Nerve conductivity is completely restored by, at the latest, 12 weeks [77]. Due to the rapid recovery, there are normally no specimens for histological evaluation available and hence the recovery process is less understood [76].

1.5.2 Sunderland grade 2 – Axonotmesis

If the endoneurial tube around the axon is still intact but the axon itself is severely damaged so that distal degeneration takes place (Wallerian degeneration), the injury grade is described as Sunderland grade 2 or axonotmesis (Figure 5 C). Functionally, a sensory, motor and sympathetic loss is noted [76]. Especially crush injuries are responsible for this axon dying and myelin degradation. Axon regrowth in the endoneurial tube is stated to be 1 mm per day [77]. Complete functional recovery is possible but depending on how proximally the axon is injured. In brachial plexus injuries, for example, the distance of axon reinnervation can be up to one metre, where regeneration would take two to three years. During this time, muscle fibrosis and atrophy already occurred and the reinnervation process can be strongly inhibited. In these cases, incomplete recovery is common [77].

1.5.3 Sunderland grade 3 – Axonotmesis

In this injury grade, the endoneurium is additionally damaged to the axon (Figure 5 D). Wallerian degeneration will take place as in grade 2. The disorganisation of the endoneurial tube can cause a misguidance of regenerating axons to their original and functional tubes. Spontaneous recovery is possible but accompanied haemorrhages, fluid accumulations and disturbed blood supply can lead to scar formation, which inhibits the regeneration process drastically [76].

1.5.4 Sunderland grade 4 – Axonotmesis

Injury grade 4 is described as similar to Sunderland grade 3 but with additional disruption of the perineurium, whereat nerve continuity is not disturbed (Figure 5 E). Nerve fascicles are not held together anymore and misguidance of regenerating axons is highly expected. The probability of scar formation is higher than in all other grades, which

makes this injury grade more severe, accompanied with a high possibility of incomplete recovery [76].

1.5.5 Sunderland grade 5 – Neurotmesis

Sunderland grade 5 or neurotmesis is the most severe grade of PNI, where spontaneous recovery is missing. In this case, all connecting tissue layers are disrupted and the nerve partially or completely torn apart (Figure 5 F). A complete functional loss is present. If the nerve gap is minimal, remaining Schwann cells and fibroblasts can infiltrate and guide the axons through the gap but with increasing gap size this process will fail and recovery will be incomplete. Like in grade 2 to 4, scar formation is a threat for the recovery process. Clinically, injuries categorised as Sunderland grade 5 will undergo surgery to restore nerve continuity [76]. The gap between the stumps is then critical for the selected repair technique (see section 1.6, Chapter 1).

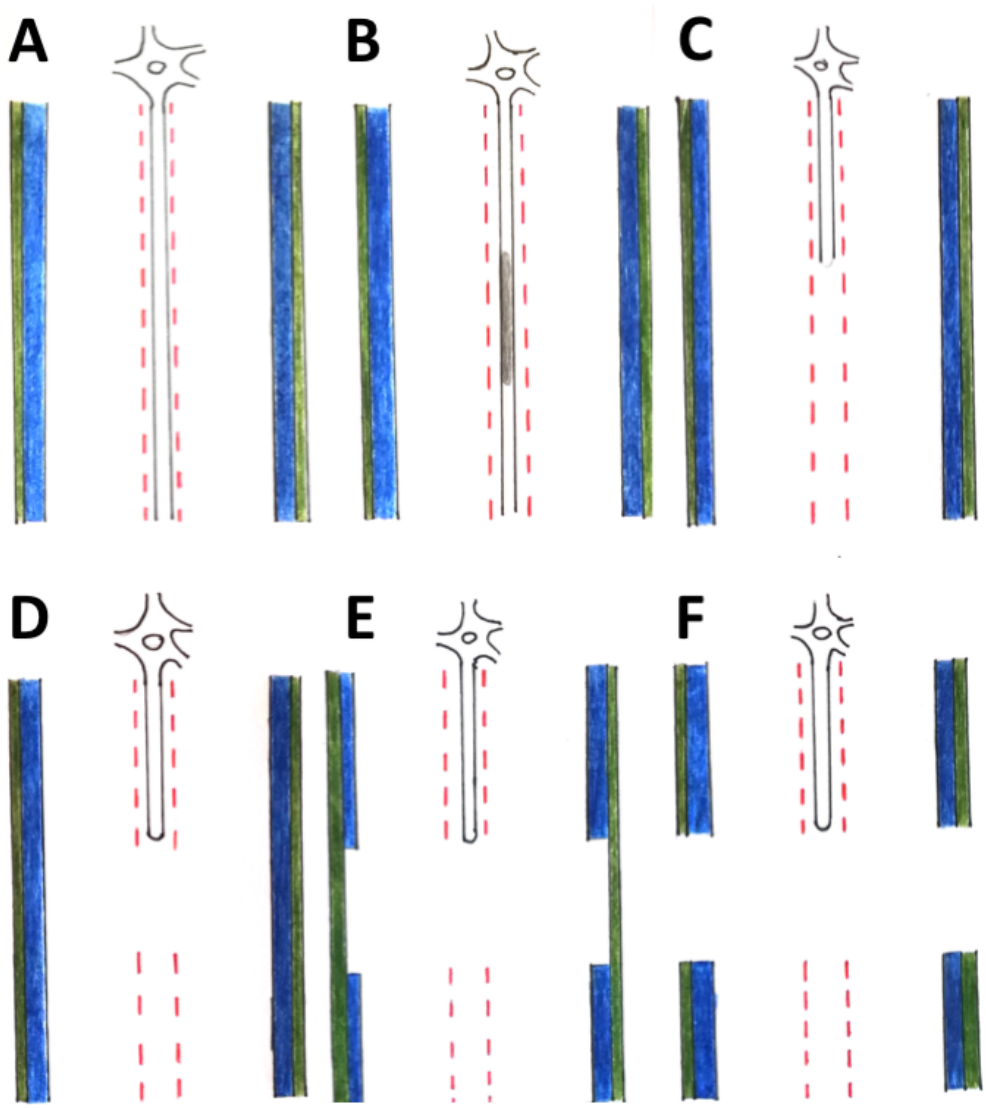

Figure 5 Sunderland's five grades of peripheral nerve injury

A demonstration of Sunderland's five grades of peripheral nerve injuries which increase in severity with increasing grade. A) demonstrates a healthy nerve with an intact endoneurium (red line), perineurium (blue) and epineurium (green), B) Sunderland grade 1 (neurapraxia), C) Sunderland grade 2 (axonotmesis), D) Sunderland grade 3 (axonotmesis), E) Sunderland grade 4 (axonotmesis) and F) Sunderland grade 5 (neurotmesis). Sunderland categorised Seddon's axonotmesis grade into Sunderland grade 2, 3 and 4. Injury grade 5, neurotmesis, is the most severe injury grade with a complete transection of the nerve. Image used with the kind permission of Laleh Louise Behbehani.

1.6 Current clinical treatment

In the clinic, the grade of nerve injury determines the chosen repair mechanism, where injury grades 1 – 3 will recover by itself, grade 4 and 5 need surgical treatment to result in successful nerve recovery [78]. In some cases, however, a specific injury grade is difficult to establish due to a lack of diagnostic tests and the presence of mixed injury grades. Surgical examination of the nerve is often essential to picture the severity of nerve injury in more detail [79]. The nerve gap length will then further determine the chosen repair technique. If the gap is minimal and most nerve tissue layers intact, end-to-end suturing is conducted through epineurium micro-suturing. In this process, tension at the suture sites needs to be avoided at all times including surgery and the following healing process [80]. Arising tension negatively affects the blood flow through the nerve and may result in inhibited regeneration [81]. End-to-end suturing is normally conducted 3 – 7 days after injury or as soon as the patient is presented to the clinician. In some cases, necrotic tissue around the nerve ends needs to be removed prior to suturing to enable the reconstruction of two normal-appearing nerve ends [79]. In general, a patient's poor health status or infected wounds around the nerve gap can result in delayed treatment which negatively affects regeneration outcomes [77]. This is often seen in patients who suffer from large nerve gap injuries. Furthermore, big nerve gaps require more specific medical attention than small suturable nerve lesions by using autografts or nerve guidance conduits (NGCs). In general, the rule of thumb recommends the reconstruction of human nerve gaps smaller than 3 cm with NGCs or autografts. If the gap size is greater than 3 cm, conduits cannot provide results as beneficial as autografts. In these cases, gaps will be bridged by autografts alone or by a combination of auto- and allografts (nerve graft provided by a human donor) [77]. With the use of grafts or even end-to-end suturing, blood vessels and nerve fascicles need to be aligned between the proximal and distal nerve stump to ensure an uninhibited ingrowth of regenerating cells [79].

In most injury grades, the time between injury and surgical nerve reconstruction is crucial for a successful and functional nerve recovery. If diagnosis of nerve injury is delayed by weeks, there is an increased risk of unrecoverable nerve damage. The influence of delayed nerve reconstruction on recovery outcomes has been shown

previously, where a reconstruction delay of four months resulted in a reduction of regenerating axons by 33 % [82, 83]. This delay can not only be due to delayed surgical treatment but is also influenced by the site of injury. More proximal nerve lesions comprise of a longer regeneration path for axons than more distal nerve injuries do. With a nerve regeneration rate of 1 mm/day [77], more distal nerve injuries, for example in the wrist, would recover over a distance of 100 mm in 100 days. On the contrary, a brachial plexus injury involves distances up to 100 cm for which recovery would take 2 – 3 years. Full functional nerve recovery can only be achieved if muscle tissue is still available at the motor end plate when axons reach the distal target effectors. This is dramatically depending on the time regeneration takes as muscle fibrosis and atrophy occurs immediately after nerve degeneration, where 60 – 80 % of the muscle will be lost after 4 months [77]. The success of nerve repair is further influenced by the patient's age which was shown to decrease the chance of successful recovery by 50 % [84]. Interestingly, this impaired regeneration was found to be caused by age-related changes in the neural pathways and target tissues but was not due to a limited growth capacity of neurons themselves or due to a lack in response to neurotrophic factors [85].

1.7 Autografts – Advantages and limitations

Nerve autologous grafts or autografts describe the harvest of a healthy nerve of the patient's own body and its transfer and implantation in the injured nerve gap. The very first documented use of autografts dates back to 1870 where Philipeaux and Vulpian conducted autografting in a 2 cm nerve gap in 7 dogs from which 2 animals showed promising results with successful regeneration outcomes [86]. Nowadays, autografts are still a frequently used technique in peripheral nerve repair and are even recognised as the gold standard treatment when bridging large injury gaps. Autografts are usually taken from a sensory nerve and are most commonly harvested from the sural nerve in the leg [87]. Although, there are also other reports on using other nerves like for example the medial and lateral cutaneous nerve of the forearm or superficial and deep peroneal nerves [78]. Furthermore, the type of nerve that is injured determines the graft repair technique used. There are single, cable, trunk, interfascicular and vascularised grafts. Single grafts describe the harvest of a donor nerve with similar diameter to the injured nerve where cable grafts comprise of multiple small diameter donor nerves that

are used to approximate a bigger diameter injured nerve [88]. The use of larger nerves for grafting is called trunk grafting which can be used to fit a large injured nerve with large diameter. However, this repair technique has been associated with poor functional outcomes due to fibrosis occurring inside the donor nerve due to missing vascularisation which acts like a barrier for regenerating nerves [88]. The use of interfascicular grafts was first described by Millesi *et al.* who reported on the bridging of nerve gaps by connecting single nerve fascicles of the graft with fascicles of the nerve stump [80]. Additionally, it has been shown that trunk grafts that underwent necrosis after implantation could be implanted as vascularised grafts by transferring connected veins and arteries with the graft which prevented the formation of necrotic tissue [89]. After the harvest of the autograft, Wallerian degeneration occurs in the graft, clearing up axon and myelin debris. The advantage of using fresh human nerve implants is the matrix and components they provide such as resident Schwann cells and their basal laminae, trophic factors and adhesion molecules and all three intact nerve tissue layers [77]. Considering a long nerve gap, the native nerve autograft can provide the best structural support and regeneration environment throughout the entire nerve lumen and over a long distance. Autografting was recommended to be conducted sooner rather than later but should be conducted within 6 months to ensure best recovery outcomes [90]. The choice of graft and graft location depends on the surgeon and on the location and severity of injury. In practice, nerve blocks on the to-be-harvested nerve are often initiated prior surgery to help patients understand the functional deficit resulting after the harvest [88]. However, autografts have limited availability which describes one of the multiple disadvantages with its use. It is known that one autograft alone is often not sufficient to bridge a larger nerve gap, so that multiple autografts are needed to bridge a single gap [91]. Although, it has been mentioned that around 30 – 40 cm graft material can be harvested from the sural nerve alone [88], it has been recently discovered that long autograft sections cause a cell change within the graft that impedes axon regeneration [92].

Although autografts are the current gold standard treatment in peripheral nerve repair, full functional recovery is not always guaranteed. It is known clinically that with each coaptation site (coaptation = aligning two nerve segments) there is a 50 % loss of axons. Autografts require two coaptation sites and therefore only 25 % of axons will regenerate into the distal stump. It is believed that there might be a further loss in regenerating

axon numbers due to muscle fibrosis and chronic axotomy [77]. Furthermore, Lee and Wolfe indicated that only 50 % of patients whose nerve gaps were bridged by autografts achieved full or useful function [93].

In addition, the harvest of an autograft is always associated with the sacrifice of a healthy and functional nerve, normally a sensory nerve for a more important (usually motor) nerve. As mentioned earlier, autografts often originate from the sural nerve in the leg. This sensory nerve is present in the skin around the heel and can also innervate the side of the foot with the little toe. In 2013, Hallgren *et al.* published a survey of 41 patients, who underwent sural nerve harvesting between 1973 and 2010, showing the functional impairments after surgery. More than 90 % of the patients confirmed a sensational loss around the operated area shortly after extraction and in half of the patients the sensory loss remained. Nearly 30 % complained about sometimes experiencing cold intolerance in the operated foot [87]. Despite the occurring functional loss on donor site, further physical consequences due to scaring and potential neuroma formation need to be taken in to account [78].

Furthermore, autograft treatment requires at least two surgical interventions, on the injury site as well as on donor site which goes along with a higher risk of complications, e.g. infections, scar formation and fibrosis [94]. This surgical risk has a greater impact on patient's health if PNIs occurred during polytrauma, which further compromised patient's health condition. On injury site, autografts often lack appropriate sizes to the injured nerves where nerve diameter and fascicle structure do not align [95]. Besides this potential size discrepancy, a functional mismatch exists when grafting motor nerve lesions. Sensory autografts are used by default although studies showed that motor nerve gaps achieved best regeneration outcomes when motor autografts were used [96]. This finding is supported by the study of Höke *et al.*, who discovered a difference in gene expression pathways between Schwann cells of sensory and motor nerves. This indicates that motor nerves are specialised in motor nerve regeneration and vice versa [97].

Nerve allografts taken from human donors were suggested as an alternative treatment to autografts to minimise surgical interventions and prevent the sacrifice of a healthy and functional nerve. The mixed use of auto- and allografts in large nerve gap injuries has already been established in clinics [77]. Although they are attractive devices for

nerve repair structurally, they contain foreign Schwann cells, which very likely will induce an immune response in the patient. Therefore, the use of allografts requires the intake of immunosuppressive drugs over years until the patient's own Schwann cells populate the allograft.

It is of particular note that although autografts are referred to as the "gold standard" in treating peripheral nerve injury gaps, in practice, outcomes are rather disappointing. Therefore, there is an urgent demand for alternative treatments, although so far, no alternative solutions have been found that result in equally good or even better functional outcomes in long > 3 cm nerve gaps [77, 92, 98-100].

1.8 Nerve guidance conduits – An alternative to autografts

NGCs are tubular devices which connect the proximal with the distal nerve end and provide a guided growth path for regenerating cells inside the conduit lumen. At the moment, the most active research in biomedical engineering is directed at the development of NGCs to study their suitability as an "off-the-shelf" alternative to autografts [100]. Thus far, the autograft gold standard is the only available technique that can support nerve regeneration over a critical 4 cm nerve gap in humans (1.5 cm in rats). The critical gap is defined by the degradation time of the fibrin cable that forms between the proximal and distal nerve stump and is essential for the regeneration of axons across the nerve gap. In humans, this fibrin cable degrades within 4 weeks and in rats within 2 weeks [101].

Thus far, the use of conduits overcame a series of disadvantages that have been associated with autografts such as donor site morbidity and sensory loss on donor site as NGCs do not require the sacrifice of a healthy nerve. Furthermore, it has been shown that NGCs decrease the risk of scar and neuroma formation in comparison to autografts [102, 103]. It is additionally believed that secreted neurotrophic factors accumulate in the tube lumen which might be beneficial for axon regeneration [104]. With the use of NGCs, the alignment of blood vessels and nerve fascicles can further be avoided.

Conduits can be fabricated from natural or synthetic biomaterials through a range of different techniques such as melt extrusion, injection moulding, electrospinning and UV or laser-based stereo-lithography. Material braiding or rolling can be alternatively used

for conduit manufacturing [104]. In general, the chosen process should enable easy fabrication of different tube designs such as diameter, wall thickness and length in order to address different nerve diameters and gap lengths. In 2015, Pateman *et al.* reported on the use of micro stereo-lithography for the fabrication of polyethylene glycol (PEG) conduits from photocurable PEG diacrylate [105]. Although the presented conduit was not suitable for clinical use as devices were not degradable, PEG conduits showed convincing performance as an experimental material for peripheral nerve regeneration. Of particular note is the demonstrated micro-structure topography on the conduit surface where aligned grooves altered the outgrowth orientation of neuronal and Schwann cells as well as the outgrowth of DRG cells in a longitudinal direction to the conduit length [105]. Furthermore, 3D-printed PEG conduits were biocompatible and showed regenerative support in a 3 mm mouse injury model, where axon numbers counted at the distal stump were similar to those with autograft treatment. Pateman and colleagues further highlighted that micro stereo-lithography describes an easy polymer processing technique while simultaneously resulting in detailed, high resolution structures [105]. The induction of surface topography on the conduits was additionally achieved by Jiang and colleagues who used electrospinning to manufacture aligned micro- and nanofibre conduits [106]. Conduit implantations in a rat 15 mm sciatic nerve gap revealed that fibre diameter influenced the regenerative outcomes, where the use of nanofibre conduits resulted in enhanced nerve regeneration as well as functional recovery compared to microfibre conduits. Neither conduit however resulted in comparable outcomes as autografts [106].

The optimal nerve regenerative support by nerve guides has been intensively discussed in the past with researchers identifying key requirements for an ideal nerve conduit. The chosen material if from synthetic or natural sources should be biocompatible and degradable in order to minimise immune responses and second surgery. The internal conduit diameter should be big enough to account for polymer swelling during the degradation process [107]. NeuraGen nerve guides are available in different sizes, where internal diameters vary between 1.5 and 7 mm depending on the application which could be considered as a benchmark for internal conduit dimensions [108]. The ideal degradation time of conduits is highly discussed and depends on nerve location, injury gap, the species and the age of the patient [109]. However, researcher agree that

degradation products must be non-toxic, non-immunogenic, non-mutagenic and non-carcinogenic and have to be excreted and should not accumulate in the body [110]. The push for using degradable materials for NGCs developed in particular after case studies reported on immune rejections and developed nerve compression syndromes in patients after the implantation of non-degradable silicone tubes [111, 112]. Furthermore, conduits should be rigid enough to support the injured nerve but should be flexible enough, with adequate wall thicknesses to withstand suturing and to hold sutures in place over time. This is of particular importance to allow movement and bending especially when the conduit is located over a joint [107]. The stiffness of the NGC should be close to the elastic modulus of native peripheral nerve which has a Young's modulus of around 0.45 MPa [30]. Porosity or permeability of the conduit walls is desirable to allow the diffusion of nutrients and oxygen to the injured nerve. However, the infiltration of myofibroblasts, which cause scar tissue formation, and inflammatory cells must be prohibited and robust axon guidance maintained [113]. The ideal pore size for conduit walls was defined as 10 – 20 µm, where pores bigger than 30 µm allowed an infiltration of inflammatory cells [114].

The next section will discuss the clinical performance of FDA approved hollow nerve guides.

1.9 FDA approved nerve guides

An entire research field has focussed on new designs and material combinations for novel NGCs. In this review, I will focus on devices which were approved by the American federal agency for Food and Drug Administration (FDA) and were declared as safe (Figure 6). The FDA is responsible for public health protection by controlling and supervising pharmaceutical drugs, medical devices and many more. Seven NGCs (Neuroflex/ Neuromatrix®, NeuraGen®, AxoGuard®, Avance®, Neurolac®, SaluTunnel®) and four nerve protecting wraps (NeuroMend®, NeuraWrap®, AxoGuard®, Salubridge®) composed of different materials and with different degradation properties were approved between 1999 and 2013. The majority of these devices consist of natural materials. Neuroflex/ Neuromatrix®, the associated nerve protection wrap NeuroMend®, NeuraGen® and the corresponding NeuraWrap® are made from type I collagen. The two device groups only differ in their degradation rates. Neuroflex/Neuromatrix® and NeuroMend® degrade

faster than NeuraGen® and NeuraWrap® in about 4 to 8 months [115]. Different opinions on NeuraGen® degradation times exist. Based on the distributors website the resorption rate is 9 – 12 months [108], where Archibald *et al.* (1995) and Schlosshauer *et al.* (2006) indicated a much longer degradation time of up to 4 years [116, 117]. AxoGen Inc. supply natural NGCs of collagen matrix derived from porcine small intestinal submucosa (SIS) (AxoGuard® and AxoGuard® wrap) and human decellularised nerve grafts (Avance®). Avance® grafts and conduits made from SIS last for a life time, just like endogenous nerves [118]. Synthetic approved conduits are available in three different materials, polyglycolic acid (PGA), poly-L-lactide-co-ε-caprolactone (PLCL) and polyvinyl alcohol (PVA). Neurotube® conduits, made from PGA, have the fastest degradation time of all FDA approved nerve guides with a complete material break-down in 3 months [116]. PLCL Neurolac® nerve guides degrade much slower and are fully resorbed after 2 years [119]. SaluTunnel® and the nerve wrap Salubridge® consist of PVA and are not resorbable. Although all the named devices received FDA approval, clinical data that proves functional efficacy, varies or is in some cases even missing.

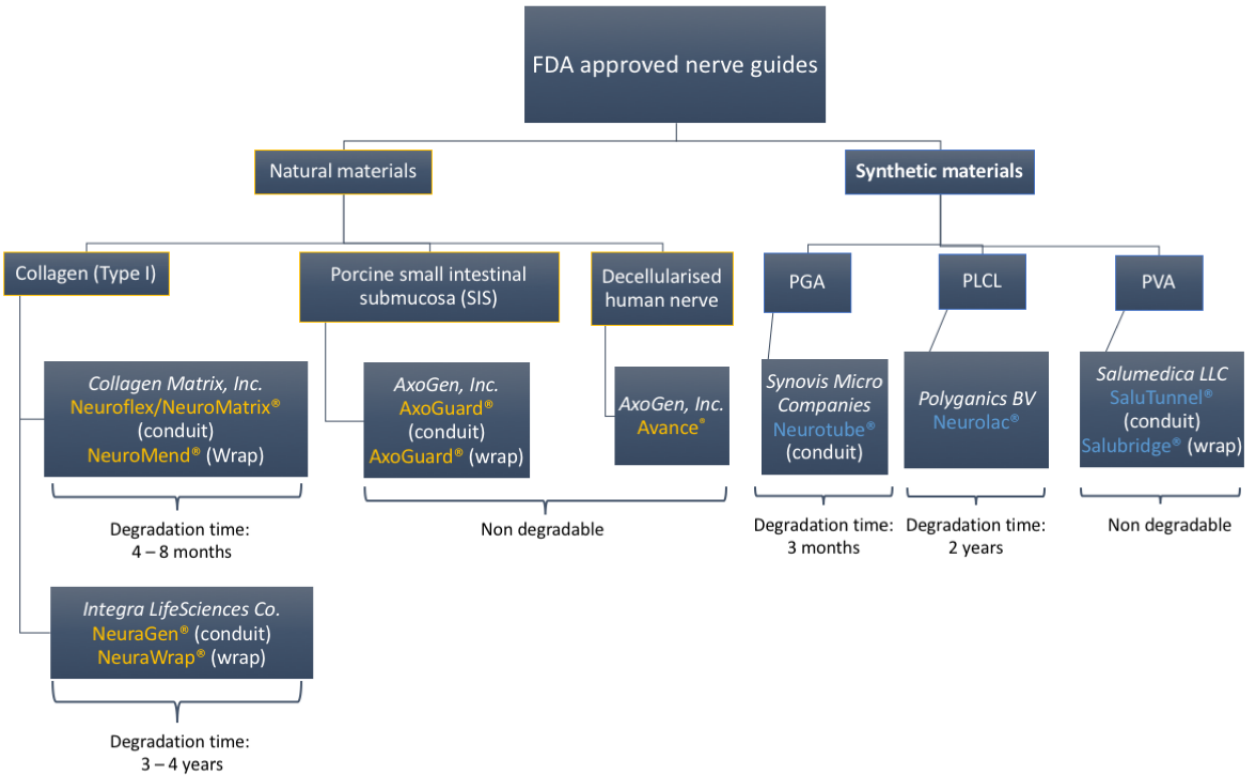

Figure 6 Diagram of FDA approved nerve guides

A hierarchical list of the seven FDA-approved nerve guides as well as four nerve wraps from different natural and synthetic materials. The degradability of devices depends on the chosen material as demonstrated.

The implantation success of NeuraGen® is well documented in several clinical trials [120-124]. The latest and most comprehensive data available was based on a follow-up study between 2002 and 2007 with 96 patients and 126 nerve lesions. A total of 35 – 45 % of 64 patients, seen for follow-up examination, achieved complete sensory nerve recovery [124]. In a pre-clinical study, Archibald *et al.* showed comparable results of NeuraGen® conduits to autografts in a 5 mm nerve gap in monkeys [117]. Clinical data and non-human primate studies showed functional success of NeuraGen® implantation but nerve gap sizes restricted in all cases to ≤ 2 cm. Additionally, it has to be taken into account that collagen from non-human sources might cause immune responses in patients as well as inflammation and in severe cases even guide rejection if not purified stringently [125]. Furthermore, naturally sourced materials bear the risk of irregular uniformity in the final product due to batch-to-batch variations [125].

AxoGuard® conduits are sold in standard lengths of 10 mm and can only bridge gaps less than 5 mm gaps [126]. The efficacy of this device could not yet be comprehensively assessed due to the lack of clinical data. Furthermore, graft-versus-host disease or disease transmission remains a risk when implanting conduits derived from porcine SIS [114]. In contrast, Neurotube® made from PGA, shows a broad set of clinical data. Rosson *et al.* reviewed nerve regeneration outcomes in patients in Maryland, US, who underwent nerve reconstructions with Neurotubes® between 1999 and 2006. Six patients with a mean age of 47 years (9 – 61 years) were identified with nerve gaps averaging 2.8 cm (ranging from 1.5 cm to 4 cm). All patients regained some degree of motor function [127]. However, a randomised clinical trial highlighted that Neurotubes® were only as efficient as autografts in gap lengths smaller than 2 cm [128]. Furthermore, Schlosshauer *et al.* called attention to PGAs quick breakdown and released degradation products. The degradation of PGA yield in pyruvate, glycolates and finally H_2O and CO_2 that causes a decrease in pH which acidity, if not neutralised, can cause serious cell damage and necrosis [116]. PGA starts to lose its strength as soon as 1 – 2 months [129]. Considering a 4 cm nerve gap and an axon regeneration rate of 1mm/day, a gap innervation could ideally be completed after 40 days. The rapid PGA degradation hence may negatively affect the regeneration processes through structural impairments and degradation products. Additionally, PGA conduits are stiff, where the Young's modulus differs widely from the Young's modulus of native nerve (12.5 GPa in comparison to 0.45 MPa) [129]. In comparison, Neurolac® PLCL conduits are more elastic than PGA NGCs but still measure a Young's modulus of 3 GPa [114]. However, PLCLs degradation products are known to be less acidic than products released when PGA breaks down [130]. Polyganics reported a complete mass loss of Neurolac® after 2 years which was confirmed by a follow-up examination of implanted Neurolac® conduits in rats which showed a complete degradation of the polymer after 2 years. However, some degradation fragments were found near the epineurium and weren't metabolised at this time point. Immune reactions against these fragments were observed after 2 years of implantation [131]. Although the degradation of PLCL is comparably slow compared to PGA, a rapid material strength loss has been observed after 10 weeks. This early strength loss may result in insufficient support for nerve regeneration in long nerve gaps. However, Neurolac® is only an appropriate nerve guide choice for gaps smaller than 2 cm

[130]. Sufficient outcomes have been reported in gap lengths of 4 mm where treatment was suggested as a replacement to end-to-end suturing of the same gap length [132]. The same clinical study found that 2 cm nerve gaps could be treated equally well with Neurolac® conduits and autograft treatment. However, the performance of Neurolac® in longer defects is not confirmed [132]. Additionally, it has to be mentioned that Neurolac® has been associated with severe body responses and conduit swelling that resulted in complete lumen blockage. In addition, device collapse and neuroma formation highlight the limitations of Neurolac®. Furthermore, PLCLs inflexibility caused needle breakages while suturing and bears a risk of the nerve end being torn out of the conduit as a consequence of its rigidity [131, 133].

SaluTunnel® is the only synthetic FDA approved conduit which is non-degradable. The lifetime presence of the conduit may have critical side effects after nerve regeneration is completed such as nerve compression and might result in surgical conduit removal. No experimental or clinical data is available on the regeneration success using SaluTunnel® [134].

1.10 Internal conduit architecture – The importance of alignment

Bands of Büngner formed by fibroblasts and Schwann cells are the landmark for regenerating axons into a nerve lesion. In hollow conduits in particular, nerve regeneration depends further on the successful formation of a fibrin matrix between the two nerve stumps that forms from infiltrating tissue fluid and blood inside the nerve lesion [102]. If the fibrin cable fails to form a bridge between the two nerve ends, regeneration will fail respectively. This has in particular been observed in longer nerve gaps [102]. This might explain the poor performance of hollow conduits in critical nerve gap injuries as there is no support substrate to sufficiently guide cells through the nerve gap. The only structural support hollow conduits provide are the conduit walls which keep sprouting axons in the nerve lesion area. However, the misguidance of axons inside those devices which leads to regeneration failure or poor reinnervation outcomes is widely acknowledged [76, 135]. Autografts, however, were able to prevent this misguidance through their internal aligned basal lamina tubes which provided a growth path for regenerating axons and Schwann cells. The provided physical and biochemical

support inside the graft are the main reasons for autograft's reputation as the gold standard and hence used for bridging larger nerve gaps.

The present engineering challenge therefore is to improve the regeneration success of current hollow nerve guides in order to be a suitable choice for treating long and critical nerve gap injuries. This is further highlighted by the fact that nerve regeneration is fully dependent on the remaining living neurons which survived injury. This loss has been reported to be 40 % [98]. It is hence broadly believed that the incorporation of physical guidance cues like fibres, filaments or channels inside hollow nerve guides would improve current regeneration outcomes [62, 113, 136]. Such internal aligned structures would provide an increased surface area for cell attachment, migration and proliferation [136]. Furthermore, and more importantly, aligned internal scaffolds could reduce axon misguidance by providing a directional "growth path" for fibroblasts, endothelial cells, Schwann cells and axons (Figure 7). Such guidance substrate is of particular significance as it has been shown that axon growth is strictly dependent on the attachment of axon's filopodia and lamellipodia membranous protrusions to a solid surface [104]. Furthermore, an even distribution of the internal NGC scaffold would enable an even formation of bands of Büngner throughout the entire tube lumen and hence would result in a regenerated nerve of the same diameter as its original dimensions. It is of particular note that a regenerated nerve inside a hollow conduit is often visibly thinner than its dimensions on proximal and distal side [99]. This is caused by the fibrin cable forming into an hourglass shape which is particularly thinner in the middle than at its ends. It is known that this cable decreases in diameter with increasing nerve gap length [103]. Therefore, cell migration and axon regeneration is strictly limited to the thinnest cable portion. This further suggests that neural guidance inside hollow conduits is only provided by the forming fibrin cable and not by the conduit walls as is often mistakenly assumed. Only a few researchers have taken this effect into account with a large body of literature still addressing the importance of physical guidance cues on the inside of the conduit wall to enhance the performance of hollow nerve guides [137-139].

The alignment of internal NGC guidance scaffolds is additionally of critical importance in order to provide best chances of successful nerve recovery by artificially mimicking the aligned basal lamina tubes in native nerve and hence preventing axon misguidance and

providing the shortest guidance path through the nerve gap. The latter can be demonstrated with the mathematical definition of velocity which is described as a distance covered in a specific time. As the velocity of nerve regeneration remains constant with 1 mm regrowth per day, a shorter distance through the nerve gap, e.g. through highly aligned guidance features in comparison to unaligned structures, would reduce the regeneration time accordingly. NGCs with an adequate aligned filler may then be able to bridge larger nerve gaps. A direct comparison of longitudinal and horizontal aligned collagen and laminin gels in silicone nerve conduits showed that longitudinal alignment significantly increased the number of myelinated axon through a 6 mm mouse sciatic nerve gap in comparison to horizontally aligned gels [140]. Additionally, the alignment of poly(acrylonitrile-co-methacrylate) nanofibres in nerve conduits was reported to promote sensory as well as motor axon regeneration and muscle reinnervation *in vivo* in comparison to randomly oriented nanofibres. It should be noted that a rat tibial nerve injury model with a nerve gap length of 1.7 cm was used, exceeding the critical nerve gap length in rats [141]. Four years later, Neal *et al.* implanted random and aligned laminin-coated polycaprolactone (PCL) nanofibres in a 10 mm tibial nerve defect in rats. Interestingly, both fibre scaffolds improved regeneration outcomes in comparison to the hollow nerve guide control irrespective of their alignment. However, aligned fibres restored motor and sensory function to significantly greater extent than randomly aligned fibres [142].

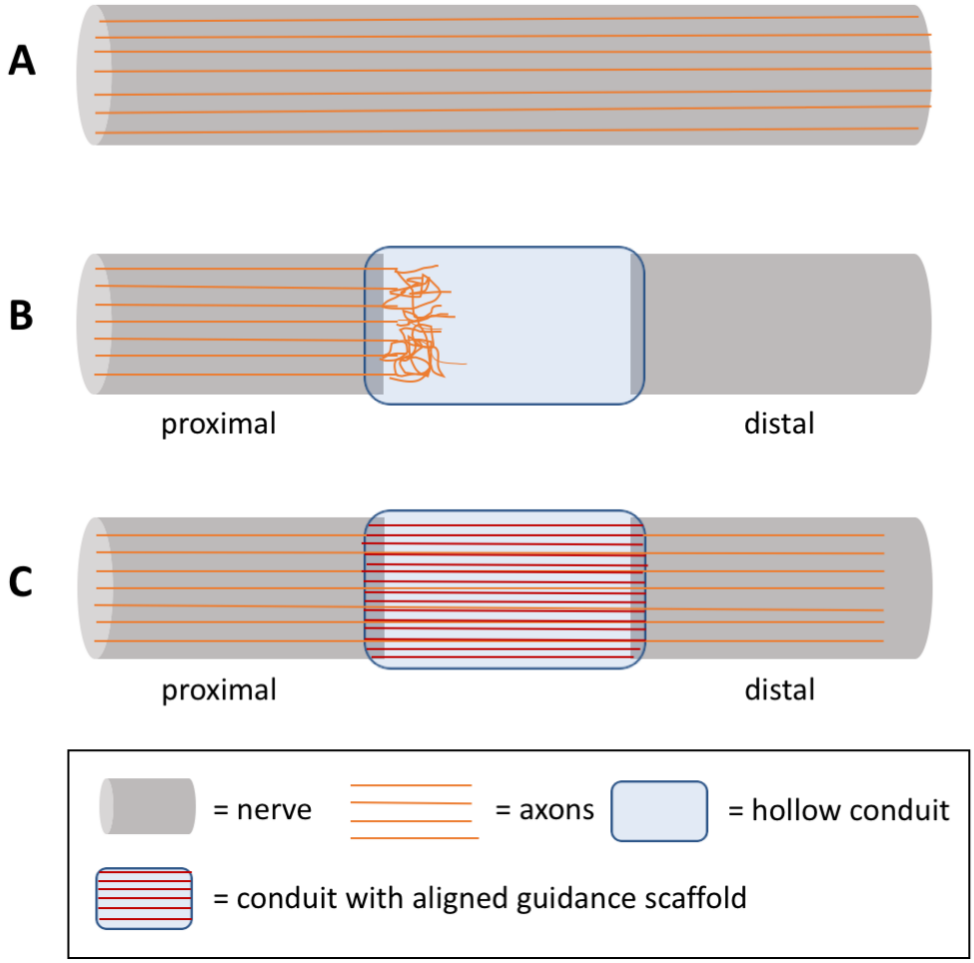

Figure 7 **The role of aligned internal scaffolds in hollow nerve guides for critical nerve gaps**

Simplified graphical representation of A) a healthy nerve with intact aligned axons (orange lines). B) An injured peripheral nerve displaying the most severe injury grade of neurotmesis. The distal nerve end has degenerated and the nerve gap is bridged with a hollow nerve guide (blue). From the proximal site, axons (orange) start regenerating but are unorganised and do not reach the distal nerve stump. C) The same nerve gap being bridged with a nerve guide and an internal aligned microfibre scaffold (red). Aligned and organised regeneration of proximal axons along the fibre scaffold with axons reinnervating the distal stump.

1.11 Aligned fibres as an internal scaffold for nerve guides

The previous section highlighted the advantages of internal conduit scaffolds, where this section will focus on the performance of internal fibre scaffolds to improve hollow nerve guide outcomes. Bands of Büngner, for example, can be mimicked much more easily in

the form of aligned fibres than using gels, sponges or films due to its longitudinal architecture [143]. Additionally, the density of fibres in a conduit can be tailored to specific regeneration needs like varying axon numbers in nerves, which isn't possible when using for example gels. Furthermore, fibre containing conduits don't require an adaption of nerve fascicles at the proximal and distal nerve stumps which could be necessary when choosing channels as an internal guide [79].

A considerable amount of literature has been published on the *in vivo* performance of internal NGC fibre scaffolds for peripheral nerve regeneration (Table 2). In 1997, Lundborg and colleagues reported on the implantation of eight 250 µm thick polyamide fibres in silicone tubes. A rat sciatic nerve injury model was used with a critical nerve gap length of 1.5 cm [144]. After four weeks of implantation, Lundborg *et al.* reported on regenerated sensory axons in the distal nerve end and a sensibility in pinch reflex tests. Myelinated axons were detected as well. Interestingly, in most samples, the silicone conduit alone showed an accumulation of fluid and no sign of axon regeneration with pinch reflex tests remaining negative as well [144].

Fibres from naturally derived collagen with much smaller diameter compared to Lundborg's scaffolds were implanted in 2000 and 2003 [145, 146]. Matsumoto *et al.* incorporated 50 µm thick collagen fibres in PGA tubes and implanted them in 8 cm peroneal nerve gaps in dogs. It is of note, that the chosen nerve gap far exceeded the critical nerve gap size and therefore outcomes are of high relevance. After 12 months, conduit outcomes were compared to healthy and injured nerves, which were not grafted with conduits. Histology and electrophysiology studies showed the reinnervation of target muscles in grafted nerve gaps, where non-grafted gaps demonstrated incomplete recovery. Regenerated myelinated axons were observed to be thinner compared to the healthy nerve control but axon numbers increased due to axon sprouting. After 10 – 12 months, dogs could walk without any sign of limping [146]. In a later study, collagen filaments of 20 µm in diameter were implanted in two different densities with 2000 or 4000 filaments without the use of a nerve conduit. Remarkably, fibres were implanted into a 3 cm nerve gap, far exceeding the critical nerve gap size of 1.5 cm in rats. Axons regenerated along the microfibres, where empty collagen tubes couldn't promote

regeneration. Additionally, the use of 4000 filaments resulted in a higher number of regenerated axons [145].

In a study in 2005, 16 aligned polylactic acid (PLA) fibres of 60 – 80 µm in diameter were incorporated in silicone or PLA conduits and filled with matrigel. Implantation was conducted in a 1.8 cm rat sciatic nerve gap. Fibres showed enhanced bands of Büngner formation and axon regeneration in comparison to the empty PLA and silicone tube control [147]. Five years later, in 2010, Koh *et al.* reported on the use of electrospun polylactic-*co*-gycolic acid (PLGA) fibre yarn as an internal guidance scaffold in PLA conduits. Fibre yarns comprised of 200 – 600 nm thick fibres and approximately 360 yarns were incorporated inside conduits. Yarn-filled conduits were implanted in a 1.5 cm rat sciatic nerve gap and compared to a hollow conduit and autograft control. All animals formed a nerve cable between the proximal and distal nerve stump when a yarn-filled conduit or autograft was used. In hollow conduits, nerve cables were formed in 80 % of the animals. It was furthermore noticed that 50 % of hollow conduits collapsed but this number was reduced to 10 % if yarn-filled conduits were used. At the mid-section of the nerve cable, significantly larger axon diameters were found in the autograft control in comparison to both conduit samples. However, conduction velocity and amplitude measurements were similar between all implants. In all animals, a certain degree of muscle atrophy was found but the mass of reinnervated muscles measured was similar between autografts and all conduit devices. However, a major difference was detected in sensory recovery. Interestingly, only 42 % of animals regained thermo-sensitivity after the recovery period of 12 weeks, where all animals with yarn-filled conduits had already recovered sensory responses after 6 weeks. 50 % of animals with hollow conduits regained thermo-sensitivity after 12 weeks [148].

In 2011, Radtke *et al.* reported on an entirely naturally derived conduit device comprising of a decellularised vein graft with internal spider silk fibres. The implantation was conducted in adult sheep tibial nerves with a gap length of 6 cm. Results were analysed based on histological sections and electrophysiological studies. After 10 weeks post-surgery, no significant difference in functional outcome could be observed in comparison to the autograft control [149]. Aligned and random nanofibres as nerve conduit fillers were reported by Neal *et al.* in 2012. Fibres were inserted into fibrous PCL conduits and

applied in a 1 cm rat tibial nerve gap. Nerve gaps bridged with nanofibre-filled conduits showed best functional restoration in comparison to empty PCL conduits after 6 weeks. Comparing aligned and random fibres, aligned PCL nanofibres achieved best motor and sensory nerve recovery [142]. In the same year, Daly *et al.* published on the use of eighteen 50 µm thick collagen fibres incorporated in hollow collagen conduits to bridge 1 cm rat sciatic nerve gaps. After 16 weeks, it was found that more axons regenerated in conduits with fibre scaffolds than in hollow collagen tubes, where regeneration outcomes were similar to the autograft control. Interestingly, the degree of axon misguidance was decreased in fibre-containing conduits compared to the autograft control [135]. Fibres inside nerve conduits not only showed their advantages *in vitro* but also animal implantations resulted in promising outcomes suggesting that fibre-containing NGCs enhance nerve regeneration successfully compared to empty NGCs [135].

Table 2 Implantation outcomes of nerve guidance conduits with internal fibre scaffolds

Year	*Author*	*Animal species*	*Nerve*	*Nerve gap (cm)*	*Internal fibre material*	*Fibre size*	*Conduit*	*Control*	*Time passed until evaluation (weeks)*	*Evaluation techniques*	*Outcome*
1997	Lundborg *et al.*	Rat	Sciatic	1.5	Polyamide	250 µm	Silicone	Empty silicone tubes	4	Histology, Pinch reflex test	Regenerated and myelinated axons, positive pinch reflex test
2000	Matsumoto *et al.*	Dog	Peroneal	8.0	Collagen	50 µm	PGA	Healthy uninjured nerve, injured nerve without bridging de-	52	Histology, electrophysiology, walking study	Complete recovery, reinnervation with target muscles; walking without limping after 10-12 months
2003	Yoshii *et al.*	Rat	Sciatic	3.0	Collagen	20 µm	/	Collagen tube	4 – 12	Histology	Succesful axon regeneration, . unsucessfull regeneration in empty tubes
2005	Cai *et al.*	Rat	Sciatic	1.8	PLA	60-80 µm	PLA or silicone	Empty PLA/silicone tubes	10	Histology	Enhancend band of Büngner formation and axon regeneration vs. empty tubes
2011	Radtke *et al.*	Sheep	Tibial	6.0	Spider silk	?	Decellularised	Autograft	40	Histology, Electrophysiology	Results similar to autograft control
2012	Neal *et al.*	Rat	Tibial	1.0	PCL aligned and random	100 nm	PCL fibre conduit	Empty conduits	6	Histology, electrophysiology, motor and sensory tests	Better motor and sensory nerve recovery when using nanofibre-filled conduits vs. empty tube control
2012	Daly *et al.*	Rat	Sciatic	1.0	Collagen	50 µm	Collagen	Autograft, hollow collagen conduit	16	Histology, retrograde neuronal tracing	10 % of animals showed irritations; larger number of regenerated axons in fibre-filled conduits vs. hollow tubes

1.12 The role of fibre diameter and density inside conduits

The incorporation of aligned fibres inside NGCs has been shown to enhance the regenerative performance of hollow nerve guides *in vivo*. For this fibres of cellular and supracellular size ranging from diameters between 20 and 250 µm were predominantly used (see Table 2). More recently, literature has emerged that identified that fibre diameters of cellular and subcellular size might be more suitable to guide and promote axon and Schwann cell outgrowth in comparison to bigger fibre diameter. Although there is an agreement that supracellular size fibres of hundreds of microns are too big to support efficient cell outgrowth, the debate continues about the best fibre diameter range to manage critical nerve gaps. Herein, I would like to highlight three publications of different authors that showed the most relevant findings in this area and which conflictive views gave further indication on identifying the optimal fibre diameter range.

Wen *et al.* studied the relationship between five different filament diameters on the outgrowth of both axons and Schwann cells from postnatal day 1 rat DRG explants [150]. Polypropylene filaments of 5, 30, 100, 200 and 500 µm in diameter were arranged in fibre bundles and cultured for 7 days. An increased cell alignment of cells was identified with a decrease in fibre diameter. Furthermore, 5 and 30 µm filaments supported the outgrowth of axons and Schwann cells significantly better than 200 and 500 µm filaments. It has been strongly suggested that aligned fibres of 5 and 30 µm in diameter have significant potential in repairing critical nerve gap lesions similar to autografts [150]. Wang and colleagues further decreased the investigated fibre diameter to the size of nanometres, where electrospun PLA fibres of around 1.3 µm, 760 nm and 293 nm in diameter were investigated in chick embryo (embryonic development day 9) DRG cultures for 5 days [151]. A significant shorter axon length was associated with small 293 nm fibres in comparison to intermediate 760 nm and large 1.3 µm fibres, where differences accounted 42 % and 36 %, respectively [151]. Some years later, Daud *et al.* studied the relationship between 1, 5 and 8 µm PCL fibres and axon and Schwann cell outgrowth in mono- and DRG cultures [152]. Larger 8 µm fibres supported the outgrowth of axons significantly better than 5 and 1 µm fibres as revealed from NG108-15 neuronal cell monocultures. Interestingly, monocultures of primary rat Schwann cells showed different responses to the different fibre diameters, where Schwann cell's phenotype

was significantly more elongated on 1 µm fibres in comparison to 5 and 8 µm fibres. However, in DRG explant cultures no significant difference was found between axon and Schwann cell outgrowth distance and 1, 5 and 8 µm fibres [152]. All three studies indicated that the fibre diameter influenced the outgrowth behaviour of axons and Schwann cells. Furthermore, it can be concluded that fibres should measure larger than a few nanometres as indicated by Wang *et al.* but should be smaller than 30 µm as shown by Wen *et al*. Daud *et al*. further indicated that axons and Schwann cells respond differently to different fibre diameter where no outgrowth differences were identified in DRG cultures [152]. This emphasises that an ideal fibre diameter to support optimal nerve regeneration is still elusive and that further research needs to be done to fill this gap. Additionally, and very importantly, very little explanation has been given on the relationship between cell outgrowth and fibre diameter, where a sophisticated justification still needs to be given.

In 2003, two studies highlighted the importance of fibre densities inside the conduit lumen and its effect on peripheral nerve regeneration. Although the publication of Yoshii *et al.* had its focus on the general performance of collagen filaments in nerve repair *in vivo*, they also investigated two different fibre densities. Collagen filaments of 20 µm in diameter were arranged in either 2000 or 4000 filament conduits and implanted in a 3 cm rat sciatic nerve defect. A greater number of myelinated axons was found at the distal end in 4000 filament conduits compared to 2000 filaments. Interestingly, the average diameter of myelinated axons was significantly larger in 2000 filament conduits versus 4000 filament ones. No regenerated axons were found at the distal end for empty collagen conduits [145]. Yoshii *et al.* proposed that a greater number of filaments enhanced the area for axons to regenerate on which would explain the increased number of myelinated axons in 4000 filament conduits but restricted the space for axons to get fully myelinated [145]. A more comprehensive analysis on fibre densities was conducted by Ngo *et al.* in the same year [153]. Silicone conduits were filled with PLA filaments to 3.75, 7.5, 15 and 30 % and implanted in a 1 cm rat sciatic nerve injury model. All conduits containing fibre scaffolds significantly increased the outgrowth of axons *in vivo* in comparison to the hollow silicone conduit control. Similar to Yoshii *et al.* findings, a greater fibre density resulted in an increased nerve cable area on the distal nerve site but where conduits with 3.75 % filling density showed a significant increase in

myelinated axon numbers in comparison to the control and 30 % filament-packed conduits. Furthermore, silicone conduits with 3.75 and 7.5 % filaments were implanted into a long gap 1.8 cm nerve lesion which surprisingly showed a reduction in axon outgrowth in comparison to the hollow conduit control. Ngo *et al.* suggested that too many filaments might increase the number of proliferating and migrating macrophages and fibroblasts in the tubes which might physically inhibit the outgrowth of axons. On the other side, it was observed that too few filaments clumped together in the centre of the conduit lumen and hence failed to provide enough guidance support [153]. Surprisingly, there has been little data on the influence of fibre or filament densities on peripheral nerve repair. Furthermore, far too little attention has been paid to the analysis of internal packing volumes if fibres were used as an internal NGC scaffold. A great number of studies used NGC fibre scaffolds but information is missing on fibre incorporation techniques to fill conduits, the validation of fibre densities in the conduits and the prediction of fibre densities prior to fibre incorporation [135, 145-148, 153].

1.13 Electrospinning

The idea behind the electrospinning process emerged more than 100 years ago when Boys discovered the process of electrospraying which described the formation of polymer droplets caused by electrostatic forces [154]. The first electrospinning process was invented by Formhals in 1934 [155]. Nowadays, solution electrospinning is a versatile technique to produce polymer fibres at room temperature, where fibres can be as small as a few tens of nanometres [156]. The first step towards the spinning of polymer fibres is the dissolving of the polymer in an appropriate solvent which then is charged with a certain polarity using a high voltage source. In general, the dissolved polymer is taken up into a syringe, which is topped with a needle and clamped into a syringe pump. The needle is further connected to a high voltage supply. The pump ensures the polymer acceleration in direction to a grounded collector of opposite polarity. By turning on the voltage source, an electric field is created which cause an electrostatic repulsion between like-charges in the polymer solution which changes the round-shaped solution meniscus at the capillary to a cone, called the Taylor cone. When the generated electrical field is strong enough it will exceed the surface tension of the polymer, forming a fibre jet that travels towards a grounded collector of opposite

polarity. Although the fibre jet appears stable during the spinning process to the human eye, high speed photography revealed that the fibre jet forms an unstable whipping motion on the way to the collector [157]. The solvent in the polymer evaporates on the way to the collector resulting in the collection of a solid polymer fibre. A stationary plate or rotating collector are the most common collector types used resulting in random or aligned fibres, respectively [158]. Furthermore, it has been reported that collector conductivity influences the density of collected fibres, where non-conductive collectors resulted in a lower density of fibres in comparison to conductive collectors [159]. Liu *et al.* explained the low-density distribution of fibres with a remaining charge in the fibre itself that causes the repulsion in-between fibres when non-conductive collectors were used. Conductive collectors, on the other hand, could dissipate the charge in the fibre which enabled a tighter packing of fibres on the collector [159].

During the electrospinning process, several parameters can be modified to manipulate fibre properties (see Table 3). The flow rate of polymer which defines the volume of polymer that gets pumped through the connected needle in a specific time, has been shown to influence the fibre diameter. An increased flow rate therefore leads to an increase in fibre diameter [160, 161]. However, if the flow rate reaches its maximum critical point, bead formation within the fibre may occur. Megelski *et al.* explained this with the increased fibre diameter that is too large to completely dry on its way to the collector [160]. The fibre diameter can furthermore be tailored by adjusting the distance between the needle and the collector, where longer distances result in smaller fibre diameters [162] (Table 3). This is due to the prolonged time that the fibre travels towards the collector which further stretches the polymer jet. Additionally, the concentration of the polymer solution is a critical component in the electrospinning setup as it affects solution viscosity, surface tension and fibre diameter (Table 3). Solution viscosity is a critical parameter and needs to be defined carefully. Less viscous polymer solutions might result in a fibre break-off before the collector is reached or might result in beaded fibres. This is due to the entangling of polymer chains in the fibre which is caused by the applied electric field and surface tension. Low polymer concentrations lead to the breakage of polymer chains into fragments which are the reason for the bead formation [163]. On the other side, more viscous polymer solutions might completely inhibit the formation of a fibre jet as the polymer flow inside the syringe/needle gets hindered,

where the polymer solution dries at the needle tip and blocks it [163]. A steady fibre jet is further dependent on a sufficient electrical field. It has been shown in the past that insufficient voltage may lead to fibre formation failure or to the formation of polymer droplets within the fibres [164]. In general, an increase in voltage results in a decreased fibre diameter (Table 3).

Table 3 Electrospinning parameters influencing fibre diameter

Fibre diameter	Spinning parameter
Increase	Increase in solution concentration
	Increase in polymer flow rate
	Decrease in needle to collector distance
	Decrease in voltage
Decrease	Decrease in solution concentration
	Decrease in polymer flow rate
	Increase in needle to collector distance
	Increase in voltage

Another way to spin fibres is by melt electrospinning, where the polymer is liquefied by melting. It is important to ensure that the polymer cools quickly enough to be collected as a solid and round fibre thread. A main advantage of melt electrospinning is the avoidance of hazardous and harsh solvents [158]. However, polymers need to be kept at elevated temperatures to maintain their liquid state. In general, melt electrospinning is a useful technique to fabricate larger fibre diameters in the micrometre range of about 5 – 200 µm [160]. This technique, however, is not suitable for spinning thermosensitive polymers and such that contain proteins, polysaccharides and nucleic acids [165].

Fibres consisting of a core and a shell can be fabricated by either emulsion or coaxial electrospinning. In emulsion electrospinning, the core and shell are separated by chemical means, whereas a core-shell phase separation is caused by physical means in coaxial electrospinning. This chemical separation is usually caused by a change in solution viscosity. A polymer fibre containing an active agent can be fabricated by emulsion electrospinning. Therefore, the polymer is dissolved in an organic solvent and the active agent in water. During the spinning process the solvent will evaporate and

cause an increase in solution viscosity. Through the established gradient in viscosity, water droplets carrying the agent will migrate into the centre of the polymer fibre resulting in a core-shell polymer fibre [166]. The spinning of lipophilic and hydrophilic polymers could additionally eliminate the use of solvents by using a water in oil emulsion. The distribution of polymer components in the fibres may be hard to control which is particularly unsuitable when used for drug delivery applications [167]. Coaxial electrospinning, on the other hand, results in a core-shell polymer fibre by keeping two polymer solutions separate from each other until the last moment through the use of two separate syringes and needles. During the spinning process, the "shell polymer" will enclose the "core polymer". Both, emulsion and coaxial electrospinning techniques are suitable and frequently used for the incorporation of drugs and proteins in the polymer fibre to act as drug-eluting device which releases the agent from either its shell or core through diffusion or degradation [158].

1.14 Fibre surface topography

The electrospinning process further influences the fibre surface morphology leaving behind a unique groove or pore like structure. Although this phenomenon has been studied in the past, most studies have only focused on the fibre diameter and did not address the nanotopographical features on fibre surfaces.

Nanotopographical features on fibre surface can be either caused by thermally-induced phase separation (TIPS) or vapour-induced phase separation (VIPS) [156, 160]. TIPS is based on the thermodynamic instability occurring in the polymer solution which could be caused by the decrease in temperature on the fibre surface and the loss of solvent in the fibre. This instability causes a phase separation between the solvent and the polymer chains in the polymer solution resulting in polymer- and solvent-rich areas. During the spinning process, the polymer-rich regions solidify, where solvent-rich regions leave behind nanotopographical features on the fibre surface [156, 160]. This effect was associated with high volatile solvents which vapour pressure influenced the formation of depressions on the fibre surface. Bognitzki *et al.* demonstrated that the replacement of the solvent dichloromethane (DCM) with chloroform reduced the likelihood of pore formation significantly. The authors explained this effect with chloroform's much lower vapour pressure compared to DCM [156]. VIPS, on the other hand, is caused by a rapid

cooling effect on the fibre surface due to the fast travelling speeds of the fibres and the evaporation of solvent. As a consequence, moisture in the air condenses and builds up to small water droplets on the fibre surface. This further causes a phase separation in the polymer solution to polymer- and water-rich regions as the water droplets act as hard spheres due to convection currents on the surface of the polymer jet [160]. As the fibre dries on the way to the collector, water droplets leave behind an imprint on the fibre surface in form of spherical pores [160]. The described water condensation effect has furthermore been found to be more pronounced in hydrophobic polymers [168]. The relative humidity present during the electrospinning process was identified to play a major role in the formation of such fibre surface depressions. Casper *et al.* and Schaub *et al.* both showed that humidity levels of less than 28 % resulted in smooth fibre surfaces where humidity levels higher than 33 % resulted in nanoscale depressions on the fibre surface [168, 169].

A few researchers furthermore investigated the direct effect of nanotopographical features on the surface of electrospun fibres on cell behaviour. Yang *et al.*, for example, studied how smooth and pitted PLA fibres influenced neurite outgrowth from PC12 neuronal cells [170]. The authors reported on a significantly longer outgrowth of axons on pitted fibres in comparison to smooth ones [170]. Additionally, Moroni *et al.* noticed that human mesenchymal stem cells showed an elongated cell morphology and increased cell proliferation on nanoporous poly(ethylene oxide terephthalate)–poly(butylene terephthalate) copolymer fibres versus smooth fibres [171]. Taskin *et al.* and Leong *et al.* hypothesised that the change in cellular response to fibre surface topographies is due to an increase in surface area which increases the number of anchoring points for cells to adhere and elongate on [172, 173]. Taskin *et al.* demonstrated with human umbilical vein endothelial cells (HUVECs) that cell adhesion markers vinculin and phosphorylated focal adhesion kinase were increasingly expressed in cells cultured on porous fibres in comparison to smooth ones. Furthermore, the authors reported enhanced proliferation rates on porous versus smooth fibres [173]. Leong and colleagues gave further insights on the enhanced cell attachment on nanoporous fibres by studying the amount of proteins being adsorbed to the fibres. They tested the adsorption of proteins from culture medium containing 10 % FBS and identified that nanostructured fibres bound 80 % more protein to its surface than

smooth fibres. This effect was associated with the increased surface area on structured fibres where surface areas measured 62 % greater than on smooth fibres. Hence, porcine esophageal epithelial cells attached with significantly greater numbers to fibres with surface structures in comparison to smooth ones [172].

Although some research has highlighted that nanotopographical features influence the behaviour of cells in form of attachment, morphology and proliferation, only very little research has discussed this effect when reporting on cellular responses to electrospun fibres. In addition, research on the subject of fibre nanotopographies has been mostly restricted to limited analysis on the surface features themselves, where a range of publications only reported on the existence or absence of surface features evident by scanning electron microscopy (SEM) images with no attempt shown to measure the existing structures [156, 160, 170, 174, 175].

1.15 Polycaprolactone and its use in peripheral nerve repair

Like other resorbable polymers, polycaprolactone had its prosperity in the 1970s and 1980s. However, during this booming period, faster degradable materials like PGA and PLA overran PCL fairly rapidly and so PCL lost its importance in the field of biomaterials [176]. Nowadays, PCL's slow resorption time is well appreciated especially in the field of tissue engineering and as a device for drug delivery. A commercial example is Capronor®, a contraceptive made of PCL which received clinical phase II approval in 1991. PCL capsules of 4 cm in length, containing levonorgestrel, were shown to maintain a contraceptive environment for one year [177]. Additionally, PCL has proven to be a popular choice for extending the degradation time of more quickly degrading polymers also due to its exceptional blending properties with other polymers. MONOCRYL® (Ethicon Inc.), for example, is a degradable suture material made from a blend of PCL and PGA that completely degrades within 91 – 119 days [178]. Neurolac®, as introduced earlier, is another example which comprises of a blend of PCL with PLA [119]. Furthermore, a new generation of PCL-PLA nerve guides with an internal micro-groove architecture are currently being tested in a phase I clinical trial at Manchester University (expected study completion by August 2019) [179].

PCL is a semi-crystalline polyester with the chemical structure presented in Figure 8. Usually PCL is used at molecular weights ranging from 3,000 to 80,000 g/mol [176]. It has a tensile strength of about 10.5 – 16.1 MPa, a Young's modulus of around 343.9 – 364.3 MPa and a high elongation at break coefficient of about 300 % [180]. Although materials with a similarly low Young's modulus of native nerve (about 50 kPa) were recommended for scaffold fabrications in peripheral nerve regeneration, other reports showed that rather stiffer materials supported the outgrowth of axons and Schwann cells [181]. The latter was highlighted by Tuft *et al.* who showed that neurite alignment and length increased with increasing substrate stiffness of up to 1500 MPa [182]. Furthermore, it was found that Schwann cells were relatively insensitive to varying substrate stiffness which ranged from 40 kPa to 4 MPa, where no significant changes were seen in cell morphology and the activation of mechanotransducers between the stiffness values tested [183].

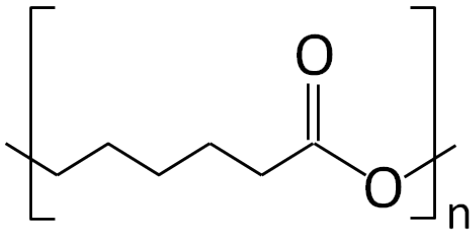

Figure 8 Structural formula of polycaprolactone

PCL's low melting temperature of 59 – 64 °C and solubility in a range of different solvents such as chloroform and dichloromethane make PCL a suitable polymer for solution and melt electrospinning applications. Furthermore, PCL is a bioresorbable material which makes it suitable for the use in medical devices. It is of note that bioresorption is often confused with biodegradation although both terms describe different processes. Biodegrading polymers will be decomposed by microorganisms but there is no evidence of elimination by the body. However, biodegradable polymers can also be bioresorbable which process describes a complete elimination of the polymer without occurring side effects [184]. Although PCL can biodegrade outdoors through bacteria and fungi, biodegradation in the human body does not occur through enzymatic pathways due to the insufficient availability of enzymes [185, 186]. Nevertheless, PCL is degradable *in vivo* but rather through a two-stage process of hydrolysis and intracellular degradation. First, ester groups in PCL are cleaved by water which results in a breakdown of long polymer

chains into smaller ones. The hydrolysis affects the amorphous regions of PCL which results in a molecular weight decrease but without causing changes in mass and shape as still hold together by crystalline regions. As soon as PCLs molecular weight drops below a certain threshold, the polymer falls apart at which stage macrophages clear up the fragments via phagocytosis [176]. In agreement with this, Sun *et al.* observed a decrease in PCL's molecular weight from 66,000 g/mol to 24,000 g/mol 480 days post-surgery of 2.3 cm long PCL capsules that were implanted under the skin of rats. It was noted that PCL maintained its strength at that point but showed first signs of strength loss as soon as the molecular weight dropped below 15,000 g/mol. A further decrease in molecular weight down to 8,000 g/mol caused the collapsing of PCL capsules to small pieces [187].

Degradable polymers can either break down via bulk or surface degradation. Hydrolysis in surface degradation or erosion is limited to the surface of the polymer where the molecular weight in the polymer bulk is maintained. This process results in a device thinning from the outside in. It has been mentioned that this process occurs if the rate of bond cleavage via hydrolysis happens faster than the penetration of water into the polymer bulk [176]. The break-down mechanism of PCL, however, was mostly described through bulk degradation [188-190]. Bulk degradation describes the entry of water into the polymer bulk where hydrolysis affects the entire medical device at once. [176]. Produced polymer mono- and oligomers diffuse out of the bulk establishing an equilibrium between the hydrolysis of chain cleavage and product diffusion out of the bulk. However, if this equilibrium becomes imbalanced, autocatalysis is likely to be provoked by hydroxyl and carboxyl by-products [176]. Relatively fast degrading polymers might therefore induce autocatalysis in the polymer bulk due to the relatively fast accumulation of acidic by-products which cause a localised decrease in pH which hence results in an accelerated break-down [110]. This process might cause complications as soon as the tissue surrounding the implant fails to buffer the acidic environment due to compromised metabolic activities and/or poor vascularisation [176]. This effect has not been associated with PCL, however, it has been observed in PLA and PGA which resulted in localised induced inflammation and foreign body responses [191, 192].

PCL owes its slow degradation time to its crystallinity and hydrophobicity that both slow down water penetration into the polymer bulk [193]. The degradation time of PCL

usually lies between 2 and 4 years, depending on the molecular weight used [188]. As degradation times are long, *in vitro* degradation experiments were often conducted as accelerated studies using acidic or alkaline medium. However, such experiments might be suitable for comparing degradation times of different PCL scaffolds or implants but fail to provide actual degradation times that apply to *in vivo* conditions. Therefore, physiological media such as phosphate-buffered saline (PBS) were recommended instead. The differences in translation between degradation studies in accelerated media and physiological medium has been highlighted by Lam *et al.* PCL (80,000 g/mol) stored in sodium hydroxide showed a complete mass loss of 100 % after 6 weeks. In comparison, an approximate mass loss of 20 % was reported on PCL stored in PBS at 37 °C after 60 months [188]. Nevertheless, most degradation studies looked at bigger PCL parts such as rods or squares in the millimetre to centimetre range. A degradation study of PCL nanofibres in physiological Ringer solution at 37 °C of PCL was presented by Bölgen *et al.* [189]. This study is of particular interest to the focus of this study and further highlights the differences in degradation time with different polymer mass. The authors showed that small fibres (196 nm in diameter) showed a 70 % mass loss after 6 months, where bigger fibres (689 nm in diameter) lost 35 % of their mass after the same time [189].

The degradation products of PCL are harmless resulting in 6-hydroxycaproic acid and acetyl co-enzyme A which are both eliminated via the citric acid cycle and excreted through the kidneys [194]. This has been further confirmed by Sun *et al.* who found traces of PCL in plasma after 15 days of implantation, where 95 % was excreted through urine and faeces after 4.5 months. The authors then injected radioactive-labelled PCL. Furthermore, radioactive traces found in heart, liver, spleen, lungs, kidneys, stomach, intestine, brain, ovary or uterus were not significantly different to the background readings [187].

1.16 Surface modification of biomedical polymers for tissue engineering applications

Surface characteristics such as chemical properties and surface topographies of a biomaterial scaffold determine material biocompatibility and furthermore over cell fate like cell adhesion, proliferation and differentiation. Cell adhesion to the biomaterial

scaffold is depending on a sufficient adsorption of ECM proteins like fibronectin and vitronectin to the surface of the scaffold from the cell culture medium *in vitro* or from physiological fluid *in vivo* [195]. Interactions between the cell and the protein layer on the scaffold surface are formed through integrin, a cell membrane receptor, which binds to specific domains on the adsorbed proteins such as the arginine-glycine-aspartate (RGD) and proline-histidine-serine-arginine-asparagine (PHSRN) domain. The surface properties of the scaffold hence determine the availability and accessibility of RGD domains for cell attachment [196]. The adhesion of proteins to a scaffold is furthermore favoured through rough surface morphologies; hydrophilic surfaces; positively charged surfaces that complement the negatively charged cell surface; scaffolds that present hydroxyl, amino, carboxyl, sulfonic or acylamino functional groups on their surface and surfaces with high surface free energies [197]. However, the adhesion of proteins to a scaffold surface is not only depending on material surface properties but also on the protein itself, where protein size, surface charge, stability and unfolding rate influence the adhesion process [197].

Although PCL, PLA and PGA are biocompatible polymers, their hydrophobic nature is often associated with poor cell adhesion and growth. Modifications to the polymer surface showed to be beneficial in increasing the attachment of proteins to the polymer scaffold by altering the material surface without affecting the polymer's bulk properties. Surface modifications of biopolymers should ideally be conducted at low temperatures, in a low or completly solvent-free environment and under low energy irradiation in order to limit degradation effects which could arise from chemical treatment, (e.g. solvents, acids, bases) or radiation, (e.g. UV, gamma rays) [197]. Furthermore, it is highly accepted that stabilised surface modifications are rather achieved through covalent bonding of functional groups to the surface than using physical coating methods [197]. The adsorption of proteins to polymer surfaces through physical coating has been shown with adhesive proteins such as collagen, fibronectin, laminin, vitronectin or ECM-like molecules such as gelatine and chitosan before (reviewed by [198]). Although the integration of such proteins to the polymer surface greatly enhances cell adhesion, the origin of isolated proteins from different biological sources might be of concern regarding a potential induction of an immune response when introduced *in vivo*.

Furthermore, protein coatings suffer from short lifetimes due to proteolytic degradation *in vivo* [197].

Alternatively, chemical modifications such as surface activation and functionalisation can be used. In general, polymer surfaces are activated prior to covalent bonding of ligands to the polymer surface by creating functionalities on the material surface. For this, alkali hydrolysis is commonly used to activate the surfaces of aliphatic polyester surfaces such as PCL [199]. This technique proved to be particularly valuable for the activation of three-dimensional (3D) scaffolds as small and highly mobile protons could penetrate easily inside porous 3D scaffolds. The treatment with bases such as sodium hydroxide (NaOH) induces a surface hydrolysis effect which results in polar hydroxyl and carboxyl functional groups on the polymer surface [199]. Although alkali hydrolysis treatment was found to enhance the hydrophilicity of scaffolds, its controllability is limited where prolonged treatment may lead to changes in polymer's physical structure and mechanical integrity [200].

However, the presentation of hydroxyl and carboxyl groups may be used to either directly bind ligands to the polymer surface such as ECM proteins, RGD peptides or other bioactive molecules like growth factors, or to further functionalise the material by mobilising specific functionalities like, e.g. amine groups [197]. The latter, so called aminolysis, has been used to either directly aid the attachment of cells through static interactions or to bind negatively-charged molecules, for example heparin, which has been used as an antithrombotic agent directly or as a delivery vehicle for binding cell growth factors [201-203]. A stable mobilisation of amine groups to the activated polymer surfaces can be achieved through 1-Ethyl-3-(3-dimethylaminopropyl)-carbodiimide (EDAC) and N-hydroxysuccinimide (NHS) coupling. EDAC interacts with carboxyl groups on the activated polymer surface by forming active o-acylisourea esters which then further react with NHS or sulfo-NHS to form stable amine groups [204]. In support of this notion, Koh *et al.* demonstrated the successful binding of laminin to PLA nanofibre mats through EDAC/NHS coupling after samples were activated with air plasma. This enabled the formation of significantly longer neurites in PC12 cells on laminin-coupled fibres in comparison to untreated nanofibres [205]. Furthermore, surface activation can be achieved through acid oxidation using for example Piranha solution, a 3:1 mixture of

hydrogen peroxide and sulfuric acid. Due to its strong oxidative effects, Piranha solution has been extensively used as a cleaning agent for the removal of organic compounds from metals, glass and silicone surfaces (as demonstrated, e.g. in [206] and mentioned in several protocols in [207]). However, this oxidative effect has also been used to modify hydrophobic surfaces to hydrophilic ones. On the surface of polydimethylsiloxane (PDMS), for example, the treatment with Piranha solution caused the formation of polar silanol groups and therefore enhanced the wettability of PDMS surfaces [208]. The formation of hydroxyl groups on polyvinylidene fluoride membranes has been furthermore used to bind amino groups to its surface through silane coupling agents containing amino groups [209].

Polymer surfaces can further be activated and functionalised by gas plasma. For this, low pressure gases like air, oxygen, argon, ammonia, sulphur dioxide or other organic compounds are introduced into a glass vessel under vacuum. Electric discharge, radio-frequency energy, heat, or microwaves ionise the gas into ions, protons, free radicals, electrons and gas atoms [197]. These created high-energy species bombard the polymer surface and subsequently cause an energy transfer to the material that results in chemical and physical changes on the substrate surface. There are generally two types of plasma: hot plasma and cold plasma. The first can be achieved at atmospheric pressure but has been associated with difficulties in maintaining the plasma treatment effect due to the thermal motion of molecules. Therefore, cold plasma treatments under vacuum are frequently used and are furthermore suitable for modifying surfaces of low-melting polymers such as PCL [210]. Gas plasma has the advantage of changing the polymer's surface functionality while retaining its bulk properties but furthermore eliminates the risk of solvent residues on the surface like the case in chemical treatments. However, the hydrophilic effect on polymer surfaces through gas plasma proved to be of limited lifetime [211-215]. Murakami *et al.* highlighted that this so called "hydrophobic recovery" effect is depending on the "ageing" medium the polymer is immersed in, e.g. water or air. The authors found that functional groups were either orientated towards the polymer surface or towards its bulk which was controlled by the surface free energy of the polymer itself and the ageing medium [216].

The positive effect of air and oxygen plasma treatment on cell attachment and behaviour in response to polymer surfaces has been reported on excessively in the past. The most common known example for the use of air and oxygen plasma is the treatment of cell culture polystyrene-ware which significantly enhanced the adhesion of cells. By the mid 1970s, most researchers only used plasma-modified tissue culture polystyrene (TCP) for the culture of cells over its hydrophobic unmodified form [217]. Recek *et al.* and Jaganjac *et al.* further associated the increase in cell attachment with the significantly greater adsorption of proteins from the cell culture medium after oxygen plasma treatment as demonstrated on polyethylene terephthalate surfaces with human osteosarcoma and epithelial cells, respectively [218, 219]. Thanks to its simple use, the treatment of polymer surfaces with air and oxygen plasma filled numerous reports with authors highlighting the improved cell-material interaction. Ni *et al.*, for example, demonstrated the great value of air plasma treatment on PLA nerve guides in a 10 mm rat sciatic nerve injury model with performance significantly increased regarding the area of regenerated nerve, number of blood vessels and myelinated axons in comparison to unmodified conduits [220]. Furthermore, Wang *et al.* showed that air plasma-modifed PLGA fibre scaffolds increased the attachment of neuronal PC12 cells and Schwann cells accompanied with an enhancement of Schwann cell proliferation and neuronal differentiation [221]. A positive effect associated with oxygen plasma-modified PCL scaffolds was additionally demonstrated by Yildirim *et al.* and Abbasi *et al.* on osteoblasts and mouse embryonic stem cells, respectively, where osteoblasts showed an accelerated differentiation behaviour, and embryonic stem cells showed significantly better viability and proliferation rates in comparison to unmodified PCL [222, 223]. Another report compared the effect of oxygen, ammonia and sulphur dioxide plasma-modified PCL scaffolds on HUVECs proliferation and attachment which showed that all plasma treatment methods significantly enhanced cell attachment and proliferation. However, oxygen and ammonia plasma performed significantly better than sulphur dioxide plasma in regard to HUVEC attachment and proliferation [224].

Polymer surfaces can further be modified with UV rays, where highly energetic UV lasers irradiate the polymer surface causing the breakage of C-C and C-O bonds. Subsequently radicals are formed which further react with ambient oxygen forming oxygen-containing functional groups on the polymer surface such as carboxyl and carbonyl groups [225].

In order to characterise the changes caused by gas plasma treatment or other surface modification techniques on surface morphology and chemistry, the five most popular analysis methods will be highlighted herein (Table 4). Morphological changes on the sample surface are mostly identified by SEM or atomic force microscopy (AFM). As the name already implies, SEM uses a focused electron beam to scan the sample in a specific raster pattern. This beam is either created by a cold or thermal field emission gun. The energy of the electron beam is transferred to atoms in the sample which cause a "scattering" effect of those atoms away from the electron beam. This produces amongst others secondary electrons and back-scattered electrons as well as X-rays. For high resolution imaging, secondary electron imaging is usually used due to their emission from the sample surface. Back-scattered electron images, on the other hand, are useful for analysis as the signal of those electrons closely mirrors the atomic number arising from deeper origins in the material [226]. AFM, on the other hand, uses a tip connected to a cantilever which runs along the sample surface. A representation of the surface morphology is recorded through a laser beam which is focused on the cantilever and deflects the movements of the tip that "feels" the sample surface. The same procedure can be used in "tapping" mode where the tip repeatedly taps the sample in a quick motion while moving along the surface. Due to the decreased number of contact points, this method is considered to preserve the sample more and be more accurate. Both techniques, SEM and AFM, have their advantages, SEM gives a high-resolution image of the sample and its surface, whereas AFM bears quantitative information about the sample surface and the height or depth of features like small ridges and pits. Furthermore, AFM can be operated on wet samples which allows the visualisation of cells on a material surface in its natural conditions without risking damage to their morphology during the dehydration process as required in SEM imaging [227].

In order to analyse the changes in chemical structures on a sample surface, attenuated total reflectance Fourier transform spectroscopy (ATR-FTIR), X-ray photoelectron spectroscopy (XPS) and time-of-flight secondary ion mass spectroscopy (TOF-SIMS) are the most commonly used spectroscopy techniques. ATR-FTIR uses an infrared beam which enters a crystal positioned underneath the sample. Based on the angle the beam enters the crystal, total internal reflection of the beam is achieved within the crystal. During this process, an evanescent wave is formed which extends beyond the crystal and

penetrates the surface of the sample. Parts of the wave will be absorbed by the sample surface which causes a loss in wave energy at frequencies identical to the sample absorbance. An absorption spectra is subsequently recorded at the detector [228]. ATR-FTIR has a sample penetration depth of about 0.5 – 5 µm depending on incident wave number [229]. Although this technique is suitable for the chemical analysis of many material surfaces, it is less suitable for samples where modifications only affect a few nanometres on the surface. Hillborg *et al.*, for example, reported on the thickness of PDMS surfaces that were affected by oxygen plasma which measured 130 – 160 nm [230]. FTIR-ATR, therefore, might show limitations in detection sensitivity. In support of this notion, it has been further mentioned that PLA and PCL in particular showed bulk IR absorptions so strong that characteristic peaks of certain functional groups on their surface could not be detected by FTIR-ATR [231]. XPS and TOF-SIMS, on the other hand, are suitable techniques to analyse chemical compositions of particularly thin surface layers as surface penetration depths measure around 1 – 5 nm and 1 – 2 nm, respectively [229, 231]. XPS analysis uses X-rays which bombard the material surface and will eject all atoms from their electron shells with binding energy less than the one of the X-ray. Finally, an electron analyser measures the kinetic energy of the emitted photoelectrons which correlates with specific functional groups and chemical bonds [232]. In comparison, TOF-SIMS provides even more sensitivity by analysing an even thinner surface layer. In this case, the material surface is bombarded with energetic ions which will cause a "sputtering" effect which describes the removal of single atoms or atom clusters from the material surface. Secondary ions form as part of the ionisation process of those sputtered elements and are accelerated to a certain kinetic energy. The time that secondary ions fly through a field-free space of certain distance correlates with their mass and is recorded on a detector. The mass of those ions is then used to identify chemical components present on the material surface [231]. Among XPS and TOF-SIMS, the latter is the more sensitive analysis method. However, regarding the analysis of chemical components on plasma-modified surfaces, XPS is the more frequently used technique. This was concluded from a PubMed search on either "("gas plasma" OR "oxygen plasma" OR "air plasma" OR "atmospheric plasma" OR "ammonia plasma" OR "sulphur/sulfur plasma" OR "argon plasma") AND XPS" or using the same search thread but including "TOF-SIMS" instead of "XPS". Between 1970 and 2018, 209 publications

were found that used any kind of the named plasma and analysed the surfaces with XPS. Only 13 reports matched those requirements on TOF-SIMS. It is of note that the search was narrowed down to hits that include the exact word order that was indicated with quotation marks in order to exclude hits that refer to plasma in blood.

Table 4 Overview of surface analysis techniques

Technique	Information on surface …	Qualitative	Quantitative	Technique characteristics
SEM	Morphology	X		High-resolution imaging of sample surface
AFM	Morphology		X	Information on surface roughness
FTIR-ATR	Chemical composition		X	Penetration depth: 0.5 – 5 µm
XPS	Chemical composition		X	Penetration depth: 1 – 5 nm
TOF-SIMS	Chemical composition		X	Penetration depth: 1 – 2 nm

1.17 3D models

Monolayer cell culture in two dimensions (2D) became a routine technique to grow eukaryotic cells with TCP being the most common growth surface. Ross Harrison was one of the first researchers to study the development of growth cones in frog neurons in a hanging drop of media outside the frogs body [233]. Later, researchers moved away from Harrison's pioneering but complex culture setup to the culture in polystyrene Petri dishes, well plates and culture flasks. Due to polystyrenes hydrophobic nature cells attached with limitations to the new culture substrates. Around 1970, corona discharge and gas plasma were first introduced to enhance the wettability of polystyrene culture-ware which is now a substantial part of every TCP product [234]. Today, well-established protocols and fast culturing and imaging techniques make monolayer cultures a convenient choice for culturing cells. However, the more complex the addressed scientific problem becomes, the more 2D cultures reach their limitations of representing

in vivo-like conditions. It is well known that cell-cell and cell-matrix connections are key factors in controlling homeostasis and tissue characteristics but these essential tissue-related functions are quickly lost in monolayer cultures [235]. Furthermore, hard and flat TCP or glass are a misrepresentative substrate for culturing cells in comparison to their softer native tissue environment [236]. As a consequence of flat substrate cultures, cells appear to have a much flatter morphology compared to in native tissue and further lose their differentiated phenotype causing a proliferative behaviour [237].

In contrast, animal models give a much more complex experimental environment as studies are conducted in whole organisms. Such use, however, is highly debatable due to ethical concerns and as animals do not recapitulate human physiology. In order to improve animal welfare and address or abate ethical concerns, Russel and Burch established the "3Rs" principle in 1959 [238]. The regulation focuses on the Reduction, Replacement and Refinement (3Rs) of animal tests by keeping up research quality standards. The Reduction of animal experiments aimd to use fewer animals for studies or to obtain more information from the given number of used animals. Refinements of animal experiments address the minimisation of stress and pain during experiments [238]. Furthermore, the principle aims to replace animals from experimental research with other methods such as tissue cultures or tissue slices. In the UK, the 3Rs principle is supported by the National Centre for the Replacement, Refinement and Reduction of Animals in Research (NC3Rs) [239].

Although animals are extensively used for evaluating drugs, toxins or medical devices, they often fail to represent human health responses. This has been critically reviewed by Hartung who highlighted that frequently used in-bred animal strains reduce the number of variables between animal populations due to close similarities between them [240]. Furthermore, he raised awareness about the common use of young animals which should keep down costs but ignores the important factor of arising health defects with increasing age [240]. The named arguments are only a small number of many more which demonstrate the difficulty of comparing animal and human health responses. Especially the testing of drugs and toxins in animals showed that results often do not show same effects in humans. A published report by the FDA in 2004 stated that only 8 % of all drugs that reach phase I clinical trials were produced for commercial use afterwards [241]. A

dramatic failure of animal tested drugs in humans was shown in 2006 in which six healthy men volunteered for a clinical trial of the TGN1412 antibody. This drug was stated to be safe in monkeys, where 500 times higher concentrations were used then intended in humans. Shortly after the antibody administration which was in fact of a much lower doses than in monkeys, resulted in multiple organ failure in the men [242].

In order to bridge those two extremes of primitive and flat monoculture studies and ethically questionable animal experiments with often limited human representation, 3D culture models could be the answer. These models can provide a "closer-to-*in*-*vivo*" environment in comparison to monolayer cultures and are ethically acceptable compared to animal studies. There already is a broad application field for 3D culture models for instance in cell differentiation [243-245], drug discovery and pharmacology [246-248], tumour and cancer biology [249, 250], cell adhesion and migration studies [251] as well as in apoptosis research [252]. 3D cultures are normally built using filter well inserts, sponges, gels, foams, microcarriers or tissue engineered models such as deepidermalised human dermis [253-256]. In native tissue, the ECM plays a critical role for cellular support and cell-matrix interactions. In order to mimic a close *in vivo* behaviour of cells, 3D models try to reconstruct this important matrix by using natural components such as collagen, laminin and agarose or synthetic substrates [257]. More complex and larger 3D culture models can be achieved by choosing either scaffolds from biomaterials or organ transplantation to culture which can be maintained as slices, in gels or semipermeable membranes. The latter in particular has seen large investigation in the field of brain and neural physiology [258]. Nevertheless, scaffolds from biomaterials need to be designed carefully to ensure sufficient elimination of cell waste products and exchange of nutrients and gas to maintain cell health [236, 259]. Porous scaffolds, for example, could help to achieve these requirements. Furthermore, the chemical composition of such biopolymers needs to be carefully chosen in regard to surface functionalities such as wettability to ensure sufficient protein binding for cell adhesion, and polymer stiffness to resemble the native tissue as closely as possible [260].

1.17.1 3D models for peripheral nerve studies – The use of dorsal root ganglia

The difference in neuron and Schwann cell response to 3D culture has been highlighted in several studies in the past. Furthermore, 3D cultures can accommodate a greater

number of cells as they exist in their native environment without inducing cell death in culture due to over-confluence. In the brain cortex, for example, neurons are highly packed together with 10^5 neurons per mm^3 [261]. Despite the missing three-dimensional architecture, 2D cultures could not cope with such high cell numbers on such a small space. Edelman and Keefer, for example, demonstrated that neurons grew longer neurites in a 3D collagen gel compared to neuronal monolayer cultures on glass coverslips [262].

However, 3D models in neurosciences are commonly addressed to the CNS such as for 3D reconstructions of the brain [263, 264], whereas the number of 3D culture models for peripheral nerve are rather small. Kraus *et al.* recently reported on the influence of a multi-layered environment on axon outgrowth and maturing in presence of Schwann cells. The authors compared the culture of neurons and Schwann cells in 3D spheroids to 2D cultures, where cells were covered by a collagen gel. A significantly longer outgrowth of axons was reported on neurons embedded in spheroids in comparison to 2D cultures [265]. Furthermore, Gingras *et al.* showed how 3D cultures can be used for myelination studies with implications for pathogenesis and neuron-Schwann cell interaction studies. Collagen-chitosan sponges were pre-cultured with fibroblasts and primary Schwann cells for 2 weeks, where primary motor neurons, extracted from the mouse spinal cord, were seeded on top of the cell layers. A stable 3D culture could be achieved without the addition of neurotrophic factors. Sensible motor axons extended into the collagen sponges and were myelinated by Schwann cells after 4 weeks of culture [266]. The use of a polymer scaffolds for building a three-dimensional growth environment for neurons and Schwann cells has been presented by Daud *et al.* [152]. The authors investigated the outgrowth of neurites and Schwann cells on PCL fibre scaffolds of varying diameters (1, 5 and 8 µm). The study showed that primary Schwann cells elongated the longest on 1 µm fibres, where neurites grew out the longest on 8 µm fibres. In rat DRG explant experiments, however, all fibre diameters supported the outgrowth of axons and Schwann cells with no differences. Furthermore, Daud *et al.* noticed a close physical relationship between the two cell types. The presented model was therefore suggested to have future value in fundamental peripheral nerve research as well as in scaffold development for peripheral nerve regeneration [152]. Although reported as a 3D model, the culture of cells and DRG explants was conducted on fibre mats which strictly

speaking only comprised of two dimensions. This study is an interesting example of the difference in interpretation of the third dimension between authors.

The use of dorsal root ganglia as, e.g. shown on the study of Daud *et al.* are a frequently used cell culture tool for conducting peripheral nerve studies. The key benefit of DRGs for cultures is its source of primary cells which comprise of sensory neurons, Schwann cells, satellite cells, macrophages and fibroblasts [267]. This arrangement of cells can either be maintained in whole DRG body explant cultures or dissociated through trypsin [39]. Often the use of DRG explants is preferred over the use of dissociated cultures; as explants maintain the native cell relationship between neurons and Schwann cells. This is of particular importance when studying axon/neuron and glial cell interactions as well as the degeneration and regeneration of axons [39]. Furthermore, Geuna *et al.* raised awareness that dissociated DRG cultures may induce great changes in the dissociated cell which raises caution for result interpretation [268]. However, adult DRG explants frequently showed limited cell outgrowth success also due to its tough surrounding collagen membrane which therefore made dissociation cultures an often-preferred choice [269, 270].

The use of DRGs in three-dimensional cultures for peripheral nerves has been reported by a range of authors. Huval *et al.*, for example, demonstrated its use for a model of pre-clinical physiological measurements. The authors developed a 3D nerve-on-a-chip model using rat embryonic day 15 DRGs which were placed on one side of a dual hydrogel channel. After 7 days in a specialised NGF-containing medium, axons populated the entire 3 mm long channels. This model demonstrated its suitability for the evaluation of new therapeutics regarding nerve compound action potential and nerve fibre density [271]. Furthermore, Vyas *et al.* presented a complex 3D model of peripheral motor nerve to study the involvement of growth factors in pathways of nerve regeneration in detail. For this, the authors connected spinal cord slices which motor neurons expressed yellow fluorescent protein (YFP), with grafts of peripheral nerves. A profound outgrowth of YFP-positive axons was observed from the spinal cord slices inside the connected nerve grafts [272]. In addition, evaluation studies of biomaterials for peripheral nerve repair benefitted, although rarely, from the use of DRGs. Bozkurt *et al.*, for example, evaluated a developed orientated collagen scaffold for peripheral nerve repair with the outgrowth

of 6 weeks old adult rat DRGs. DRG explants were cultured as hemisections on top of collagen scaffolds. After 21 days of culture, a mean axon outgrowth of 756 ± 318 µm and a maximum outgrowth of 1496 µm was reported [273]. Furthermore, Rangpappa *et al.* reported on the comparison of PLA microfilaments with and without laminin coating for use in peripheral nerve repair with new-born rat pup DRGs. After 8 days of culture, NGF-cultured DRGs measured significantly longer neurites on laminin-coated fibres (5.8 ± 0.2 mm) versus non-coated ones (2.0 ± 0.2 mm) [274]. Strictly-speaking, this DRG model was not conducted in three dimensions.

It might have become clear from the studies of Huval *et al.* and Rangpappa *et al.* that DRGs from embryonic tissues are a frequently used alternative to DRGs from adult animals which are commonly isolated from rats, mice or chicks [39, 275]. The use of embryonic DRGs is highly driven by the high yield in neurons and glial cells and the profound enhancement in outgrowth success compared to adult DRGs [276]. A PubMed search on "chick DRG OR chick dorsal root ganglion OR chick dorsal root ganglia AND culture" revealed 587 publications which were published between 1970 and 2018. In order to exclude articles which studied the development or embryogenesis of chicks, the search parameters were refined to exclude the words "embryo development" and/or "embryogenesis" from the search which resulted in 405 hits. Regarding the use of embryonic DRGs for culture, chick embryos were the most frequently reported species as a source for DRGs, followed by rat embryos with 199 reports and mouse with 149 publications between 1970 and 2018 (search thread: "mouse embryo DRG OR mouse embryo dorsal root ganglion OR mouse embryo dorsal root ganglia AND culture NOT embryo development NOT embryogenesis" and "rat embryo DRG OR rat embryo dorsal root ganglion OR rat embryo dorsal root ganglia AND culture NOT embryo development NOT embryogenesis"). The translation, however, between embryonic and adult DRGs in regard to peripheral nerve repair and differences between species are still frequently asked questions. To the authors knowledge, there are very limited publications available that address this matter. However, an attempt has been made to still give some indications. In 1977, Scott found the same morphological and electrophysiological features between adult and embryonic mouse DRGs and furthermore reported that nerve fibres regenerated were comparable between adult and immature neurons [277]. Vogelaar *et al.* additionally studied axonal mRNA from embryonic and adult rat DRG

neurons, where similar levels of transcription for molecules involved in axon growth were detected [278]. There is even less evidence available to compare chick and rat nerve regeneration or DRGs with each other. However, there are some publications that might indicate similarities. Chick and rat embryos are similar regarding their time frame of development, where chicks hatch at day 21 and rats are born between day 21 and 23. In 1996, Matsuda *et al.* compared the development of neurons between chick and rat embryos. The authors found that the differentiation of bipolar neurons to unipolar neurons happened earlier in chicks (day 6) than in rats (day 14). Furthermore, 57 % of chick neurons showed unipolar morphology on day 14, where rats showed only 7 %. However, directly after birth, rats indicated the majority of unipolar neurons with 97 % in comparison to chicken with 87 % [279]. Furthermore, Ibanez *et al.* compared the biological and immunological properties of human, rat and chick NGF on human neuronal PC12 cells. Morphological changes, dose-response curves and maximal stimulation values were practically undistinguishable between the NGF from different species [280]. In a broader context, the effect of riboflavin-deficiency in chicken feed caused peripheral neuropathies to the animals which were equally observed in rats, mice, monkey and humans [281].

Furthermore, until development day 14, chick embryos are not classified as living animals in most countries. Therefore, the harvest of DRGs before this date does not require approval from ethics committees' due to the lack of pain perception until this day [282]. Additionally, chick embryos are an attractive choice from an economical point of view as the purchase of fertilised chick eggs are much more cost effective than the purchase of rodents.

Although information on the differences between chick and rat DRGs is lacking, new data has compared human and rat DRGs with each other [283]. Schwaid *et al.* studied the proteome of both human and rat DRGs and furthermore looked into differences in the proteome of DRGs when harvested from different locations in the spine (thoracic to lumbar region) [283]. The authors mentioned noticeable differences in morphology of harvested DRGs from different spine regions but proved that there were no differences in their proteome. 5245 proteins and 4959 proteins were identified in human and rat DRGs, respectively, from which about 80 % of proteins were detected in both species.

The authors stated that in most cases, DRGs from rat and human could be used interchangeably and further indicated that rat DRGs could generally be used as models for human tissue [283].

1.18 Summary

Peripheral nerve injuries are commonly caused by traffic, domestic or industrial accidents and can affect everyone and all age groups. Axons severed from neuronal bodies undergo Wallerian degeneration distal to the injury site, where blood and wound fluid fill the nerve gap and form a thin fibrin cable between the two nerve stumps. This cable aligns Schwann cells, endothelial cells and fibroblasts to bands of Büngner which guide the regeneration of proximal axons. Although autograft treatment is the gold standard procedure for treating nerve transection injuries, they have many drawbacks such as donor site morbidity. An alternative treatment is the use of hollow nerve guidance conduits from synthetic or natural materials. However, these fail to support regeneration in critical nerve gaps (> 4 cm in humans) due to missing internal guidance cues. To artificially mimic bands of Büngner, aligned guidance features and in particular microfibres, have been incorporated inside hollow conduits and have shown promising regeneration outcomes *in vivo*. Most degradable polymer fibres are, however, hydrophobic which limits interactions between the material and cells. Researchers overcame this issue with great success by using surface modification techniques such as air or oxygen plasma. The diameter and density of incorporated fibres have also been shown to further influence regeneration, however, little data has been presented so far and no attempt has been made on testing these parameters in a 3D nerve guide *in vitro*. Furthermore, it is difficult to compare existing data due to differences in experimental conditions. A comprehensive and reliable 3D model with an easy setup for peripheral nerve and in particular peripheral nerve regeneration is still urgently needed. Development of such a model would help evaluating, comparing and identifying ideal nerve guide scaffolds and would hence reduce the number of test animals for future evaluation *in vivo*.

Aims & Objectives

The work in this thesis had two key aims:

1. To develop an *ex vivo* model of peripheral nerve regeneration for evaluating and comparing different internal NGC scaffold design variables directly in a three-dimensional architecture of nerve guides.
2. Using this information, to identify an optimal PCL fibre scaffold for improving nerve regeneration inside a hollow NGC.

The work was conducted in the context of the 3Rs principles for reducing the number of test animals in medical research. As such, the development of an *ex vivo* model in the future will have the potential to directly compare NGC designs in a more physiologically relevant environment and lead to informed decision making on optimally performing NGC scaffolds prior to conducting a limited number of highly detailed animal studies.

The objectives of the thesis were divided into five parts.

a. To investigate the effect of electrospun PCL fibre morphologies of diameter and surface topography on neuron and Schwann cell behaviour analysed *in vitro*.
b. To develop a 3D model that utilised nerve conduits with internal fibre scaffolds to examine scaffold performance directly within NGCs using in *in vitro* cultures or *ex vivo* dorsal root ganglia.
c. To investigate air plasma treatment of PCL fibre scaffolds and its effect on material hydrophilicity and in turn neuron and Schwann cell outgrowth.
d. To further refine and develop the *ex vivo* DRG model, in order to improve reliability and accuracy, and further explore compatibility of the model for evaluating other scaffold materials (as PHA) and potential cell therapy approaches (as Schwann cells) inside NGCs to aid peripheral nerve repair.
e. To identify an ideal PCL fibre scaffold for NGCs by investigating scaffold variables of fibre diameter, fibre density and air plasma-modified scaffold surfaces.

Chapter 2 Materials & Methods

2.1 Fabrication of nerve guides

Three-dimensional conduits were fabricated by laser-based layer-by-layer 3D printing using microstereolithography. For this, polyethylene glycol (PEG) diacrylate (M_n = 700 g/mol, Sigma-Aldrich) was mixed with 4 % diphenyl-(2, 4, 6-trimethylbenzoyl)-phosphineoxide/2-hydroxy-2-methylpropiophenone 50/50 photo-initiator (wt/wt, Sigma-Aldrich) and mixed well. An image (1024 × 768 pixels) showing the tube cross-section (circle) was designed using the GNU Image Manipulation Program (GIMP, version 2.8). The image was uploaded to a digital micromirror device (DMD, Texas Instruments Incorporated, USA) with associated software (ALP-3 Basic, ViALUX GmbH). The beam of a 10 mW 405 nm laser (Vortran Laser Technology Inc., USA) was expanded and aligned while running through a spatial filter and a mirror set. The beam then reached the DMD and was reflected in the shape of the uploaded cross section image. The liquid pre-polymer was positioned under a motorized z-axis translation stage (Thorlabs Ltd., UK with associated software: APT software) with the stage mounted at the liquid-air interface. The z-stage moved down into the liquid polymer with an acceleration speed of 0.01 mm/s. The top layer of polymer on the stage was crosslinked while the stage moved down, building a three-dimensional crosslinked polymer tube. Once 5 mm tube length was reached, the laser power was turned off and the stage returned to its original position, carrying the complete 3D conduit structure (Figure 9). Unreacted pre-polymer was washed-off with isopropyl alcohol (IPA, Fisher Scientific UK). All fabricated structures were washed in IPA for 7 days with an IPA change every 2 days to ensure full removal of unreacted pre-polymer and photoinitiator. The internal diameter and wall thickness of conduits was determined with the “straight-line tool” in Fiji based on SEM images (see section 2.16).

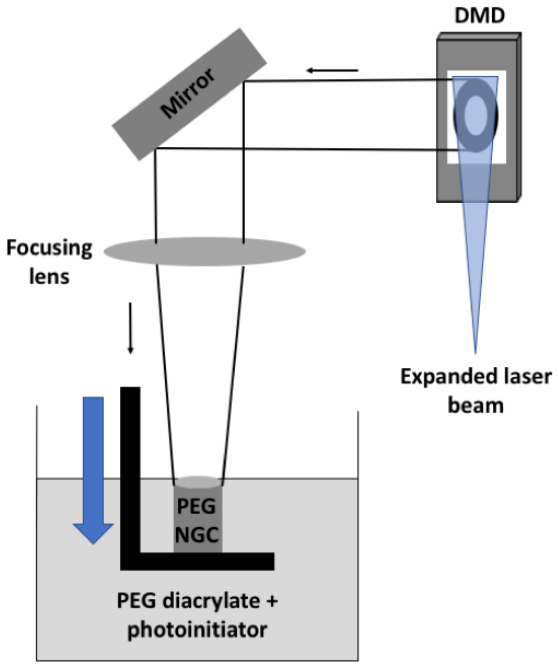

Figure 9 Microstereolithography setup

Illustration of PEG conduit fabrication by microstereolithography. An expanded laser beam reached the DMD and was reflected in the shape of the uploaded cross section image of the nerve guide (laser path indicates by small arrows). The liquid polyethylene glycol (PEG) diacrylate solution with photoinitiator was positioned under a motorized z-axis translation stage with the stage mounted at the liquid-air interface. The z-stage moved down into the liquid polymer (blue arrow), where the top layer of polymer on the stage was crosslinked while the stage moved down, building the three-dimensional crosslinked PEG tube.

2.2 Fabrication of aligned PCL microfibres

Aligned polycaprolactone (PCL) microfibres with average diameters of 1, 5, 8, 10 and 13 µm were fabricated by electrospinning. Fibres were made from PCL (Mn 80,000 g/mol, Sigma-Aldrich) at a concentration of either 10 % or 20 % in dichloromethane (DCM, vol/vol, Sigma-Aldrich) depending on diameter spun (see Table 5 for a parameter overview). A 1 mL plastic syringe with an internal diameter of 4.699 mm (Becton Dickinson) was filled with the PCL solution and topped with a 20 G blunt stainless-steel needle (Fisnar Europe). The needle was connected to a high voltage supply (Genvolt UK) and the polymer-loaded syringe placed in the mount of a programmable syringe pump (WPI-Europe). The polymer was constantly pumped through with a flow rate ranging from 1 – 20 mL/h depending on the desired fibre diameter (Table 5). Polymer jet

formation was achieved with a voltage of 10 or 18 kV (Table 5). The formed fibres were collected on an earthed rotating aluminium collector (IKA Works) wrapped in aluminium foil with a rotation speed of 2000 rpm. The collector to needle distance comprised 20 cm (see Figure 10 for an illustration of the electrospinning setup). Electrospinning was performed at ambient temperatures with humidity levels ranging between 33 and 37 %. For cell culture experiments, 1 mL of polymer solution was spun per aluminium sheet. The characterisation of microfibres using scanning electron microscopy (SEM) was performed on sheets with a lower density of fibres, where fibres were spun for approximately 30 – 40 s (see section 3.3.1 for more details on fibre characterisation).

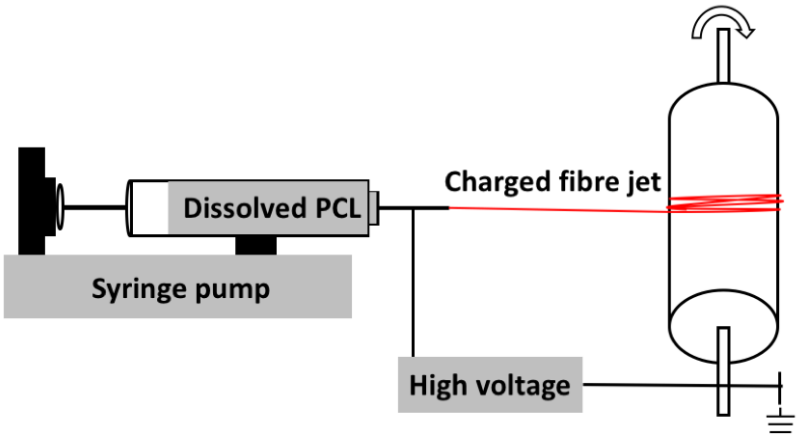

Figure 10 Electrospinning setup

Illustration of the used electrospinning setup. The dissolved PCL polymer was loaded into a plastic syringe topped with a blunt needle and connected to a syringe pump. The needle was connected to a high voltage supply and the collector grounded. A charged fibre jet formed between the needle and the collector and was collected on aluminium foil surrounding the collector.

Table 5 Electrospinning parameters

Average fibre diameter (µm)	% PCL in DCM	Flow rate (mL/h)	Voltage (kV)	Collector speed (rpm)	Collector to needle distance (cm)
1	10	1	10	2000	20
5	20	4	18		
8	20	6	18		
10	20	9	18		
13	20	20	18		

2.3 Preparation of aligned PCL microfibre scaffolds for cell culture

Electrospun microfibre sheets were cut to 15 × 15 mm squares and carefully removed from the aluminium foil using tweezers. To avoid the fibre scaffolds floating in cell culture medium, scaffolds were glued down using a silicone-based aquarium sealant (King British, UK). Stainless-steel rings (1 cm^2) were used to seed cells in a defined area on the scaffolds. Depending on the performed assay, fibres were glued to the middle of a well of a 6-well plate or directly to stainless-steel metal rings. Therefore, a thin layer of adhesive was applied to either well plates or rings and the scaffold gently pressed onto. Before experimental use, the sealant was dried for at least 24 h in a fume cupboard. Once dried, samples were sterilised in 70 % ethanol (in deionised water (dH_2O), Fisher Scientific UK) for 30 min. Ethanol was removed and samples were left to air dry in a sterile cabinet.

2.4 Combining nerve guides and aligned microfibres

PEG nerve guides (see section 2.1 for details) were filled with aligned PCL microfibres (see section 2.2 for details) of different fibre diameters and densities. Electrospun fibres on aluminium foils were cut into strips, where the length of strip was recorded for the calculation of required fibre bundle weight to fill conduits with a specific fibre volume (see section 2.5 for more information) thereafter. One end of the fibre strip was manually peeled off in fibre direction (1 – 2 cm) and twisted between the fingers to form a needle-like fibre tip. Glue (cyanoacrylate low viscosity adhesive, Sigma-Aldrich) was applied to fibre-needle to stabilise it. After glue was dried (10 – 20 s), PEG NGCs were

threaded onto PCL fibres (non-bunched end) like pearls on a chain using the twisted fibre-needle. Fibre excess on both sides of the tube was cut with conventional scissors. A more detailed description of the developed threading process (with pictures) can be found in section 4.4.2.

2.5 Adjusting fibre densities in conduits

In order to fill conduits with either different fibre diameters of the same density or with the same fibre diameters but with different densities, conduits were filled with a specific percentage of fibres in their lumen following a method based on calculated fibre weight (Figure 11). Based on the average conduit lumen diameter of 1.12 ± 0.11 mm (analysed in section 4.4.1) and the tube length of 5 mm, the internal tube volume (V_{tube}) was calculated (see below Equation 1).

$$V_{tube} = \pi \cdot {r_{tube}}^2 \cdot h$$

Equation 1

r = internal conduit diameter/2 h = height equalled the length of fibre bundle

The fibre bundle volume ($V_{fibre\ bunde}$) that was needed to fill the conduit with a specific percentage of fibres was calculated as follows (Equation 2):

$$V_{fibre\ bundle}(mm^3) = \frac{\%\ fibre\ density \times V_{tube}\ (mm^3)}{100}$$

Equation 2

% fibre density = required fibre density V_{tube} = calculated from Equation 1

Using the fibre bundle volume, the required weight of the fibre bundle ($m_{fibre\ bundle}$) was calculated based on the following equation (Equation 3):

$$m_{fibre\ bundle}(g) = V_{fibre\ bundle}(cm^3) \times \rho_{PCL}\left(\frac{g}{cm^3}\right)$$

Equation 3

$V_{fibre\ bundle}$ = calculated from Equation 2 ρ_{PCL} = PCL density = 1.145 g/cm^3

Aligned fibres electrospun to aluminium foils were cut to a set length determined in Equation 1 (usually 10 cm) and then assembled to fibre bundles of the calculated weight. In order to make weighing more sensitive, a plastic weighing boat (StarLab Ltd.) was

placed on a micro balance (Precisa 125A) and the weight recorded. This weight was summated with the calculated weight for the fibre bundle, which determined the required weight for the fibre bundle. Afterwards, fibres were threaded into conduits and cut as described in section 2.4 and in more detail in section 4.4.2 and 4.4.3.

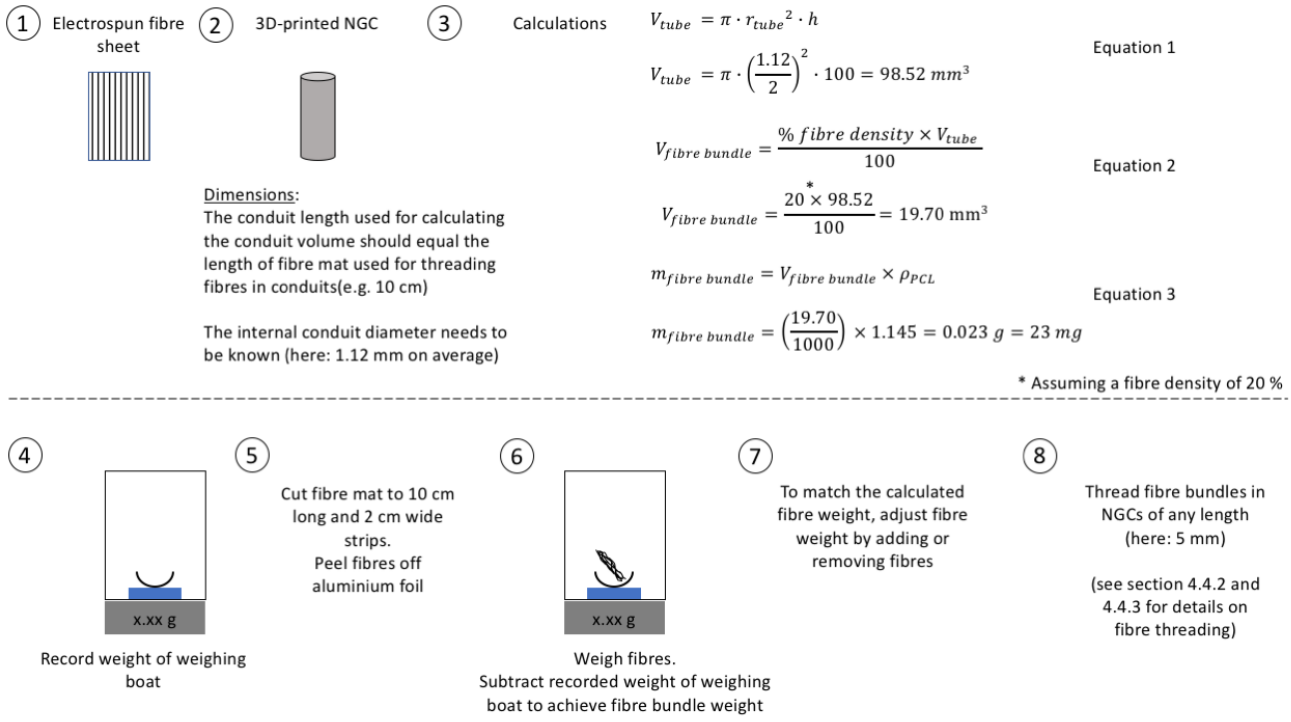

Figure 11 Schematic of steps involved to fill nerve guides with a specific density of electrospun fibres

2.6 Preparation of conduits with microfibre scaffolds for cell culture

Custom-made polystyrene adapters were used to hold conduits with fibre scaffold in an upright position. Therefore, polystyrene 200 µL pipette tips (Sarstedt AG & Co. KG) were cut to small cone-shaped adapters the small end of which fitted through the holes of a stainless-steel perforated metal grid (in-house manufactured) and through which opening could carry the conduit structure. Depending on the size of the adapter opening, adjustments were needed at the adapter tip by squeezing the opening with scissors to fit the conduit tightly. Nerve guides with incorporated fibre scaffolds were sterilised in 70 % ethanol for 1 h after being fitted into polystyrene adapters. Afterwards, conduits were washed twice with phosphate-buffered saline (PBS, Oxoid Ltd., 5 tablets dissolved in 500 mL of dH_2O and then autoclaved) and stored in PBS overnight before being used. Adapters carrying conduits were inserted into holes of sterile stainless-steel metal grids

to hold conduits in an upright position, which were then placed in wells of a 6-well plate. Before culturing, fibre scaffolds inside conduits were pre-wetted by injecting warm growth medium onto the scaffold using a 1 mL syringe (Becton Dickinson) with a 19 G stainless-steel needle (Becton Dickinson).

2.7 Preparation of PCL films

Flat PCL films were spin-coated from a 10 % PCL solution in DCM (vol/vol) using a spin coater from Laurell Technologies Corporation (model WS-400B-6NPP/LITE). Hundred microliter of polymer solution were applied onto 22 × 22 mm coverslips (Thermo Fisher Scientific) and spun at a vacuum using a speed of 3000 rpm for 30 s. Coverslips were removed from the spin-coater and dried in a fume cupboard.

2.8 Air plasma treatment

Samples were placed on a well plate lid covered in aluminium foil which was scratched with a scalpel to make the foil permeable to air to prevent the lifting of samples when ventilating the chamber. Air plasma was generated in a Diener Electronic commercial plasma system (model ZEPTO, chamber volume: 2.6 L) with connected pump (Pfeiffer Vacuum Technology AG), operating at radio frequency powers of 50 W (40 kHz) at a vacuum of 0.4 mbar for 60 s. Afterwards, samples were removed and either used immediately or at most 3 days thereafter. For air plasma treatment on PCL fibre scaffolds, microfibres were mounted to 1 cm^2 stainless-steel rings using a silicone-based aquarium sealant prior to treatment (see section 2.3 for details).

2.9 Cell culture

2.9.1 General handling of cells

Cells used in this study were handled under sterile conditions using aseptic techniques in a class II biological safety cabinet operating under laminar air flow. Culture medium was warmed to 37 °C in a water bath prior to all applications if not otherwise specified. Solutions indicated as “warm” refer to a temperature of 37 °C. All cells were maintained in a humidified 95 % air and 5 % CO_2 atmosphere at 37 °C (herein referred to as “CO_2 incubator”). Throughout this study, cells were maintained in T75 culture flasks of 75 cm^2

culture area from VWR International and plated in 6-, 12- or 24-well plates from CytoOne (StarLab, UK).

2.9.2 Resurrection and maintenance of cells

Frozen cell vials were either taken from liquid nitrogen or -80 °C freezer storage and immediately thawed in a 37 °C water bath. Frozen vials were gently shaken in the water to speed up the thawing process. Prior to the removal of cells from storage, one T75 culture flask (per vial of cells) was prepared with 24 mL warm culture medium per flask. Cells were immediately transferred to the sterile hood after thawing and the contents of the vial was transferred to the prepared T75 flasks. This way, the 10 % dimethyl sulfoxide (DMSO) concentration in the freezing medium was diluted to 0.4 % DMSO content, which is below the toxicity level. The thawing process of cells was carried out quickly as thawing procedures are in general stressful to cells and as DMSO in the freezing medium may additionally have toxic effects on cells when left for prolonged times. Flasks were incubated in a CO_2 incubator overnight to allow cell attachment. The next day, culture medium was replaced by fresh warm culture medium to ensure the complete removal of DMSO from the medium. Cells were further incubated until confluence was reached before experiments were conducted. All cells were maintained in a medium containing Dulbecco's Modified Eagle Medium (DMEM, Sigma-Aldrich), 10 % foetal bovine serum (FBS, vol/vol, Sigma-Aldrich), 0.25 µg/mL amphotericin B (Sigma-Aldrich), 200 mM L-glutamine (Sigma-Aldrich), 100 units/mL penicillin and 100 µg/mL streptomycin (Sigma-Aldrich) (herein referred to as "growth medium") if not otherwise specified.

2.9.3 Cell passaging

The culture medium in confluent T75 flasks was discarded and cells gently washed once with PBS to remove serum residues from the flasks that may interfere with applied trypsin in the next step. PBS was removed and 5 mL of trypsin-ethylenediaminetetraacetic acid (EDTA) (0.5 % trypsin (wt/vol), 0.2 % (wt/vol) EDTA, Sigma-Aldrich) was added for either 1 min (NG108-15 neuronal cells, primary chick Schwann cells) or 3 – 4 min (primary rat Schwann cells). Before trypsin-EDTA was inactivated by 10 mL of growth medium per T75 flask, full cell detachment was checked under a light microscope (Motic Electric Group Co. Ltd., model: AE2000, objective: 10× NA 0.3). Cells were then centrifuged at room temperature at speeds depending on cell

type. The supernatant was removed and cell pellets resuspended in a cell type-dependent volume. The cell suspension was diluted by a factor depending on cell type into new T75 flasks, containing warm culture medium. Flasks were maintained in a CO_2 incubator with medium changes occurring every 3 days until cells reached confluence.

2.9.4 Cell counting

Trypan blue was used to count the number of living cells per millilitre as the dye cannot penetrate intact cell membranes and therefore living cells appear translucent, whereas dead cells show blue. 20 µL of the cell suspension were transferred to a 1.5 mL Eppendorf tube and mixed with 20 µL of trypan blue (1:1 dilution, factor = 2) (0.4 %, Sigma-Aldrich). Next, 10 µL of cells were transferred to one chamber of a Neubauer haemocytometer (0.1 mm depth, 0.0025 mm^2, Hawksley UK). Cells were counted in three primary squares containing 16 squares each. The number of living cells/mL was calculated as follows (Equation 4):

$$\frac{Cells}{mL} = \frac{Number\ of\ counted\ cells}{Number\ \ of\ primary\ squares\ counted} \times 10^4 \times dilution\ factor \qquad \textbf{Equation 4}$$

2.9.5 Cell storage

Cells of confluent T75 flasks were harvested and suspensions centrifuged to cell pellets. Cell pellets were resuspended in 1 mL each of cold freezing medium (growth medium with 10 % FBS and 10 % sterile-filtered DMSO). DMSO was added to prevent the formation of ice crystals in the freezing process. As DMSO is toxic to cells, cell suspensions were quickly transferred to cryo vials (1 mL/vial) and placed in a pre-chilled but not frozen suitable freezing container. Containers were placed at – 80 °C, where isopropanol in the container slowly decreased the temperature by 1 °C per minute. For temporary cell storage (up to 1 month), cells were maintained at – 80 °C, whereas cells were transferred to liquid nitrogen for longer storing periods.

2.10 Mouse neuroblastoma × rat glioma hybrid (NG108-15) cell culture

NG108-15 neuronal cells were purchased from the European Collection of Authenticated Cell Cultures (ECACC, Porton Down, UK) and were cultured in growth medium as stated above. For the passaging of cells, trypsin-EDTA was added and cells incubated in the

sterile hood for less than 1 min. Neuronal cells were centrifuged at room temperature at 250 g for 5 min. Cells were kept for all experiments at 37 °C in CO_2 incubator and were used at passages between 15 – 20.

2.10.1 NG108-15 neurite outgrowth assay

NG108-15 neuronal cells were cultured in serum-free growth medium to encourage the formation of neurites and cells fixed, labelled and imaged. Cells were analysed on neurite length and incidence using Fiji [284]. Therefore, images were uploaded to Fiji and scales set based on imaged frame size, magnification and zoom (information embedded in image files). Neurite lengths were defined by the distance of the tip of a neurite to the neuronal cell body. Neurites were traced manually using the "segmented-line tool" in Fiji. For neurite incidence, cells were counted manually using the "multi-point tool" in Fiji. Neurite incidence was defined as the percentage of all imaged neurons that had formed neurites. Therefore, the number of neurons, which formed neurites was calculated as below (Equation 5):

$$\%\ neurite\ incidence = \frac{Number\ of\ neurons\ with\ neurites}{Total\ number\ of\ neurons} \times 100 \qquad \textbf{Equation 5}$$

2.11 Primary Schwann cell culture

2.11.1 Isolation of primary rat Schwann cells

The isolation of Schwann cells from rat sciatic nerves was performed following instructions from Kaewkhaw *et al.* [285]. Male Wistar rats, 10 – 12 weeks old, were sacrificed by a cervical dislocation schedule I procedure following the Animals Act 1986 regulations. Whilst the ventral side was facing down, legs were skinned and the whole length of the sciatic nerves (one nerve per leg) removed. Nerves were placed in a Petri dish of warm growth medium and excess tissue around the nerves was removed. The nerve was scraped with a scalpel to disorganise nerve fascicles and then placed in a filter-sterilised solution of 10 mL 0.15 % collagenase (from *Clostridium histolyticum*, Sigma-Aldrich) in serum-free growth medium. Nerve pairs were incubated at 37 °C in a CO_2 incubator for 30 min, vortexed and incubated for another 30 min. The dissociated nerve mixture was homogenised using a sterile plastic Pasteur pipette. The mixture was passed through a 40 µm cell strainer (Falcon, Corning Inc.) to remove debris and centrifuged at room temperature at 400 g for 6 min. The supernatant was discarded, the

cell pellet washed with fresh, warm growth medium and centrifuged again. The cell pellet was resuspended in 2 mL of Schwann cell purification medium containing DMEM-D-Valine (Biosera), 2 mM L-glutamine, 10 % (vol/vol) FBS, 1 % (vol/vol) N2 Supplement (100X) (containing 1 mM human transferrin, 0.0861 mM insulin recombinant, 0.002 mM progesterone, 10.01 mM putrescine and 0.00301 mM selenite; Invitrogen), 20 µg/mL (wt/vol) bovine pituitary extract (Sigma-Aldrich), 5 µM forskolin (Sigma-Aldrich), 0.25 µg/mL amphotericin B, 100 units/mL penicillin and 100 µg/mL streptomycin. The cell suspension was divided between two 35 mm^2 Petri dishes (CytoOne, StarLab, UK), which were pre-filled with 1.5 mL of cell suspension. Before use, Petri dishes were coated with 1 mL poly-L-lysine (0.01 %, Sigma-Aldrich) and incubated for 10 min at room temperature. Poly-L-lysine was removed and the dishes left to dry at room temperature in a sterile cabinet. Dried Petri dishes were coated with 1 mL 0.1 % laminin solution in PBS (vol/vol, Sigma-Aldrich) and incubated for 30 min at 37 °C. The dishes were washed twice with PBS before use. Isolated Schwann cells were incubated in a 37 °C CO_2 incubator for 7 days. In this time, the Petri dishes were not touched or moved to avoid cell detachment. On day 7, 1 mL of fresh Schwann cell purification medium was added to the cultures and were further incubated for another 4 days. Until cells reached confluence (about day 30), 50 % of the medium was replaced by fresh culture medium every 3 – 4 days.

2.11.2 Purity analysis of isolated primary Schwann cells

Confluent cells from Petri dishes were passaged 1:1 into 75 cm^2 flasks (passage 1). When confluence was reached, cells were further expanded 1:2 into 75 cm^2 flasks and additionally seeded into 2 wells of a 6-well plate (2 wells per 75 cm^2 flask). After 70 % confluence was reached in 6-well plates, Schwann cells were fixed with 3.7 % *para*-formaldehyde (PFA) for 20 min. Cell membranes were permeabilised with 0.1 % Triton X-100 (vol/vol, Fluka) and protein binding sites blocked with 3 % bovine serum albumin (BSA, wt/vol, Sigma-Aldrich) for 1 h. In order to quantify the purity of isolated Schwann cells, the Schwann cell marker S100β was used as well as 4',6-Diamidino-2-phenylindole (DAPI) to identify cell nuclei. All nuclei and cells that were not co-localised with the S100β protein were seen as impurities in the culture (fibroblasts). Anti-S100β primary rabbit antibody (1:400 or 10 µg/mL in 1 % vol/vol BSA, Dako, Z5116) were added to the samples for 48 h at 4 °C, followed by three washes in PBS. The secondary antibody, goat

anti-rabbit Alexa 546 (0.8 mg/mL in 1 % BSA; Life Technologies, A11010), was added to the samples and incubated for 120 min at room temperature. After two PBS washes, cell nuclei were labelled with 300 nM DAPI (Sigma-Aldrich) for 30 min at room temperature. Before imaging, samples were washed, then re-submerged in PBS. Schwann cell purity was calculated as follows (Equation 6):

$$\%\, purity = \frac{Total\ number\ of\ S100\beta - positive\ cells}{Total\ number\ of\ nuclei} \qquad \textbf{Equation 6}$$

Primary Schwann cells were experimentally used at purities greater than 98 % as recommended by Kaewkhaw *et al.* [285].

2.11.3 Maintenance culture

Purified primary Schwann cells were cultured in growth medium. To detach cells from culture flasks, trypsin-EDTA was applied and incubated in a CO_2 incubator for 3 – 4 min. Cells were centrifuged at room temperature at 400 g for 6 min. Primary Schwann cells were used in passages of 3 – 8 and incubated for all experiments at 37 °C in a CO_2 incubator.

2.12 Immunocytochemistry

To visualise specific cell proteins, indirect immunofluorescence was used. A primary antibody raised against the target protein was visualised with a secondary antibody conjugated to a fluorophore which was raised against the primary antibody. Cells were fixed with 3.7 % PFA for 20 min and washed twice with PBS afterwards. Cell membranes were permeabilised and protein binding sites blocked simultaneously using 0.1 % Triton X-100 and 3 % BSA in PBS for 1 h. After two PBS washes, primary antibodies were applied at an antibody-dependent concentration and left for 24 – 48 h at 4 °C. Afterwards, unbound antibodies were removed and cells washed with PBS twice. Secondary antibodies were incubated at an antibody-dependent concentration for 3 h at room temperature. Negative controls were conducted by omitting the primary antibody. Under the same conditions, secondary antibodies were used if no nonspecific staining was visible. Samples were washed twice with PBS before nuclei were labelled with 300 nM DAPI in PBS for 30 min at room temperature. Samples were stored in PBS before imaging.

2.13 F-actin labelling

Samples were fixed with 3.7 % PFA for 20 min, washed with PBS twice and subsequently permeabilised with 0.1 % Triton X-100 in PBS for 30 min. F-actin labelling was conducted with 0.8 nM phalloidin either conjugated to fluorescein isothiocyanate (FITC) or to tetramethylrhodamine B isothiocyanate (TRITC) in PBS (1 mg/mL in DMSO, both Sigma-Aldrich) for 1 h at room temperature. Unbound phalloidin was removed and samples washed twice with PBS. Samples were kept hydrated in PBS before being imaged.

2.14 Live/dead cell staining overview and analysis

In order to visualise living and dead cells, two DNA stains, Syto-9 and propidium iodide were used. Based on the dyes water solubility properties, cell membranes were crossed or dyes excluded from it. The water-soluble propidium iodide could not enter the lipid bilayer of cells and therefore stained dead cells red, whereas Syto-9 stained living cells green.

The cell culture medium on cells was removed and replaced with 0.02 % Syto-9 (vol/vol, Thermo Fisher Scientific) and 0.03 % propidium iodide (vol/vol, Thermo Fisher Scientific) in serum-free medium (growth medium deprived from serum). Cells were incubated in the staining solution for 60 min at 37 °C in a CO_2 incubator. Confocal imaging was conducted in z-stacks in PBS immediately after staining (see section 2.17). Each sample was imaged in three randomly chosen positions. Z-stacked images were combined to maximum intensity projections and further analysed in Fiji [284]. Cells were counted manually using the “multi-point tool" in Fiji. The distribution of living and dead cells was calculated as follows (Equation 7):

$$\%\ living/dead\ cells = \frac{Number\ of\ counted\ living/dead\ cells}{Total\ number\ of\ cells\ (living + dead\ cells)} \times 100 \qquad \textbf{Equation 7}$$

2.15 Resazurin metabolic activity assay

Metabolic activity rates of cells were determined via a fluorometric resazurin reduction assay. The blue resazurin salt could pass through cell membranes and was reduced to the fluorescent pink resorufin using mitochondrial enzymes in metabolic active cells. Dying or dead cells could not reduce resazurin or only with limitations. As cells diffused

resorufin out into the surrounding medium, the assay was performed as repeated measures.

A 1 mM resazurin stock solution of resazurin salt (Sigma-Aldrich) in PBS was diluted to a working solution of 100 µM in assay-dependent culture medium. The culture medium on cells was removed and replaced with warm resazurin working solution in an assay-dependent volume (specified in each chapter). Well-plates were incubated in the dark in a 37 °C CO_2 incubator for 4 h. The reduced formazan product was transferred in triplicate of 100 µL to a black 96-well plate (if not otherwise indicated) and the fluorescence read in a FLx800 fluorescent plate reader (Biotek Instruments Inc.) at 540/635 nm. Prior to plate reading, the remaining resazurin solution on cells was replaced with warm growth medium and plates further incubated at 37 °C in a CO_2 incubator until next assay time point. In order to determine background fluorescence from the culture medium, a control with no cells present and just the resazurin working solution was used. Background fluorescence readings were subtracted from all other fluorescence values.

2.15.1 Resazurin reduction assays on PCL fibre scaffolds

Resazurin reduction assays on microfibres were performed in 1 cm^2 metal rings, which the fibre scaffolds were glued onto. In order to measure the metabolic activity of cells, which have attached to microfibres only, rings with attached microfibres were transferred to customized polydimethylsiloxane (PDMS) moulds (Figure 12).

PDMS was made by mixing curing agent and PDMS polymer in a ratio of 1:10 (Sylgard, Dow Chemical Company Ltd.). Air bubbles in the mixture were removed by centrifugation. The polymer solution was poured into wells of a 6-well plate. 1 cm^2 stainless-steel rings were glued to the well plate lid, where one ring was attached in the middle of each well. The lid was closed and moulds set at 60 °C for 4 h. The lid with attached rings was carefully removed thereafter.

For the resazurin assay, the cell culture medium in rings was removed and rings transferred to customized PDMS moulds. Each ring was filled with 600 µL resazurin working solution (100 µM, see section 2.15) and left to incubate at 37 °C in a CO_2 incubator for 4 h. The reduced formazan product was transferred and read as described in section 2.15. Remaining resazurin solution was removed from rings. Rings were

transferred back to sterile well plates and covered with fresh, warm growth medium and further incubated at 37 °C in a CO_2 incubator until next assay time point.

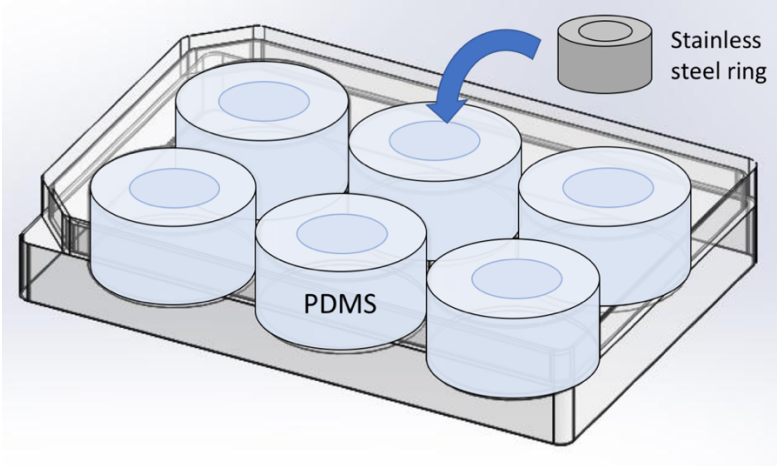

Figure 12 Customised PDMS moulds

Custom-casted PDMS moulds were fabricated inside wells of a 6-well plate. Stainless-steel rings were mounted to the lid of a 6-well plate so that PDMS inside wells set around the rings. After PDMS had set, lids with rings were removed, leaving a ring-shaped mould where fibre scaffolds at the bottom of rings were transferred into to conduct further analysis.

2.16 Scanning electron microscopy

For SEM, 12 mm Leit adhesive conductive carbon stickers (Agar Scientific) were adhered to 12.5 mm SEM pin metal stubs (Agar Scientific). Samples were mounted to the carbon stickers and coated with a layer of gold of approximately 20 nm thickness using an Emscope sputter coater. Gold coated samples were imaged using an Inspect F field emission gun scanning electron microscope (FEI company, US) operating at 10 kV with a spot size of 3.5.

2.17 Confocal and 2-photon laser microscopy

Micrograph images (1024 × 1024 pixels) were obtained using a Zeiss LSM 510 META upright confocal microscope (Carl Zeiss AG, Germany). Samples were arranged in either 6-well plates or 35 mm^2 Petri dishes and imaged in PBS using a 10× magnification ZeissW Plan Achromat water-dipping objective lens (numerical aperture (NA): 0.3) (Carl Zeiss AG, Germany). Green-fluorescing features were excited using a 488 nm laser (25 % transmission, 30 mW) and emission detected at 525 nm. Red-fluorescing features were

excited using a 543 nm laser (1.2 mW) with emission captured at wavelengths of 576 nm. Blue fluorescing cell nuclei were excited with a 780 nm 2-photon laser (Chameleon Ultra III, Coherent Inc., USA) and emission detected at 480 nm. Multi-layered and 3D samples were imaged in z-stacks with stack sizes ranging from 100 – 500 µm. Z-stacked images were combined to maximum intensity projections using Fiji [286].

2.18 Light-sheet microscopy

Imaging was conducted using a Z.1 light-sheet microscope (Carl Zeiss AG, Germany) with accompanied ZEN imaging software. Samples were immobilised in 0.8 % agarose (vol/vol in dH_2O, Sigma-Aldrich) inside glass capillaries with an inner diameter of 2.15 mm (size 4, Carl Zeiss AG, Germany). 0.8 % agarose was melted inside Eppendorf™ tubes at 70 °C using a heating block (Thermo Scientific) and once melted maintained at 40 °C prior to sample embedding. A size-equivalent plunger with Teflon tip (size 4, Carl Zeiss AG, Germany) was used to take up samples into the capillaries. Capillaries were rolled in hands until agarose had set. Capillaries were mounted inside the accompanied sample holder (Carl Zeiss AG, Germany) and inserted in the sample chamber. The chamber was filled with deionised water prior to imaging. Samples were then localised, positioned and focused using the build-in infra-red camera. Green, blue and red fluorescent signals were excited using a 488 nm (50 mW), a 405 nm (20 mW) and a 561 nm (20 mW) laser, respectively. The laser beams passed through the two 10x/0.2 illumination optics (Zeiss) which illuminated a single thin section of the sample (Figure 13). Perpendicular to this, a W plan-apochromat 10x/0.5 objective (Zeiss) captured the fluorescent signals (Figure 13). Each sample was imaged in z-stacks and was rotated in 90° increments (0, 90, 180 and 270 °) to capture the whole nature of samples. For each rotational position, several fields of view were taken per sample allowing an overlap of views. Each field of view z-stack was combined to a maximum projection image using the accompanied ZEN software. All maximum projection images of one rotating position were stitched together to one image using the grid/collection stitching tool in Fiji [286].

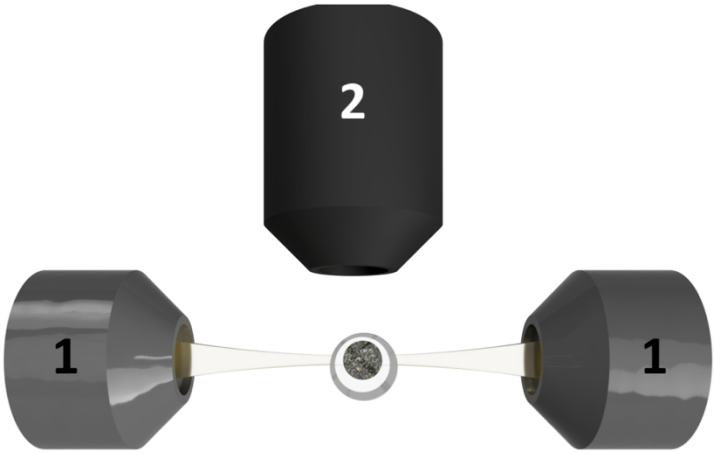

Figure 13 Light path in the light-sheet microscope

Illustration of the light path in a light-sheet microscope, where the light-sheet passes through the illumination optics (1) and illuminates a thin section of the in-focus plane of the sample. Fluorescence is captured with the detection optics (2) which sits perpendicular to the illumination path. Image used with the kind permission of Liam Boyle.

2.19 Statistical analysis

All statistical analysis was performed in GraphPad Prism (version 7.0). Datasets were analysed using either unpaired Student t-test for comparing two populations with each other or one- or two-way analysis of variance (ANOVA) with Tukey's post-hoc multiple comparisons test for comparing more than two populations with either one or two factors involved. Differences were considered significant when $p<0.05$. Values were presented as mean + standard deviation (SD) if not otherwise stated in the figure legend. Experiments were performed a minimum of two times in duplicate, where total number of replicates (n) is stated in the figure legend.

Chapter 3 Fibre diameter & topography – An *in vitro* study

3.1. Introduction

The following section has been partially taken from Behbehani *et al.* [287] which was published under an open access CC BY 4.0 licence agreement that allows the free copying and redistribution of the material when appropriate credit is given.

Injuries to peripheral nerves can affect the general public in all age groups, mostly caused by domestic, industrial or traffic accidents. Severe transection injuries are often life-changing and may result in defects of motor and sensory function. These injuries can often be repaired through a self-regeneration mechanism after Wallerian degeneration takes place [57]. However, a major concern is the increasing risk of incomplete functional and motor recovery with increasing degree of injury [76]. Current clinical treatments of complete peripheral nerve transection injuries comprise surgical end-to-end suturing, autografting, allografting or the use of nerve guidance conduits (NGCs), depending on nerve gap size and severity of injury. Despite its reputation as the gold standard, autografts suffer from several major drawbacks: the sacrifice of a healthy nerve, donor site morbidity, at least two surgical interventions on donor and injury site, potential size discrepancy between harvested nerve and injured nerve and possible functional mismatch when treating motor nerve lesions with commonly used sensory sural nerve grafts [60, 87, 96].

In recent years, bioengineers have focused on the development of NGCs to provide an alternative treatment to autografts, where different materials and designs have been explored, resulting in a number of devices that have gained FDA approval. However, these commercial NGCs lack internal guidance structures and cannot exceed injury gaps greater than 3 cm, which is shorter than the defined critical nerve gap of 4 cm in humans [114, 288]. To this date, no other commercial solution has been presented. Therefore, key challenges now focus on enhancement of NGCs by including internal conduit guidance structures for targeted axon regeneration through the nerve gap to maximise the number of regenerating axons and therefore improving the regeneration outcome. Aligned fibres are one approach to improve hollow nerve guides [148, 153, 289, 290] by

mimicking the natural regeneration guidance cues of bands of Büngner, where Schwann cells and fibroblasts form aligned bands between the proximal and distal nerve end to guide axons to their target effectors [143]. With adjustment of the fibre density in the NGC lumen, specific regeneration needs can be addressed such as varying axon numbers in nerves. In comparison, hollow nerve guides only provide an outer guide for the injured nerve to keep both nerve stumps connected but cannot provide relevant internal guidance support for regenerating cells and tissue. Furthermore, fibre containing conduits would not require an adaption of nerve fascicles and blood vessels between the proximal stump and the conduit which is necessary when using autografts [79].

It has been previously shown that the fibre diameter is of particular importance when being considered as a scaffold for nerve repair. Wang and colleagues showed an inhibited neurite outgrowth and Schwann cell migration from embryonic development day (EDD) 9 chick dorsal root ganglion (DRG) bodies on fibre diameters smaller than 0.8 µm [151]. Looking at a bigger fibre diameter range from 5 to 500 µm, Wen *et al.* noticed a gradual increase in neurite and Schwann cell outgrowth from rat DRG bodies with decreasing fibre diameter, where the greatest outgrowth has been seen on 5 µm fibres [150]. Additionally, Daud *et al.* reported on a more pronounced neurite outgrowth on polycaprolactone (PCL) fibre diameters of 8 µm when studying a fibre range from 1 to 8 µm [152]. These findings suggest that nerve regeneration is supported best by a specific range of fibre diameters. Although the reported results point in a promising direction, where fibre diameters should be of subcellular size, a specific fibre diameter range has still not been identified.

Taking this knowledge and moving beyond what has been previously shown, we aimed to define a critical PCL fibre diameter range, where 1 to 13 µm fibres were studied in regard to neuronal and Schwann cell performance. To our knowledge, the study of Daud *et al.* is the only one that showed this close similarity to our study in regard to polymer and microfibre choice. However, major limitations were found with the main weakness being that no explanation was given on the relationship between cells and fibre diameter. One weakness was the reported analysis of Schwann cells on microfibres, where the length of attached Schwann cells to microfibres was measured [152] but where important nerve regeneration aspects like proliferation and metabolic activity of Schwann cells were not

addressed. This raises general awareness about the choice of *in vitro* assays when studying neuronal and Schwann cell behaviour for peripheral nerve repair. The choice of cell assay for studying biomaterials for nerve regeneration, the response of Schwann cells and neuronal cells to peripheral nerve damage needs to be considered. It is common knowledge that Schwann cells are a major contributor for driving nerve repair by leaving their differentiated myelinated stage, starting to proliferate and to release cytokines, matrix molecules and growth factors, which are essential for axon regeneration [57, 64, 291]. Damaged axons and those that were separated from neuronal cell bodies, however, degenerate, where intact and healthy axons start regenerating. Although these facts are common knowledge, there are still studies that have reported on the use of unrepresentative neuronal proliferation cultures to evaluate biomaterials for nerve regeneration [292-294]. Therefore, this chapter studied the response of neuronal cells to the different fibre diameters under differentiation-like conditions in order to mirror the morphology of mature primary neurons. The length and incidence of neurites was studied as well as the performance of Schwann cells on microfibres regarding attachment, metabolic activity and proliferation behaviour.

Furthermore. Daud *et al.*'s study failed to consider the nanotopographical features on the fibre surface when discussing the observed cellular changes seen on the different fibre diameters. Although SEM images showed topographical features on fibre surface, they were not mentioned or analysed in the report [152]. Similar was seen in other studies, where surface topographies on electrospun fibres were differentiated and discussed based on SEM images but not quantified [156, 160, 170, 172, 174, 175, 295]. Only a very limited number of reports measured those topographical features and mainly addressed groove diameter [169, 171] and in one case also groove length and density [168]. Herein, the morphology of fibres was closely investigated and topographical features quantified regarding their area, length, shape and density. Additionally, the morphology of both cell types on the fibres was closely studied using SEM. The obtained results were analysed and brought in context to analysed topographical features on the fibre surface.

3.2 Aim & Objectives

Aligned PCL fibre scaffolds inside NGCs were hypothesised to enhance peripheral nerve injury outcomes in comparison to hollow conduits by providing contact guidance through the nerve gap. Fibre alignment and dimensions were proposed to play a major role in the regeneration process. So far, no specific fibre diameter range has been identified. In order to address the proposed hypothesis, the study aimed to understand the interaction between PCL fibre morphologies and neurons and glial Schwann cells in *in vitro* cell cultures. This should determine a defined fibre diameter range that best supports the guided outgrowth of axons and Schwann cells.

In order to achieve this, the following objectives were formulated:

- To electrospin aligned PCL fibres in dimensions between 1 and 13 µm
- To analyse the relationship between nanotopographical features on the fibre surface and fibre diameter
- To evaluate the biocompatibility of fibres by assessing neuronal and primary Schwann cell viability
- To study the dependency between directional axon outgrowth and fibre diameter
- To investigate the performance of fibre diameters on Schwann cell attachment, metabolic activity and proliferation potential

3.3 Materials & Methods

3.3.1 Characterisation of electrospun PCL fibres

PCL was prepared and electrospun according to section2.2. Generated microfibres were retained on aluminium foils and prepared for SEM. Conductive carbon stickers were placed on top of SEM metal stubs. Microfibres on aluminium foil were stuck to carbon stickers, where two random positions of each aluminium sheet were imaged. Gold-coating on samples and SEM was performed as described in section 2.16. N=5 experiments were conducted for the characterisation analysis of fibre diameter and alignment, whereas the characterisation of nano-topographies was conducted as an N=2. Each fibre sample was imaged in at least 20 random positions. For fibre topography analysis, 10 images were captured per fibre diameter group. Obtained SEM images were uploaded to Fiji (Version 1.0, National Institute of Health, US) and scales set based on the embedded scale bars in the SEM images. Fibre diameter was measured using the straight-line measuring tool in Fiji. Fibre alignment was measured by drawing a straight line along the fibre directionality and setting the line as a reference angle to 0°. All neighbouring fibres to the reference fibre were measured in the same way, where the resulting angle demonstrated the varying angle to the reference fibre. Fibre scaffolds for the analysis of surface nano-topographies were imaged at a magnification of 10,000× with the exception of 1 µm fibres which were taken at 40,000× magnification. At least 20 grooves per image were analysed. The area of grooves was measured by tracing the circumference of grooves with the polygon selection tool in Fiji. Height and length of the grooves were measured using the line tool in Fiji. The width of grooves was divided by its length to express their ratio to each other and presented in percent. The number of grooves per μm^2 was determined by drawing a 2 × 2 µm square in the middle of the fibre, counting the number of present grooves in the area of interest and diving the number by 4.

3.3.2 *In vitro* toxicity study of aquarium sealant

A silicone-based aquarium sealant was tested for its effect on cell morphology and metabolic activity in NG108-15 neuronal and primary Schwann cell cultures. For this assay, cells were not exposed physically to the adhesive but maintained in the same culture medium. Therefore, 0.15 g of aquarium sealant (King British, UK) was applied

equally to stainless-steel metal grids and was left to dry in the fume cupboard for 24 h. Grids without the addition of glue defined the control group. For sterilisation, grids were covered in 70 % (vol/vol) ethanol in water (Fisher Scientific, UK) for 30 min. Ethanol was removed and grids left to dry in a class II biological safety cabinet with a sterile laminar flow. Cells were seeded in cell type-specific numbers in wells of a 6-well plate and left to attach overnight at 37 °C in a CO_2 incubator. The following day, the medium was removed and metal grids with aquarium sealant and control grids were placed into the wells. Subsequently, wells were filled with 10 mL of medium to cover grids. Resazurin reduction assays were performed based on the described methodology in section 2.15 at cell-specific time points. Resazurin solution was applied with 1 mL per well, where grids were removed before the addition of resazurin. Grids were washed in PBS and stored in a sterile hood before being placed back into the wells after resazurin incubation had finished. Resazurin assays were performed as repeated measures. Cell morphology was additionally observed and captured before each resazurin assay using a Motic light microscope (Motic Electric Group Co., Ltd) with a 10x objective (NA 0.25). Assays were performed in triplicate with two independent repeats.

3.3.2.1 Primary Schwann cells

Primary rat Schwann cells were trypsinised and counted as described in sections 2.9.3 and 2.9.4. Cells were seeded with 3×10^4 cells/well in a 6-well plate (3,158 cells/cm^2) in growth medium containing 10 % FBS (see section 2.9.2 for details). Schwann cells were maintained in growth medium throughout the experiment. The described resazurin assay was performed on days 1, 3, 5, 7, 14 and 21.

3.3.2.2 NG108-15 neuronal cells

NG108-15 neuronal cells were trypsinised and counted according to sections 2.9.3 and 2.9.4. Cells were seeded in numbers of 2×10^4 cells/well in a 6-well plate (2,105 cells/cm^2) in growth medium containing 10 % FBS (see section 2.9.2 for details) and were left to attach overnight. After grids were placed into the wells, wells were filled with 10 mL of serum-free medium to encourage the formation of neurites. Neuronal cells were maintained in serum-free medium throughout the experiment. The described resazurin reduction assay was performed on days 1, 7, 14 and 21. Assays were not additionally performed on day 3 and 5 as in Schwann cell cultures due to neuronal cell's sensitivity to

cell detaching. Time points after day 3 and 5 were excluded to limit the number of medium changes on the cells as resazurin assays were performed in repeated measures.

3.3.3 Cell culture medium optimisations

3.3.3.1 Neuronal cell study in different FBS concentrations

Different serum concentrations in the culture medium were investigated in order to define optimal culture conditions that support a maximum outgrowth of neurites and neurite incidence. Therefore, NG108-15 neuronal cells were seeded in triplicate in numbers of 5×10^3 cells/well in a 12-well plate (1,316 cells/cm^2). Cells were maintained in growth medium containing 10 % FBS (see section 2.9.2 for details) for one day to support cell attachment. Afterwards, medium was replaced with growth medium containing FBS concentrations of 0, 1.25, 2.5 or 5 %. After 4 days of culture, medium was removed and cells washed once with PBS. Cells were fixed with 3.7 % PFA and subsequently stained for F-actin using phalloidin-TRITC as described in section 2.13. Neuronal cells were imaged using a Nikon Eclipse Ti microscope with a Nikon intensilight HGFI illuminator (Nikon Instruments Europe B.V.) and a neo sCOMS camera (Andor Technology Ltd., UK). In each well, images were taken in three random positions. Neurite incidence and length was measured as described in section 2.10.1. Experiments were performed in triplicate and repeated three times.

3.3.3.2 Primary Schwann cell study in different FBS concentrations

In order to define optimal culture conditions, different serum concentrations in the medium of Schwann cells were investigated on the effect on cell's metabolic activity. Primary Schwann cells were seeded in triplicate in numbers of 5×10^3 cells/well in a 12-well plate (1,316 cells/cm^2) and kept in growth medium containing 10 % FBS (for details see section 2.9.2). After one day, growth medium was replaced with medium containing 10, 5, 2.5, 1.25 or 0 % FBS. Resazurin reduction assays were performed after day 1 before medium was replaced and 24, 48 and 72 h thereafter. Assays were performed as described in section 2.15 in repeated measures. Prior the conduction of resazurin assays on days 1, 7, 14 and 21, Schwann cell's morphology was captured using a Motic light microscope. Experiments were independently repeated three times and run in triplicate.

3.3.4 Cell morphology studies on microfibres

In order to closely examine the morphology of cells on PCL microfibres, SEM imaging was conducted, which involved the dehydration of samples after culture. Therefore, microfibre samples needed to be handled differently to withstand the multiple washing steps involved in the dehydration protocol. PCL fibres of 1 – 13 µm in diameter on aluminium sheets were cut to rectangular size. The fibre ends were carefully lifted off and aquarium sealant was applied to both fibre ends in order to robustly connect fibre ends without disturbing the alignment of fibres. Samples were dried for at least 24 h in a fume cupboard. Fibres were sterilised in 70 % ethanol for 30 min and subsequently left to dry in a sterile cabinet. Cells were seeded in 1 cm^2 sterile stainless-steel rings that were placed on top of the fibres in cell type-defined numbers using 500 µL/ring. After 6 days of culture, medium was removed and cells gently washed twice with PBS. Cells were fixed with 3.7 % PFA for 20 min and afterwards placed in PBS for 15 min. PBS was replaced by dH_2O for 5 min and samples subsequently submerged in an ascending series of ethanol using 35, 60, 80, 90 and 100 % ethanol for 15 min each. The dehydration process finished with a 1:1 solution of ethanol and hexamethyldisilazane (HMDS, IUPAC name: 1,1,1-Trimethyl-N-(trimethylsilyl) silanamine, Sigma-Aldrich) for 60 min, followed by 100 % HMDS for 5 min. Samples were left to air dry for at least 1 h. All chemical work was conducted in a fume cupboard. Following drying, samples were prepared as usual for SEM analysis (see section 2.16). This experiment was independently repeated two times.

3.3.4.1 NG108-15 neuronal cell culture

Neuronal cells were trypsinised and counted as described in sections 2.9.3 and 2.9.4. As described above, cells were seeded in stainless-steel rings in numbers of 4×10^4 cells/ring. Neurons were cultured in growth medium containing 10 % FBS (see section 2.9.2 for details) for 1 day to mediate cell attachment. Afterwards, growth medium was removed and replaced with serum-free medium, which was placed inside and around the rings. Neurons were cultured for another 5 days in serum-free medium with one medium change occurring after 3 days in serum-free conditions. Cells were fixed and prepared for SEM as described above.

3.3.4.2 Directionality measurements of axons to PCL fibre

The directionality of axons to PCL fibres was measured in Fiji. The alignment of PCL fibres was determined by drawing a straight line (straight line tool in Fiji) along the directionality of one representative fibre, where the displayed angle was considered as the reference angle. The directionality of all axons was measured the same way. The difference between axon angle and fibre reference angle accounted for the angular difference between the two. Angular differences were plotted in a histogram in bin centres of 10 – 110 and a bin width of 20 to cover angular differences from 0 – 120°.

3.3.4.3 Primary Schwann cell culture

Primary rat Schwann cells were trypsinised and counted as outlined in sections 2.9.3 and 2.9.4. 5×10^4 cells were seeded per 1 cm^2 stainless-steel metal ring onto fibre scaffolds using a volume of 500 µL/ring. Following one day of cell attachment, growth medium was topped up in and around the rings and cells maintained for a total of 6 days. A medium change was conducted on day 4. Cells were fixed and prepared for SEM as described above.

3.3.5 Live/Dead cell evaluation on microfibres

Aligned PCL microfibre scaffolds (ranging from 1-13 µm) were arranged and sterilised in wells of a 6-well plate as outlined in section 2.3. PCL films and tissue culture polystyrene (TCP) were used as the control surfaces, where PCL films were fabricated as in section 2.7. Sterile 1 cm^2 stainless-steel rings were placed on top of fibre samples to define the growth area. Both neuronal NG108-15 cells and primary rat Schwann cells were trypsinised and counted as in 2.9.3 and 2.9.4 and were seeded in 500 µL with 2×10^4 and 4×10^4 cells per ring, respectively. Cells were seeded in growth medium (see section 2.9.2 for details) and left to attach for 2 h at 37 °C in a CO_2 incubator. Afterwards, medium was topped up inside and around the rings. After 1 day of culture, neuronal cells were withdrawn from FBS to encourage the formation of neurites and to slow down proliferation. After 5 days of serum withdrawal (neuronal cells) or 5 days of culture in growth medium (Schwann cells), a live/dead cell overview stain was conducted as explained in section 2.14. Stained samples were visualised using confocal microscopy (see section 2.17) and thereafter analysed using Fiji (see section 2.14. Samples were prepared in duplicate and experiments repeated three times.

3.3.6 Neurite outgrowth analysis on microfibres

To immobilise aligned PCL microfibres to the bottom of wells of a 6-well plate, a silicon-based aquarium sealant was used as described in section 2.3. Besides fibre scaffolds, PCL films that were fabricated according to section 2.7 and TCP acted as control surfaces. NG108-15 neuronal cells were seeded in 500 µL with 2×10^4 cells per 1 cm^2 stainless-steel ring that was placed on top of samples. Following cell seeding in growth medium containing 10 % FBS, cells were left to attach for 2 h before medium was topped up in and around the rings. After one day of culture, serum was withdrawn from the culture to support neurite formation. In total, cells were maintained in serum-free medium for 5 days with a medium change on day 3. Afterwards, cells were fixed, permeabilised and immunolabelled as described in section 2.12. Therein, a primary antibody of mouse anti-βIII Tubulin (G7121, Promega) was used at a concentration of 2.5 µL/mL (1:400) for 48 h. A donkey anti-mouse FITC antibody (A24501, Life Technologies) was used at a concentration of 0.6 mg/mL for the secondary antibody. Cell nuclei were visualised with DAPI as described in 2.12. Samples were imaged using confocal microscopy (see section 2.17) and neurite incidence and length analysed according to 2.10.1. All samples were prepared in duplicate and experiments repeated three times.

3.3.7 Crystal violet assay on microfibres

For crystal violet assays, microfibres were glued to 1 cm^2 stainless-steel rings and subsequently sterilised as described in 2.3. PCL films and TCP represented the control surfaces, where metal rings were glued onto surfaces following the same steps as in 2.3 (Chapter 2). Metal rings with microfibres and PCL films were placed in wells of a 12-well plate. Primary Schwann cells were trypsinised and counted as in 2.9.3 and 2.9.4. Afterwards, cells were seeded in 500 µL with 4×10^4 cells per 1 cm^2 ring in growth medium (see section 2.9.2 for details). Cells were cultured on samples for 1 day to allow attachment. Before fixing cells with 3.7 % PFA for 20 min, scaffolds were washed three times with PBS to remove unattached cells. Rings with attached microfibres were removed and transferred to a new 12-well plate. Next, transferred scaffolds and wells of the remaining 12-well plate were covered with 500 µL 0.2 % crystal violet solution (Sigma-Aldrich) in 10 % ethanol (Fisher Scientific UK) and incubated for 10 min at room temperature. Crystal violet was discarded and samples washed with PBS until all unbound solution came off. Afterwards, the stain was eluted from the samples using 600

µL of 10 % acetic acid (in dH_2O, BDH). The eluted product was transferred in triplicate of 100 µL to a black 96-well plate and the absorbance read using a ELx800 absorbance plate reader (Biotek Instruments Inc.) at 630 nm. In triplicate, 100 µL of 10 % acetic acid was additionally transferred to act as a background control. Samples were prepared in duplicate and experiments repeated three times. For analysis, absorbance readings were subtracted from the blank acetic acid absorbance reading. Values were expressed in percent in relation to the TCP control, where it was assumed that 100 % of cells attached to TCP.

3.3.8 Resazurin reduction assay on microfibres

The metabolic activity of primary Schwann cells on the different microfibre scaffolds, PCL films and glass coverslips was measured using a resazurin reduction assay. PCL films were fabricated as described in 2.7, where round 19 x 19 mm glass coverslips were purchased (Thermo Fisher Scientific). Microfibres, PCL films and glass coverslips were glued to 1 cm^2 stainless-steel metal rings and sterilised thereafter following the descriptions in 2.3. Schwann cells were trypsinised and counted according to 2.9.3 and 2.9.4 and then seeded with 4×10^4 cells per 1 cm^2 ring using 500 µL/ring. Schwann cells were maintained in growth medium throughout the experiment (see section 2.9.2 for details). Resazurin reduction assays were performed as described in 2.15.1 on days 1, 3 and 5.

3.3.9 Ki67 proliferation study on microfibres

In order to assess the ratio of proliferating Schwann cells on microfibre scaffolds, cells were stained for Ki67, a protein strictly associated with cell proliferation. Microfibres were mounted to the well bottom of 6-well plates as described in 2.3. Microfibres and control surfaces of TCP and PCL films were sterilised with 70 % ethanol for 30 min and were left to dry in a laminar sterile air flow thereafter. Culture areas were defined with 1 cm^2 sterile stainless-steel rings that were placed on top of samples. Primary Schwann cells were seeded in 500 µL with 4×10^4 cells per 1 cm^2 ring. Schwann cells were seeded and maintained in growth medium throughout the experiment (see section 2.9.2 for details). After one day of culture, growth medium was topped up inside and around the rings. Experiments were set up in duplicate, where one set of samples was fixed with 3.7 % PFA on day 3 and the other set on day 5. For cells that were fixed on day 5, an

additional medium change was conducted on day 3. Samples in each experimental set were run in duplicate, where experiments were independently repeated three times.

Immunocytochemistry was performed as described in 2.12. A rabbit monoclonal anti-Ki67 antibody (ab16667, Abcam) was used at a dilution of 1:300 as the primary antibody and incubated for 24 h at 4 °C. As a secondary antibody a goat anti-rabbit Alexa 546 (A11010, Life Technologies) antibody was used at a concentration of 0.8 mg/mL for 2 h at room temperature. The cytoskeleton of Schwann cells was additionally stained for F-actin using phalloidin-FITC as described in 2.13 in order to visualise the cell's full size. Nuclei were stained with DAPI as outlined in 2.12. Stained samples were imaged in z-stacks using a confocal microscope as described in 2.17, where z-stacks were combined to a maximum intensity image. The ratio of proliferating and therefore Ki67-positive cells was expressed in percent relative to the total cell number. Calculations were made as follows (Equation 8):

$$\%\ of\ Ki67-positive\ cells = \frac{\#\ of\ Ki67-positive\ cells}{Total\ cell\ \#\ (DAPI-positive)} \times 100 \qquad \textbf{Equation 8}$$

3.4 Results

3.4.1 Characterisation of electrospun PCL fibres

3.4.1.1 PCL fibre diameters and alignment

Five different PCL microfibre scaffolds were investigated for performance as internal NGC scaffolds to treat peripheral nerve injuries. Fibres were generated by electrospinning, where aligned fibres with five different diameters were produced. To assess the diameter and alignment of fibres, SEM analysis was performed and images analysed in Fiji. Five different polymer flow rates were used to fabricate five PCL microfibre scaffolds of different diameters. The SEM micrographs in Figure 14 are revealing in several ways. First, it was apparent that irrespective of the applied flow rate, fibres could be spun in a highly aligned orientation (Figure 14 A – E), where fibres were deposited in parallel to each other. Second, the flow rate was found to influence fibre diameter, where an increase in flow rate was found to correlate with an increase in fibre diameter (Figure 14 A-E). Microfibres spun with a flow rate of 20 mL/h (Figure 14 E), for example, appeared approximately 13 times bigger than fibres manufactured with a flow rate of 1 mL/h (Figure 14 A). Third, surface topographical features were observed on top of the microfibres but this effect was influenced by the polymer flow rate and hence fibre diameter. Fibres spun with low flow rates of 1 and 4 mL/h (Figure 14 A and B) showed no topography or only weak pitted structures on top of the fibres, where in contrast higher flow rates resulted in a more distinct pattering on the surface of fibres (Figure 14 C – E).

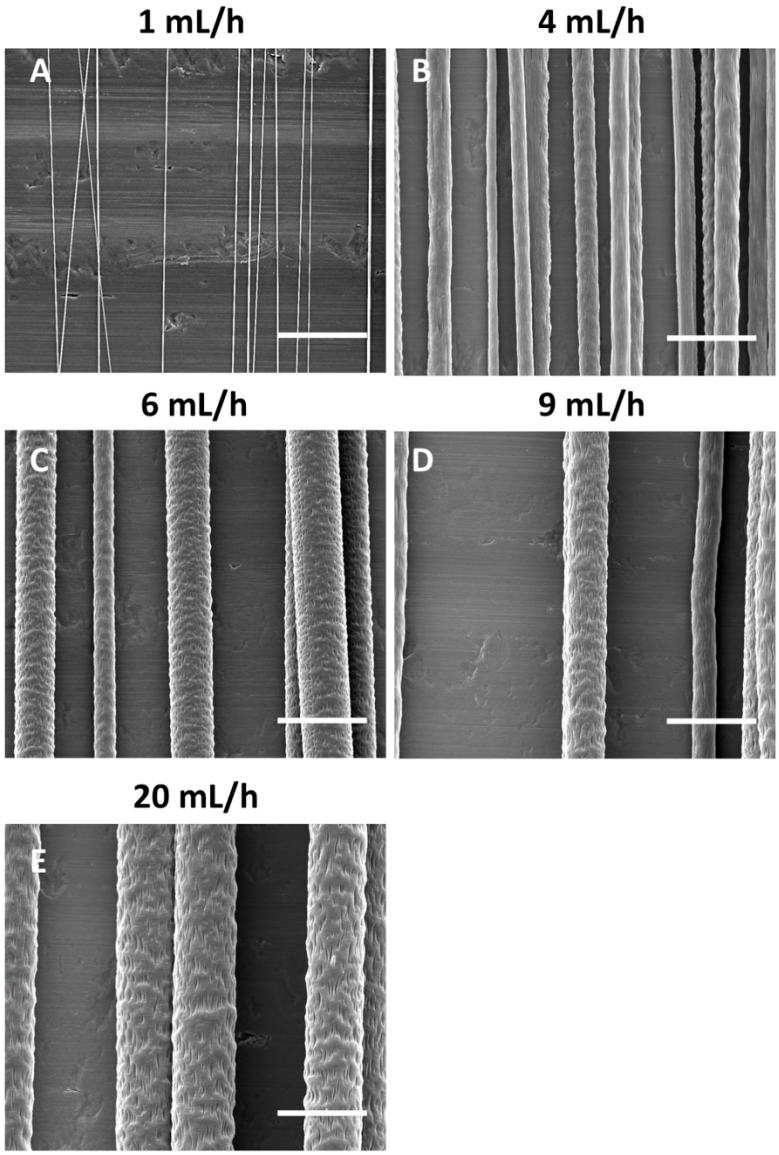

Figure 14 Scanning electron micrographs of aligned PCL microfibres

Aligned PCL microfibres were electrospun to specific diameters (1 – 13 µm) using different polymer flow rates of either (A) 1 mL/h, (B) 4 mL/h, (C) 6 mL/h, (D) 9 mL/h or (E) 20 mL/h. For all samples, a collector speed of 2000 rpm and a collector-to-needle distance of 20 cm was used. A polymer concentration of 20 % in DCM was used when spinning with flow rates ≥ 4 mL/h. Flow rates of 1 mL/h required a 10 % PCL in DCM solution. Fibres were imaged by SEM. Representative images are shown of five independent experiments. Scale bar = 20µm.

The results in Figure 14 were generated by altering the polymer flow rate and also the polymer-to-solvent ratio. Figure 15 A shows a trend of increasing fibre diameter with an increase in the applied flow rate. Flow rates of 4, 6, 9 and 20 mL/h, when using a 20 % PCL in DCM solution, resulted in fibre diameters of 5.02 ± 0.55 µm, 7.96 ± 1.0 µm, 9.64 ±

0.78 µm and 13.14 ± 1.75 µm, respectively. A lower polymer concentration of 10 %, combined with an applied flow rate of 1 mL/h, resulted in fibre diameters of 0.89 ± 0.53 µm (Figure 15 A). A one-way ANOVA with Tukey's multiple comparisons test revealed that fibre diameters could be spun reproducibly with significant differences between fibre diameters when altering the flow rate of polymer solution (1 vs. 4 mL/h, 4 vs. 6 mL/h, 9 vs. 20 mL/h $p<0.05$). Based on these results, fibres were categorised in groups of 1, 5, 8, 10 and 13 µm. Besides the fibre diameter, the alignment of fibres of all five fibre groups was analysed. Figure 15 B shows the percentage distribution of angular differences between fibres, where the angular difference between a centrally aligned fibre (set as 0°) and the neighbouring fibres was measured. It is clearly demonstrated that fibres of all fibre groups were highly aligned with a maximum angular variation of 8°, where it is apparent that only few fibres showed an angular variation of 6 – 8°. More than 60 % of all measured fibres beyond the five diameter groups showed an angular difference of less than 2°, where less than 40 % aligned in a 3 – 8° difference to the reference fibre.

These results indicate that the chosen processing conditions enable the manufacturing of highly aligned fibres with precise dimensions, which could herein be classified into five diameter groups ranging from 1 – 13 µm.

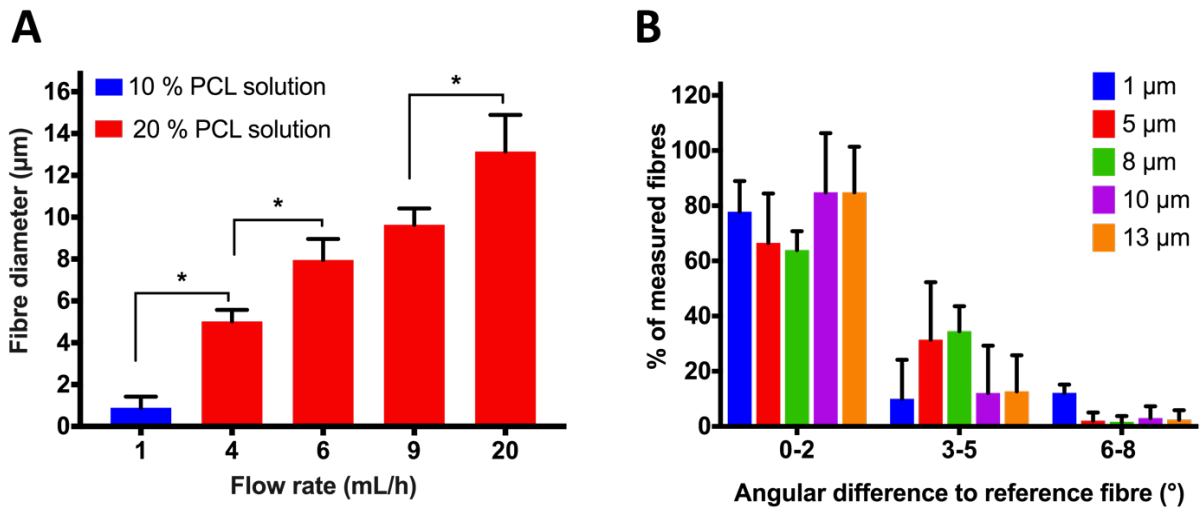

Figure 15 Diameter and alignment evaluation of PCL microfibres

PCL microfibres were electrospun using flow rates of 1, 4, 6, 9 and 20 mL/h and imaged using SEM. Fibres were analysed in Fiji on (A) fibre diameter and (B) fibre alignment. Fibre diameter was dependant on the flow rate used (A), where the majority of fibres aligned with an angular difference of 0 – 2° to a reference fibre (B). Values represent the mean + SD of five independent experiments. Statistical significance was analysed by ordinary one-way ANOVA with Tukey's multiple comparisons test and displayed as * $p<0.05$.

3.4.1.2 Morphology of electrospun PCL fibres

The implied surface topography on the five different electrospun PCL fibres of different diameter was further investigated. SEM images, taken at magnifications of either 10,000× or 40,000× are presented in Figure 16. From this, two types of topographical structures were identified on the surface between the different fibre diameter, where surface structures on 1 µm fibres differed (Figure 16 A) from features on 5, 8, 10 and 13 µm fibres (Figure 16 B – E). The surface of 1 µm fibres was covered in shallow and circular-shaped depressions that enfolded uniformly over the entire fibre surface (Figure 16 A). In comparison, bigger fibre diameter of 5, 8, 10 and 13 µm presented surface topographies of elliptic shape showing elongated grooves in fibre direction (Figure 16 B – E). Like on 1 µm fibres, grooves were evenly distributed on the fibre surface but appeared less frequent with a smaller number of grooves in the same area (Figure 16 B – E). Depressions seen on fibre surfaces in Figure 16 B – E appeared deeper than on 1 µm fibres, where structures were of shallow depression (Figure 16 A).

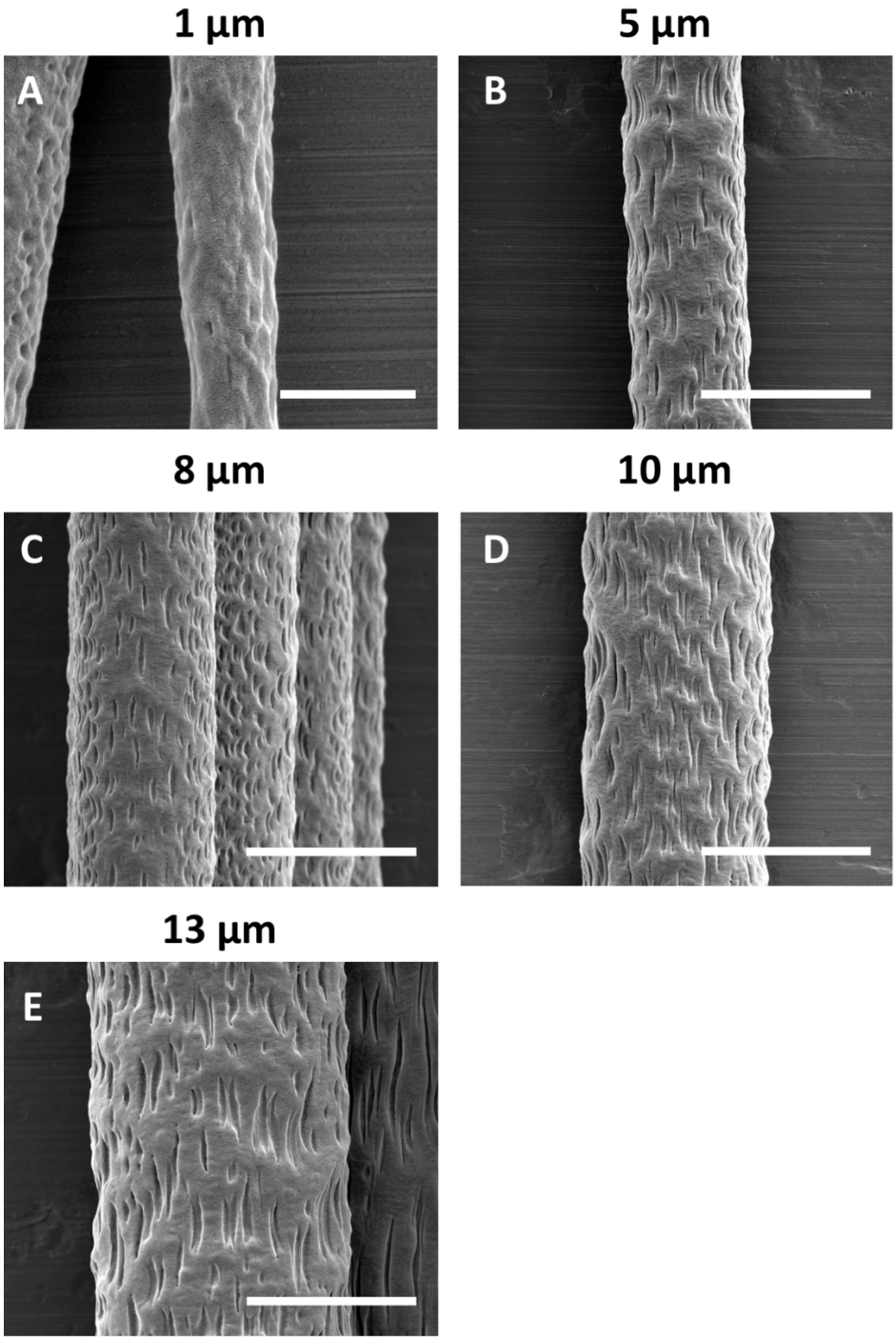

Figure 16 Topographies on the surface of electrospun PCL fibres

Scanning electron micrographs presenting electrospun PCL fibres of different diameters showing topographical features on the fibre surface. A) 1 µm PCL fibres electrospun with a flow rate of 1 mL/h from a 10 % PCL in DCM solution. Magnification of 40,000× with a scale bar = 2 µm. B) – E) Fibre diameter of 5, 8, 10 and 13 µm in ascending order fabricated from a flow rate of 4, 6, 9 and 20 mL/h, respectively using a 20 % PCL in DCM solution. Images were captured at a magnification of 10,000×. Scale bar = 10 µm. Representative images are shown.

Fibre surface topographies demonstrated in Figure 16 were further quantified in Fiji and results presented in Figure 17. Topographical grooves on fibre surface were analysed on area, length, the ratio between groove width to length and the frequency of features per μm^2. The differences in groove area between the five different fibre diameter is presented in Figure 17 A. Changes in between groups were classified into three classes of small, medium and large groove area. On average, 1 µm fibres presented the smallest grooves with an area of about 0.02 μm^2 which differed significantly from 5, 8, 10 and 13 µm fibres. Medium groove areas ranging from 0.44 to 0.55 μm^2 were seen between 5 – 10 µm fibres. Significantly larger grooves were present on 13 µm fibres that showed an average groove area of 0.84 μm^2 (Figure 17 A). In Figure 17 B, similar differences between groove length and different fibre diameter were found. The shortest grooves were seen on 1 µm fibres with an average length of 0.23 $\pm$ 0.06 µm. Significantly longer grooves were visible on 5 – 10 µm fibres with lengths ranging between 1.77 and 2.22 µm. 13 µm fibres presented the longest grooves with an average length of 3 $\pm$ 0.88 µm (Figure 17 B). Figure 17 C provides information about groove shape, expressed as the ratio of groove width to length, where a ratio of 50 % would indicate a circular topography. The ratio between groove width and length accounted in average 42.4 $\pm$ 8.8 % on 1 µm fibres and measured significantly lower on 5 – 13 µm fibres with a ratio ranging between 15.3 – 17.7 % (Figure 17 C). From the data in Figure 17 D, it is apparent that the surface of 1 µm fibres bore significantly more grooves per μm^2 than 5 – 13 µm fibres. On average, 6.5 $\pm$ 2.2 topographical features were found per μm^2 on 1 µm fibres and more than three times less grooves on 5 – 13 µm fibres that showed 1.4 – 1.7 grooves/μm^2 (Figure 17 D).

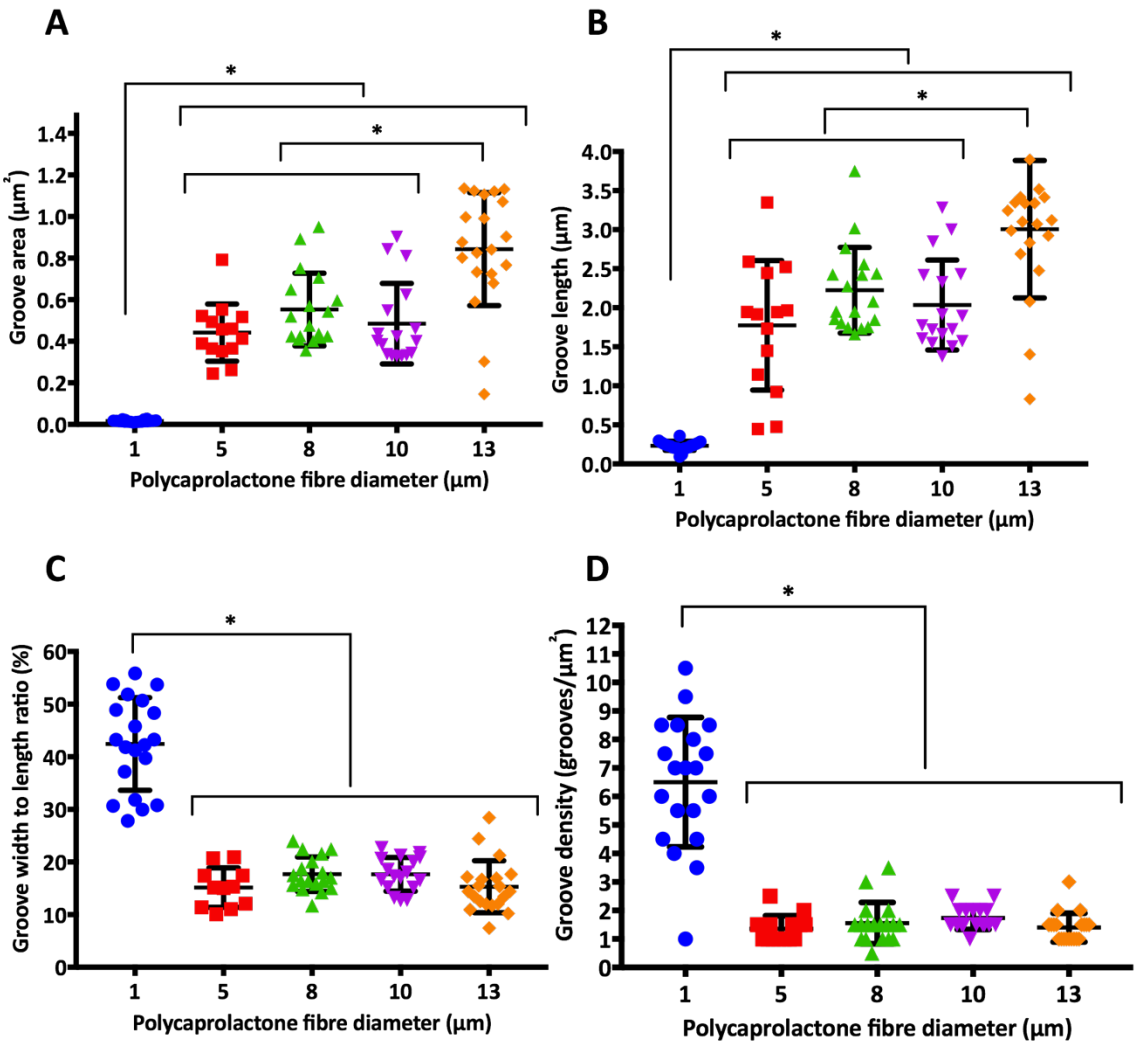

Figure 17 Quantitative analysis of topographical features on fibre surface

Topographical features (grooves) on electrospun PCL fibres with diameters of 1, 5, 8, 10 and 13 µm were measured and analysed to give information about A) groove area, B) groove length, C) groove width to length ratio and D) the number of grooves per µm^2. Measurements were conducted in Fiji based on SEM images as presented in Figure 16. N=2 experiments showing values as mean + SD. Statistical analysis was performed with one-way ANOVA using Tukey's post-hoc multiple comparisons test. Statistical differences were indicated as * $p<0.05$.

3.4.2 Optimising experiments for cell culture

3.4.2.1 Toxicity evaluation of a fibre scaffold adhesive on NG108-15 neuronal cells

Electrospun PCL microfibre scaffolds were tested and analysed in *in vitro* cell culture studies to investigate its supportive potential in peripheral nerve repair. In order to practically use fibre mat scaffolds in culture, scaffolds needed to be immobilised at the

bottom of the cell culture substrate to prevent lifting off and floating when culture medium was added to provide an even substrate for cells to adhere on. Herein, a silicone-based aquarium sealant from King British was used (referred to as "glue") to adhere fibre scaffolds to the bottom of TCP well plates. In all cell culture experiments where glue was used, cells were never in direct contact with the glue. Instead, an equal amount of glue was applied to metal grids which were then submerged into the cell culture medium, where both NG108-15 neuronal cells and primary rat Schwann cells were not in direct physical contact with the glue but kept in the same medium. Resazurin reduction assays were performed over 21 days to measure the effect of any potential elution of the adhesive into the culture medium on cell's metabolic activity, where any changes in cell morphology were additionally documented over the same time period using light microscopy.

NG108-15 neuronal cells were seeded in culture medium containing 10 % FBS to promote the attachment of cells to TCP. Light microscope images in Figure 18 A showed that neurons attached evenly to the TCP substrate after one day of culture disregarding the addition of glue to the culture medium. Cells on control surfaces of TCP alone and in co-appearance with glue showed the same morphology, where some cells still appeared in a convex form, while others already showed a flatten morphology, where small processes started to emerge from the cell body. After one day of culture, serum was withdrawn and cells were further cultured under serum-free conditions to stimulate the formation of neurites. After 7 days of culture, light microscope images revealed a notable increase in cell number for both experimental groups compared to images taken on day 1 (Figure 18 B). Additionally, a robust network of neurites was formed between cells, where neurons appeared in a bipolar shape with two axonal processes emerging from one cell body. These observations applied for both experimental groups. Where an even distribution of neurons was evident after 7 days of culture (Figure 18 B), cells appeared in clustered groups after 14 days of culture, where axonal processes were less visible in both experimental conditions (Figure 18 C). After 21 days of culture, clustered cell groups disappeared but neurites were still visible for both cell groups (Figure 18 D).

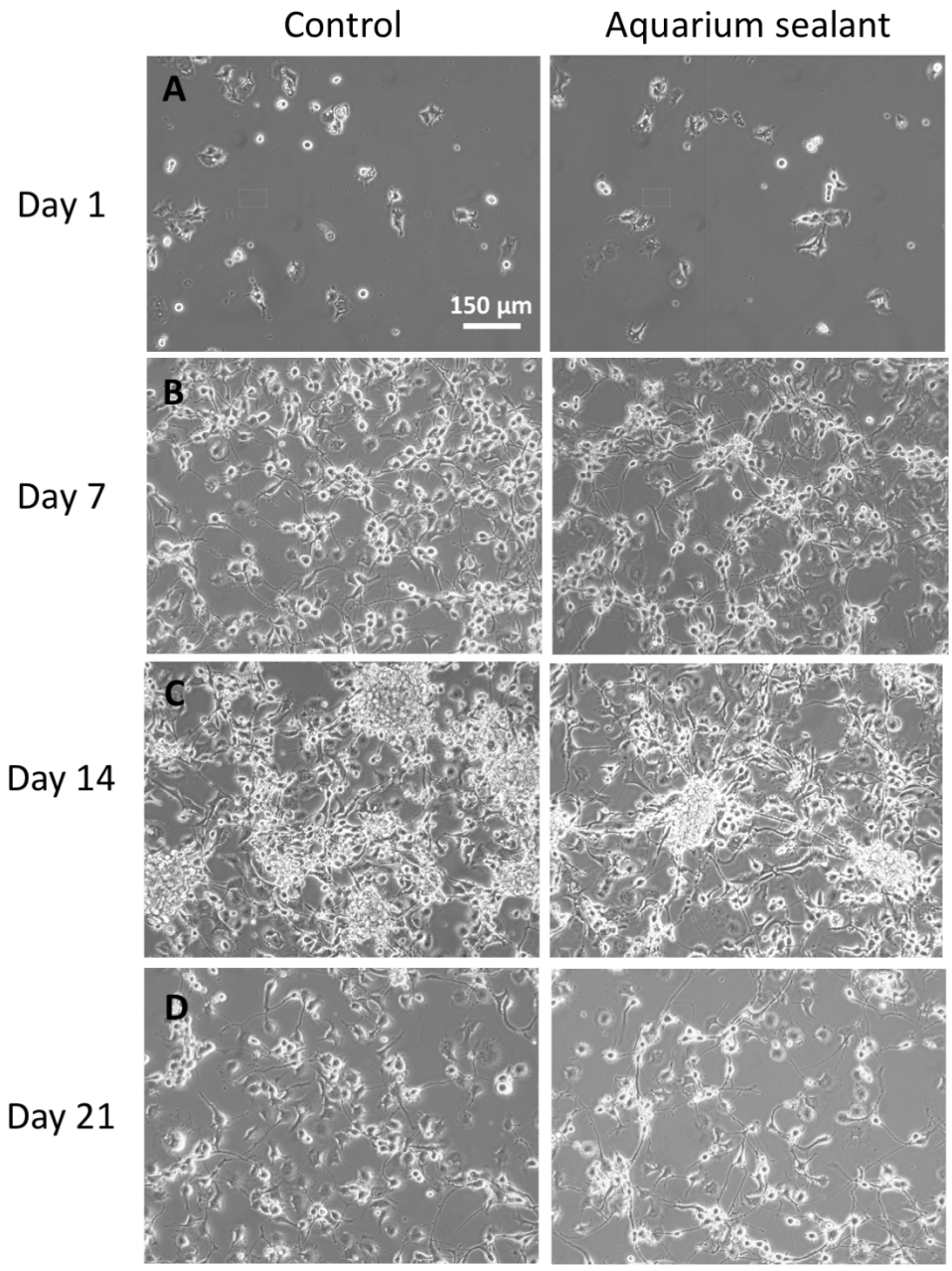

Figure 18 Culture of neuronal cells with aquarium sealant

Light microscope images of neurons cultured with (right column) and without (left column) aquarium sealant. NG108-15 neuronal cells were seeded with 2,105 cells/cm^2 in 6-well plates using 10 % FBS supplemented medium, where cells were withdrawn from serum the following day. After one day, cells were incubated with either metal grids carrying 0.15 g aquarium sealant ("aquarium sealant") or metal grids without glue ("control"). Light microscope images were taken in three random positions per well after A) 1 day, B) 7 days, C) 14 days and D) 21 days. Representative images are shown of two independent experiments with triplicate used within experiments. Scale bar = 150µm and applies to all images.

In addition to the observed changes in cell appearance, findings were further quantitatively studied in resazurin reduction assays, where changes in cell metabolic activity was measured at days 1, 7, 14 and 21. Corresponding findings were summarised in Figure 19. A continuous increase in metabolic activity was found from day 1 to 14, starting off with similar activity levels in both the control and experimental group on day 1. In both experimental groups the activity level increased by more than 3.5 times from day 1 to day 7 and even further, measuring 5 times greater on day 14 compared to day 1. Additionally, it is apparent from Figure 19 that metabolic activity levels in both groups reached a maximum at day 14. This increase in activity from day 1 to 14 was found to be significant but was similar between the experimental groups, where differences were not statistically different (day 1 vs. 7: $p<0.05$ (aquarium sealant and control), day 1 vs. 14: $p<0.05$ (aquarium sealant, control)). These findings correlate with what has been observed in Figure 18, where an increase in number of cells was visible on day 7 compared to day 1 and further increased by day 14. Although Figure 18 C and D indicated a decrease in cell number in both groups between day 14 and day 21, there was no significant difference in the measured metabolic activity in the groups between day 7, 14 and 21 (Figure 19). Overall, no significant differences between the two experimental groups were found at any time point of measure (Figure 19), which additionally corresponded with the similar morphological appearance of cells presented in Figure 18.

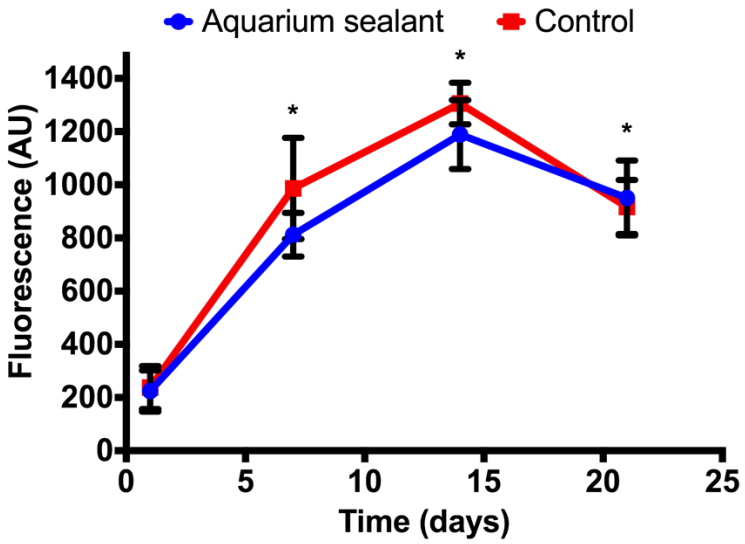

Figure 19 Metabolic activity rates of neuronal cells with aquarium sealant

Neuronal cells were seeded and cultured as described in figure 5. Resazurin reduction assays were performed on day 1, 7, 14 and 21. Values are displayed as mean ± SD of three independent experiments. Assays were performed as repeated measures. Statistical differences were confirmed by two-way ANOVA with Tukey's multiple comparisons test. Differences were displayed as * $p<0.05$ in relation to day 1. Assays were performed in triplicate with two independent repeats.

3.4.2.2 Toxicity evaluation of a fibre scaffold adhesive on primary Schwann cell cultures

Furthermore, primary rat Schwann cells were exposed to the same aquarium sealant using the same experimental procedure with the exception that Schwann cells were cultured in 10 % FBS growth medium throughout the experiment.

Figure 20 demonstrates the morphological appearance of Schwann cells in both experimental groups over a time period of 21 days that was observed by light microscopy. On day 1, cells of both experimental groups attached to the TCP substrate and showed a flattened morphology, with an elongated and widely spread cytoskeleton, where cells reached sizes up to 200 µm (Figure 20 A). It is apparent from the images in Figure 20 A that cells attached in an even arrangement on the TCP substrate with sufficient free space between cells. A notable increase in cell number and decrease in empty substrate space was observed in Figure 20 B, C and D. Schwann cells remained their elongated morphology but appeared to be in physical contact with each other with

no free space being apparent in-between cells. No striking difference in cell number or morphology could be seen between time points 7, 14 and 21 (Figure 20 B – D). Additionally, it was noted that the changes in cell appearance within 21 days of culture were similar between the two experimental groups.

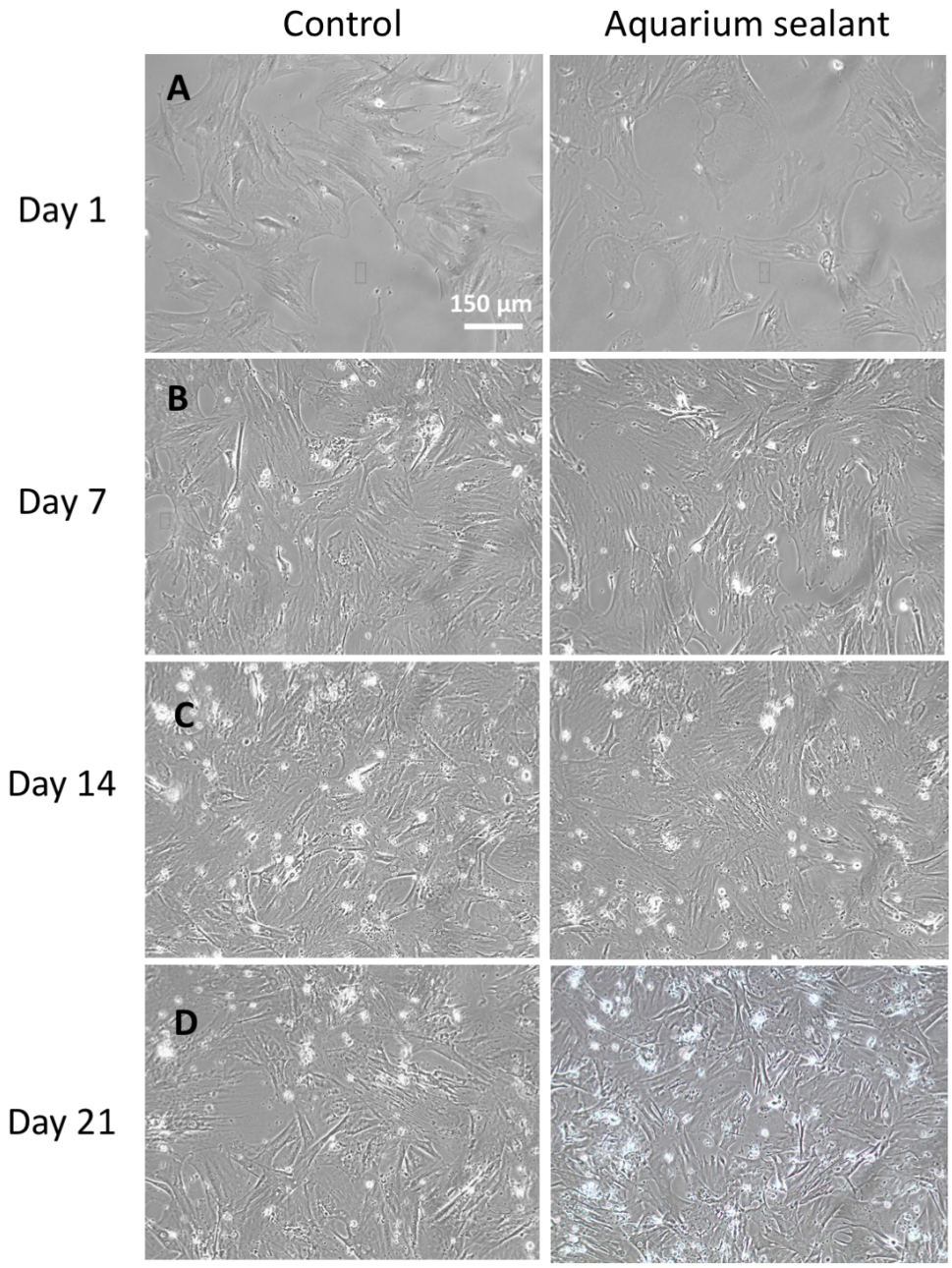

Figure 20 Culture of primary Schwann cells with aquarium sealant

Light microscope images of primary rat Schwann cells cultured on TCP with metal grids carrying 0.15 g aquarium sealant or metal grids alone (control) on day A) 1, B) 7, C) 14 and D) 21 days of culture. Representative images are shown of two independent experiments. Scale bar = 150µm and applies to all images.

Additionally, the effect of aquarium glue on Schwann cell metabolic activity was studied on days 1, 3, 5, 7, 14 and 21. Results are summarised in Figure 21. A continuous incline in metabolic activity was observed within the first 7 days of culture, where activity levels increased by more than 3.5 times within 7 days compared to day 1. This increase was tested to be significant for both experimental groups (day 1 vs. 7: $p<0.05$ (control and aquarium sealant)) but were tested negative in-between the groups. Additionally, it was found that a further increase in metabolic activity was not observed after 7 days in culture. Beyond 7 days, metabolic activity levels were similar until day 21. Overall, there was no decrease in metabolic activity associated with the addition of glue to the medium. A repeated measures two-way ANOVA with Tukey's multiple comparisons test confirmed that data points were not significantly different to each other.

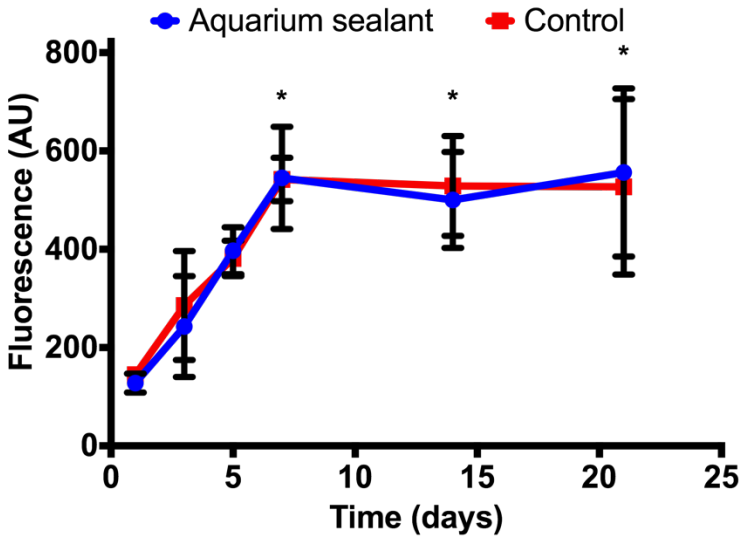

Figure 21 Metabolic activity rates of primary Schwann cells with aquarium sealant

Primary rat Schwann cells were seeded and cultured as described in figure 7. Resazurin reduction assays were performed on day 1, 3, 5, 7, 14 and 21. Values are displayed as mean ± SD of three independent experiments. Assays were performed as repeated measures. Statistical differences were confirmed by two-way ANOVA with Tukey's multiple comparisons test. Differences were displayed as * $p<0.05$ in relation to day 1. Assays were performed in triplicate with two independent repeats.

In summary, these results indicated that the morphology of both neuronal and Schwann cells and their metabolic activity levels remained unchanged after the addition of aquarium sealant to the culture medium., suggesting the safe use of aquarium sealant as a scaffold adhesive in future studies.

3.4.2.3 Culture medium optimisations for NG108-15 neuronal cells

Herein, PCL fibre scaffolds with different dimensions were evaluated in neuronal cell cultures. In order to determine the best culture environment for NG108 neuronal cells to form and grow neurites, different concentrations of FBS were applied to the growth medium. Cells were cultured on TCP in growth medium containing 10 % FBS for one day and were then exposed to either 0, 1.25, 2.5 or 5 % FBS for another four days. To assess the effect of different FBS concentrations on neurites, the incidence and length of neurites was measured using F-actin labelling.

Analysis was based on endpoint fluorescent microscope images as shown in Figure 22 that demonstrates neuronal cells labelled for F-actin with phalloidin-TRITC on TCP substrates exposed to different FBS concentrations. It was noted that following the addition of FBS to the growth medium, cell number increased with a correlating decrease in neurite length and incidence (Figure 22 A – D). These described differences can be clearly seen when comparing Figure 22 A and D. NG108-15 neuronal cells that were cultured in serum-free medium (Figure 22 A) showed notably less cells per area compared to cells that were maintained with 5 % FBS in the growth medium (Figure 22 D). Additionally, longer neurites were apparent in serum-free medium (Figure 22 A) compared to medium containing 5 % FBS (Figure 22 D).

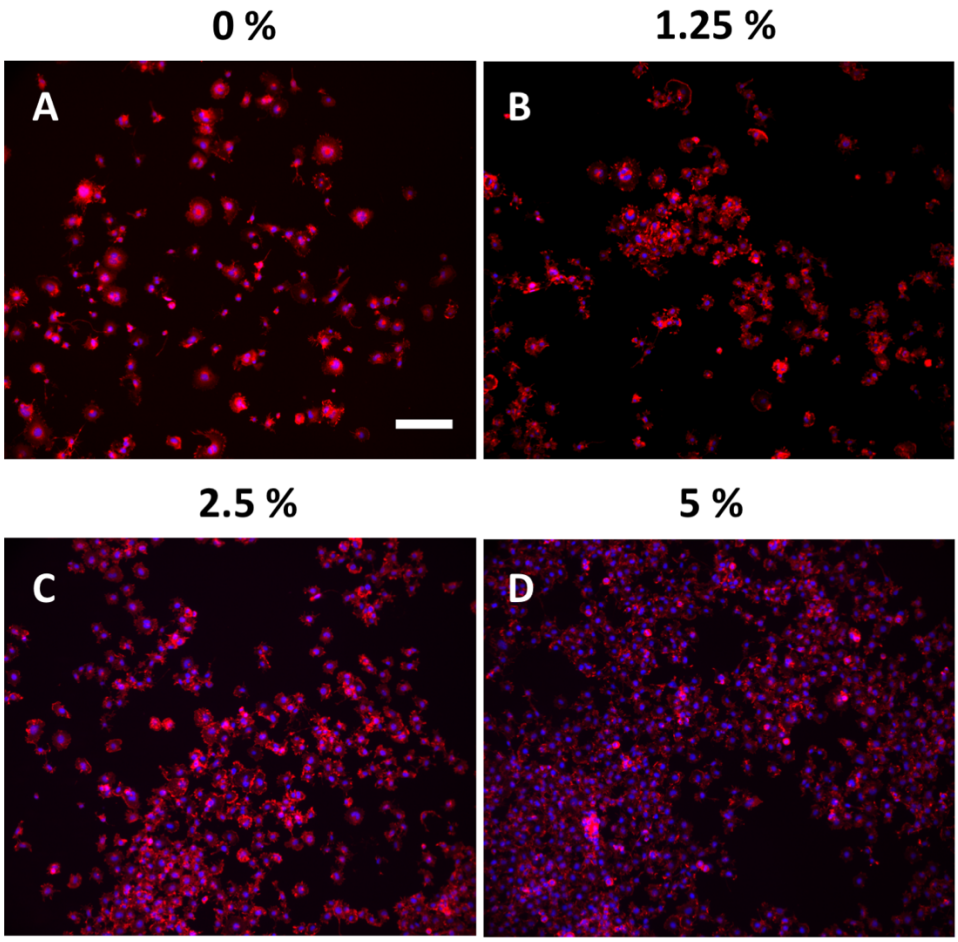

Figure 22 Changes in neuronal cell morphology in different serum concentrations

NG108-15 neuronal cells were seeded with 1,316 cells/cm^2 in 12-well plates using 10 % FBS supplemented medium for 1 day. The medium was replaced by either A) 0 %, B) 1.25 %, C) 2.5 % or D) 5 % FBS supplemented growth medium the day after. Neurons were cultured for 5 days in total and subsequently fixed, permeabilised and labelled for F-actin using phalloidin-TRITC (red). Nuclei were visualised using DAPI (blue). Cells were imaged in three random positions using a fluorescence microscope. Representative images are shown of three independent experiments with triplicate used within experiments. Scale bar = 200 µm and applies to all images.

The relationship between neurite incidence and applied FBS concentration was studied in Figure 23 A. It was found that neuronal cells cultured without FBS formed on average 31.1 ± 5.3 % neurites. FBS concentrations of 1.25 % resulted in 30.6 ± 6.2 % of neurites formed. A further increase in FBS concentration to 2.5 % and 5 % in the culture medium, resulted in 28.9 ± 7.7 % and 27.9 ± 5.1 % of neurons bearing neurites, respectively. There

was no significant relationship between neurite incidence and FBS concentration as found by one-way ANOVA with Tukey's multiple comparisons test.

Furthermore, the effect of different FBS concentrations on neurite outgrowth length was studied. In Figure 23 B there was a clear relationship of increasing neurite length with decreasing concentration of FBS. FBS concentrations of 5, 2.5 and 1.25 % resulted in average measured neurite lengths of 33.6 ± 9.7 µm, 40.0 ± 5.7 µm and 50.3 ± 5.2 µm, respectively. A significant increase in neurite length was found when neuronal cells were cultured under serum-free conditions, where neurites had an average length of 83.2 ± 10.7 µm.

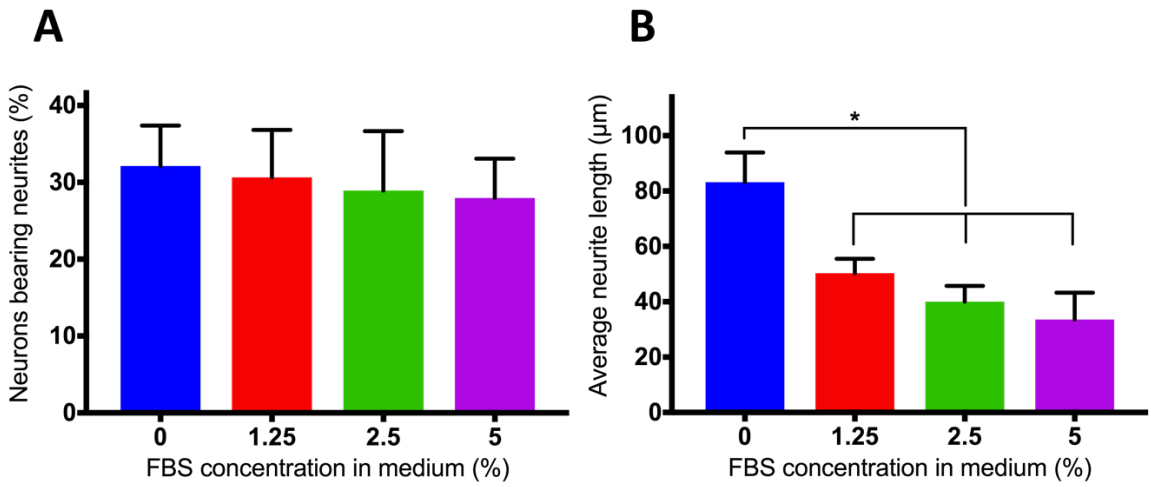

Figure 23 Effect of foetal bovine serum concentrations on neurite outgrowth

NG108-15 neuronal cells were seeded as described in Figure 22. Fluorescent images (shown in Figure 22) were analysed in Fiji with regard to A) the percentage of cells bearing neurites and B) neurite length. Significance was analysed by one-way ANOVA with Tukey's multiple comparisons test and displayed as * $p<0.05$. Values represent the mean + SD of three independent experiments.

3.4.2.4 Growth medium optimisations for primary Schwann cell cultures

In order to investigate the effect of different fibre scaffolds on Schwann cells viability, activity and proliferation rates, the best culturing conditions needed to be identified. Therefore, primary Schwann cells were seeded on TCP in five different concentrations of FBS, and their metabolic activity measured and changes in morphology observed. Cells were cultured in 10 % FBS growth medium overnight to allow cell attachment.

Afterwards, medium was replaced by either 0, 1.25, 2.5, 5 or 10 % FBS medium and cells cultured for a total of 72 h. Changes in cell morphology and metabolic activity rates were investigated every 24 h.

Morphological observations were observed in light microscope images in Figure 24. Following the addition of different serum concentrations to the growth medium, the cytoskeleton of Schwann cells appeared flat and widely spread around the nucleus on a TCP substrate after 24 h (Figure 24 A – E, far left images). The number of cells and morphological appearance was noted as being similar between experimental groups after 24 h. However, Schwann cells maintained in serum-free medium mostly displayed a flat and spread cytoskeleton, with the exception of some cells that appeared to have a deformed morphology, where thin processes were branching from the nucleus and the flat and spread appearance of the cytoskeleton around the nucleus was lost (Figure 24 E, far left image, morphological changes indicated by arrows). The number of Schwann cells increased between 48 and 72 h, where an increase correlated with serum concentration in the medium. This effect was predominantly seen for cells maintained in 10 % FBS in the medium (Figure 24 A). The morphology of cells was not affected by serum concentrations of 1.25 – 10 % (Figure 24 A-D). However, there was a visible decrease in cell number when Schwann cells were cultured in serum-free medium, where cells lost their integrity and damage to the cytoskeleton and cell debris was apparent after 48 h (Figure 24 E, cell changes indicated by arrows).

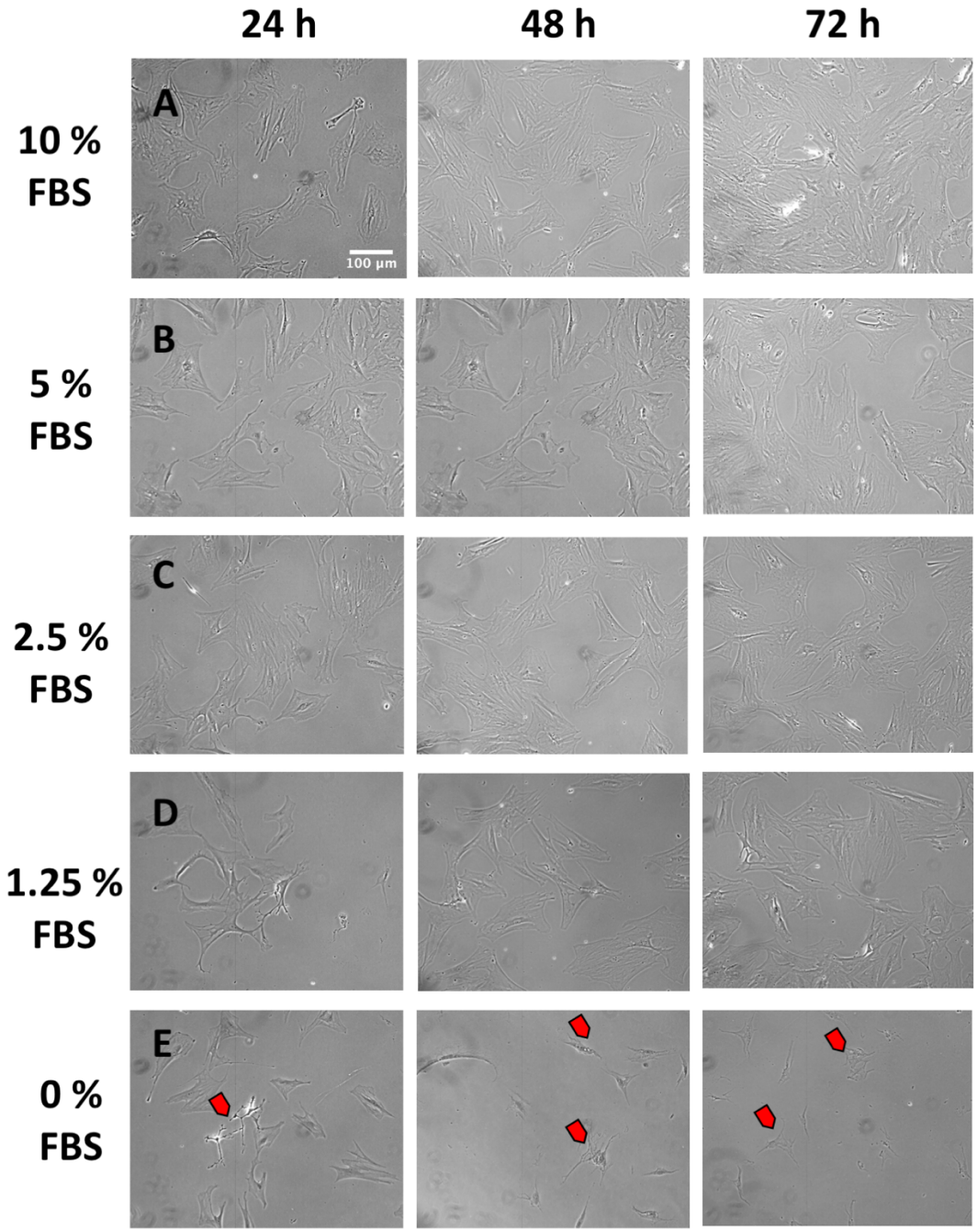

Figure 24 Changes in primary Schwann cell morphology in different serum concentrations

Primary rat Schwann cells were seeded with 1,316 cells/cm^2 in growth medium for 1 day. Afterwards, medium was replaced by either A) 10 %, B) 5 %, C) 2.5 %, D) 1.25 % or E) 0 % FBS containing medium and cells left for 72 h. Changes in cell morphology were monitored by light microscopy 24, 48 and 72 h after the medium was changed. Representative images are shown of three independent experiments with triplicate used within experiments. Arrows indicate severe changes in the cell's cytoskeleton. Scale bar = 100 µm and applies to all images.

These observations were further quantified by measuring the metabolic activity of Schwann cells over time (Figure 25). Activity rates corresponded with findings from Figure 24, and an increase in metabolic activity was found with an increase in serum concentration. After 48 h and 72 h, Schwann cells in 10 % FBS medium showed the greatest metabolic activity compared to lower serum concentrations. Activity increased more than three times after 72 h compared to initial values before medium changes were conducted. Additionally, the metabolic activity of Schwann cells in 10 % FBS medium was significantly higher than cultured in 0 – 5 % FBS after 72 h. Serum concentrations of 1.25 – 5 % equally increased the metabolic activity of cells over time but activity rates were lower compared to 10 % FBS concentrations. The observed changes in cell appearance following serum withdrawal as demonstrated in Figure 24 were found to be similar. The metabolic activity rate consistently decreased after serum withdrawal, where rates were 75 % lower after 72 h compared to initial values before medium changes were applied. After 48 and 72 h, values were significantly lower than using 10 % FBS medium.

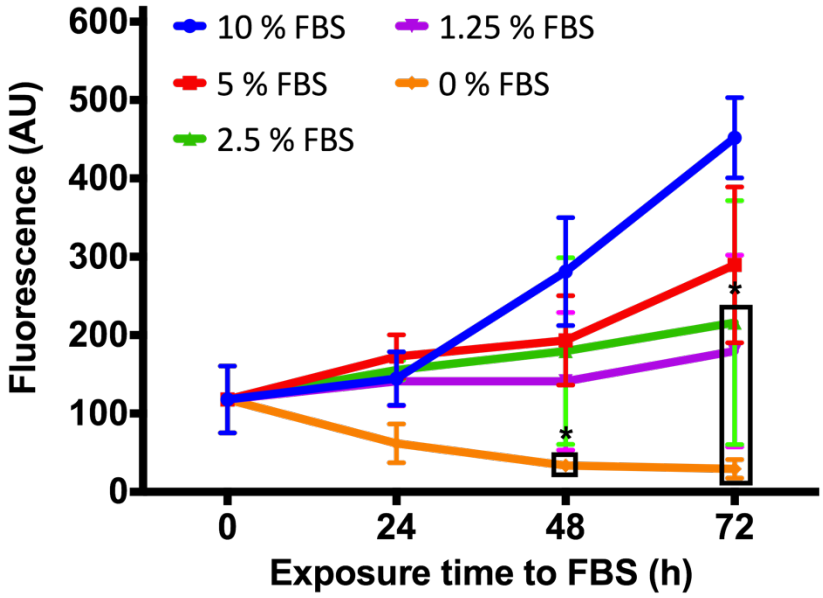

Figure 25 Effect of different serum concentrations on the metabolic activity of Schwann cells

Primary rat Schwann cells were cultured as described in Figure 24. Resazurin reduction assays were performed before serum concentrations were altered, indicated as time point 0, and every 24 hours after for a total period of 72 hours. Values are displayed as mean ± SD of three independent experiments. Assays were performed as repeated measures. A two-way ANOVA with Tukey's multiple comparisons test was performed, comparing between conditions at each time point. Each box indicates the data points that were significantly different in comparison to 10 % FBS (* $p<0.05$).

3.4.3 An *in vitro* study of PCL fibre scaffolds in neuronal cell culture

3.4.3.1 Viability analysis of neuronal cells on different PCL microfibre diameters

The correlation between different fibre diameters and the number of living and dead neuronal cells was analysed using a live/dead cell overview stain. Neuronal cells were seeded on 1 – 13 µm fibres and control surfaces of PCL films and TCP. Assays were performed after 5 days of culture in serum-deprived conditions. The confocal microscopy images in Figure 26 were taken in z-stacks, which were overlaid and demonstrated as maximum projection images. It is apparent from Figure 26 A – G that cells were predominantly alive on all fibre diameters, the PCL film control and on TCP with only a few dead cells (red) visible. Neuronal cells generally aligned with the direction of

microfibres, where cells on TCP and PCL films did not show a specific orientation (Figure 26 F and G). Interestingly, this pattern of alignment could not be seen with cells on 1 µm fibres (Figure 26 A), where cells showed a random attachment pattern similar to both the control surfaces. Additionally, a greater number of dead cells was observed on 1 µm fibres compared to the other fibre diameters, PCL films and the TCP control (Figure 26 A).

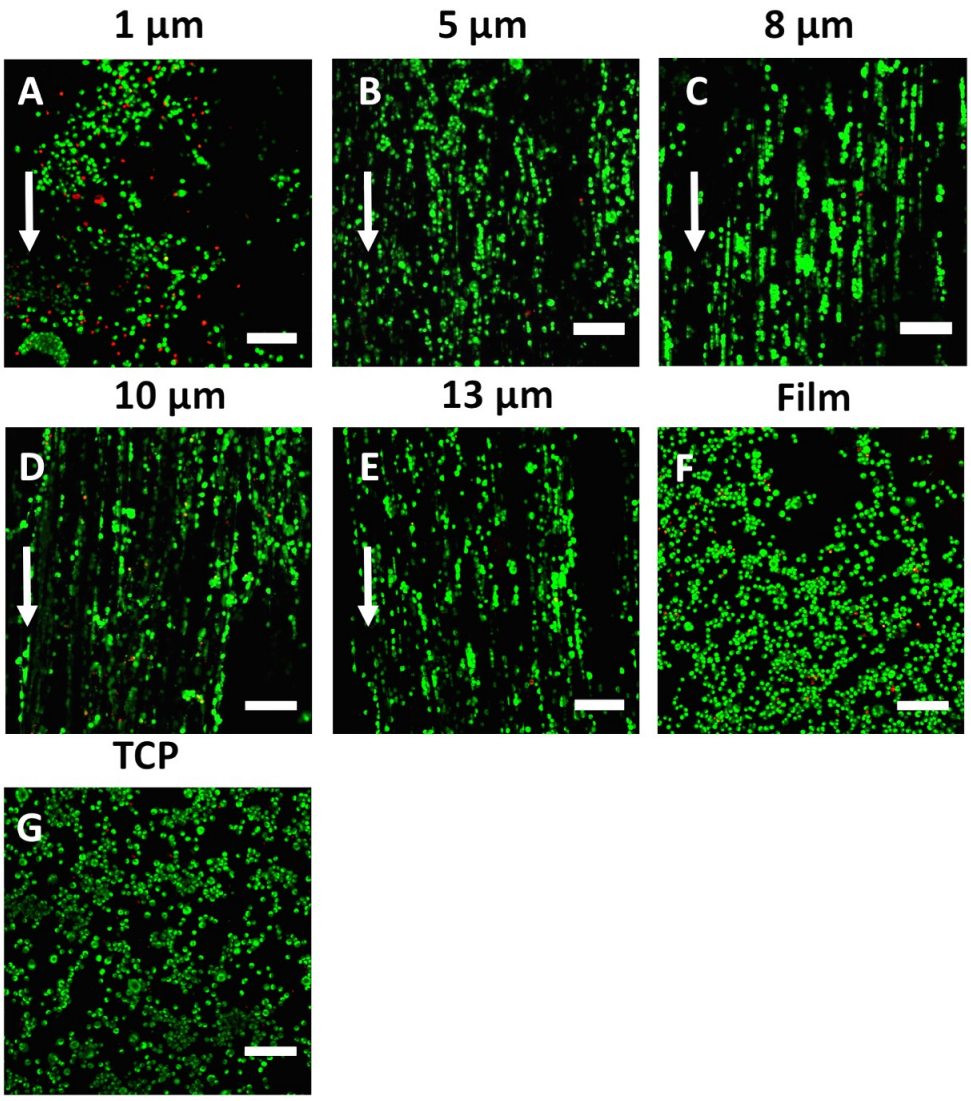

Figure 26 Overview of living and dead neuronal cells on five different PCL fibre diameters

Maximum projection confocal microscopy images of living (green) and dead (red) NG108-15 neuronal cells cultured on A) 1 µm, B) 5 µm, C) 8 µm, D) 10 µm and E) 13 µm PCL fibres and on F) flat PCL films and G) TCP after 5 days of culture. Cells were cultured in serum-free conditions and confocal images taken in three random positions per sample in z-stacks. Arrows indicate the direction of fibre alignment. Representative images are shown of three independent experiments. Scale bar = 200 µm.

Further quantification of the results presented in Figure 26 were conducted, and presented in Figure 27. From this data, it can be seen that there was a positive and significant correlation between living and dead cells on all samples tested. Over all culture substrates tested, living cell numbers consistently dominated over dead cells with values ranging from 81.2 ± 8.7 % and 93.0 ± 4.1 % depending on the substrate. More than 90 % of neuronal cells were alive when cultured on fibre diameters of 5 – 13 µm, PCL films or on TCP over 6 days of culture. Following the culture of neuronal cells on 1 µm fibres, 81.2 ± 8.7 % of living cells and 18.8 ± 8.7 % of dead cells were detected. No significant correlation between fibre diameter and increased cell death was found.

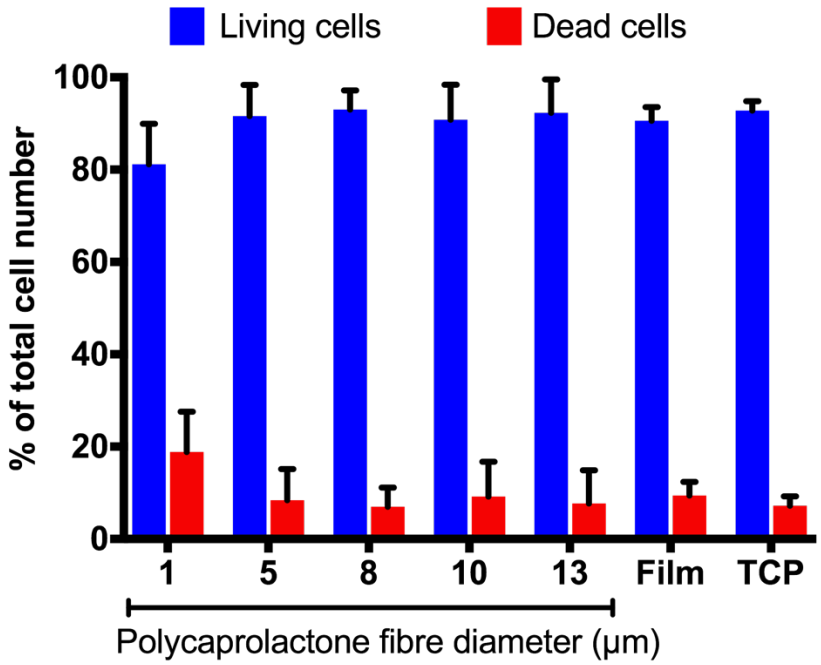

Figure 27 Effect of different PCL fibre diameters on neuronal cell viability

Neuronal cells were seeded on 1, 5, 8, 10 and 13 µm PCL fibres, PCL films and TCP as described in Figure 26. Confocal images of living and dead cells (shown in Figure 26) were analysed in Fiji. Results are displayed as percentages of the total cell number analysed and demonstrate mean values + SD of three independent experiments. Two-way ANOVA analysis with Tukey's multiple comparisons test showed no significant differences between living cells and dead cells, respectively.

3.4.3.2 Morphology study of neuronal cells on different PCL microfibre diameters

The morphology of neuronal cells on the five different PCL fibre diameters was closely examined under high magnifications using scanning electron microscopy in order to

evaluate the relationship between neurite alignment and branching and PCL fibre diameters. Neuronal cells were cultured on the different PCL fibre scaffolds under serum-deprived conditions to support the formation of neurites. It was apparent that neuronal cells attached to all fibre diameters (Figure 28). Neuronal processes were formed on all fibre diameters, where neurites elongated in the direction to other neurons to form axonal connections between cells. It was noted that neurites on 1 and 5 µm PCL fibres branched over several fibres in order to form these connections, which were indicated by arrows in Figure 28 A and B. This described branching was mostly observed across multiple fibres in opposite direction to the fibre direction. In comparison, neurites on 8, 10 and 13 µm fibres elongated predominately along single microfibres in the direction of fibre alignment with only a few branches forming across fibres (indicated by arrows in Figure 28 C, D and E). Additionally, it was found that neuronal cell bodies on smaller fibre diameter of 1 and 5 µm mainly attached to several fibres at once (Figure 28 A – B), where on bigger fibre diameters one neuronal cell body adhered to a single fibre (Figure 28 C – E).

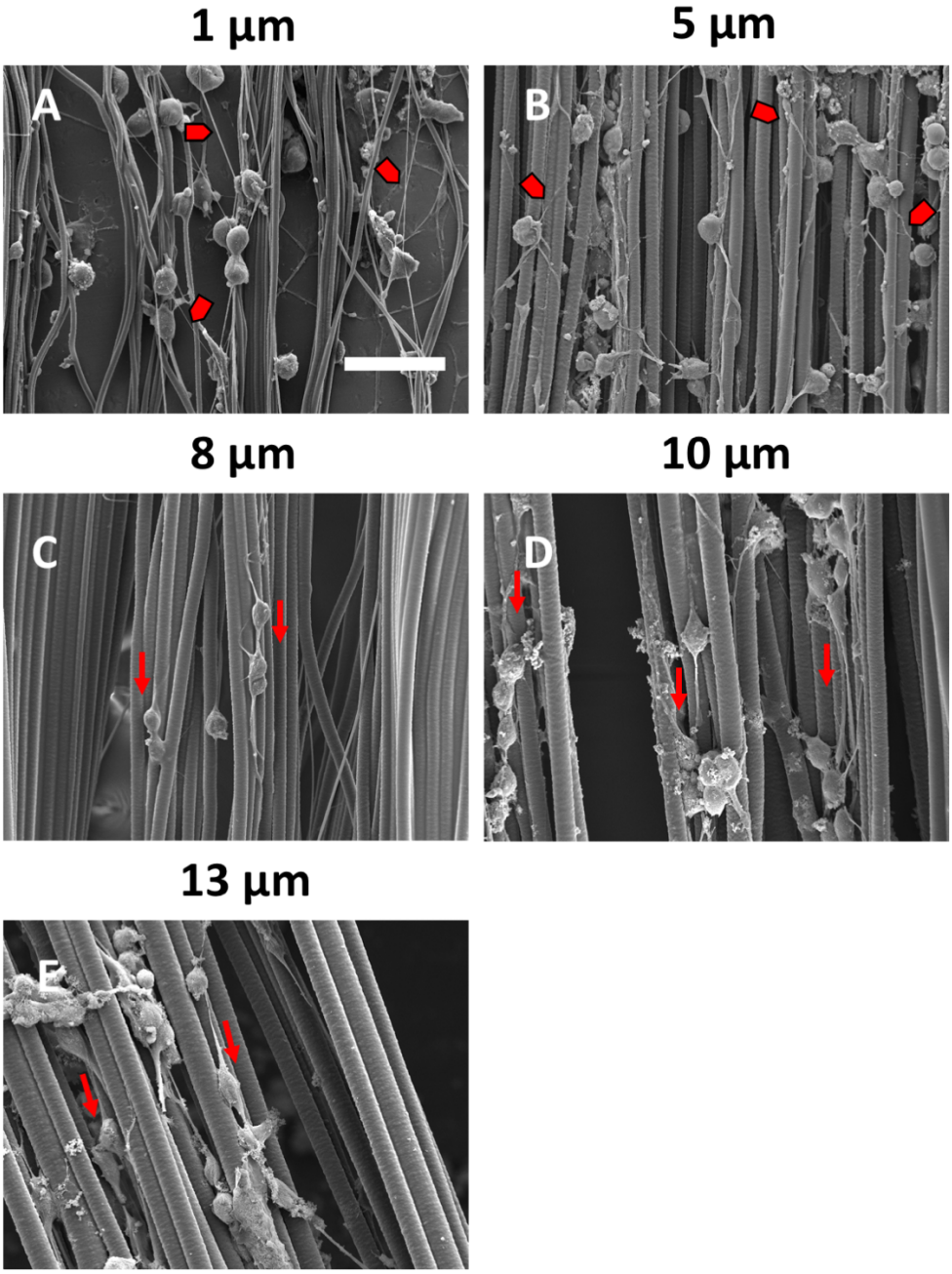

Figure 28 SEM micrographs of neuronal cells on PCL microfibres

NG108-15 neuronal cells were seeded on A) 1 µm, B) 5 µm, C) 8 µm, D) 10 µm and E) 13 µm aligned PCL fibres with 4×10^4 cells in 1 cm^2 stainless-steel rings. Before serum withdrawal, neurons were culture in 10 % FBS medium for 1 day. After 5 days of culture in serum-free conditions, cells were fixed and scaffolds dehydrated for SEM imaging. Representative images are shown of two independent experiments. Arrows point out the directionality of axons on fibres, where filled arrows in A) and B) point to branching unaligned axons. Scale bar = 50 µm and applies to all images.

Furthermore, the directionality of axons in relation to fibre alignment was investigated. Therefore, the angular difference of axons to PCL fibres was measured and expressed in a histogram in Figure 29. It is apparent that with increasing fibre diameter axons appeared more aligned with low angular differences to the reference PCL fibre. This increasing trend interestingly dropped with 13 µm fibres, where the number of misaligned axons in relation to fibre alignment was greater. When looking at an axon orientation difference of 40 – 120° (bin centres 50 – 110, dotted line box) to the polymer fibres, it was noticed that 1 and 5 µm fibres showed the greatest number of unaligned fibres, followed by 13 µm fibres. On the contrary, 8 µm fibres showed a much lower number of branched axons and with 10 µm fibres only a small number of axons showed an angular divergence of 40 – 60°, where no greater angular differences were found. In summary, fibre diameter of 10 µm supported the alignment of axons the best, where 76.7 % of axons showed alignment in the 0 – 20° range (bin centre 10), and only 3.4 % showed greater divergences in the range of 40 – 60°. In comparison, only 38.7 % of axons aligned with 0 – 20° on 1 µm fibres, where 24.5 % showed an orientation of 40 – 120° to the polymer fibres. Interestingly, 13 µm fibres showed a great number of aligned axons with 63.6 % axons (0 – 20°) but showed high numbers of misaligned axons of 17.9 % in the range of 40 – 120° (dotted line box) in comparison to axons on 10 µm fibres.

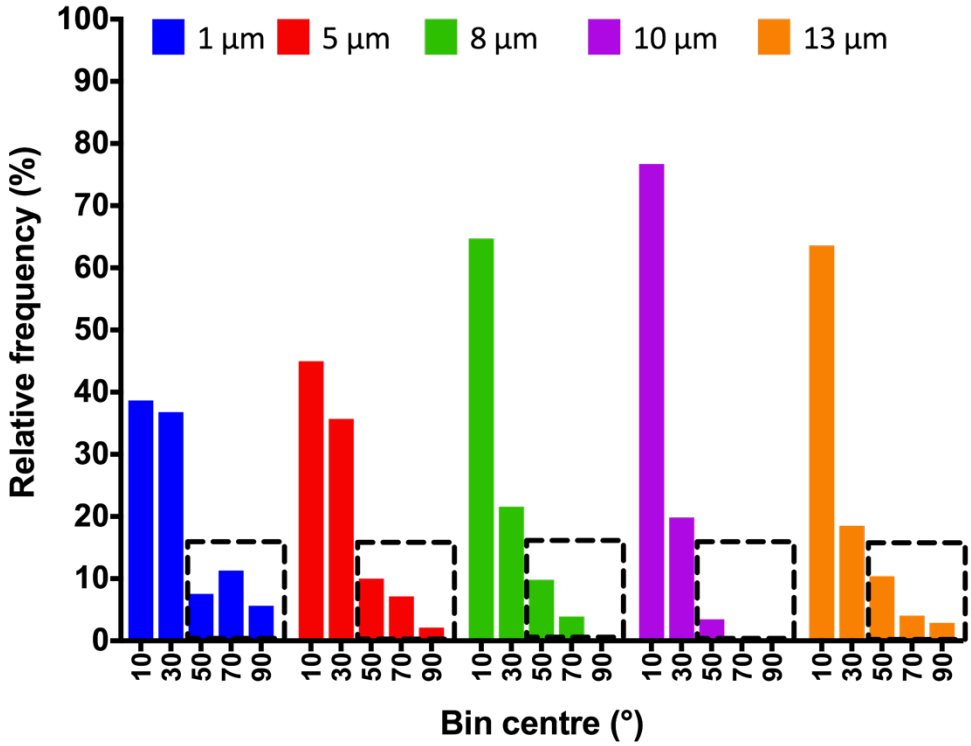

Figure 29 Analysis of axon directionality on PCL microfibres

Histogram showing the relative frequency distribution (in percent) of axon alignment in relation to fibre orientation. Results were generated based on SEM micrographs of NG108-15 neuronal cells on 1, 5, 8, 10 and 13 µm PCL fibres as shown in Figure 28. Bin centres are displayed as the angle (°) between axon and fibre directionality. A bin width of 20 was used with a bin range of 10 – 90. Dotted line boxes highlight the frequency distribution of axons with an angular difference of 40 – 90° (bin centre 50 – 90) to the fibre alignment. Relative frequency distributions were based on a complete data set of two independent repeats

3.4.3.3 Neurite outgrowth analysis on different PCL microfibre diameters *in vitro*

In this experiment, the effect of different fibre diameter on neurite formation and outgrowth was assessed. NG108-15 neuronal cells were seeded on fibre mats of diameters ranging from 1 – 13 µm with a control culture on PCL films and TCP. Cells were cultured for 6 days, where serum was withdrawn after one day of culture to encourage neurite formation. Indirect immunofluorescence was performed to reveal βIII Tubulin, an axon-specific protein, as shown in green in Figure 30. Confocal microscopy images in Figure 30 were collected in z-stacks and presented as an overlay of all stacks in a maximum projection. It is apparent from the top row of images in Figure 30 that cells successfully attached to microfibres and the control surfaces of PCL films and TCP.

Additionally, it was observed that neuronal cells appeared in an elongated morphology with an aligned arrangement in fibre direction when cultured on 5, 8 and 10 µm fibres (Figure 30 B – D). The bottom row of images in Figure 30 provides a magnified version of images presented in the top row and revealed further details on neurite extensions. From these images, it is apparent that neurites were predominantly formed on 5 – 13 µm fibres and the control surfaces (Figure 30 B – G), where neurites appeared to be the longest on 8 and 10 µm fibres (Figure 30 C and D) and the TCP control (Figure 30 G). Interestingly, only a few neurites were formed on 13 µm fibres (Figure 30 E), where neuronal processes appeared to be especially short and rare on 1 µm fibres with cells appearing with spherical morphology on the fibres (Figure 30 A). Similar was found on PCL films, which supported the formation of neurites to a certain extent but simultaneously showing a high number of round-shaped cells with no formed processes (Figure 30 F).

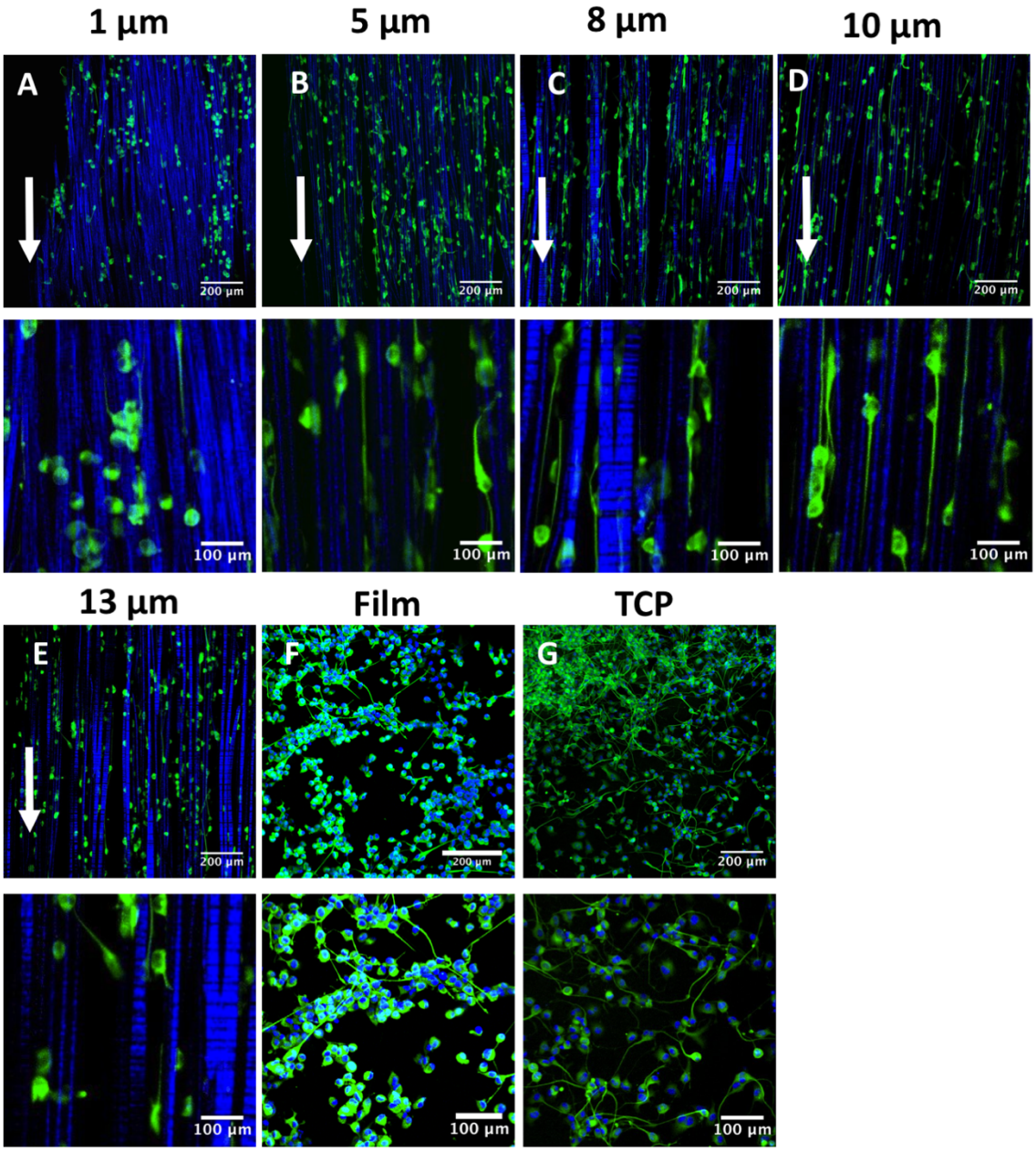

Figure 30 Neuronal cell outgrowth on five different PCL fibre diameters

Confocal microscopy images of NG108-15 neuronal cells on of A) 1 µm, B) 5 µm, C) 8 µm, D) 10 µm, E) 13 µm PCL fibres, F) PCL film and G) TCP. Cells were cultured in serum-free conditions for 5 days. Immunocytochemistry revealed neurites βIII Tubulin in green. In A) – E) the auto-fluorescence of PCL microfibres was displayed in blue. In F) and G) nuclei are visualised in blue with DAPI. Images were taken in z-stacks and are displayed as maximum projections. Top row images show scale bar = 200 µm. A closer view of microscopy images is displayed in the bottom row (scale bar = 100 µm). Arrows indicate fibre direction. Representative images are shown of three independent experiments with duplicate used within experiments.

Observations from Figure 30 were further quantified and results were summarised in Figure 31. Figure 31 A summarises the relation between the five different fibre diameters and neurite incidence, where Figure 31 B demonstrates the link between different diameters and neurite length. The number of neurons bearing neurites was influenced by the different fibre diameters, where the minimal and maximal number of formed neurites accounted of 31.1 ± 10.9 % on 13 µm fibres and 69.3 ± 3.8 %/70.2 ± 10.8 % on 10 µm fibres/TCP, respectively (Figure 31 A). An increase in neurite incidence with an increase in fibre diameter was observed from 1 µm to 10 µm fibres. Interestingly, this trend decreased with 13 µm fibres where the number of neurons bearing neurites was more than 50 % lower than on 10 µm fibres. Ordinary one-way ANOVA confirmed a statistical difference between 10 and 13 µm fibres in neurite incidence. Additionally, the number of neurons bearing neurites on 1 and 13 µm fibres and PCL films was significantly lower than on the TCP control. Furthermore, neurons on 5, 8 and 10 µm fibres formed significantly more neurites compared to cells on flat PCL films. In summary, out of all tested fibre diameters, neuronal cells on 8 and 10 µm fibres showed the highest numbers of bearing neurites with 63.8 ± 9.8 % and 69.3 ± 3.8 %, respectively, where both values were not significantly different to the TCP control. On the contrary, PCL films, 1 and 13 µm fibres supported neurite formation the least with 16.5 ± 13.5 %, 37.3 ± 15.8 % and 31.1 ± 10.9 %, respectively.

The length of neurites was also measured. Figure 31 B shows the same correlation as in Figure 31 A, where an increase in neurite length was noted with an increase in fibre diameter. Additionally, the same decrease was observed on 13 µm fibres, where neuronal cells formed significantly shorter neurites compared to neurons on 10 µm fibres. Between all fibre diameters tested, 8 and 10 µm fibres supported the maximum growth and extension of neurites with average neurite lengths of 151.7 ± 30.3 µm and 155.5 ± 21.6 µm, respectively. On the other hand, neuronal cells cultured on 1 and 13 µm fibres and PCL films showed minimal neurite outgrowth of 54.1 ± 48.8 µm, 67.7 ± 65.6 µm and 77.0 ± 35.9 µm, where the average neurite length on 1 µm fibres was significantly lower than on 8 and 10 µm fibres (Figure 31 B). Among all samples, neuronal cells formed the longest neurites on TCP control substrates with an average neurite length of 198.2 ± 17.5 µm. Ordinary one-way ANOVA revealed that the average neurite

length for PCL films, 1 and 13 µm fibres was significantly lower compared to the TCP control, where values for 5, 8 and 10 µm fibres showed no difference (Figure 31 B).

Taken together, these results suggest that there is an association between fibre diameter and neurite formation and length, where neuronal cells formed more and longer neurites when cultured on 8 and 10 µm PCL fibres compared to other fibre diameters tested.

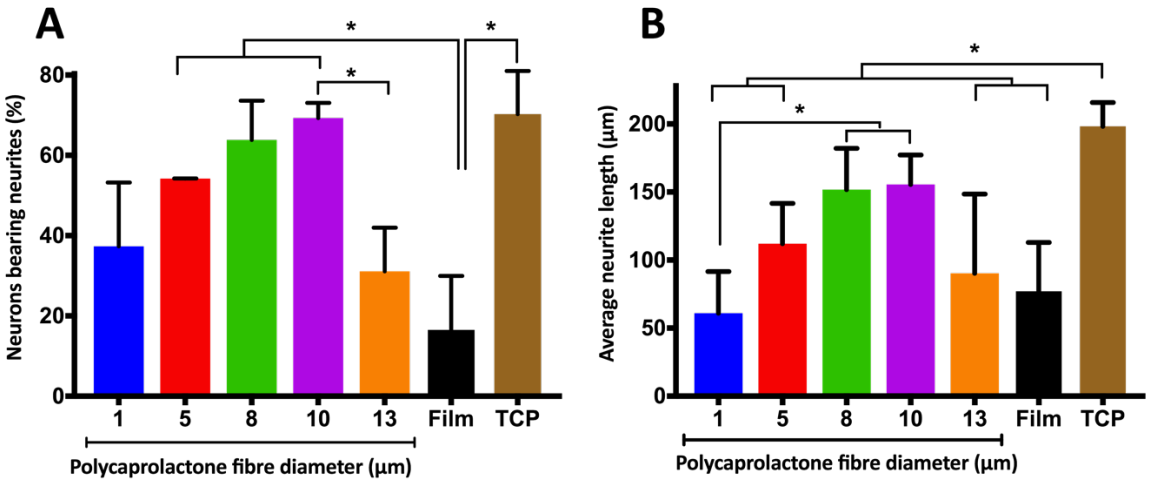

Figure 31 Effect of fibre diameters on neurite outgrowth

Neuronal cells were analysed on A) the percentage of cells that have formed neurites (neurite incidence) and B) on average neurite length after the culture on 1 – 13 µm PCL fibres, PCL films and TCP (as displayed in Figure 30). Analysis was conducted from confocal microscopy images using Fiji. Significance was analysed by one-way ANOVA with Tukey's multiple comparisons test and displayed as * $p<0.05$. Values represent the mean + SD of three independent experiments.

3.4.4 An *in vitro* study of PCL fibre scaffolds in primary Schwann cell culture

3.4.4.1 Viability of primary Schwann cells on different PCL microfibre diameters

A live-dead cell stain was used to determine Schwann cell viability when grown on fibres and the relationship between 1 – 13 µm fibre diameters, a PCL film and TCP control. Syto–9 and propidium iodide were used to distinguish living versus dead cells, visualised in green and red (Figure 32). The z-stacked images, shown as maximum projections in Figure 32 confirmed that cells were primarily alive (in green) with only a few dead cells visible (in red), independent of the culture substrate. Similar observations were found (as in Figure 32) with Schwann cells mainly aligning with the fibre direction (Figure 32 B –E).

In comparison, cells on PCL films and on TCP adhered uniformly over the entire substrate (Figure 32 F and G). Interestingly, cells on 1 µm fibres showed a clumped arrangement, where no specific orientation could be identified (Figure 32 A). Another interesting finding was the number of cells visible on the substrates, where it was noticed that less Schwann cells adhered to fibres (Figure 32 A – E) than to the TCP control (Figure 32 G) but that even less cells were apparent on the PCL film control (Figure 32 F).

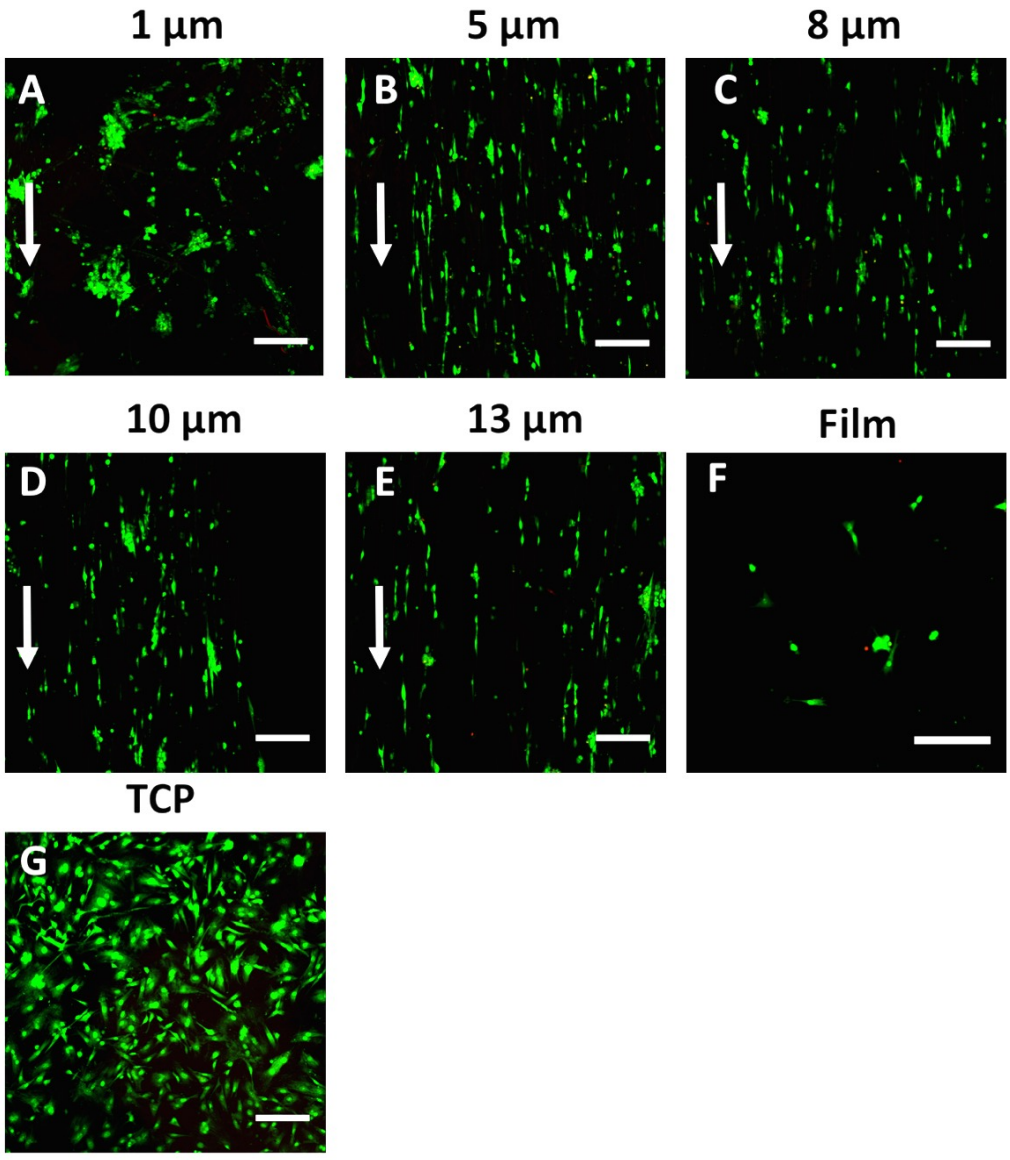

Figure 32 Overview of living and dead Schwann cells on different PCL fibre diameters

Maximum projection confocal microscopy images of living (green) and dead (red) Schwann cells on A) 1, B) 5 µm, C) 8 µm, D) 10 µm, E) 13 µm PCL fibres, F) PCL films and G) TCP after 5 days of culture. The direction of fibre alignment is indicated by arrows. Representative images are shown of three independent experiments. Scale bar = 200 µm.

Results in Figure 32 were further quantified and presented in Figure 33. A high ratio of live to dead cells noted in Figure 32, proved to be significant in this analysis. Schwann cells cultured on 1 – 13 µm fibres showed a viability of more than 91 %. TCP, 1 and 13 µm PCL fibres supported the highest Schwann cell viability, with 98.8 ± 1.2 %, 94.5 ± 6.7 % and 95.2 ± 1.8 % of living cells, respectively (Figure 33). On PCL films, 84.6 ± 9.5 % of living cells and 15.4 ± 9.5 % of dead cells were detected. Overall, fibre diameters, PCL films and TCP substrates did not affect the number of living cells differently in these measures.

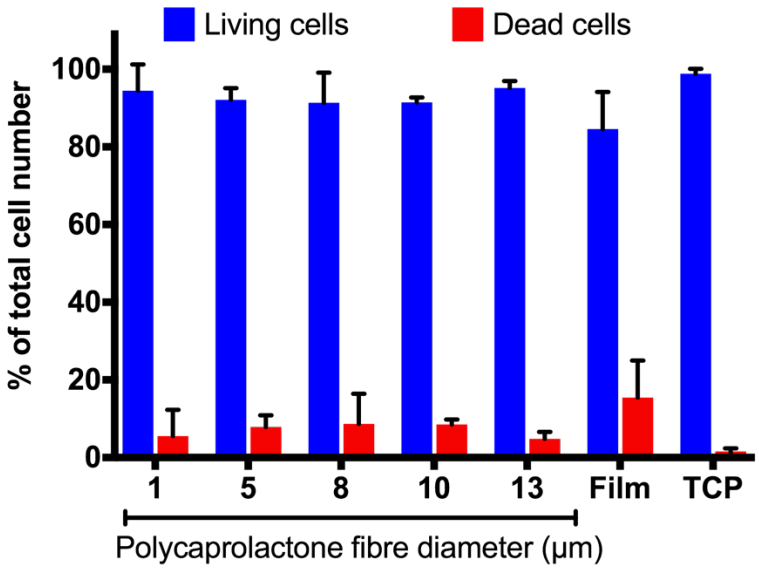

Figure 33 Effect of different PCL fibre diameters on Schwann cell viability

Quantification analysis of live and dead Schwann cells on 1 – 13 µm PCL fibres, PCL films and TCP. Analysis was conducted in Fiji based on confocal images shown in Figure 32. Values are expressed as a percentage of the total cell number analysed and shown as mean + SD of three independent experiments. Two-way ANOVA analysis with Tukey's multiple comparisons test showed no significant differences between living cells and dead cells, respectively.

3.4.4.2 Schwann cell attachment analysis on different PCL microfibre diameters

The relationship between primary Schwann cell attachment and different PCL fibre diameters was investigated using a Crystal Violet attachment assay. Crystal Violet was applied to fixed cells, which binds to DNA. Bound dye was eluted with acetic acid which allowed an indirect method to quantify cell adhesion. As shown in Figure 34 and Figure 35, the differences in cell attachment between cells on fibre scaffolds and cells that did

not attach to scaffolds but to the underlying TCP substrate were observed and analysed. Figure 34 A illustrates the different fibre scaffolds attached to metal rings inside wells of a 12-well plate, where cells were visualised with a blue-purple colour through the crystal violet stain. A deep purple colour emerged from fibre scaffolds with diameter of 8, 10 and 13 µm, where a lighter colouring was visible on 5 µm fibres and was barely visible on 1 µm fibres (Figure 34 A). It was found that Schwann cells that did not adhere to the fibre scaffolds, but rather adhered to the underlying TCP substrate as demonstrated in Figure 34 B. This figure showed the reverse, where deep blue-purple rings were visible on the TCP substrate, where fibre scaffolds with 1 µm were placed. This observation was less visible for bigger fibre diameters, where cell attachment to TCP was barely visible where rings with 8, 10 and 13 µm PCL fibres were positioned (Figure 34 B).

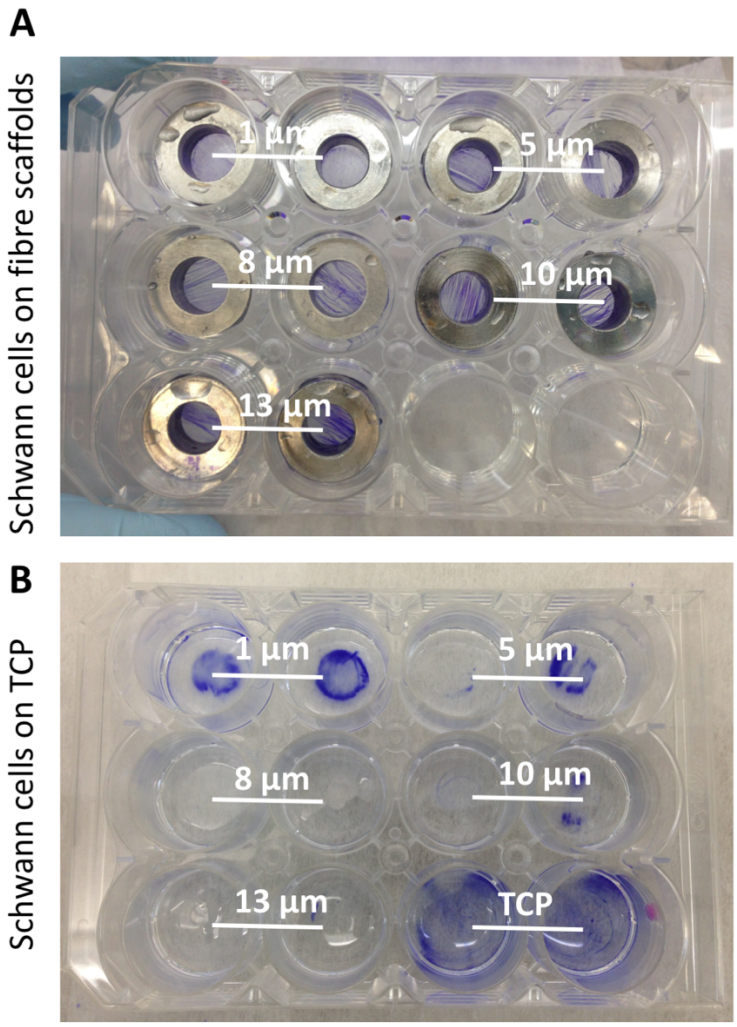

Figure 34 Crystal violet attachment assay

Primary rat Schwann cells were cultured on 1, 5, 8, 10 and 13 µm PCL fibres and TCP. Fibre scaffolds were glued to 1 cm^2 stainless-steel rings and cells seeded with 4×10^4 cells per ring. After one day of culture, rings were transferred to a new well plate. Crystal violet stain was applied to fibre scaffolds in the new well plate and to wells of the old well plate. A) Crystal violet bound to cells that attached to the fibre scaffolds, where B) demonstrates the attachment of cells to the underlying TCP substrate.

It can be seen from data in Figure 35 that values were normalised to the TCP control, assuming a complete cell attachment to TCP. First it can be seen that the attachment of Schwann cells to fibre scaffolds disregarding the diameter measured lower in comparison to the TCP control. It was also apparent that the majority of cells attached to fibre scaffolds with diameters ranging from 5 – 13 µm in comparison to the underlying TCP

substrates. Between 62.5 ± 10.23 and 69.7 ± 6.28 % of Schwann cells attached to 8 – 13 µm fibres, where the greatest attachment was noted on 13 µm fibres. A slight decrease in attachment was found on 5 µm PCL fibre scaffolds, where 57.82 ± 11.72 % of Schwann cells attached. Interestingly, cell attachment rates on 1 µm fibres measured half as much compared to scaffolds with diameters between 8 and 13 µm and showed to have the lowest attachment rates with 27.77 ± 13.6 % compared to the other fibre scaffolds. Statistical analysis further revealed a significant difference between the cell attachment to 1 µm fibres versus bigger fibre diameters. Of particular interest was the finding that PCL films showed to be the least supportive regarding cell attachment with only 11.7 ± 0.14 % of attached cells. This decrease in attachment was not significantly different to the attachment on 1 µm fibres but showed to be significant to bigger fibre diameter ranging from 5 to 13 µm.

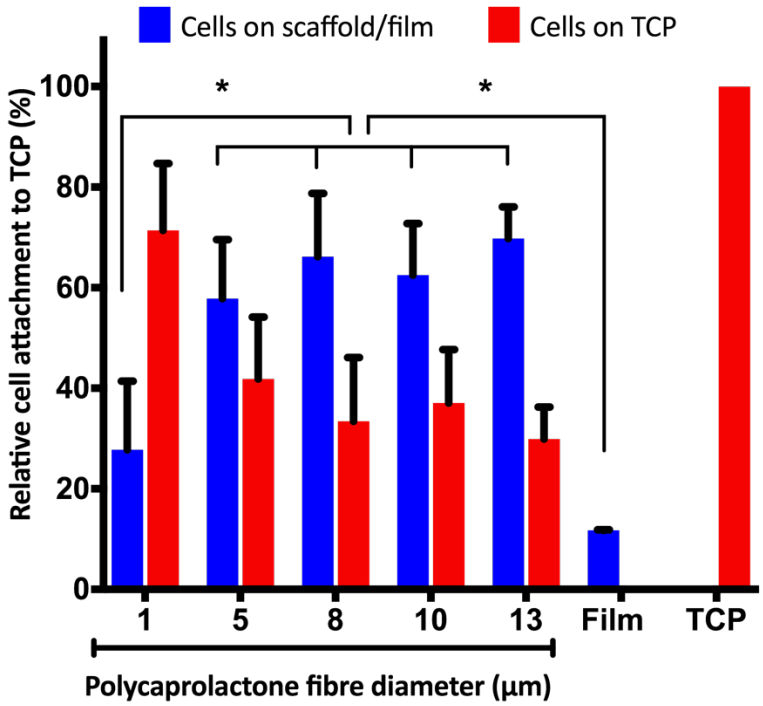

Figure 35 Relationship between different fibre diameters and Schwann cell attachment

Absorbance readings of eluted crystal violet from primary rat Schwann cells cultured on 1 – 13 µm PCL fibres, PCL films and TCP after one day of culture. Scaffolds were transferred to a new well plate prior to assay performance. Readings are displayed as relative absorbance in relation to the TCP control. Values are displayed as the mean + SD and statistical differences indicated as * $p<0.05$ (Two-way ANOVA with Tukey's multiple comparisons test).

3.4.4.3 Morphological study of Schwann cells on different PCL microfibre diameters

To assess the morphology of primary rat Schwann cells on fibre diameter ranging from 1–13 µm, scanning electron microscopy was performed. From the electron micrograph presented in Figure 36, it is apparent that Schwann cells attached to all fibre scaffolds. However, different morphological appearances were observed between the different diameters. Schwann cells with a widely spread cytoskeleton that branched over several fibres were observed on fibre diameters ranging from 1 – 5 µm (Figure 36 A and B). Additionally, the cell cytoskeleton appeared in a flat and round shape, which orientated in all directions disregarding the fibre alignment, which was noted more dominantly on 1µm fibres than on 5 µm ones (Figure 36 A and B). In comparison, cells on larger fibre diameters showed an elongated shape, whereas the cytoskeleton showed directionality with fibre alignment (Figure 36 C – E). Schwann cells on 8 µm fibres showed an aligned morphology with fibre direction but branched over several fibres with a widely spanned cytoskeleton. On the contrary, on 10 and 13 µm fibres cell cytoskeleton appeared narrow and highly elongated along single fibres, and branching over several fibres was rarely seen (Figure 36 D and E).

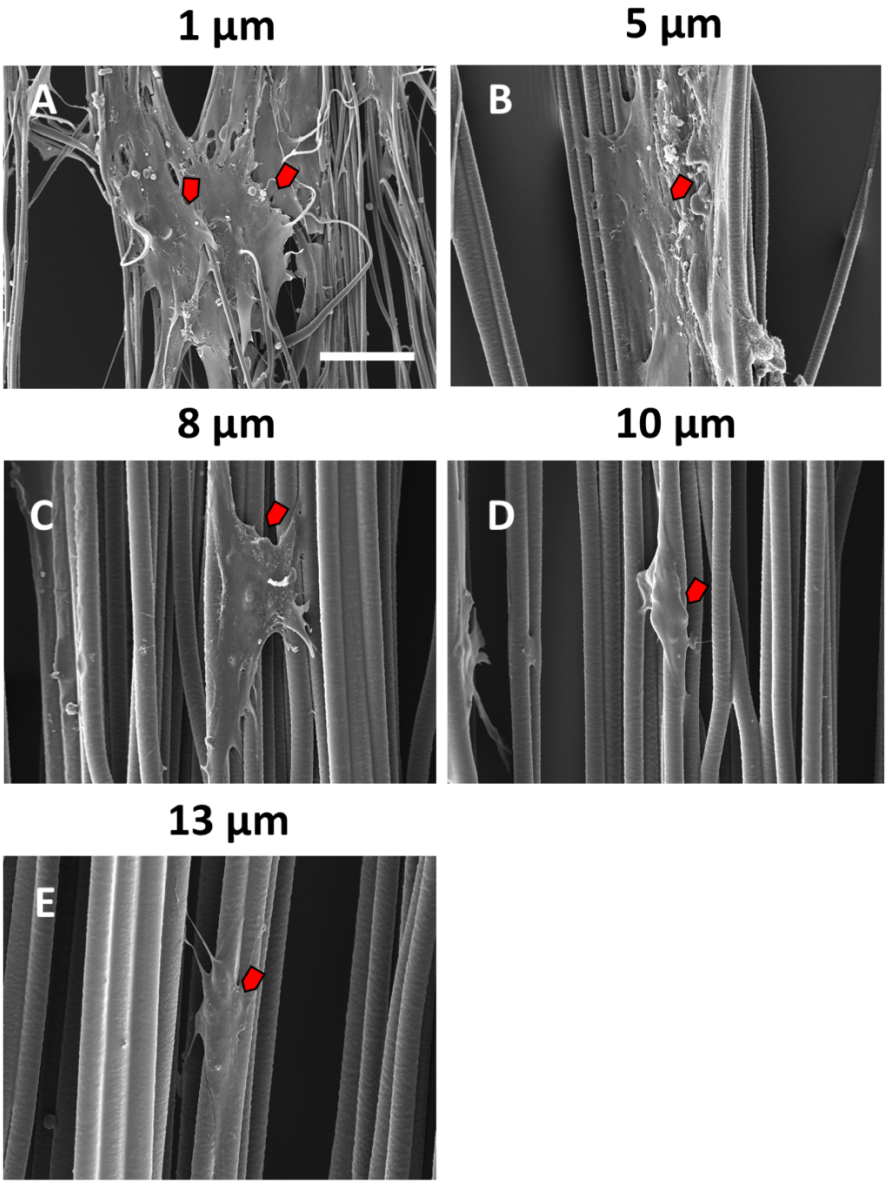

Figure 36 SEM micrographs of primary Schwann cells on PCL microfibres

SEM micrographs present primary Schwann cells on A) 1 µm, B) 5 µm, C) 8 µm, D) 10 µm and E) 13 µm aligned PCL fibres. Cells were seeded in 1 cm^2 stainless-steel rings onto fibre scaffolds with 5×10^4 cells per ring. After 6 days of culture, cells were fixed and scaffolds dehydrated for SEM imaging. Representative images are shown of two independent experiments. Arrows point to cells on the fibres. Scale bar = 50 µm and applies to all images.

3.4.4.4 Metabolic activity analysis of Schwann cells on different PCL microfibre diameters

The metabolic activity of Schwann cells was measured on 1-13 µm fibres, a PCL film control and on a glass control substrate over time using a fluorometric resazurin reduction assay. The assay was performed on days 1, 3 and 5 in order to observe changes

in metabolic activity on different fibre scaffolds over time as presented in Figure 37. From this figure, an increasing trend in metabolic activity over time was observed. On day 1, values were similarly low where fibre diameters did not affect cell's activity differently. An increase in activity was present on day 3, where cells cultured on 5 µm fibres showed an increase in activity by 166 % and more than 200 % on fibre diameters ranging from 8 – 13 µm. Interestingly, the metabolic activity rate of Schwann cells on 1 µm fibres was decreased by 21 % on day 3 compared to day 1. It was additionally noted that the metabolic activity of cells on PCL films increased from day 1 to day 3 but that numbers were small with an increase of 20.7 %. Further analysis showed that the metabolic activity on 1 µm fibres and PCL films was significantly lower than on 13 µm fibres and the glass control on day 3 (Figure 37). Between day 3 and day 5, cells on all samples showed an increase in metabolic activity with the exception of cells on PCL films. The greatest metabolic activity rates were measured on the glass control on day 5. Two-way repeated measures ANOVA with Tukey's multiple comparisons test revealed that cell activities on all fibre scaffolds were significantly different to the glass control on day 5. The lowest metabolic activity was found on 1 µm fibres and PCL films on day 5. Fibre diameters of 5 – 13 µm performed significantly better in supporting Schwann cell activity than PCL films and 1 µm fibres, where values were more than 2.5 times greater. The metabolic activity of Schwann cells on 5 – 13 µm fibres measured similarly high and was not significantly different to each other (Figure 37).

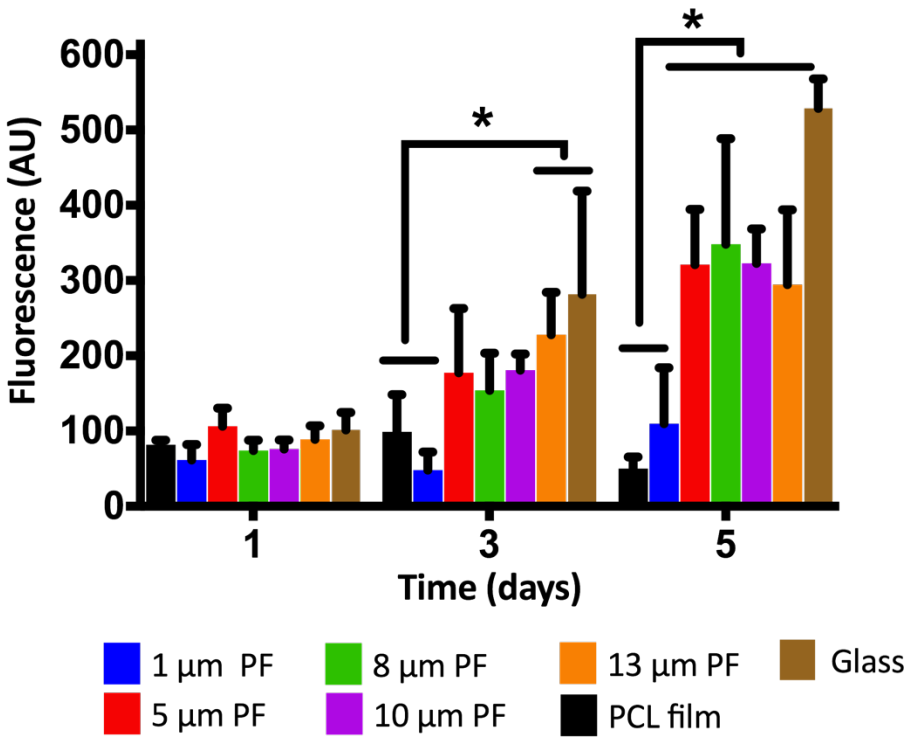

Figure 37 **Effect of different fibre diameters on the metabolic activity of Schwann cells**

Resazurin reduction assay was used to measure the metabolic activity in primary Schwann cells on 1 – 13 µm PCL fibres (PF), PCL films and glass coverslips. Substrates were transferred to custom-made PDMS moulds to carry out the assay. Readings were performed on days 1, 3 and 5 as repeated measures. Results are displayed as mean fluorescence readings + SD. Statistical differences were indicated as * $p<0.05$ (Two-way ANOVA with Tukey's multiple comparisons test).

In summary, Schwann cells were metabolically active on all fibre scaffolds but viability rates correlated with fibre diameters, where cells grew better on 5 – 13 µm diameter fibres versus 1 µm fibres.

3.4.4.5 Schwann cell proliferation on different PCL microfibre diameters

After studying the metabolic activity of primary Schwann cells on the five different PCL fibre diameters, the proliferation behaviour of cells was analysed. Schwann cells were maintained on fibre scaffolds for either 3 or 5 days and were subsequently immunolabelled for Ki67, a protein present in proliferating cells. As Ki67 is present in the cell nuclei, nuclei were further counterstained with DAPI. Samples were imaged by confocal microscopy and images analysed in Fiji. The images obtained from this are

shown in Figure 38, which presents the overlay of nuclei and Ki67 protein (left column), the orientation of the F-actin cytoskeleton (middle column) and an overlay of all three fluorescent labels (right column) after 5 days of culture. Two main observations could be made from Figure 38. First, a higher number of Ki67-positive cells relative to cell nuclei was noted on smaller fibre diameter of 1 and 5 µm (Figure 38 A and B) and the PCL film control (Figure 38 F) compared to 8 – 13 µm fibres (Figure 38 C – E) and the TCP control (Figure 38 G). Second, F-actin labelling of cells revealed that more cells were present overall on bigger fibre diameter and the TCP control, compared to smaller fibre diameter and PCL films, where cells appeared nearly confluent on 10 and 13 µm fibres (Figure 38 D and E) and on the TCP control (Figure 38 G).

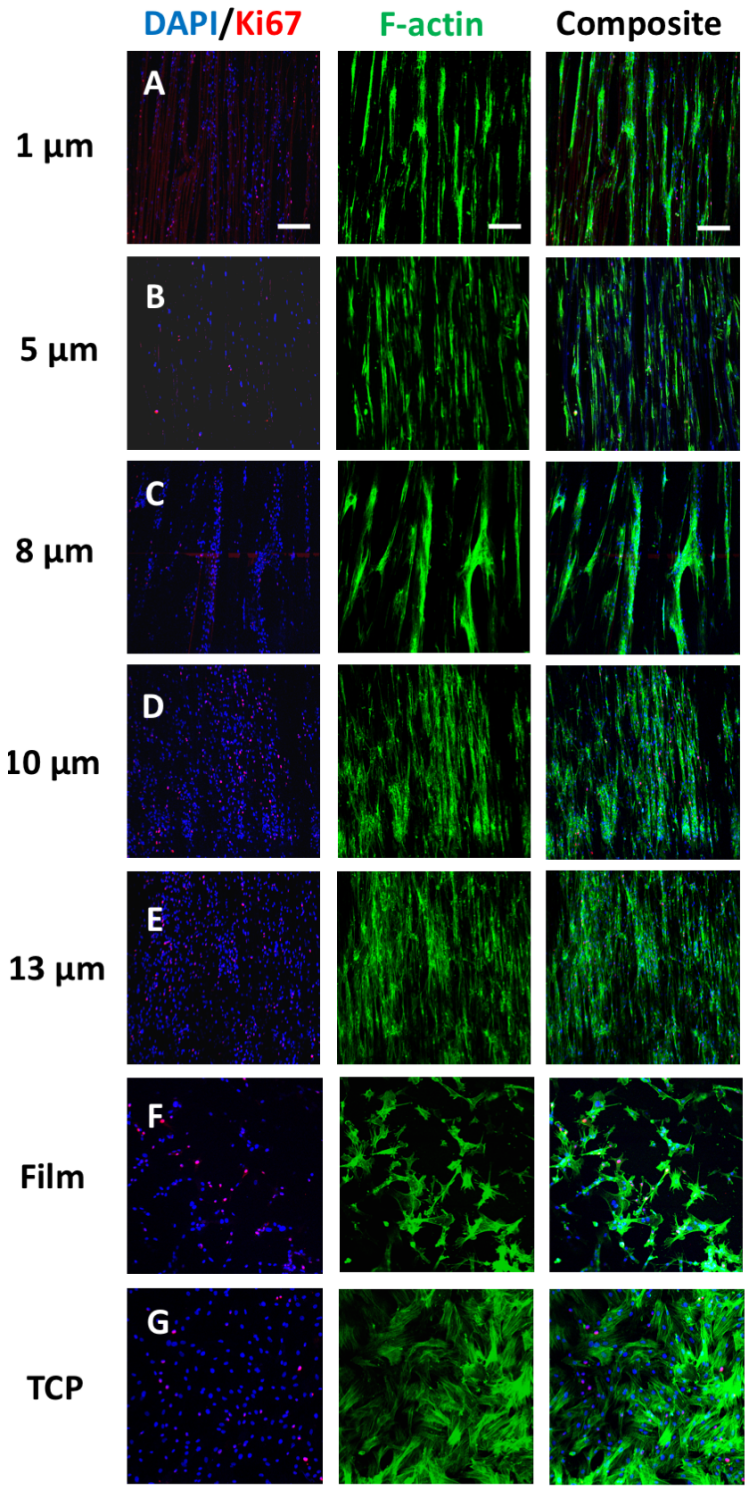

Figure 38 Ki67 expression in primary Schwann cells on PCL microfibres

Maximum projection confocal microscopy images of primary rat Schwan cells on A) 1 µm, B) 5 µm, C) 8 µm, D) 10 µm, E) 13 µm PCL fibres, F) PCL films and G) TCP after 5 days of culture. Cells were labelled for Ki67 protein (red), F-actin (green) and nuclei labelled with DAPI (blue). Representative images are shown of three independently performed experiments. Scale bar = 200 µm and apply to all images of that column.

These results were further quantified by counting all Ki67 positive cells per image, where numbers were divided by the total number of nuclei. The resulting percentage of Ki67 positive cells and therefore proliferating cells on the different fibre diameters is shown in Figure 39. On day 3 of culture, initial numbers of proliferating cells on fibre scaffolds were observed to fluctuate between 18.5 ± 4.5 % and 25.7 ± 8.6 %, where numbers of proliferating cells were lower on 8 – 13 µm fibres compared to 1 and 5 µm fibres. Cells cultured on TCP, showed 15.6 ± 7.7 % proliferating cells and 17.1 ± 3.6 % on PCL films on day 3. Interestingly, the number of proliferating cells increased on 1, 5 and 8 µm fibres and on the PCL film control from originally ranging 17.1 to 25.7 % on day 3 up to 27.1 to 32.2 % on day 5. On the contrary, a reduction in proliferating cells on 10 and 13 µm fibres was observed. Like on bigger fibre diameters, a reduction in proliferating cells was additionally noted on TCP on day 5 (Figure 39). However, these described differences in proliferative behaviour in the cell population were small and a clear benefit of a smaller diameter in the support of higher proliferating Schwann cell numbers could not be identified in this analysis.

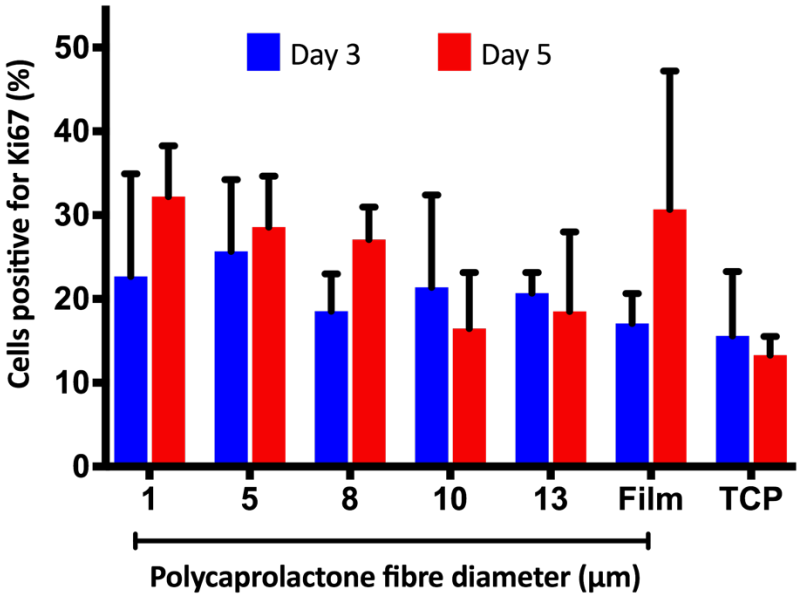

Figure 39 Effect of different fibre diameters on proliferation of Schwann cells

Quantified measurements of proliferating Schwann cells on 1 – 13 µm PCL fibres, PCL films and TCP after 3 and 5 days of culture. Cells were immunolabelled for Ki67 protein and imaged in z-stacks using confocal microscopy. Values were displayed as the mean percentage of Ki67 positive cells + SD. Experiments were performed in three independent repeats. No statistical differences were found between values (two-way ANOVA with Tukey's multiple comparisons test).

3.5 Discussion

3.5.1 The morphology of electrospun PCL microfibres

Fibres are ideal scaffolds for mimicking and regenerating tissues with aligned structures [296]. In this study, microfibres were manufactured by electrospinning for the use in peripheral nerve regeneration. Herein, high collector speeds enabled the processing of highly aligned microfibres. The importance of fibre alignment in scaffolds for peripheral nerve regeneration has been discussed in some depth previously in the literature [141, 142, 297, 298]. Besides the alignment of fibre scaffolds, fibre dimensions played an additional role in nerve regeneration [150, 152]. It was shown herein that fibre diameters could precisely and reproducibly be controlled by electrospinning. The flow rate of the polymer solution was identified to be the main contributor for controlling fibre diameter, where an increase in polymer flow rate resulted in an increased fibre diameter. This is in agreement with the findings of other studies, in which an increasing flow rate alone increased the fibre diameter [161, 299]. By additionally altering the polymer concentration between 10 and 20 %, fibre diameters between 1 and 13 µm could be manufactured. As the concentration of polymer in the solution defines the viscosity of the liquid and influences fibre formation, polymer solutions with low viscosity and concentration were needed to electrospin 1 µm fibres. These results agree with those reported in earlier studies which indicated that the average fibre diameter formed is associated with the solution concentration through a power law relationship [164, 300]. The fabrication of 1 µm PCL fibres further required a lower applied voltage of 10 kV, in comparison to 18 kV for bigger fibres. This finding is in agreement with what has been reported by Deitzel *et al.* who showed that if the voltage was increased over a critical point the fibre jet became unstable, split and bead defects on the fibre became present [164].

It has furthermore been found that the chosen electrospinning parameters not only resulted in fibres of precise diameters and alignment but also in nanotopographical structures on the fibre surface. Depressions were present on all fibre diameters but were the smallest in regard to area and length on 1 µm fibres and the largest on 13 µm fibres. The ratio of groove width to length revealed that topographical features on 1 µm fibres were of circular morphology and elongated to elliptic shapes in fibre direction on 5 – 13

µm fibres. Furthermore, it was shown that grooves were more frequent on 1 µm fibres than on the other diameter fibres. To the author's knowledge this is the first study that addressed the differences in fibre topographies between different fibre diameters and that provided detailed and quantified information about their morphology.

Bognitzki *et al*. [156] and Megelski *et al.* [160] provided valuable evidence on how such fibre topographies form. They described two methods which they termed, thermal induced phase separation (TIPS) or vapour induced phase separation(VIPS) and hence the findings herein might be explained in this way. Their theories describe a rapid evaporation of the solvent, which cools the polymer fibre in the spinning process, resulting in either concentrated solvent and polymer regions (TIPS) or the condensation of moisture on the fibre surface which results in regions of water with no polymer present (VIPS) [156, 160]. The latter is additionally reinforced by hydrophobic polymers like herein PCL, where condensed water remains on the fibre surface. The formation of topographies could be explained by the humidity levels during the electrospinning process, which were between 33 and 37 %, as Schaub *et al.* demonstrated that fibre morphology was dependent upon the humidity levels during electrospinning. The authors showed a smooth fibre morphology when electrospun at humidity levels lower than 23 % but that increased humidity levels above 33 % resulted in fibres with nanotopographies [168]. Herein, a difference was found between the morphological appearance of fibres between 1 µm and 5 – 13 µm fibres, which was hypothesised to be caused by two different mechanisms. It is assumed that the circular-shaped depressions on 1 µm fibres arose from VIPS and the elliptic-shaped grooves on 5 – 13 µm fibres from TIPS. It is suggested that 1 µm fibres cooled more rapidly than bigger fibres due to their small size as it is commonly known that smaller objects cool quicker than larger ones. The increased solvent concentration in 1 µm fibres might have additionally favoured this cooling effect. Water droplets from condensation therefore might have caused the circular morphologies on the fibre surface. This hypothesis is furthermore reinforced by the findings of Limaye *et al*. who confirmed that VIPS initiated the formation of circular pore structures from residing water droplets on the surface of polystyrene [301]. As the groove morphology on 5 – 13 µm fibres was elongated and not circular, it is believed that TIPS was responsible for this effect. It is assumed that no water condensation on the fibre surface occurred due to a milder cooling effect caused by the lower solvent content

in the fibre and a larger fibre area. Differences were furthermore seen between 5 – 10 µm fibres and 13 µm ones which showed larger grooves on their surface. To the author's knowledge, no report exists that observed a similar phenomenon. Interestingly, those topographical features were not as distinguishable by eye on the SEM images but were observed after quantifying those features. As most studies evaluated topographical differences by SEM so any such differences may have easily remained undiscovered. Nevertheless, an attempt was made to explain those topographical differences seen on 13 µm fibres. An increase in groove size on 13 µm fibres means that larger solvent regions were formed on the fibre surface in comparison to 5 – 10 µm ones. This might be explained by the increased solvent content in the 13 µm fibre due to its size while however maintaining the same solvent to polymer ratio. Therefore, 13 µm fibres might have reached a critical size that enabled the formation of larger solvent regions on the fibre surface.

3.5.2 The performance of microfibres in neuronal cell cultures

Results revealed that aligned PCL fibres irrespective of their diameter supported neuronal and Schwann cell viability to a similar extent as the TCP control, with the exception of neuronal cells on 1 µm fibres. These results match those observed by Daud *et al.* [152] and support the choice of 5 – 13 µm PCL fibres for use in nerve regeneration as cell viability plays a crucial role in tissue repair. As the damage to peripheral nerves causes damage to the surrounding tissue and cells, the number of surviving cells needs to be maintained and a positive interaction of those cells with the introduced nerve conduit is essential. As neuronal cells showed increased cell death on 1 µm fibres *in vitro*, although not found to be statically significant, a negative effect on nerve regeneration *in vivo* might still be of concern.

This study further revealed a clear range of fibre diameters that supported neurite outgrowth. One might argue the relevance of studying neurite length and incidence in immortalized neuronal cells versus primary neurons, as axons are inevitably present in primary neurons, where on the contrary not all neuronal cells form neurites in immortalized cell lines. However, when considering the ability of neurons to form neurites in culture in the context of biomaterial performance, useful information can be gained on the potential of successful axon regeneration *in vivo*. It was found herein that

PCL fibre diameters of 8 and 10 µm supported the outgrowth of neurites and neurite length the best compared to other diameters tested. These diameters did not only show the greatest outgrowth and incidence values among the diameters tested but measured also similar to the TCP control, the gold standard substrate for *in vitro* assays, with no significant differences. On the contrary, PCL films performed with significant limitations, which indicates that the material alone was not enough to promote axon outgrowth but that the material dimensions were a major contributor. This supports the findings of an earlier study by Daud *et al*., who showed a change in neurite outgrowth on different fibre diameters, where all fibres were made from PCL [152]. Additionally, neurite lengths on 1 and 13 µm fibres measured similar to flat PCL films but 5 – 10 µm fibres promoted an increase in neurite outgrowth compared to the PCL film control, which emphasises the above statement. Furthermore, a decrease in neurite length and incidence was found on 13 µm fibres which points out that there is a sweet spot in fibre dimensions that supports an optimal neurite growth.

Additionally, the orientation of fibres generally supported an aligned outgrowth of axons, where a random orientation of axons was found on the flat PCL substrate control. This finding is in agreement with the literature, which showed that aligned topographies reinforced nerve repair in comparison to randomly aligned structures [141, 302]. Going beyond this, a closer examination of axon directionality on PCL fibres revealed that processes were formed in between neuronal cells but that the directionality of those processes was dependent on the fibre diameter. It was noticed that axons on fibre diameters of 1 and 5 µm branched between fibres to form those connections with a high number of unaligned axons. The contrary was found on fibre diameters of 8 – 13 µm, where axons aligned with fibre direction. This shows that the alignment of fibres itself is not sufficient to guide axons in directionality to the fibres but that the fibre dimensions contribute to this. There is some similarity between these findings and those of Cardwell *et al*., who showed that the behaviour of mesenchymal stem cells was affected more significantly by the fibre diameter they were cultured on than by its alignment [303].

Herein it is hypothesised that two factors contribute to a directional cell outgrowth: 1) the elongated groove structure on the fibre surface and 2) the entire fibre as a directional guide. In this study, 1 and 13 µm fibres showed limited performance in

neuronal cultures in comparison to the other diameters tested which interestingly also showed a difference in topographies on the fibre surface. Small 1 µm fibres were covered in shallow circular structures and lacked the elongated groove features seen on bigger fibre diameters. It was hence concluded that those fibres lack the additional directional guidance cues on the fibre surface besides the fibre alignment itself. It can therefore be hypothesised that the small diameter alone was not sufficient to guide axons. This finding is supported by a previous study by Yang *et al.* that demonstrated a significantly higher degree of axon alignment and an increased neurite length of PC12 neuronal cells on pitted aligned PLA fibres in comparison to smooth fibres [170]. On the other hand, 13 µm fibres had elongated depressions on the fibre surface but fibre diameters were too big to support a similar axon outgrowth to 10 µm fibres. It is hypothesised that NG108-15 neuronal cells recognised such big fibre diameters as being similar to a flat surface without any directional cues. This might be furthermore reinforced by the increased groove length and area seen on those fibres the width of which might have been too wide to provide guidance directionality for axons. However, 13 µm fibres directed axon outgrowth better than 1 µm fibres. This is possibly due to the elongated groove structure on the fibres, which still provided some directionality but were not sufficient to provide optimal axon guidance alone.

In summary, these findings suggest that optimal neurite guidance on PCL fibres depend on an optimal 'fibre surface area to cell size ratio'. For the present work, 1 and 13 µm fibres were not recognised by neurons as being 'directional guides'. These results go beyond what has been found previously. For the first time a defined range of PCL fibre diameters could be identified as an optimised NGC scaffold to support axon regeneration.

3.5.3 The performance of Schwann cells grown on microfibres in culture

In this chapter, the relationship between the different PCL fibre diameters and primary Schwann cells was studied regarding their attachment, metabolic activity and proliferation potential.

As the attachment of a cell alters its behaviour and the expression of genes and proliferation, firm attachment of Schwann cells to a microfibre scaffold is of particular importance for successful nerve regeneration. Herein, crystal violet assays demonstrated

that Schwann cells attached in similar numbers to 5 – 13 µm PCL fibres, where a reduction in attachment by more than half was observed on 1 µm fibres. These results suggest that fibre diameters influence the attachment behaviour of Schwann cells. However, not only 1 µm fibres inhibited cell attachment but also PCL films appeared to have significant inhibiting effects. Additionally, SEM revealed that Schwann cells cultured on bigger fibre diameter elongated in fibre direction, whereas cells on smaller diameter spread over several fibres with no directionality.

These findings are informative in multiple ways. First, the PCL – cell interaction could be significantly improved by altering the materials geography, where certain fibre diameter was proved to significantly enhance Schwann cell attachment in comparison to flat films and 1 µm fibres. Second, the mutual difference of 1 µm fibres and PCL films in comparison to larger fibre diameters was the lack of elongated and deep depressions on the fibre surface. Although not as frequent, the increased groove area, length and depth of grooves on bigger fibre diameter was hypothesised to increase 1) the surface area of the fibre and 2) the surface roughness of fibres (roughness is herein defined as an abrupt change in surface height). A similar finding was reported by Kim *et al*. who confirmed that surface roughness on electrospun fibres increased with increasing diameter and hence increased the surface area. Subsequently, fibroblasts and endothelial cells showed increased adhesion rates on bigger fibre diameters in this study [304]. In additional agreement, Chen and colleagues showed that fibroblasts showed increased attachment rates to fibre scaffolds with increased surface areas [305]. It seems possible that the obtained results herein can be explained by the introduced surface roughness and increased surface area on 5 – 13 µm fibres from the nanotopography on the fibres surface. Although there was an identifiable difference in groove depth between SEM images of 1 and 5 – 13 µm fibres, more quantitative measurements need to be conducted to confirm this. AFM, for example, could provide valuable information on fibre surface roughness in order to predict differences in surface area more accurately. Additionally, it needs to be mentioned that Schwann cells attached significantly better to TCP than to all other PCL substrates. A possible explanation for this might be PCL's hydrophobicity that reduces the adhesion of proteins to its surface and hence influences cell attachment. It was beyond the scope of this chapter to examine this in more detail but will be addressed in Chapter 5.

Concluding, it is hypothesised that when looking at a single fibre, the enlarged surface area and roughness can favour protein adhesion to its surface. This proposed theory was confirmed by Leong *et al.*, who reported that electrospun PLLA fibres with a pitted surface adsorbed 80 % more protein from 10 % FBS in culture medium than smooth fibres. As a consequence, pitted fibres showed a greater cell attachment of porcine epithelial cells compared to smooth fibres [172]. It is also worth mentioning that the proposed theory could have additional positive impacts on directional Schwann cell migration along microfibres into the nerve lesion *in vivo*. Parson *et al*. have previously reviewed the general principle of directional cell migration, which goes back to a sufficient attachment of cell protrusions along a matrix [306] or applied in a broader sense to microfibres herein. It should be furthermore noted that herein 5 µm fibres presented a critical surface area for Schwann cell attachment, where the attachment remained unchanged with an increase in fibre diameter. This suggests that the overall fibre diameter plays an additional role towards a good cell attachment but that there was an initial threshold (here 5 µm thick fibres) of surface area and focal adhesion points to cause this effect with no further improvements seen when increasing the contact area.

The fibre diameter was not only important to mediate cell attachment but also to guide Schwann cells. Fibres of 1 µm diameter were not able to direct Schwann cells with fibre alignment, which could be explained in the same way as in the above section, which showed that an optimised cell directionality could be achieved with an optimal fibre surface area to cell size ratio. Herein, Schwann cells preferred fibre diameter of 5 µm and greater but a definite fibre diameter range could not be identified. It is assumed that this is due to the differences in cell size, where primary rat Schwann cells have a greater cell surface than small NG108-15 neuronal cells. It is encouraging to compare these findings with that found by Lee *et al*., who reported that primary rat oligodendrocytes myelinated electrospun polystyrene fibres without the presence of axons when fibre diameter were 4 µm and greater [307]. This encourages the thought that Schwann cells herein recognised fibre diameters of 5 µm and greater as they would potentially recognise axons *in vivo*.

Furthermore, differences in Schwann cell metabolic activity was observed on different fibre diameters over time. The evaluation of metabolic activity in cells is a frequently used tool in bioengineering to assess the biocompatibility of biomaterials *in vitro*. A positive response of naturally proliferating cells to biomaterials can be assessed through an increased measured metabolic activity over time. Herein, metabolic activity rates gradually increased on 5 – 13 µm fibres over time, where activity values only slowly increased on 1 µm fibres and measured significantly lower compared to the other fibre diameter. A similar trend was observed by Wang *et al*., who reported on a significantly greater Schwann cell migration and proliferation on larger fibre diameters compared to smaller fibres [151]. Additionally, fibroblasts and endothelial cells showed higher metabolic activity rates on bigger fibre diameters of 3.4 µm versus smaller fibre diameters of 0.1 µm after 5 days of culture [304].

There are three possible theories to explain this result and it is assumed that all three theories collude to a certain extent. The first two propositions are based on the initial differences in Schwann cell attachment to microfibres. As shown previously, Schwann cells attached to a greater extent to bigger fibre diameters in comparison to smaller 1 µm fibres and hence Schwann cell numbers were greater on bigger fibre diameters. Proliferating cells have an increased metabolic demand, where a gradual increase in cell number would result in an increase in overall measured metabolic activity over time. This would possibly explain the greater increase in metabolic activity on 5 – 13 µm fibres as more cells were initially present on the scaffolds.

Furthermore, the slow increase in metabolic activity on 1 µm fibres might be explained through a prolonged cell attachment phase compared to cells on fibres with a bigger surface area. Cells on 1 µm fibres might need longer to fully attach to the fibres as it was shown that Schwann cells need to attach over multiple fibres in order to form sufficient contact to the substrate in comparison to bigger fibre diameters, where a single cell attached to a single PCL fibre. It is assumed that hence the proliferation of cells might be delayed in comparison to cells on bigger fibre diameters. This suggestion matches those from Chen *et al.*, who confirmed a faster cell attachment rate to electrospun scaffolds with greater surface areas compared to low surface area scaffolds [305].

Additionally, it might be that Schwann cells grown on fibre diameters of 5 – 13 µm proliferate to a greater extent compared to 1 µm fibres. Based on the presence of deeper and larger nanotopographies on 5 – 13 µm fibres, with a potential increase in proteins on the fibre surface, the proliferation of Schwann cells might be enhanced. This theory is consistent with the studies of Moroni *et al*. and Taskin *et al*. who showed that an introduced nanotopography on the fibre surface could enhance the proliferation of either human mesenchymal stem cells [171] or human endothelial cells [173] in comparison to smooth fibres. Taskin *et al*. additionally noted a greater number of vinculin and phosphorylated focal adhesion kinase on the cell surface when cultured on fibres with nanotopographies. That puts further weight on the assumption of an increased protein adsorption on fibres with nanotopographies [173].

A greater number of Schwann cells on larger fibre diameters would additionally explain differences in proliferating cell numbers on the fibre scaffolds herein. An increase in proliferating cells was found on 1, 5 and 8 µm PCL fibres from day 3 to day 5, where a decrease was observed on 10 and 13 µm fibres. This finding supports previous research, where an increase in cell density through contact inhibition led to cells exit the cell cycle and enter the G0 phase, where proliferation had come to a stop [308]. However, it needs to be advised to interpret these data with caution as differences in proliferation levels were statistically not significant and might not mirror actual proliferation rates.

In summary, for the optimisation of existing NGCs, a rapid and positive cellular response to an introduced internal fibre scaffold is desirable as time plays a critical role in nerve regeneration. We have identified that these cell responses are dependent on the physical fibre properties like the surface area and surface roughness. Additionally, it was shown that neurons and Schwann cells sensed these fibre properties and responded. Where Schwann cells require fibre diameters greater than 1 µm to enhance attachment rates and metabolic activity rates, 8 and 10 µm fibres supported the outgrowth and incidence of neurites the best. Based on the achieved *in vitro* results, it is hypothesised that the optimal fibre diameter range for PCL fibres as a scaffold in nerve regeneration lies between 8 and 10 µm.

3.6 Conclusion

This chapter identified that PCL fibres supported directional neuronal and Schwann cell outgrowth the best in dimensions between 8 and 10 µm. The identified nanotopographical features on the fibre surface were believed to increase the surface roughness and area on the fibres but was in particular favoured by the deep, elongated and long grooves on 5 – 13 µm fibres. This showed effects on cell attachment and behaviour. Besides fibre alignment and surface structure, the diameter of fibres played a substantial role in the guidance and outgrowth of neurons and Schwann cells. The performance of fibre diameter led back to the ratio between cell and fibre size, where small 1 µm fibres were recognised with significant limitations as guidance features for cells.

In summary, it is concluded:

- PCL could be reproducibly fabricated to highly aligned fibres of dimensions between 1 and 13 µm using electrospinning which was mainly controlled by the polymer flow rate
- There was a dependency between fibre diameter and surface topographies: 1 µm fibres were covered in shallow circular pores, where 5 – 13 µm fibres presented less frequent but deep and elongated grooves in fibre direction on their surface. Grooves on 13 µm fibres were bigger than on 5 – 13 µm fibres
- All PCL fibre diameters supported the viability of Schwann cells and neuronal cells but an observed decrease in neuron viability on 1 µm fibres might be of concern *in vivo*
- Fibre alignment alone was not sufficient to guide axons
- Fibre diameter influenced axon directionality, incidence and length. In this regard, 8 and 10 µm fibres performed the best
- Small 1 µm fibres inhibited Schwann cell attachment in comparison to bigger fibres

- Schwann cell metabolic activity was reduced on 1 µm fibres
- Fibre diameters did not influence the proliferation of Schwann cells

Chapter 4 Development of a 3D *ex vivo* model of peripheral nerve regeneration

4.1 Introduction

To this day, cell cultivation in a monolayer is the traditional way of culturing cells as it has proved to be simple, convenient and generated results in a short time. Although flat two-dimensional cultures are rather simple, they have enabled researchers to discover and understand detailed signalling in the cell. However, research has consistently shown that monolayer cultures lack three-dimensional complexity compared to native tissues and therefore lack accuracy when used to evaluate biological performances of medical devices for use in complex three-dimensional tissues [235, 236]. In order to answer more complex biological questions, *in vivo* animal models have been used. Though animal studies can often mirror human biological responses, they do not always reproduce human physiology. Additionally, there is a strong motivation to bypass the use of animals in biological evaluations which is addressed with the 3Rs principle (see Chapter 1, section 1.17 for more information) and further implicit in UK law under the Animals (Scientific Procedures) Act from 1986. In this regard, animals often failed to represent human health responses and their use is furthermore ethically questionable [240-242]. The exclusive use of rat sciatic nerve injury models for the evaluation of nerve guidance conduits (NGCs), for example, has been criticized regarding the unreliable translation from rat or mouse to human. Rats and mice were mentioned to be particularly poor models for evaluating the performance of NGCs for repairing critical human nerve gaps as fibrin cable degradation differs extremely between the two species (2 weeks in rats and 4 weeks in human) [101].

As demonstrated, there is a large gap in the physiological relevance between monolayer cultures and animal experiments. In order to fill this gap, *in vitro* cell culture models are needed that replicate tissue structures in three dimensions without using laboratory animals. The last years have seen increasingly rapid advances in the development of *in vitro* 3D models especially in skin replicas [256, 309]. However, far too little attention has been paid to building 3D models for peripheral nerves. While some research has been carried out on orientating axons and Schwann cells to aligned structures in a three-dimensional environment [152, 271, 273], only one study established a peripheral nerve

model that comprised of the tubular nerve structure [272]. Vyas *et al.* built a model of motor peripheral nerve by connecting spinal cord slices with motor sensory nerves, which spinal motor axons regenerated into [272]. Although this model was successful, it was rather complicated in design and hence not practical for studying a high number of experimental variables such as different nerve guide designs.

The aim of this study has therefore been to build an *ex vivo* model of peripheral nerve regeneration using dorsal root ganglia. The outgrowth of axons and Schwann cells from DRG bodies was suggested to be used to model peripheral nerve regeneration to help investigate and compare the regenerative support of different internal nerve guidance scaffolds *in vitro* for improving the performance of currently hollow NGCs *in vivo*. A completed DRG outgrowth along selected scaffolds would then further demonstrate an *in vitro* three-dimensional replica of peripheral nerve which might be used for studying peripheral nerve diseases such as neuropathies and their development.

Here, an experimental conduit from polyethylene glycol (PEG) was used as it could either be seen as 1) any hollow conduit for nerve repair or 2) as a replication of the epineurium *in vitro* that surrounds and holds together nerve fascicles *in vivo*. As previously mentioned by Pateman *et al.*, PEG has shown suitable properties when used as an example conduit due to its plasticity that enables the accurate and rapid printing of tubular devices with additional advantages due to its commercial availability [105]. Conduits were herein filled with PCL fibre scaffolds as microfibres presented ideal candidates for guiding and orientating axons and Schwann cells to aligned structures as previously discussed in Chapter 3. Scaffolds of 5 µm PCL fibres were selected due to their promising performance as a co-culture model for peripheral nerve [152]. Daud *et al.* identified 5 µm PCL fibres as the best fibre candidate among three diameters tested (1, 5 and 8 µm) in regard to neurite formation and outgrowth in co-cultures with Schwann cells [152]. It is important to mention that the example conduit herein was purposely designed to comprise of two separate parts, the conduit and the fibre scaffold, that were combined thereafter into one device to offer the possibility of examining different scaffold and conduit designs and materials. This has additional advantages as fibre scaffolds can be removed from conduits after culture for analysis and imaging. PEG was an optimal choice for presenting a conduit architecture for studying internal guidance

scaffolds due to its commercial availability, easy processability to conduits with microstereolithography and non-fouling properties [310]. The latter reduces the adsorption of proteins and cell attachment [310] and was hence ideal for studying internal nerve guidance scaffolds as the outgrowth of cells could be limited to the internal scaffold over the conduit walls.

A number of studies have reported on the incorporation of aligned fibres inside conduits before, however, they showed some major limitations in device development regarding the documentation, verification and reproducibility of fibre densities in conduits [145-147, 153]. With one exception, all authors who reported on the incorporation of fibres inside NGCs were unable to verify the density of fibres inside conduits [145-147]. Only Ngo *et al.* validated the density of fibres inside conduits. However, the authors used conduit cross-sections for density measurements and were unable to predict those densities before the incorporation of fibres [153]. To conclude, no author has shown a reproducible method to incorporate fibres of specific densities inside conduits so far. This has therefore been addressed herein by developing an accurate and reproducible technique to precisely control fibre volumes in conduits. Additionally, those devices have exclusively been designed for use in peripheral nerve injuries [145-147, 153]. This work therefore sought to design a model that can be used for studying both peripheral nerve regeneration and general research questions regarding peripheral nerve mechanisms and disease pathways such as neuropathies in a three-dimensional complex environment.

This study investigated the significance of such a model to support cell viability, aligned cell outgrowth including axon orientation in mono- and DRG co-culture and developed an appropriate cell seeding technique as well as a suitable imaging approach. Finally, the impact of the work was discussed regarding its use as an *in vitro* peripheral nerve model and paying distinct attention to its benefit in developing internal nerve guide scaffolds for treating nerve injuries. The work in this chapter has been published in the International Journal of Bioprinting in 2018 [311] and hence there might be similarities between the two documents.

4.2. Aims & Objectives

The aim of this study was to develop an *in vitro*/*ex vivo* 3D model of peripheral nerve and peripheral nerve regeneration. It was hypothesised that axon and Schwann cell outgrowth can directly be studied inside NGCs with internal fibre scaffolds from either DRG explant cultures or seeded within the conduits. Therefore, conduits with internal fibre scaffolds were analysed on their ability to maintain cell viability, orientate cells with fibre scaffold direction and guide axon outgrowth. This study provided an exciting opportunity to advance the current testing systems on peripheral nerve and nerve regeneration by providing a relevant physiological environment which may be used to study fundamental peripheral nerve mechanisms but also evaluate and compare different internal NGC scaffolds.

The following objectives were conveyed in order to meet the expressed aims:

- To 3D-print a nerve guide from polyethylene glycol using microstereolithography that can be used in a 3 mm common fibular nerve injury model in mice
- To develop a technique that combines microfibres with hollow conduits by maintaining fibre alignment
- To fill conduits with different fibre densities and validate the developed method by micro-CT
- To design and develop a culture setup that enables the use of conduits with scaffolds *in vitro*
- To study neuronal cell distribution and viability on fibre scaffolds inside conduits
- To investigate neurite outgrowth in the culture model
- To evaluate the cell outgrowth from DRG explants in the reported 3D model

4.3. Materials & Methods

4.3.1. Fabrication of nerve guides

Nerve guides with an internal diameter of 1.1 mm and a length of 5 mm were 3D-printed from PEG diacrylate (Mn = 700 g/mol) and 4 % photoinitiator using microstereolithography. A full description of the conduit fabrication process can be found in section 2.1. Conduit dimensions were measured with the "straight-line tool" in Fiji based on SEM images.

4.3.2. Combining nerve guides and aligned microfibres for cell culture

PEG conduits were fabricated as described in 2.1. A 20 % PCL in DCM solution was used to electrospin 5 µm aligned fibres using a flow rate of 4 mL/h and a voltage of 18 kV (see section 2.2 for details). Conduits were filled with 20 % of 5 µm PCL fibres. For this, fibres on aluminium sheets were cut to 10 cm in length to a width of 1 – 2 cm. Fibres were prepared for threading into conduits as described in 2.4 and in more in detail in Results 4.4.2. It was calculated that 0.017 g of fibres would fill a conduit with internal diameter of 1.12 mm to 20 % (see section 2.5 for details). Fibres were assembled into bundles weighing 0.017 g and then threaded into 5 mm long PEG conduits. Fibre ends were cut with conventional scissors.

4.3.3. Fibre end cutting in conduits and analysis

Dry 5 mm long PEG NGCs (fabricated as in section 2.1) were filled with 20 % of 5 µm PCL fibres (see section 2.5). Fibres overhanging the conduit ends were trimmed to align with conduit ends using three different methods: laser, scalpel and scissor cutting. For cutting with laser, NGCs were placed on a glass microscope slide and were held in place using sticky tape. As guidance, two parallel lines with a distance of 5.2 mm were laser-printed onto a blank sheet of paper. The conduit was placed on the paper with the conduit ends aligning with the laser-printed lines and fixed with tape. Fibre ends were laser cut (Mini18 Laser, Epilog Laser) with an intensity of 10 %, a speed of 20 % and a frequency of 2500 Hz. For scalpel cutting, conduits were taped to a glass microscope slide and fibre ends cut with a surgical scalpel blade (Swann Morton Ltd., UK), the scalpel blade was positioned at the conduit ends and was pushed down onto the glass slide to cut fibres.

For the third method, conduits were held in hands and fibre excess cut as close to the conduit ends as possible using conventional scissors. Experiments were repeated twice independently.

4.3.4. SEM analysis of fibre alignment in the conduit

PEG conduits (5 mm long, 1.12 mm internal diameter) were filled with 20 % aligned 5 µm PCL fibres and overhanging fibre ends cut with scissors as described in section 4.3.3. The fibre bundles were then carefully removed from conduits using a pair of tweezers. SEM analysis was conducted on the removed fibre bundles as described in 2.16. For imaging the entire scaffold size, a magnification of 35× was used, whereas fibre bundle ends and middle were imaged at 300×. Fibre bundles of three independently filled conduits were imaged.

4.3.5. Conduit and fibre preparation for micro-computed tomography analysis

PEG conduits (fabricated as in 2.1) were either filled with 8 or 20 % of electrospun 10 µm fibres (fabricated as in 2.2) or filled with 20 % of either 5 or 10 µm PCL fibres. In order to determine the required weight to fill conduits with either 8 or 20 % of fibres, the equations presented in 2.5 were used. It was calculated that 0.007 g and 0.017 g of fibres (irrespective of the diameter) were needed to fill PEG conduits with an internal diameter of 1.12 mm with 8 or 20 %, respectively when a fibre bundle of 10 cm in length was used. Fibre weighing procedures were conducted as described in in 2.5.

4.3.6. Micro-computed tomography and analysis

The imaging of samples by micro-CT was performed by an experimental officer (Mrs. Holly Evans) in the Department of Oncology and Metabolism in the Medical School at The University of Sheffield (UK). Samples were scanned on a Skyscan 1272 micro-CT scanner (Bruker, Kontich, Belgium) at 40 kV and 250 µA using no filter and a detection pixel size of 3.5 µm. Images were captured every 0.7° through 180° rotation. Scanned images were reconstructed using Skyscan NRecon software (Version 1.6.8.0) and datasets analysed using Skyscan CT analysis software (Version 1.17). A 1 × 1 mm cylindrical region of interest was taken from the centre of the sample and volume (%) was assessed. Fibre volume in the conduits was also evaluated in Fiji, where cross-section micro-CT images

were converted to binary images first and then the fibre volume analysed in a 1 × 1 mm region of interest using the Analyse Particle tool (sample size: 0 – infinity) [284].

4.3.7. NG108-15 neuronal cell culture on microfibres in NGCs

NG108-15 neuronal cells were cultured on aligned 5 µm PCL fibres, which filled 20 % of the lumen of PEG conduits (see 2.1 for conduit fabrication, 2.2 for fibre fabrication, 2.4 and 2.6 for fibre and conduit assembly). Conduits with fibres were sterilised and prepared in wells of a 6-well plate as described in 2.6. Neuronal cells were trypsinised and counted as described in sections 2.9.3 and 2.9.4 and subsequently seeded in numbers of 6×10^5 in 10 µL of growth medium containing 10 % FBS (section 2.9.2). Cell suspensions of 10 µL were applied to one side of the conduit and cells left to attach in a CO_2 incubator for 30 min. Afterwards, conduits were covered with growth medium.

4.3.8. Cell orientation analysis by F-Actin labelling

NG108-15 neuronal cells were seeded in PEG conduits with 5 µm PCL fibre scaffolds in numbers of 6×10^5 as described above (see section 4.3.7). As a control, neuronal cells were seeded on TCP inside 1 cm^2 stainless-steel rings in numbers of 2×10^4 in 500 µL and left to attach for 2 h before being covered with growth medium. Cells were maintained in growth medium in a CO_2 incubator for 4 days. Cells were fixed and stained for F-actin using phalloidin-TRITC as described in 2.13. Scaffolds in conduits were removed prior to fixing. Samples were washed once with PBS and nuclei labelled with DAPI (see 2.12 for details). Experiments were repeated independently three times. Samples were imaged in z-stacks using confocal microscopy as described in 2.17. Z-stack images were either combined to maximum projection images or to 3D projections showing the volume of the sample (Volume Viewer, Fiji) [284]. Experiments were repeated three times independently.

4.3.9. Cell viability assay and analysis

Neuronal cells on fibre scaffolds inside NGCs were seeded in numbers of 6×10^5 as described above (see 4.3.7). Cells on TCP and PCL films (prepared as described in 2.7) were seeded inside 1 cm^2 stainless-steel rings in numbers of 2×10^4 in 500 µL and left to attach for 2 h before being covered with growth medium. After 4 days of culture,

scaffolds were carefully removed from conduits and cells on all substrates labelled for living and dead cells. Live/dead overview stains, imaging and analysis were conducted as described in 2.14 and 2.17. Experiments were repeated independently three times.

4.3.10. Neurite outgrowth assay and analysis

Neuronal cells were seeded at 6×10^5 cells per conduit as described above (see 4.3.7). However, cells were seeded in serum-free growth medium (see 2.9.2 for details). This removed the risk of cell detachment during washing steps when changing from serum-containing growth medium. Cultures were maintained for 21 days with a medium change conducted every 5 days. Immunocytochemistry was performed as described in 2.12 to reveal axon-specific protein βIII Tubulin, a mouse monoclonal anti-βIII Tubulin antibody (1 µg/mL, ab78078, Abcam) and donkey anti-mouse FITC antibody (0.6 mg/mL, A24501, Life Technologies) were used as primary and secondary antibody, respectively. The primary antibody was incubated at 4 °C overnight, whereas the secondary antibody was incubated at room temperature for 2 h. Nuclei were visualised with DAPI as described in 2.12. Experiments were repeated independently three times. Samples were imaged with a light-sheet microscope as described in 2.18, where each sample was captured in four views of 0°, 90°, 180° and 270°. Neurite lengths were measured as described in 2.10.1.

4.3.11. *Ex vivo* dorsal root ganglion culture

PEG conduits (see 2.1 for details) filled with 20 % 5 µm PCL fibres were prepared and sterilised as described in 2.6. DRGs were dissected from 12 – 15 week old male Wistar rats. Rats were kept and sacrificed according to the UK Home Office regulations after a schedule I procedure (cervical dislocation). With the dorsal side facing up, the back of the rat was skinned and the spine removed. The removed spine was cut open from the ventral side using scissors and the spinal cord and meninges covering the DRGs removed with forceps. Using a dissection microscope, DRGs were dissected, removed and placed in a Petri dish filled with warm PBS containing 100 units/mL penicillin and 100 µg/mL streptomycin. Nerve roots emerging from DRG bodies were trimmed using a scalpel. A DRG body was placed on top of each prepared conduit and left to attach in a CO_2 incubator for 30 min. Afterwards, DRGs on conduits were covered with growth medium. After 21 days of culture, scaffolds carrying DRGs were carefully removed from conduits

and fixed according to 2.12. Immunocytochemistry was performed to reveal axon-specific βIII Tubulin and Schwann cell marker S100β protein. Immunolabelling was performed as described in 2.12, where mouse anti-βIII Tubulin antibody (2.5 µg/mL, G7121, Promega) and rabbit anti-S100β antibody (10 µg/mL, Z5116, Dako Denmark) were used as primary antibodies, which were incubated at 4 °C for 48 h. As secondary antibodies, horse anti-mouse IgG conjugated to Texas Red (1:1000, TI-200, Vector Laboratories) and goat anti-rabbit IgG conjugated to FITC (1:1000, F1-1000, Vector Laboratories) were used and incubated at room temperature for 3 h. Nuclei were visualised by DAPI (see 2.12 for details). Fibre scaffolds were imaged in multiple positions in z-stacks by confocal microscopy. Z-stacked images were combined to one maximum projection image and images taken from multiple positions stitched together in Fiji using the grid/collection stitching tool [286]. The outgrowth of Schwann cells and axons from DRG bodies was measured as the distance between the last detectable Schwann cell- or axon-specific fluorescent signal seen distant from the DRG body. DRGs attached to scaffolds and DRGs that showed an outgrowth of cells that was detectable distant to the DRG body were counted and numbers expressed in relation to all dissected DRGs. Experiments were conducted independently three times.

4.4. Results

4.4.1. Fabrication of nerve guides

In order to investigate the performance of fabricated PCL microfibres inside the nerve guide architecture, tubular devices were manufactured. For this, microstereolithography was used to fabricate nerve guides from PEG-DA containing 4 % photoinitiator to cross-link polymer chains when irradiated by a laser beam. In microstereolithography, constructs are printed using a layer-by-layer approach, meaning dimensions can be precisely controlled based on a cross-sectional image of the construct. The microstereolithography setup herein used a digital mirror device (DMD) comprised of 1024 × 768 pixels. Each pixel represents a small mirror, which can either tilt by 12° towards the illumination or away from it. These two stages are referred to as the on or off stage, respectively. A cross-sectional image of the conduit is shown in Figure 40 A, which had the same pixel number (1024 × 768) as the DMD, where black pixels caused mirrors to turn on and reflect the laser beam, and white pixels caused mirrors to turn off. The presented cross section shows a black circle comprising of 234 × 234 pixels with an interior white circle of 176 × 176 pixels. Based on this image, conduits were printed that can be seen in the SEM micrograph in Figure 40 B. PEG nerve guides measured an average length of 4.8 ± 0.2 mm with an average internal diameter of 1.12 ± 0.11 mm. It was additionally noted that tube constructs showed micro-thin lines in same directionality as the laser illumination at the surface of the conduit on the inside and outside tube walls. The majority of conduits appeared as neat constructs with no irregularities found. Printed conduits showed a white-yellow colour with slight transparency (Figure 40 C).

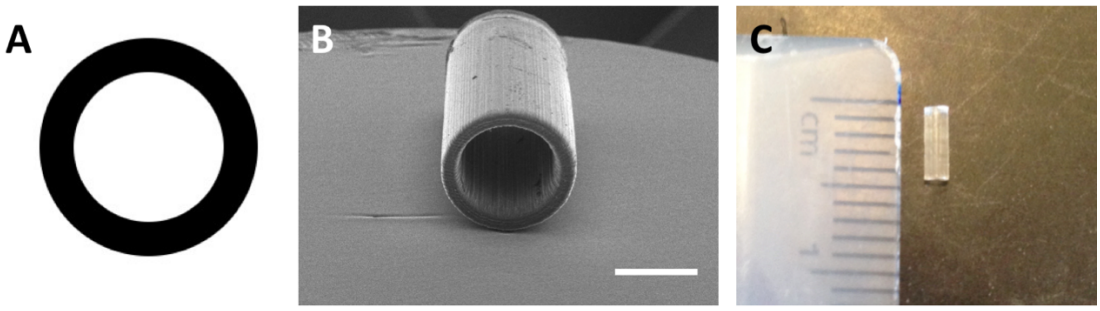

Figure 40 Conduits made by microstereolithography

Laser-based microstereolithography was used to fabricate conduits from PEG diacrylate. A) A cross-sectional image of the conduit which was uploaded to a digital mirror device which reflected the laser beam in the shape of the cross-section in order to print a conduit. B) Final PEG conduit with a length of 5 mm and an internal diameter of 1.1 mm imaged by scanning electron microscopy and measured in Fiji. Scale bar = 1 mm C) Macroscopic photograph of a 5 mm long PEG conduit. Scale illustrated by ruler in the image.

4.4.2. The assembly of fibres and conduits

In the interest of studying microfibre scaffolds in the nerve guide itself, a technique was developed to arrange aligned microfibres inside the conduit lumen. This section will describe the essential steps of the invented fibre threading procedure to insert aligned PCL microfibres into PEG conduits. Electrospun PCL fibres were collected on aluminium foil, where fibres appeared white and aligned (Figure 41 A). Pieces of aluminium foil were cut to smaller fibre strips to ease the threading procedure (here 10 cm long and 2 cm wide) (Figure 41 A). It can be seen in Figure 41 B that all fibres that directly aligned with the foil ends were carefully and only minimally rolled towards the middle of the foil. This was to prevent the catching of fibres on the foil edges when being peeled off in the threading process. Figure 41 B additionally shows that fibres at one end of the foil came together in the middle, forming a needle-like tip. This was achieved by rolling the fibres towards the middle of the foil and twisting them between the fingers. As seen in Figure 41 B the fibre tip was rigid and did not untwist. To facilitate this aim, the twisted end was stabilised with fast drying glue to result in a stiff fibre needle. The results obtained from the threading of PEG conduits onto the fibres using the twisted fibre needle are

visualised in Figure 41 C. The progressive sliding of the conduit on the fibre bundle towards the foil end can be seen in Figure 41 D, which resulted in the detaching of fibres off the foil and its assembly in the conduit. This described threading procedure was repeated for multiple conduits using the same fibre sheet, where conduits assembled on the fibre bundle like pearls on a chain.

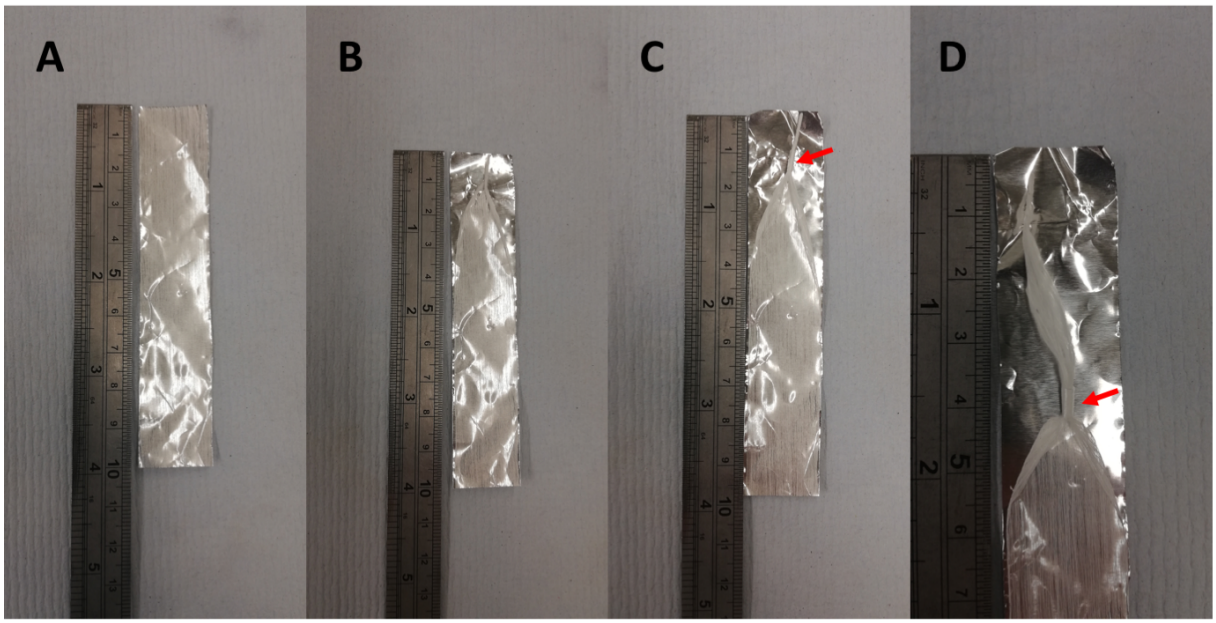

Figure 41 Assembly of microfibres and conduits

Macroscopic images of electrospun 5 µm PCL fibres on pieces of aluminium foil. A) Fibres were cut into 10 cm long strips, B) where one end was twisted between the fingers. C) This needle-like tip was used to thread PEG conduits on the fibre sheet, D) the PEG conduits were then moved towards the bottom of the fibre sheet in the direction of the fibres. Arrows indicate the position of PEG conduits. Scale demonstrated through ruler in the images.

4.4.3. Cutting techniques for overhanging fibre ends in conduits

After the treading of conduits on fibre bundles, fibres needed to be cut at the ends of the conduit. Herein, three different cutting techniques were presented and the conduit ends studied for morphological appearance using SEM. A neat cut of fibres that does not damage the assembly and organisation of fibres inside the conduit is essential for a barrier-free ingrowth of axons and Schwann cells into the conduit. Figure 42 compares fibre-filled conduits cut by a laser (A), by scissors (B) and a scalpel (C). The laser cutting

approach resulted in melted PCL fibres, which appeared as fused areas of polymer clusters in Figure 42 A. Fibres appeared evenly distributed at the interface where overhanging fibre ends were cut with scissors (Figure 42 B). The last cutting technique used a scalpel that cut the fibre excess on a hard surface. The obtained results are shown in Figure 42 C, which show that fibres were bunched together after cutting. These results indicate that best cutting results of fibres inside PEG conduits was achieved with scissors.

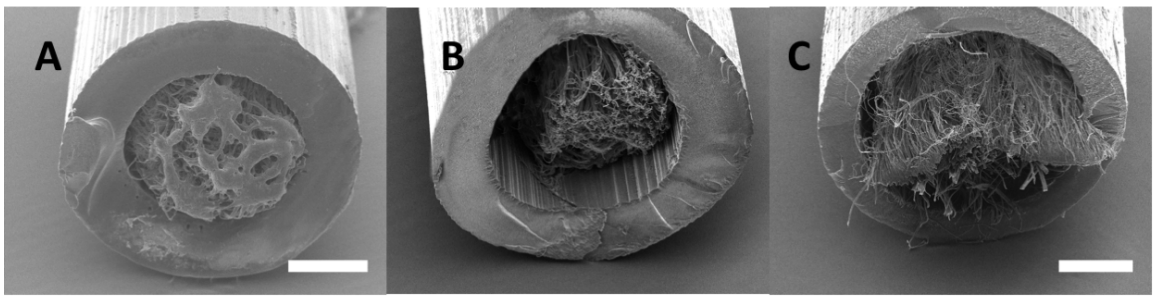

Figure 42 Techniques to trim fibres in conduits

PEG conduits were filled with an aligned 5 µm PCL fibre scaffold and overhanging ends were trimmed in three different ways. A) Fibre ends cut with a laser cutter, B) conventional scissors or C) with a scalpel. Conduits were imaged by SEM. Representative images are shown of three independent experiments. Scale bar = 500 µm.

4.4.4. Fibre alignment in the fibre bundle

So far, a successful fibre threading and cutting method has been presented. Next, the alignment of fibres inside the conduits was evaluated. Therefore, fibres were incorporated into conduits and overhanging fibres cut with scissors. Fibre bundles were carefully removed from conduits and imaged by SEM. The entire fibre bundle can be seen in Figure 43 A, where fibres showed alignment and a multi-layered arrangement. A more detailed examination of the ends and the middle of the bundle is presented in Figure 43 B – D. It was noted that fibres throughout the fibre bundle were highly aligned as well at the ends (Figure 43 B and D) as in the middle (Figure 43 C). At the fibre ends it could be additionally seen that single fibres arranged together and formed small bundle-like structures (Figure 43 B and D).

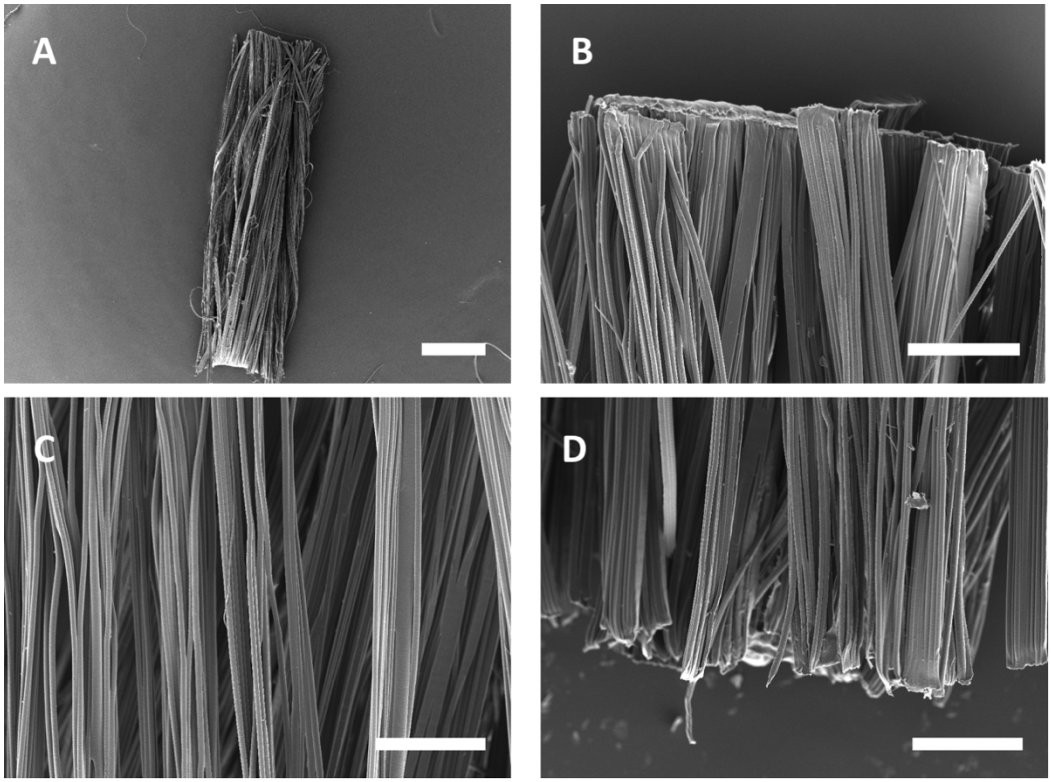

Figure 43 Scanning electron micrographs of PCL fibre bundles

PEG conduits were filled with an aligned 5 µm PCL fibre scaffold which was cut and then removed from conduits and imaged by SEM. A) Presentation of the whole fibre bundle. Magnification 35×. Scale bar = 1 mm. A magnification of 300× was used to image B) and D) the fibre ends and C) the fibre middle in more detail. Scale bar for image B – D = 200 µm. Representative images are shown of two independently performed experiments.

4.4.5. Controlling fibre volumes in the conduit

In order to control the fibre volume inside the conduits a technique was developed that uses calculations and weight measurements to obtain precise filling densities. The internal volume of the conduit was calculated based on the tube diameter and the length of the fibre bundle used to fill the conduits. Knowing the desired percentage of fibres inside the conduit and the density of PCL, the weight that was needed to result in the desired fibre percentage could be calculated (see also section 2.5). Herein, the developed method was validated by micro-CT using two different analysis approaches to calculate the fibre percentage: 1) the incorporated micro-CT software and 2) Fiji. First, fibres of the same diameter were used to fill PEG conduits with a low and a high fibre volume. Conduits were aimed to be filled with 8 and 20 % of fibres. The obtained micro-

CT results are presented in Figure 44. From the cross-sections and 3D images in Figure 44, a clear difference in fibre number and therefore fibre density could be identified between Figure 44 A – B and C – D. An even distribution of fibres was found throughout the conduit lumen for both low and high densities (Figure 44 A and C). The 3D images in Figure 44 B and E further demonstrated the alignment of fibres inside the conduit. Additional evidence on fibre alignment in conduits of both low and high fibre density was given by longitudinal sections through the conduit in Figure 44 E. This micro-CT image shows a conduit that had been cut longitudinally in the middle showing the equally thick and straight running conduit walls with fibres aligning between them. A direct correlation between calculated values and actual fibre percentages is shown in the bar chart in Figure 44 F. Conduits with a low fibre number were filled with 7.6 ± 0.3 % or 8.8 ± 0.01 % of fibres when calculated with the micro-CT software or Fiji, respectively. The average value of both applied methods measured 8.2 ± 0.7 % of fibres similar to the desired volume of 8 %. Similar was found for conduits with high fibre volumes. Fibres measured 18.9 ± 2.9 % and 21.7 ± 0.1 % inside the conduit lumens when calculated by micro-CT software or Fiji, respectively (Figure 44 F). Two-way ANOVA confirmed that conduits were filled with two different densities which were statistically different from each other. Additionally, statistics showed that the calculated density percentage equalled the measured volumes as no significant differences were found between them (Figure 44 F).

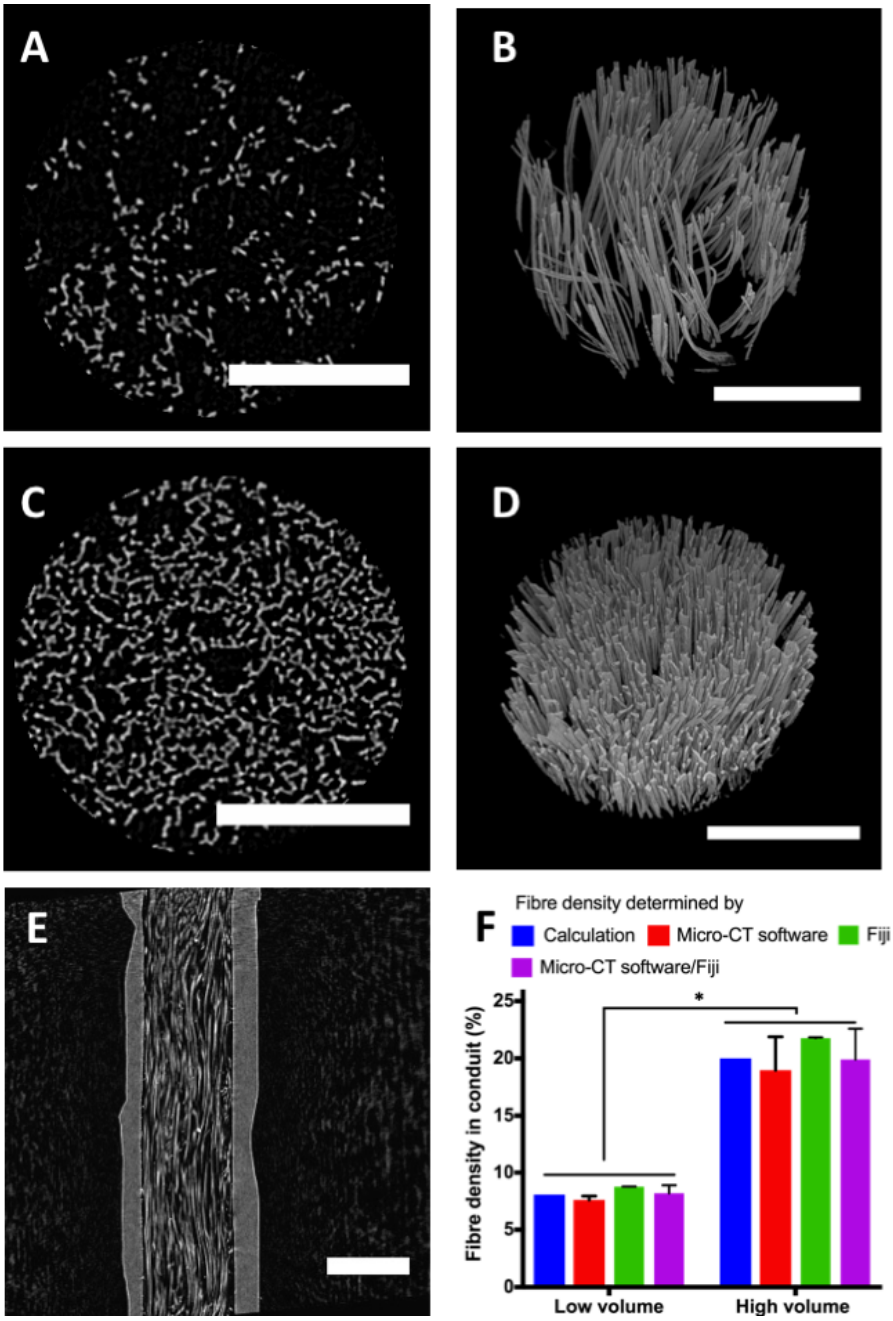

Figure 44 Conduits with low and high fibre density

PEG conduits were filled with two different densities of electrospun 10 µm fibres and micro-CT performed to validate fibre volumes inside conduits. Micro-CT images are presented as follows: A) Cross-section and B) 3D projection image of conduit filled with 8 % of PCL fibres, C) cross-section and D) 3D projection image of conduit filled with 20 % fibres. E) longitudinal cross-section of 20 % PCL fibres in a PEG conduit. Scale bar for A – D = 0.5 mm. Scale bar for E) = 1 mm. Representative images are shown. F) Comparison of calculated fibre volume and values measured by micro-CT software and Fiji. Values represent mean + SD and statistical significance was displayed as * $p<0.05$ (two-way ANOVA with Tukey's multiple comparisons test). Experiments were repeated independently three times.

It was further investigated whether conduits could be filled with fibre bundles of different diameters while resulting in the same density using the reported technique. Fibre volumes inside the conduits were visualised with micro-CT and analysed with either the accompanied micro-CT software or Fiji. It can be seen from Figure 45 A – D that the use of the same fibre weight for 5 and 10 µm fibres resulted in a similar filling volume of fibres in conduits. Fibres were distributed evenly throughout the conduit lumen as demonstrated in Figure 45 A and C. From the images in Figure 45 A – D, the different fibre dimensions in the conduit could additionally be identified, where conduits filled with 10 µm fibres (Figure 45 C –D) showed a larger cross-sectional fibre area than conduits filled with 5 µm fibres (Figure 45 A – B). Furthermore, the 3D model images in Figure 45 B and D illustrated the alignment of both small and large fibres in the conduits. Results were further quantified and presented in Figure 45 E. Conduits were aimed to be filled with 20 % of 5 or 10 µm fibres. Based on cross-sectional images, the accompanied micro-CT software calculated an average fibre density of 16.3 ± 4.1 % and 15.6 ± 1.1 % for 5 and 10 µm fibres, respectively. Interestingly, analysis using Fiji identified a fibre density of 20.5 ± 0.85 % and 19.15 ± 1.4 % for both 5 and 10 µm fibres, respectively (Figure 45 E). The average of both values analysed by the micro-CT software or Fiji were 18.7 ± 2.1 % for 5 µm fibres and 17.3 ± 0.7 % for 10 µm fibres. Although differences were detected, those were not confirmed statistically. An ordinary two-way ANOVA with Tukey's multiple comparisons test confirmed no differences between results (Figure 45 E).

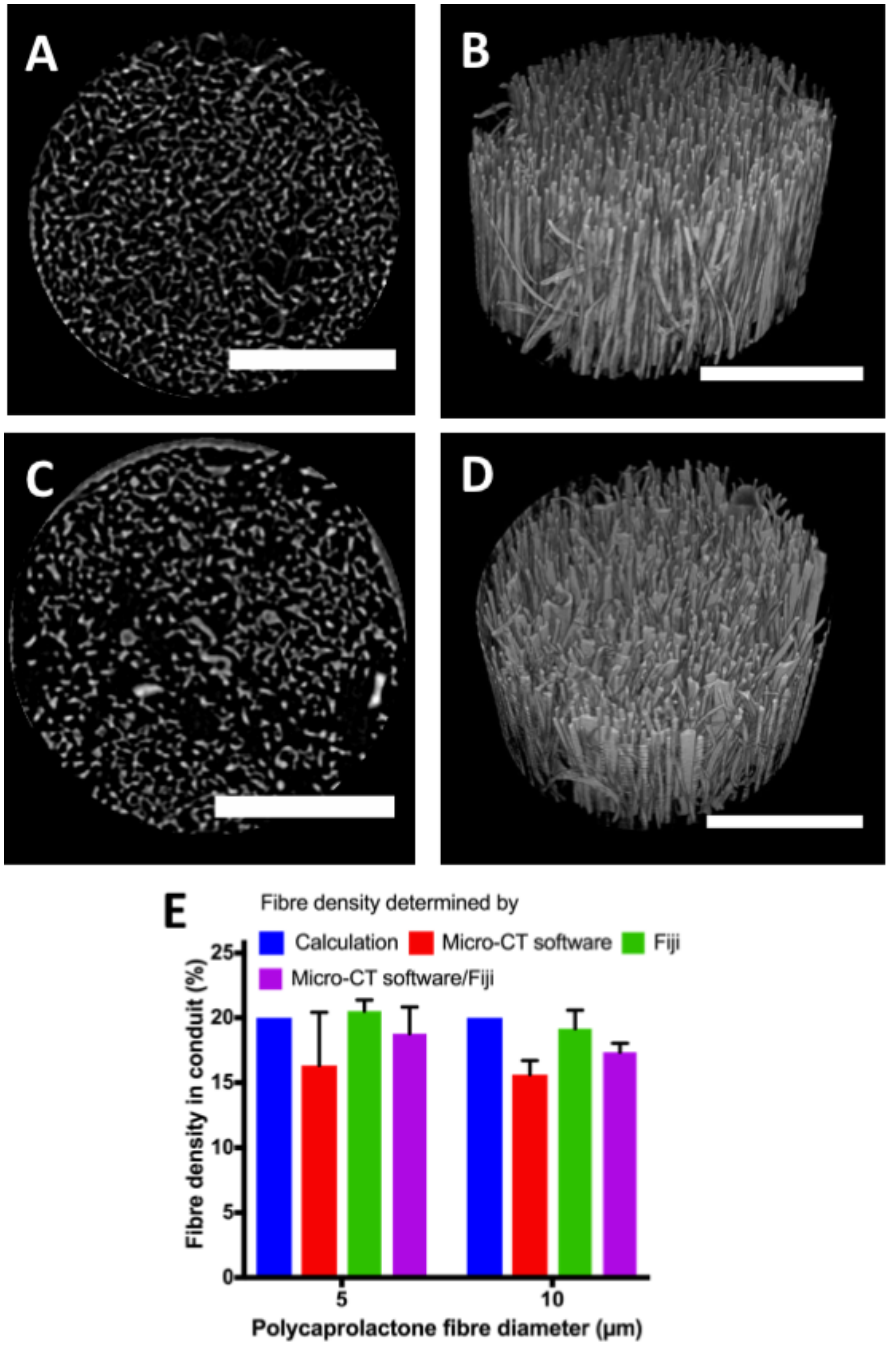

Figure 45 Conduits with different fibre scaffolds of the same density

Micro-CT images of PEG conduits filled with 20 % of 5 µm fibres demonstrated in A) as a cross-section and B) as a 3D projection image. C) shows a cross-section and D) a 3D projection image of 20 % 10 µm PCL fibres in PEG conduits. Scale bar for A – D = 0.5 mm. Representative images are shown. E) Quantitative fibre volume analysis of 5 and 10 µm PCL fibres inside conduits based on micro-CT images using the micro-CT accompanied software or Fiji. No statistical differences were found between values (Two-way ANOVA with Tukey's multiple comparisons test). Experiments were performed three times independently. Values represent mean + SD.

Overall, these results showed that the fibre volume inside the conduits can be reproducibly controlled through the described weighing procedure of fibre bundles prior to threading.

4.4.6. Design of the *in vitro* testing setup

A setup was developed that holds NGCs with internal scaffolds in an upright position during assessment, so internal NGC scaffolds could be evaluated in *in vitro* cell cultures or in DRG cultures (schematic shown in Figure 46 A). The setup used a stainless-steel metal grid connected to a small polystyrene adapter. It can be seen in Figure 46 B that metal grids were placed in wells of a conventional 6-well plate with the adapter sitting perpendicular to the grid pointing up towards the well top. Conduits were secured to the adapters, where different conduit sizes could be investigated and the length of conduit used was only limited by the well height. Additionally, it is apparent from Figure 46 B that the stability and position of the setup remained unchanged after culture medium was applied to the well. The next section will now turn to the culturing of cells inside the conduits using this developed setup.

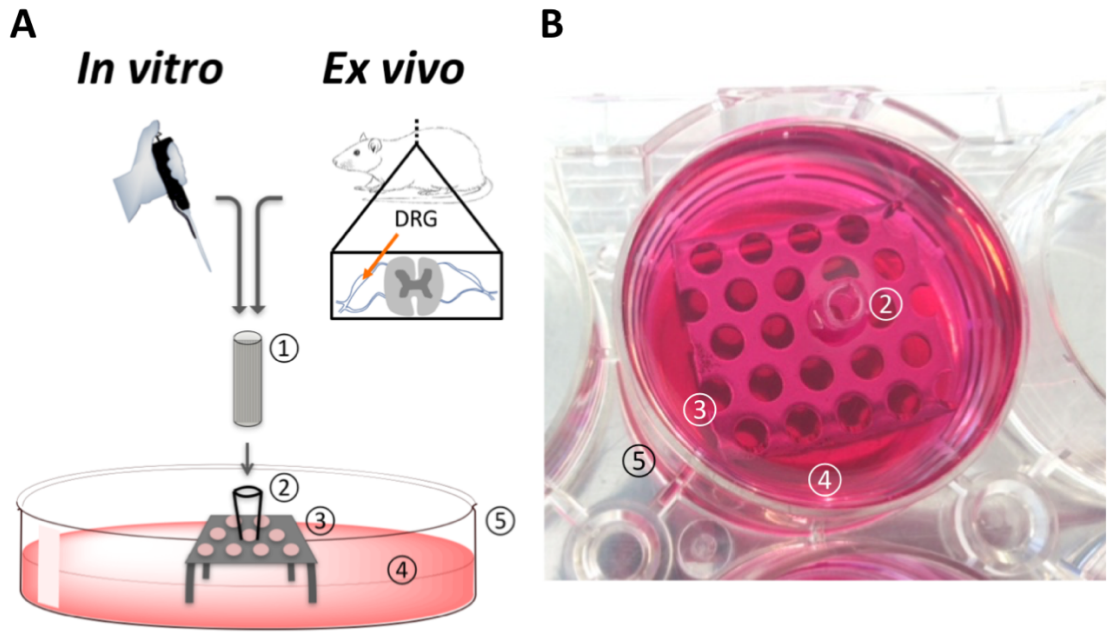

Figure 46 ***In vitro*** **culture setup**

Cell cultures were performed on fibre scaffolds inside conduits either using neuronal cells or DRG explants derived from adult rat spine placed on top of the conduit opening. A) Schematic of the designed 3D model setup to evaluate fibre scaffolds in conduits in conventional cell cultures or in *ex vivo* DRG cultures. B) Photograph of the experimental setup. The test NGC device (1) was fitted to a polystyrene adapter (2) and then to a stainless-steel grid (3). Grids were placed in wells of a commercial 6-well plate (5). For cell culture experiments, wells were filled with culture medium (4) until NGCs were covered.

4.4.7. Cell orientation analysis in the 3D nerve guide architecture

Before studying the biological performance of microfibre scaffolds inside conduits, a cell seeding technique needed to be developed to allow appropriate cell attachment and distribution throughout the fibre scaffold inside the conduits. Therefore, NG108-15 neuronal cells were seeded in PEG conduits with an internal 5 µm PCL scaffold using the described setup (Figure 47). The seeding procedure followed standard cell culture protocols by directly applying the cell suspension on the nerve guide scaffold without the need of a pump perfusion system for the supply of medium. NG108-15 neuronal cells were cultured in growth medium containing 10 % FBS for four days. The morphology of neuronal cells was investigated by revealing cell nuclei and cytoskeleton with DAPI and F-

actin-binding phalloidin respectively after fibre scaffolds were removed from conduits. Nuclei (blue) were always detected with a surrounding intact cytoskeleton (red) as demonstrated in the composite confocal images in Figure 47. This was noted for both neuronal cells on microfibre scaffolds (Figure 47 A) and on the TCP control surface (Figure 47 B). In monolayer, cells were randomly arranged and evenly attached to the TCP substrate (Figure 47 B). In Figure 47 A it is clearly demonstrated how neuronal cells changed their orientation when introduced to an aligned scaffold inside the conduit. Neurons attached along the fibres appearing as cellular bands with same directionality as the fibres (Figure 47 A).

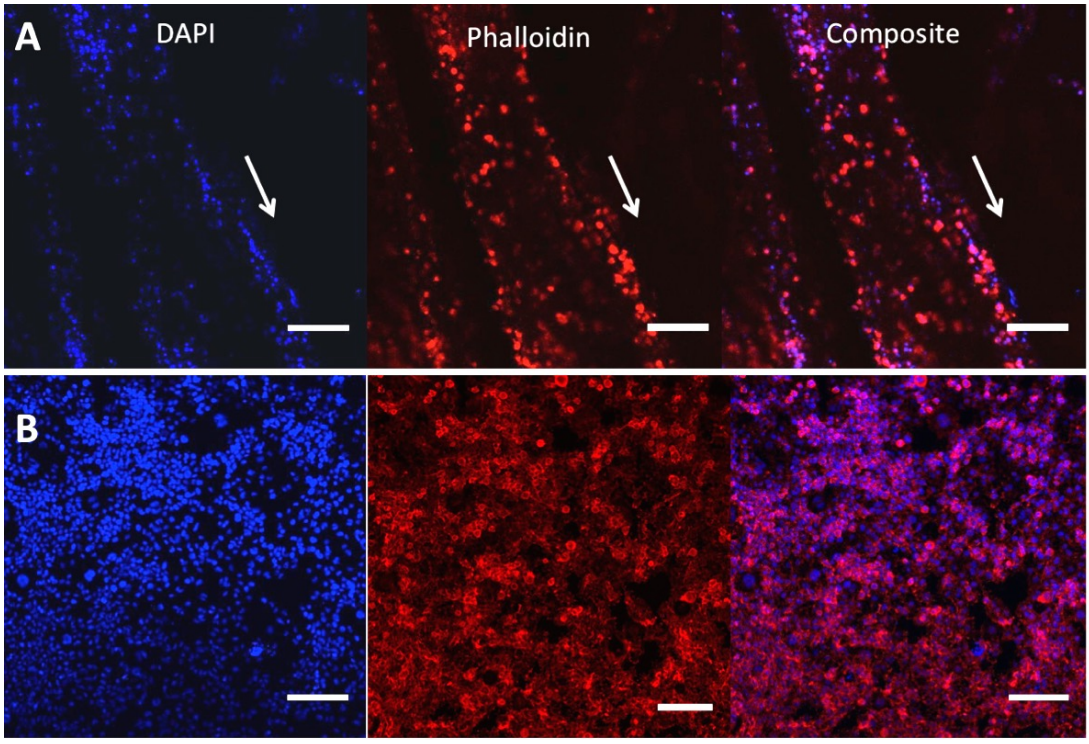

Figure 47 Neuronal cell alignment inside conduits with fibre scaffolds

NG108-15 neuronal cells were cultured in either PEG conduits with 5 µm PCL fibre scaffolds or on TCP. After 4 days of culture, neurons were labelled with F-actin-binding phalloidin-TRITC (red) and DAPI (blue) to reveal cytoskeletons and nuclei, respectively. Samples were imaged with confocal microscopy with scaffolds imaged in z-stacks. Images are presented as maximum projection images. A) Aligned neuronal cell orientation with fibre direction on 5 µm PCL fibre scaffolds after being removed from PEG conduits. B) Flat TCP substrate control with neuronal cells randomly orientated. Arrows indicate direction of microfibres in NGCs. Representative images are shown of three independent experiments. Scale bar = 20 µm.

After the successful identification of positive cell attachment to the fibre scaffolds inside conduits, the distribution of cells was investigated throughout different positions in the tube. Z-stack confocal microscopy was conducted in three positions on the scaffolds, at each of the scaffold ends as well as in the scaffold centre to reveal the multi-layered conduit architecture throughout the fibre bundle (Figure 48 A). Z-stack images were stacked and presented as 3D projection images in Figure 48 B. In all three positions imaged, neuronal cells attached along the microfibres in an aligned arrangement. Despite the presence of neurons on the entire fibre scaffold surface, cells also attached to the different fibre layers illustrated in the 3D projections (Figure 48 B). Aligned neuronal attachment was detected both throughout the length of the scaffold (illustrated by images taken on three different positions) as well as in the scaffold core (illustrated by single images) (Figure 48 B).

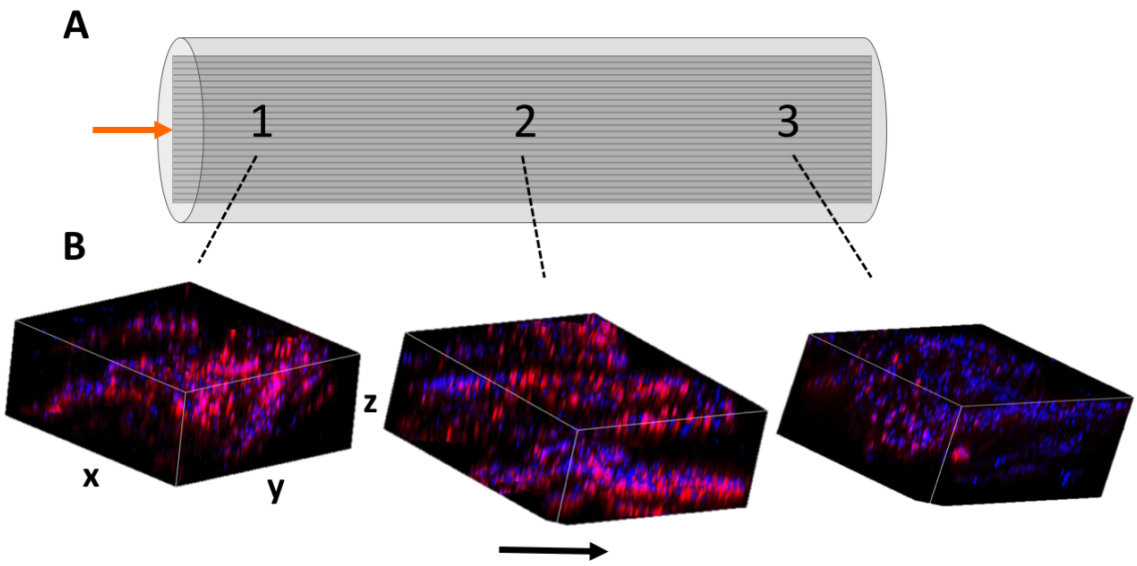

Figure 48 Neuronal cell distribution on fibre scaffolds in conduits

NG108-15 neuronal cells were cultured on 5 µm PCL fibre scaffolds inside PEG conduits. After 4 days of culture, scaffolds were removed from conduits and neurons labelled with F-actin-binding phalloidin-TRITC (red) and DAPI (blue) to reveal cytoskeletons and nuclei, respectively. A) Orange arrow indicates cell seeding position in conduits. Confocal microscopy images were taken in three positions (indicated by numbers) and demonstrated in B) as 3D z-projection images. Arrow indicates the direction of microfibres in the NGCs. Images in B) are representative of three independently performed experiments.

Together, these results provide insights into neuronal attachment, alignment and distribution on PCL microfibres incorporated into NGCs when using the reported culture model.

4.4.8. Cell viability on fibre scaffolds in NGCs

It has been shown that cells could be successfully seeded in the conduits with cells present throughout the three-dimensional fibre scaffold. Although cytoskeletons appeared intact and undamaged after seeding, a more detailed analysis was conducted regarding the viability of seeded neurons. Therefore, a comparative overview staining of live and dead neuronal cells was conducted between cells on PCL microfibre scaffolds inside conduits (Figure 49 A) and on monolayer PCL films (Figure 49 B) and TCP (Figure 49 C). It was noted that neurons in the centre of PCL fibre scaffolds and on TCP were predominately alive with only a few dead cells apparent (Figure 49 A and C). Although of the same material, neurons on PCL films showed an increased number of dead cells in comparison to cells on PCL scaffolds (Figure 49 B). Additionally, it was noted that neuronal cells appeared as aligned cellular bands along the fibre scaffold (Figure 49 A), where cells on TCP and PCL films lacked this directionality and rather appeared randomly distributed and partially clustered. Further quantification analysis confirmed the above observations and results were summarised in Figure 49 D. The greatest number of living cells was seen on PCL fibre scaffolds and TCP with 91 ± 4.7 % and 92.8 ± 2 %, respectively. The number of living cells on PCL films measured 85.6 ± 3.9 %. No statistical differences were detected between samples.

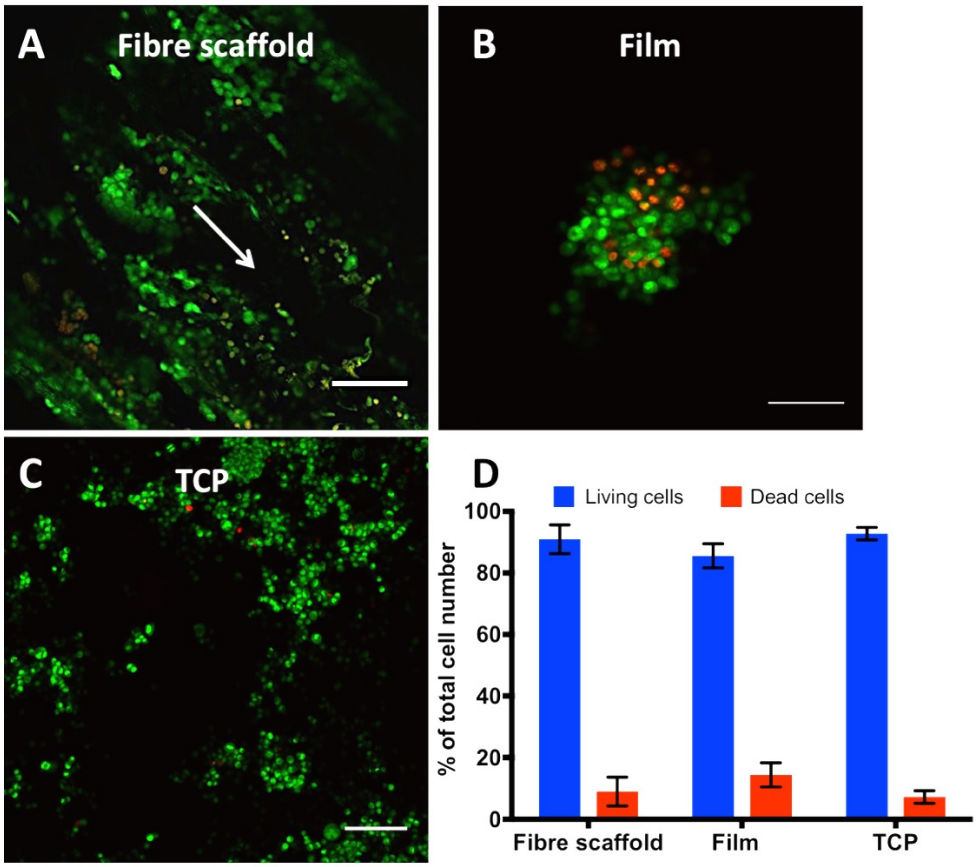

Figure 49 Overview of live and dead neuronal cells on fibre scaffolds in conduits

NG108-15 neuronal cells were seeded on A) 5 µm PCL fibre scaffolds inside PEG conduits in numbers of 6×10^5 or on flat substrates of B) PCL films or C) TCP in number of 2×10^4. After 4 days of culture, cells were labelled with Syto9 and propidium iodide to reveal living (green) and dead cells (red), respectively. Samples were imaged with confocal microscopy, where fibre scaffolds were captured in the middle of the scaffold in z-stacks. Images were illustrated as maximum projection images. Arrow indicates the fibre orientation in NGCs. Representative images are shown of three independently repeated experiments. Scale bar = 150 µm. D) Quantitative analysis of live and dead cell distribution on fibre scaffolds inside conduits, PCL film and TCP, demonstrated as a percentage of total cell number. No significant differences were detected between data points of living or dead cells, measured by Two-way ANOVA with Tukey's multiple comparisons test. Values show mean ± SD of three independent experiments.

4.4.9. Neurite outgrowth on fibre scaffolds inside NGCs

In this experiment, the ability of neuronal cells to grow and extend neurites on fibre scaffolds inside NGCs without the use of a medium perfusion system was investigated. In order to evaluate neurite outgrowth, NG108-15 neuronal cells were seeded on 5 µm PCL

fibre scaffolds inside PEG conduits using the described seeding and culturing method. Neurons were cultured under serum-deprived conditions to encourage the formation of neurites. After 14 days of culture, axons were visualised through axon-specific protein βIII Tubulin on the removed fibre scaffolds and imaged with light-sheet microscopy. Fibre scaffolds in its full length and in four different imaging positions can be seen in Figure 50. Through the rotation of scaffolds while imaging important information could be gathered regarding cell distribution, alignment and neurite outgrowth on the entire scaffold architecture. After the seeding of neurons at one end of the scaffold, neuronal cells distributed evenly throughout the scaffold length and all scaffold sides as apparent from Figure 50 A. Additionally, it is visible that cells attached successfully to microfibres inside the conduits showing alignment with fibre direction (Figure 50 A). It could further be confirmed that neurons successfully grew axons that extended along microfibres in the same direction as the fibre alignment (Figure 50 B). This was observed throughout the entire scaffold length and in all four positions imaged. The average neurite length measured 86.3 ± 11.4 µm.

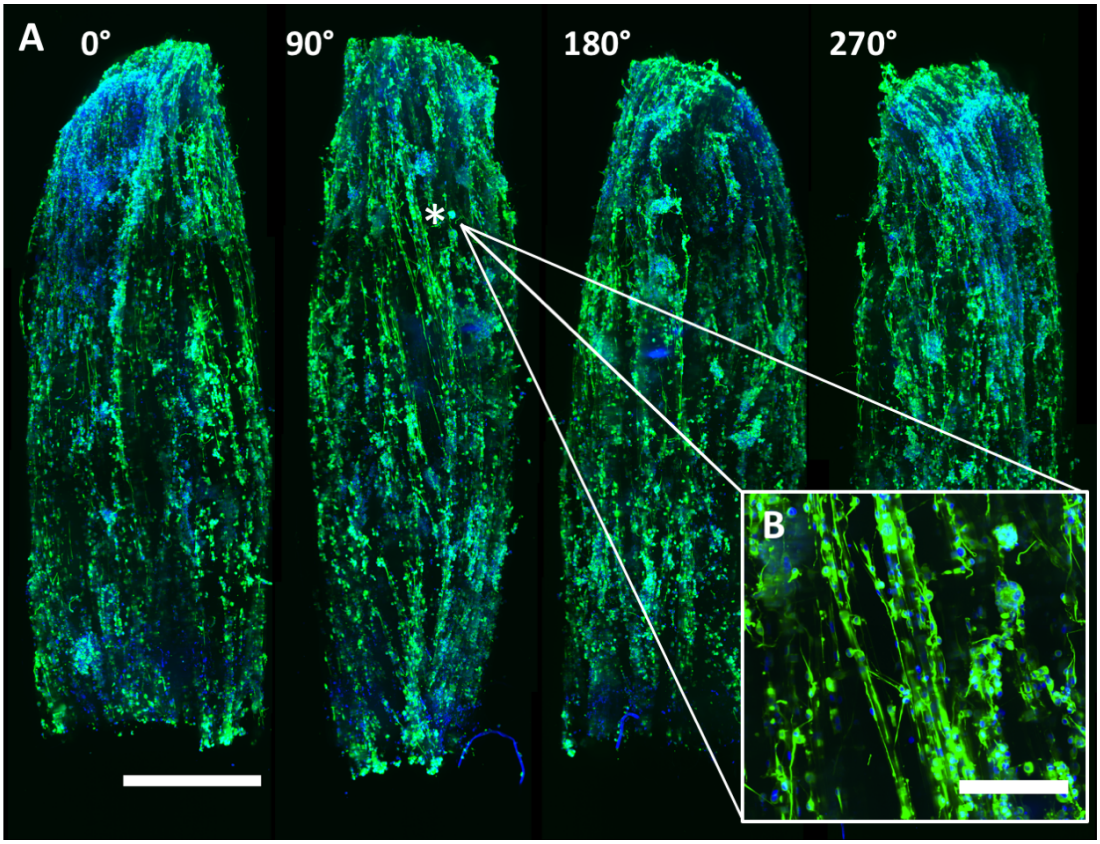

Figure 50 Neurite outgrowth on fibre scaffolds inside conduits

NG108-15 neuronal cells on 5 µm PCL fibre scaffolds inside PEG conduits with an initial seeding number of 6×10^5 after 21 days of culture. Serum-free medium was used to initiate the formation of neurites. Removed scaffolds were immunolabelled for axon-specific protein βIII Tubulin (green) and nuclei visualised with DAPI (blue). Scaffolds were imaged by z-stack light-sheet microscopy in Multiview's to capture the entire scaffold length with a rotation of the scaffold every 90° to capture the entire scaffold. A) Maximum projection images with Multiview's stitched together to one image showing neurite outgrowth (green) at four scaffold angles (0° – 270°). Scale bar = 1 mm. B) Magnified view of axon outgrowth at the position indicated by the asterisk on the fibre scaffold sample. Scale bar = 200 µm. Representative images are shown from three independently performed experiments.

4.4.10. *Ex vivo* dorsal root ganglion culture

In order to simulate the proximal nerve stump after injury *in vitro*, rat dorsal root ganglia were used and placed on top of the example NGC device for investigations on internal scaffold performance. Schwann cells and axons grew along the microfibre scaffold from

the explant towards the tube end (illustrated in Figure 51 A). In order to analyse the cell outgrowth distance from the DRG body towards the tube end, the fixed PCL microfibre scaffold was removed from the conduit after 21 days of culture and Schwann cells labelled for S100β (green fluorescent signal) and axons for βIII Tubulin protein (red fluorescent signal) (Figure 51 B). Both axons and Schwann cells grew out away from the DRG body in an aligned manner along the microfibres (Figure 51 B). It was furthermore apparent from Figure 51 that only a small number of axons and Schwann cells grew out. Schwann cells were detected in close relation to each other, which was visible through the overlay of green and red fluorescence appearing in a yellow-orange colour (Figure 51 B). As a result, the performance of the designed setup and dissection method was evaluated. First, it was investigated whether DRGs successfully attached to the conduits and second, whether cells grew out from the DRG body. As shown in Figure 51 C, 47.1 ± 27.6 % of DRGs attached to the conduits without detaching when medium was applied afterwards. Cell outgrowth from DRG explants was detected distal to the explant in 27.6 ± 4.1 % of all DRGs (Figure 51 C). In comparison to the number of attached DRGs, cell outgrowth from DRG explants was shown to be less likely, which was confirmed statistically, where significantly less DRGs showed an outgrowth of cells than DRGs attached. The distance that neuronal and Schwann cells infiltrated into the conduit was defined as the last detectable signal seen distant from the DRG body. The distance of outgrown cells was of particular importance as demonstrating the microfibres efficiency to support cell infiltration in a simulated nerve lesion *in vitro*. Schwann cells migrated and proliferated on average 2.2 ± 0.8 mm along the aligned microfibre scaffold inside the NGCs, where neuronal cells showed the extension of axons by 2.1 ± 0.8 mm (Figure 51 D). Together, Schwann cells and axons infiltrated 43 % of the 5 mm long conduit *in vitro* in 21 days.

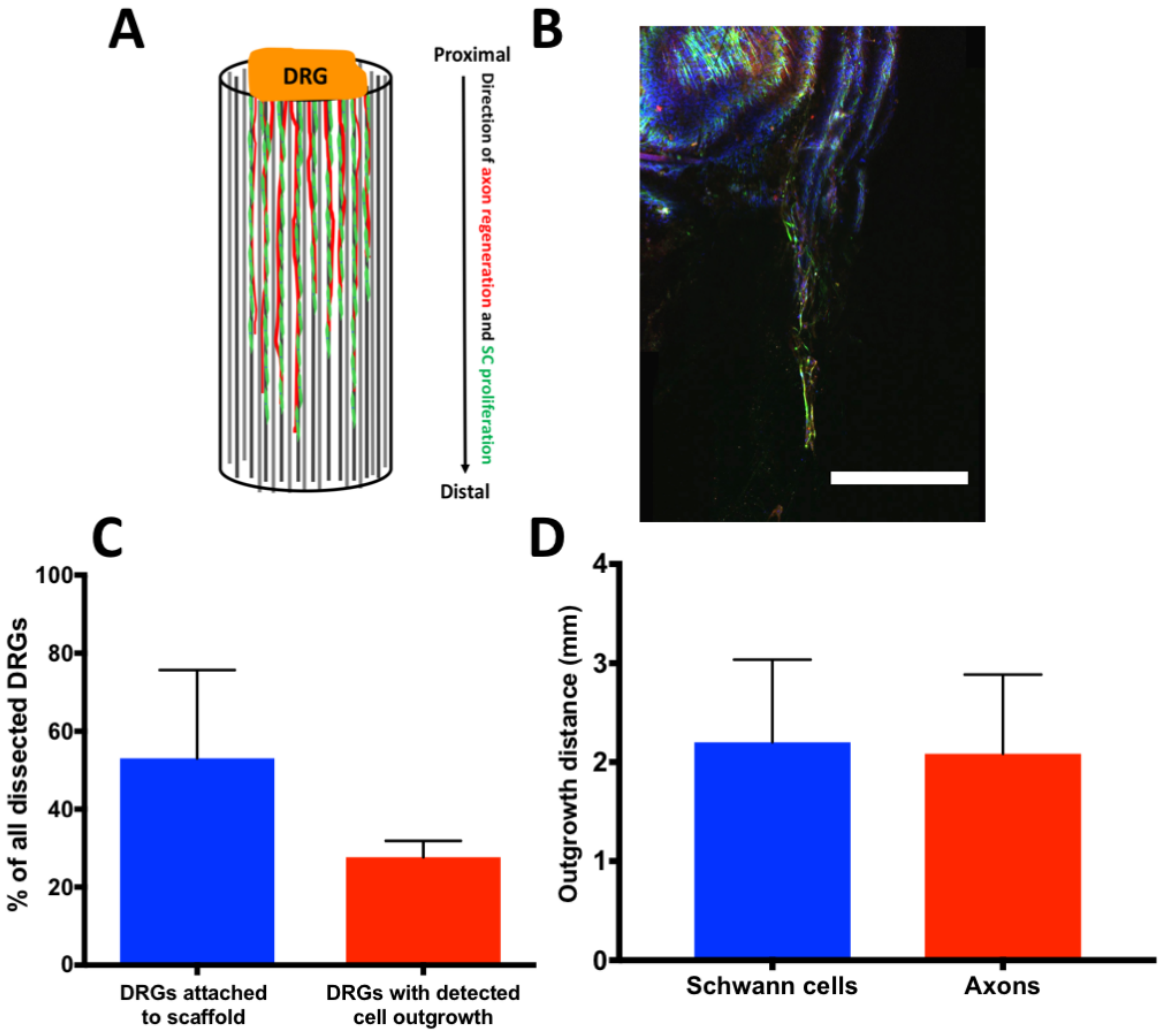

Figure 51 ***Ex vivo*** **evaluation of microfibres in whole nerve guides**

Rat DRGs were placed on top of PEG conduits which were filled with 20 % of 5 µm aligned PCL fibres. A) Graphical illustration of the outgrowth of proliferating/migrating Schwann cells (SC, illustrated in green) and the extension of axons from sensory neuronal cell bodies (illustrated in red) from the DRG body (proximal site) along the microfibres to the tube end (distal site). B) Confocal microscopy z-projection of DRG outgrowth of Schwann cells (labelled for S100β, green) and axons (labelled for βIII Tubulin, red) along PCL microfibres in an NGC. Representative images are shown of three experiments. Scale bar = 1 mm. C) Quantified measurements of attached DRGs to fibre scaffolds and attached DRGs with a detected cell outgrowth distal to the DRG body expressed as a percentage of all dissected DRGs. Values are displayed as mean + SD. N=3, n=4. D) Quantification of axon and Schwann cell outgrowth on the fibre scaffold measured as the last detectable cell-specific signal distal to the DRG body. Values demonstrate means + SD. N=3, n=4.

4.5. Discussion

4.5.1. An *in vitro* peripheral nerve model

This chapter reports on the development of an *in vitro* peripheral nerve model to organise axon and Schwann cell alignment in either neuronal mono-cultures or in primary DRG co-cultures. A device for the multi-level culturing of cells was developed and its reproducibility, as well as cell viability and orientation in the device, examined using z-stack microscopy. This *in vitro* approach results in a more representative model that replicates neuron and Schwann cell organisation similar to that in native peripheral nerve.

Three-dimensional cell culture models present a "closer-to-*in-vivo*" environment with higher physiological relevance than standard monolayer cultures. Due to the presented microenvironment that is similar to the native three-dimensional structure in tissues and organs, 3D *in vitro* models are of increasing interest for studying fundamental and applied biological mechanisms in trauma, disease or drug testing (reviewed in [258]). Although 3D models are in increased demand, only little data has been reported on such models for peripheral nerve (see section 1.17.1).

Herein, microfibres were used as a support scaffold to organise the alignment of cells on multiple levels inside tubes to replicate the three-dimensional nerve architecture. This study set out with the aim to fabricate a model device comprising a tubular outer structure with an internal aligned microfibre scaffold. The current study showed that the alignment of electrospun PCL microfibres inside tubes was retained when threaded using the developed fibre threading technique. This supports previous work which demonstrated fibre alignment inside conduits [135, 145-148, 153]. However, those results are different from the herein developed technique in a number of respects. It was noted that previous studies could not achieve incorporation of individual and separate single microfibres inside conduits as it has been shown here, where fibre bundles or filaments of diameters ranging from 20 to 80 µm were used instead [135, 145-148, 153]. Furthermore, the majority of the studies have been unable to demonstrate the validation of fibre densities inside conduits [145-147]. Only Ngo *et al.* validated the density of fibres through conduit cross-sections, however, they were not able to predict those densities

before the incorporation of fibres [153]. In comparison, this study showed that fibre volume could be reproducibly and precisely controlled in the tube structure using a method based on fibre weight. Micro-CT presented a useful tool to validate fibre densities inside conduits in a non-destructive way which is particularly helpful when analysing 3D devices before conducting *in vitro* or even *in vivo* studies. Examinations of peripheral nerve fascicles have benefitted from micro-CT imaging in the past [312], although it has never been reported for analysing topographies of artificial 3D nerve constructs. Therefore, these findings go beyond what has previously been shown with important implications for studying peripheral nerve mechanisms *in vitro*. This may for example help us to study different nerve types with varying axon numbers *in vitro* by using similar fibre numbers in conduits as there are axons in nerves.

The second question in this research was whether the developed 3D nerve construct could be used to organise and study neuronal cells and DRGs in three dimensions using an enclosed tube architecture. In reviewing the literature, no data was found on the direct culturing of neuronal or glial cells in such nerve-like devices. There has been one study which successfully reported on the organisation of axons and glial cells to form physical cellular interactions with the use of aligned fibres [152]. However, this model used flat fibre mats, which rather showed a primitive replicate of peripheral nerve structures as it failed to accomplish the detailed hierarchical organisation of nerve components.

Herein, two approaches are presented to organise cells using either a cell seeding or DRG culture method. The first achieved neuronal cell organisation by seeding cells inside the complete nerve construct due to cell attachment along aligned microfibres. As cells attached to several fibre layers throughout the tubes, an *in vitro* 3D model was built. Results revealed that the developed fibre scaffold supported the controlled growth of neuronal cells inside conduits with no cytotoxic effects detected. Neuronal cell viability remained high (more than 90 %) after seeding cells inside the conduits, which was no different to the measured viability on control surfaces. Those viability rates correlated to those on 5 µm PCL fibre mats shown earlier (Chapter 3) and those from Daud *et al.* [152]. This further points out that the nearly twenty-times higher cell concentrations used here, as well as the culture of neurons in an enclosed tube, did not affect cell viability rates.

Additionally, this exceeds findings of previous studies, which either did not test for neuronal viability in 3D scaffolds or conducted testing in a culture system with less physiological relevance, where cells had unlimited access to culture medium and were completely surrounded by it [152, 265, 266]. Although not directly tested, it could conceivably be hypothesised that the centre of the scaffolds herein contained sufficient nutrients and oxygen to maintain neuronal cell viability. Therefore, this achievement is of specific importance as the delivery of necessary nutrients to the scaffold core is still a challenge when designing 3D *in vitro* models (reviewed by [260]). Herein, this was achieved without the need for perfusion systems or bioreactors to supply medium inside the scaffolds, which was of additional economic value due to saved costs and time for pump and reactor setup.

Neuronal cells were found evenly distributed throughout the fibre scaffold inside the conduits, this suggests the seeding medium was able to infiltrate throughout the inside of the conduits. These findings suggest that fibre diameter, orientation and density inside the conduits supported the infiltration of liquids. The conduit interface, where fibres were cut with scissors, additionally proved to positively support the penetration of medium inside conduits. This further emphasises the importance of fibre alignment and density which both determine a successful ingrowth of cells by providing enough space in-between fibres and preventing fibre clumping which might cause ingrowth blockages. In accordance with the present results, Li *et al.* found a similar even distribution of cells after seeding Schwann cells on PLA fibre bundles using conventional cell seeding techniques [313]. This highlights that traditional cell seeding methods which are commonly used for the culture of cells in monolayers can be equally used for the seeding of cells in more complex 3D structures. The even distribution of cells inside conduits therefore set the basis for engineering a peripheral nerve replica, where cells adhered and grew in a longitudinal device to make up a nerve-like structure. Furthermore, it was shown that the proposed 3D nerve construct supported the aligned outgrowth of neurites from neuronal cells inside the conduits. This correlates with previous studies which showed a robust neurite outgrowth when neurons were maintained in a three-dimensional environment [152, 266, 314]. However, those studies were unable to demonstrate such outgrowth in an enclosed tubular nerve-like environment as shown here. The aligned outgrowth of neurites herein was supported by the aligned fibres

inside conduits (the ability to guide cells through fibre alignment has in detail been addressed in Chapter 1). This alignment was crucial in order to create an *in vitro* peripheral nerve model. Herein, fibres allowed the replication of neurite orientation as in native peripheral nerves, where axons aligned in parallel directions to each other without being in direct physical contact. These findings advance standard monolayer cultures and have important implications for studying more complex cellular and molecular nerve mechanisms *in vitro*.

Such aligned outgrowth was not only achieved in neuronal mono-cultures but also in more complex primary DRG co-cultures. From the DRG body, axons and Schwann cells were observed to grow out along microfibres towards the tube end. DRGs as they were used herein presented a lucrative tool for replicating nerve structures *in vitro* as they demonstrated a primary multi-cell type source containing sensory neurons which were surrounded by satellite glial cells; Schwann cells and fibroblasts which were arranged in a collagen-dominant extracellular matrix [315].

Although the outgrowth distance of axons and Schwann cells reached more than 2 mm after 21 days, data needs to be interpreted with caution due to the small number of experimental repeats caused by a poor cell outgrowth incidence from DRGs of less than 30 % with only a small number of outgrown axons. The work herein proved that DRGs in general could be useful for establishing an *in vitro* peripheral nerve model but that whole DRG explants from adult rats were not a suitable choice as they resulted in a small number of replicates that compromised data interpretation. The use of adult rat DRGs would further require a greater number of sacrificed animals in order to account for the high failure rate of DRG outgrowth which strongly disagrees with the scope of the 3Rs. Interestingly, the evident limitations of cell outgrowth from adult rat DRG explants were not mentioned in other publications but the predominant use of DRGs from embryos or pups might indicate that others encountered similar issues. It furthermore needs to be mentioned that the analysis of cell outgrowth distances from confocal microscopy images was limited to features on one sample side and could not capture the entire fibre scaffold. Hence, hidden axons and Schwann cells on the scaffold back were not accessible and could not be included in the analysis. Although those limitations exist, confocal microscopy remains the standard commercial imaging technique for visualising

moderately thick 3D specimens [236] and has been used by a number of authors for axon outgrowth analysis in 3D constructs [271, 273, 274].

Additionally, a co-localisation of Schwann cells and axons was detected in DRG cultures. This outcome may be explained by the aligned microfibre scaffold inside conduits which brought axons and Schwann cells in close contact to each other as a consequence of growing on the same fibre. This *in vivo*-like phenomenon has been replicated in culture before [150, 152] but could not be achieved in a sophisticated similar-to-nerve-architecture as shown herein. This direct physical interaction of Schwann cells and axons can also be found in native healthy peripheral nerves which has been shown to be essential for the formation of myelin in Schwann cells controlled via neuregulin-1 and Necl4 [316, 317]. The present study therefore fulfilled the mandatory requirements to develop a myelinated nerve model *in vitro* in the future which could be used to explore mechanisms on myelin formation and disruption caused by injury or disease. The latter in particular would be of great benefit to study cellular and molecular pathways that trigger neuropathies caused by HIV, diabetes, chemotherapy, hereditary demyelination or inflammatory immune responses [318]. This DRG model could make further contributions to the discovery of new therapeutics for neuroprotection or the testing and validation of newly developed drugs. This could be particularly advantageous as current therapies predominantly focus on the management of symptoms, since mechanisms causing neuropathies are still poorly understood [318]. It has been shown before that DRGs are an ideal means to study neuropathies [318]. This research would further advance existing work by representing an enclosed sensory nerve-like structure. The replication of sensory nerves *in vitro* is of particular interest as sensory neurons are affected more severely by neuropathies than motor nerves [318]. Despite the study of neuropathies, the present work could also be used to study fundamental biological processes at the neuron-glial interface or for the development of treatments for peripheral nerve injuries.

4.5.2. A model for peripheral nerve regeneration

The replication of sensory nerves *in vitro* greatly profited from the use of DRGs, where cells grew out of and naturally built an aligned nerve-like organisation following mechanisms based on injury responses in peripheral nerve. With some refinements, this

model may be additionally used as a model for peripheral nerve injury and repair. The anatomical morphology of DRGs that were placed on top of conduits represented the proximal nerve stump in injury from which regeneration occurred. Maintaining the three-dimensional tissue structure of DRGs by using whole explants on top of conduits had additional benefits regarding the maintenance of cell function in DRG bodies as it had been shown that commonly used DRG dissociation cultures caused profound changes in the dissociated cells which raised caution for result interpretation [268]. Based on the presented model concept, nerve repair strategies could be developed like internal guidance scaffolds for hollow nerve conduits. PCL fibres of 5 µm diameter as used herein showed to have great potential as an internal NGC scaffold in nerve repair. A full discussion of the advantages and performance of PCL fibres in nerve repair lie beyond the scope of this chapter but have in detail been discussed in Chapter 3.

To this date, no commercial solution has been presented on an improved nerve guide with an internal scaffold to improve clinical outcomes of currently used hollow nerve guides. Although more and more NGC scaffolds have been developed, scaffold assessment has predominantly been conducted on a flat scaffold equivalent that comprised of the same material or surface structure but as a flat sheet, (e.g. [152, 319, 320]). A serious weakness with these studies, however, is the assumption that cell culture results obtained from flat two-dimensional substrates mirror the cellular performance of complex three-dimensional scaffolds. Such differences between 2D and 3D cultures have been pointed out by a large body of literature in the past [236, 254]. On the other side, a great number of developed NGC scaffolds were directly assessed in animal experiments, (e.g. [148, 321, 322]). Between both evaluation approaches there is a large gap in relation to ethics and physiological relevance. This outlined gap has been directly addressed in the present study which presented an evaluation platform for NGC scaffolds in a complex three-dimensional environment. Herein, conduits were used with dimensions that would fit a mouse common fibular nerve and therefore would be suitable for implantation in a 3 mm nerve injury model. This further highlights the future implementations of the developed system to correlate and compare *in vitro* results with *in vivo* performance as NGC scaffolds could be assessed in conduits that would be compatible with animal injury models. Furthermore, in this model, internal guidance scaffolds could directly be evaluated in newly developed conduits as well as in

commercial and FDA approved ones. This is mainly possible due to the model setup which comprised of two separate parts, the conduit and the internal scaffold where the latter could be removed from the conduit prior to analysis. With this fibre removal technique, z-stack confocal microscopy was conducted without the need for time consuming sample sectioning as described by Thevenot *et al.* [323]. Additionally, the intraluminal guide complexity was maintained where z-stack microscopy revealed Schwann cell migration and axon sprouting through the whole depth of the internal scaffold. Keeping the internal fibre scaffold and conduit separate would further enable the testing of different NGC scaffolds in the same NGC device using one experimental setup that would additionally ensure reproducibility of experiments. Previous research on NGC scaffold performance *in vivo* have been compared favourably to conduits without internal scaffolds and autografts [135, 290, 324, 325]. However, new designs have, for the most part, not been directly compared to previous generation NGCs, or to commercial nerve conduits. This indicates the need to understand the performance of various other NGC scaffolds in order to comprehensively define an optimal scaffold for nerve repair. The current study therefore suggests using DRGs to evaluate multiple scaffold structures inside the NGC in one experimental environment. This use of DRGs as an evaluation tool for peripheral nerve repair studies is not a new idea and has been presented by several research groups in the past [152, 271, 273]. However, the described *in vitro* assessment methods were mainly confined to the evaluation of a single internal NGC scaffold.

In the present study, one DRG was used to test one NGC *in vitro*. It is worth noting that multiple DRGs were dissected from one animal which allowed the testing of several NGCs by only sacrificing one animal. In comparison, direct *in vivo* implantations of all potential nerve repair scaffold candidates would use a greater number of laboratory animals as one animal can only be used to test one scaffold. The presented model may therefore act in terms of the reduction of the 3Rs in animal testing. This has not only advantages from an ethical point of view, but is also advantageous in terms of time and resources. However, the use of adult rat DRGs are still not optimal due to poor outgrowth rates from DRG explants. This limitation could be overcome through the use of DRGs from embryonic or neonatal sources which may show more favourable outgrowth potential.

Additionally, it has to be mentioned that no DRG culture, irrespective of the species or state of maturity, can mirror similar recovery rates to *in vivo* nerve regeneration as some major contributors such as the immune system, cannot yet be replicated in one *in vitro* culture system. Nevertheless, the presented model is to the author's knowledge the most recent state of the art platform for cross-comparing different NGC scaffolds in one experimental setup under controlled conditions. This study provides an important opportunity to advance the development of ideal nerve guides particularly in regard to internal scaffold design like fibre diameter and fibre density in the future.

4.6. Conclusion

This study was undertaken to design a 3D *in vitro* model of peripheral nerve and evaluate its support in orientating axons and Schwann cells as in native nerve tissue. The evidence from this study indicates that axons from either neuronal or DRG explant cultures can be orientated along aligned microfibre scaffolds in a three-dimensional environment that mimics the epineurium by a conduit wall. This aligned outgrowth together with the detected co-localisation of axons and Schwann cells from DRG cultures advances standard monolayer cultures and can be used to study new treatments for neuropathies or nerve injuries.

The following conclusions can be drawn from the present study:

- Nerve guidance conduits from PEG diacrylate could be precisely manufactured using microstereolithography
- An even distribution of microfibres inside conduits was achieved through the developed fibre threading technique that used a twisted “fibre needle” while fibres maintained their initial alignment inside the conduits
- The use of conventional scissors for trimming fibre ends in conduits maintained the even distribution of fibres in the conduit
- Fibre densities inside conduits could be reproducibly controlled using a method based on fibre weight
- Conduits with internal fibre scaffolds could be secured in an upright position in conventional well plates for cell cultures
- Neuronal cells distributed evenly throughout an aligned fibre scaffold inside conduits when a conventional cell seeding approach was used
- Neuronal cells orientated along fibre alignment on scaffolds inside conduits
- Cell viability was maintained when seeded on fibre scaffolds inside conduits

- Fibre scaffolds inside conduits supported the outgrowth of axons and orientated processes to aligned bands along fibre direction
- DRGs mirrored the proximal nerve stump after nerve injury, where the outgrowth of axons and Schwann cells inside the conduit could be measured
- Cell outgrowth incidence from adult rat DRGs was poor with more than two-thirds of DRGs failing to grow out, resulting in little data for analysis.
- Fibre scaffolds inside conduits encouraged the co-localised positioning of axons with Schwann cells

Chapter 5 Air plasma treatment of PCL scaffolds

5.1. Introduction

There is no doubt about polycaprolactone (PCL) being a highly suitable material for tissue engineering and medical device applications, which is especially highlighted by its degradable properties and biocompatibility. Medical products from PCL, have furthermore received Food and Drug Administration (FDA) approval and Conformité Européenne (CE) marking which gives confidence to an accelerated avenue to the market for newly developed medical PCL devices. The latter is of particular importance considering the many existing barriers and hurdles between the concept of a medical device and its translation to the clinic [326].

PCL, however, suffers from one major drawback: It's hydrophobicity which compromises the desired interaction between the cell and the biomaterial [176]. A consequence of this has been previously mentioned in Chapter 3, which found a significant reduction in primary Schwann cell adhesion to PCL substrates in comparison to the tissue culture polystyrene (TCP) control (see Figure 35). Other studies have reported a similar impact of PCL's hydrophobicity on cell adhesion and behaviour [222, 223]. More recently, literature has emerged that offers a solution to this problem by chemically functionalising hydrophobic material surfaces via surface activation or wet chemistry approaches in order to convert the hydrophobic surface to a more hydrophilic one [199, 205, 208]. Surface functionalisation methods bear the main advantage of having limited penetration depths which ensures a restricted surface effect while maintaining the material's bulk properties [230]. In this regard, gas plasma treatment and in particular air and oxygen plasma, have been popular choices. The most commonly known example on the use of oxygen plasma treatment is polystyrene lab-ware which includes well plates, culture flasks and Petri dishes which demonstrate the standard growth substrate for cell cultures in monolayers. Considering the significant enhancements seen on protein and cell adhesion to biomaterials after air or oxygen plasma administration [218-221] this work suggests using air plasma treatment on PCL fibres to enhance the wettability of PCL and achieve an enhanced cell-material interaction. This study hence hypothesised that air plasma-modified nerve guides with internal PCL fibre scaffolds will improve the

regeneration outcome in comparison to unmodified PCL fibre scaffolds and therefore could realistically address the unmet clinical need on critical nerve gap regeneration.

In this study, air plasma treatment was used to modify the surface of PCL. The following factors led to this decision: First, plasma treatment bears great benefits regarding the chemical modification of entire implant surfaces, where the whole fibre-filled nerve guide can chemically be modified within seconds. In contrast, wet chemistry approaches involving several "dipping" or coating steps carry the risk of incomplete liquid penetration in the conduits due to PCL's hydrophobicity and might result in incomplete or uneven surface modifications. If successful, the latter bears the chance of undesirable chemical residues in the device. Second, plasma treatments are performed on dry samples in comparison to other wet chemistry approaches where the fibre alignment within the conduits might be affected in particular by the many washing/coating steps. Third and finally, air plasma systems are commercially available which brings benefits in regard to processing time and simple use, and are due to the low processing temperatures suitable for modifying low-melting polymers such as PCL. Furthermore, the use of air plasma is safe and can be performed on the laboratory bench without requiring fume extraction systems.

Although plasma treatment on polymer surfaces has seen great success in the past, its application has predominantly been demonstrated on flat 2D substrates. Only a few authors applied gas plasma to three-dimensional scaffolds and hence more relevant surface structures for tissue engineering applications. Two reports of Armentano *et al.* and Chim *et al.* applied oxygen plasma to porous 3D PLA scaffolds which showed enhanced cell specific functions and attachment. However, chemical changes to PLA surfaces were only analysed on films and were not investigated in the scaffold core [327, 328]. Wan *et al.* further investigated this effect by measuring the penetration depth of ammonia plasma into 4 mm thick PLA porous scaffolds and noticed that prolonged plasma exposure was key for a sufficient surface modification in the scaffold core. However, those measurements were conducted qualitatively and surface chemical changes were not analysed [329]. Barry *et al.* additionally found that allylamine vapour penetrated entire porous PLA scaffolds which was confirmed by XPS. However, differences were found between allylamine grafting and deposition where grafting

included an additional surface activation step using oxygen plasma. The authors found that grafted amine groups were more homogeneously present within the 10 mm long and 3 mm thick scaffolds. The deposition method, however, showed an increased nitrogen concentration on the scaffold edges which was about four times higher than in the scaffold middle. However, the lowest nitrogen concentration found on deposited scaffolds was still greater than on grafted scaffolds [330].

This study set out to investigate the effect of air plasma on PCL films and how this change was demonstrated chemically. This formed the basis for further in-depth studies to explore the penetration depth of air plasma into fibre-filled nerve guides. Furthermore, the biological responses of Schwann and neuronal cells on air plasma-modified PCL films were evaluated. The latter was performed on films in order to provide best comparability between flat TCP and flat film surfaces. In this particular application, TCP demonstrated an ideal control surface as it is recognised as the gold standard substrate for monolayer cell culture and also represented a commercial air/oxygen-modified surface.

5.2. Aims & Objectives

Although extensive research has been carried out on protein and cell responses to air or oxygen-modified polymers, it is not yet clear how this treatment would impact the performance of PCL guidance scaffolds in peripheral nerve repair. It was therefore hypothesised that air plasma treatment of PCL would increase PCL's wettability and cause a positive change in neurite outgrowth and Schwann cell activity. It was believed that those introduced chemical changes may be critical for enhancing the performance of internal NGC PCL fibre scaffolds in nerve regeneration. This study further aimed to provide insights on storage conditions of air plasma-modified nerve guides by exploring the effect of different storage media on PCL wettability.

Therefore, the following objectives were addressed:

- Assess whether air plasma treatment affects the contact angle of PCL films
- Examine the change in surface elemental composition of air plasma-modified PCL films
- Investigate the effect of air plasma treatment on surface elemental composition of PCL fibre bundles inside PEG conduits
- Observe how different storage media affect the wettability properties of air plasma-modified and unmodified PCL films
- Assess whether air plasma-modified PCL films cause a change in neurite incidence and outgrowth in NG108-15 neuronal cells
- Measure the change in metabolic activity of primary rat Schwann cells when introduced to air plasma-modified PCL films

5.3. Materials & Methods

5.3.1. Air plasma treatment

PCL films were fabricated as described in 2.7 and air plasma-modified as outlined in 2.8.

5.3.2. Water contact angle

Contact angle measurements were performed with a Krüss drop shape analyser (model DSA100, Krüss GmbH, Germany) at room temperature. A 5 µL ultra-pure water (ELGA LabWater) droplet was deposited on the surface using a 1 mL plastic syringe with a stainless-steel needle (size NE44, Krüss GmbH). The syringe with needle was automatically withdrawn and a picture of the water droplet taken. The contact angle was measured on the captured droplet based on the sessile drop technique using the vendor-supplied software. Samples were analysed in duplicate, where three measurements per sample were taken.

5.3.3. Contact angle analysis on substrates stored in different conditions

Contact angle measurements were performed as outlined in 5.3.2 on PCL films which were stored under different conditions and TCP over a period of 29 days. PCL films were air plasma-modified as described in 2.8 and stored in PBS at 37 °C, in an ambient environment or in vacuum-sealed bags. Non-modified PCL films were stored in either PBS at 37 °C or in an ambient environment. Films stored in PBS were placed in a 50 mL centrifuge tube and covered with 25 mL of PBS. Samples stored in an ambient environment were placed in a 6-well plate on a work bench in the laboratory with the lid left open. Vacuum-packed samples were sealed with an Andrew James vacuum sealer (Andrew James, UK) using the accompanied Andrew James vacuum sealer bags. The bottom of a 35 mm^2 Petri dish was removed with a hammer and used as the TCP substrate control. Contact angle measurements were performed on day 0, 5, 12, 22 and 29. On day 0, initial contact angles of PCL films with and without air plasma treatment and TCP substrates were taken and samples exposed to chosen storage conditions thereafter. Wet samples were dried prior analysis. Two samples per condition were analysed, where three measurements per sample were taken.

5.3.4. XPS analysis

X-ray photoelectron spectroscopy (XPS) was performed by the EPSRC National Facility for XPS at Cardiff University (UK). Analysis was performed on PCL films and PCL fibre bundles. PCL films (see 2.7 for fabrication details) were air plasma-modified (see 2.8) or left unmodified, where analysis was conducted in the middle of the films. Electrospun 10 µm PCL microfibres (see 2.2 for fabrication details) were incorporated inside 5 mm long PEG conduits (20 % fibre density) and air plasma-modified or left unmodified. Fibre bundles were removed from conduits and XPS conducted on the fibre bundle ends and middle. Spectroscopy was performed on a K-alpha$^+$ spectrometer (Thermo Fisher Scientific). A micro-focused monochromatic Al X-ray source was used to analyse samples over an area of approximately 200 µm. Pass energies of 150 eV for survey scans and 40 eV for high resolution scans recorded data with a step size of 1 eV and 0.1 eV, respectively. A combination of both low energy electrons and argon ions neutralised sample charging. Data analysis was performed in CasaXPS using a Shirley type background and Scofield cross sections, with an energy dependence of - 0.6. Peak fitting was achieved using a Finite Lorentzian function. Full width at half maximum (FWHM) were between 1.1 and 1.5 eV depending on the samples and were typically measured from the FWHM of the C(1s) peaks at 289-290 eV.

5.3.5. Cell culture on air plasma-modified samples

NG108-15 neuronal cells and primary Schwann cells were cultured on PCL films (see 2.7 for fabrication details) which were air plasma-modified (see 2.8 for more information) or left unmodified. TCP demonstrated the control surface. PCL films were glued onto 1 cm^2 stainless-steel rings and sterilised thereafter as described in 2.3. Films were left to air dry in a sterile cabinet prior to cell seeding.

5.3.6. Neurite outgrowth on air plasma-modified samples

NG108-15 neuronal cells were trypsinised and counted as in 2.9.3 and 2.9.4, respectively. Cells were seeded in numbers of 2×10^4 inside 1 cm^2 stainless-steel rings in volumes of 500 µL in growth medium. After letting cells attach at 37 °C in a CO_2 incubator overnight, growth medium was replaced by serum-free growth medium to encourage the formation of neurites. After 5 days in serum-free medium, neurons were fixed and prepared for

immunocytochemical labelling as described in 2.12. As the primary antibody, a mouse anti-βIII Tubulin antibody (G7121, Promega) was used at a concentration of 2.5 µL/mL (1:400) for 48 h. For the secondary antibody, a donkey anti-mouse FITC antibody (A24501, Life Technologies) was applied at a concentration of 0.6 mg/mL. Cell nuclei were labelled with DAPI as described in 2.12. Samples were imaged using z-stack confocal microscopy as described in 2.17 and neurite length and incidence measured and analysed as defined in 2.10.1. All samples were prepared in duplicate and experiments repeated three times.

5.3.7. Schwann cell metabolic activity analysis on air plasma-modified samples

Primary rat Schwann cells were trypsinised and counted as mentioned in sections 2.9.3 and 2.9.4. Cells were seeded inside 1 cm^2 stainless-steel rings with 2×10^4 cells in 500 µL growth medium per ring. After 2 h of letting cells attach to substrates, the inside and outside of the rings was filled with growth medium. On day 1, 3 and 5, the metabolic activity of primary Schwann cells was measured using a resazurin reduction assay as described in 2.15. Each experiment was conducted in duplicate and repeated three times.

5.4. Results

5.4.1. Changes in PCL wettability after air plasma surface modification

Air plasma deposition was hypothesised to increase the outgrowth of regenerating cells in peripheral nerve injuries compared to PCL alone. In order to analyse the changes in surface wettability, the water contact angle of air plasma-modified and non-modified PCL films and TCP was compared. Test PCL films were air plasma-modified at 50 W for 60 s. The results obtained are shown in Figure 52 A. Native control PCL films showed an average water contact angle of 117 ± 4.4°. When plasma treatment modified the PCL surfaces, a significant change in the wettability behaviour of samples was detected. The application of air plasma decreased the contact angle of PCL by more than one third, where contact angles measured 78.8 ± 12.8° after deposition. This reduction in contact angle was measured to be statistically significant. Interestingly, water contact angles for TCP and plasma-modified PCL films showed equally low measures of 77.4 ± 9.1° and 78.8 ± 12.8°, respectively, where no significant differences were found between the two substrates.

Additionally, the stability of air plasma-modified surfaces was investigated under different storage conditions, where changes in water contact angles were monitored over a period of 29 days (Figure 52 B). Air plasma-modified PCL films were stored in physiological medium of PBS at 37 °C, on the usual work bench exposed to the surrounded environment or in vacuum-sealed bags. Non-modified PCL films, stored in PBS at 37 °C or on the work bench, demonstrated the control. TCP was additionally used as a control. Before applying the different storage conditions to substrates, TCP discs, non-modified PCL films and freshly plasma-modified films were measured for their initial contact angles. Similar to the results presented in Figure 52 A, TCP and PCL plasma-modified films both showed a significantly lower initial contact angle of 78.8 ± 12.8° and 77.9 ± 13.4°, respectively compared to non-modified PCL films with a contact angle of 114 ± 1.8° (Figure 52 B). As shown in Figure 52 B, the applied storage conditions influenced the surface wettability of substrates.

TCP and non-modified PCL films wettability remained unaffected by their surrounding environment, where contact angles measured 73.9 ± 0.6° and 114 ± 1.7°, respectively

after 29 days which was similar to initially taken measurements. Air plasma-modified films which were stored on the work bench or in vacuum-sealed bags, lost their wetting properties over time, where contact angles increased gradually and finally showed similar wettability properties, 112.6 ± 0° and 120.7 ± 4.5°, respectively, to native PCL films after 29 days. This change occurred faster when the air plasma-modified PCL films were stored in vacuum-sealed bags, where contact angles measured similar to non-modified PCL after 12 days. This effect was slightly delayed on plasma-modified films, which were stored on the work bench, where contact angles were similar to non-modified PCL after 22 days (Figure 52 B). Although, both plasma-modified PCL films showed initially significant differences to unmodified PCL films, no significant differences were found between the two modified films and unmodified films after 12 days.

Interestingly, the storage of both modified and unmodified PCL films in PBS over 29 days gradually decreased the contact angle by more than half compared to initial values. On day 12, contact angles on unmodified PCL films stored in PBS measured significantly lower than on unmodified PCL films that where left on the work bench. The water contact angles of plasma-deposited films in PBS dropped from 79.6 ± 1.2° to 35.2 ± 0.3° between day 5 and day 12. From there onwards, values stayed similarly low and finally measured 32.6 ± 5.1° after 29 days. This sudden drop in contact angle was also observed on non-modified PCL films, however, this change occurred at a much later time point of 22 days, where values dropped from 94.6 ± 5° on day 22 to 50.8 ± 0° on day 29. The measured differences in contact angle between modified and unmodified PCL films both stored in PBS was significant on day 12 and 22. Interestingly, on day 22, the measured contact angle for unmodified films stored in PBS showed no significant differences to TCP, unmodified PCL films and plasma-modified films stored on the work bench or in vacuum-sealed bags. On the other side, on day 22, modified PCL films stored in PBS showed a significant lower contact angle compared to all other measured substrates. Nevertheless, after 29 days, the contact angle on both in PBS stored PCL films were not significantly different to each other (Figure 52 B).

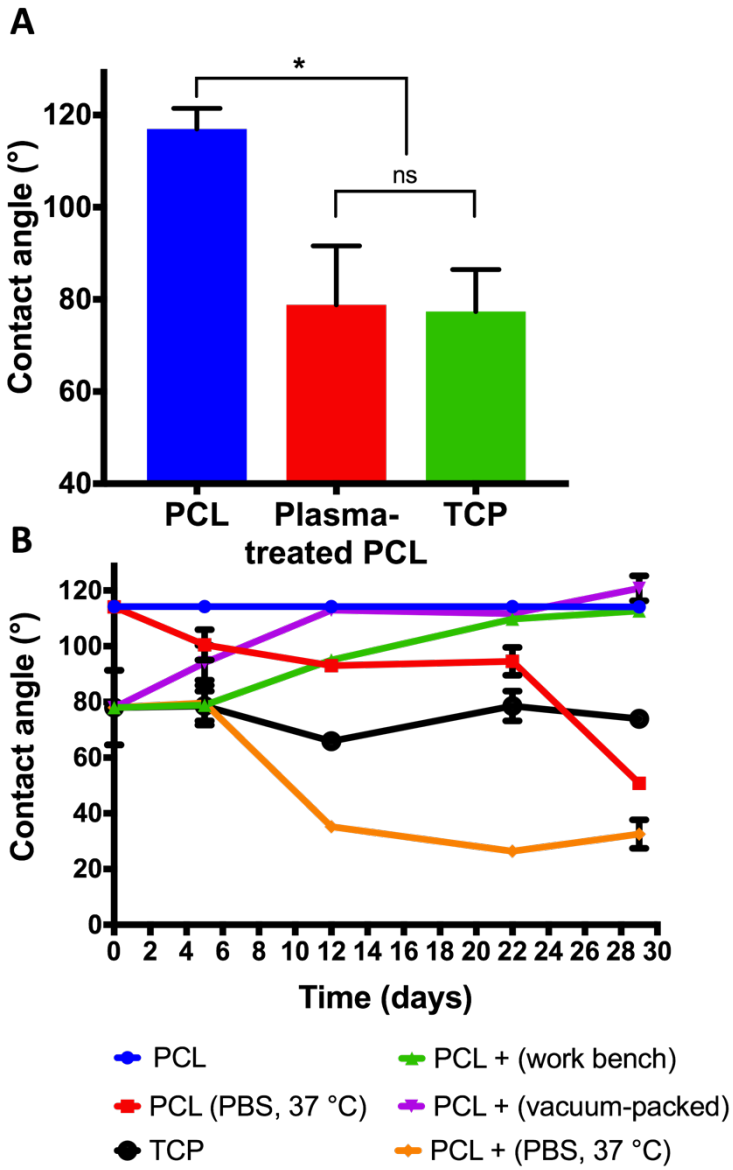

Figure 52 **Influence of air plasma treatment and different storage conditions on PCL's wettability**

A) Water contact angle measurements of air plasma-modified PCL films, unmodified PCL films and TCP immediately taken after plasma treatment. Data presented as mean+ SD. One-way ANOVA revealed significance if $p<0.05$. B) Water contact angle measurements over a period of 29 days of plasma-modified PCL films (PCL +) stored on the laboratory work bench, inside vacuum bags or in PBS at 37 °C and unmodified PCL films, stored in either PBS at 37 °C or on the work bench. TCP demonstrated the control surface and was stored on the work bench. Values are displayed as the mean ± SD. Statistical differences were analysed with two-way ANOVA (significant if $p<0.05$) and were indicated in the text above the figure (no illustration in the graph to maintain clarity). Both experiments were repeated three times independently.

5.4.2. XPS surface analysis of air plasma-modified PCL substrates

XPS was performed to evaluate the change in elemental composition on the surface of PCL films and microfibres due to air plasma deposition. The deposition of air plasma was performed for 60 s at 50 W and 0.4 mbar. Flat PCL films were used as a control substrate, where films were either air plasma-deposited or left unchanged. Aligned PCL microfibres of 10 µm in diameter were incorporated into 5 mm long PEG conduits and air plasma-deposited. Non-modified fibres inside conduits were used as a control. In order to evaluate the depth penetration of plasma inside the conduits, fibre bundles were removed from conduits prior to XPS analysis. On each fibre bundle, measurements were performed on three different positions, where both ends and the middle of the bundles were analysed. PCL film control samples were analysed in the centre of the films. CASA XPS software was used to quantify peak intensities and peak positions on XPS spectra. Narrow scans of the C1s and O1s regions revealed the presence and composition of carbon and oxygen on the PCL substrates. A maximum of five different peak positions in the C1s region could be identified: C-C (284.6 – 284.9 eV), C-C-O (285.2 – 285.4 eV), C(O)-O-C (286.4 – 286.6 eV), C=O (287.6 – 287.8 eV) and COO (288.8 – 289.2 eV) (Figure 54 A and Figure 54). The presence of oxygen could be identified at binding energies of 532.1 – 532.6 eV and 533.4 – 533.7 eV and corresponded with oxygen environments of C=O and C(O)-O, respectively (Figure 53 B, Figure 55). Wide scans additionally identified the presence of nitrogen at peak positions of 399.8 – 402.2 eV on particular samples. Figure 53 and Table 6 both compare the differences in elemental compositions between air plasma-modified PCL films and control films. Table 6 summarises the variation in percentage atomic concentrations between the two sample conditions. Herein, it is apparent that the overall amount of carbon in both samples accounted about 78 %, where oxygen made up 21 % of plasma-modified film surfaces and 22 % oxygen of non-modified samples (Table 6).

Table 6 Wide and narrow scan analysis of the C1 and O1 region on air plasma-modified and unmodified PCL films

Sample	Wide scan (%)			Narrow scan						
				C1s region (%)					O1s region (%)	
	C	O	N	C-C	C-C-O	C(O)-O-C	COO	C=O	C=O	C(O)-O
No Plasma	78.0	22.0	0	39.4	13.4	13.4	11.8	0	10.3	11.7
Plasma	78.3	21.0	0.7	29.8	24.0	12.5	6.3	5.7	11.7	9.3

Additionally, plasma-modified films contained 0.7 % nitrogen, where control samples did not show this presence. Although there was no change in overall carbon and oxygen amounts between the two sample conditions, notable changes were found in the arrangement of carbon and oxygen atoms. In the C1s region, most remarkable changes could be seen between C-C, C-C-O and COO bonds (Table 6 and Figure 53 A). Air plasma treatment decreased the concentration of C-C bonds, where 39.4 % of C-C bonds were initially present on PCL films and became reduced to 29.8 %. This can also be seen in Figure 53 A as a reduction in peak intensity at around 284.5 eV. On the other hand, the amount of C-C-O bonds has strikingly increased from 13.4 % on PCL films to 24 % on plasma-modified films (Table 6, Figure 53 A). Additionally, there was a sharp decrease in COO bonds from 11.8 % to 6.3 % on plasma-modified films. This decrease can also be seen in Figure 53 A, where the peak intensity at a binding energy of around 289 eV was reduced by about half when comparing control with plasma-modified films. Air plasma treatment also resulted in the formation of a new carbonyl (C=O) bond which was detected at binding energies of 287.6 – 287.8 eV and accounted for 5.7 % (Figure 53 A). Looking at the O1s region, changes can be seen in concentrations of C=O and C(O)-O bonds (Table 6 and Figure 53 B). Plasma treatment increased the amount of C=O bonds from 10.3 % to 11.7 %. Similar to what was found in the C1 region, the amount of C(O)-O bonds was reduced by air plasma treatment from 11.7 % to 9.3 %. The corresponding spectra in Figure 53 B shows that the C(O)-O corresponding peak at around 533 eV was

decreased in its intensity by about 20 % when comparing unmodified and plasma-modified films.

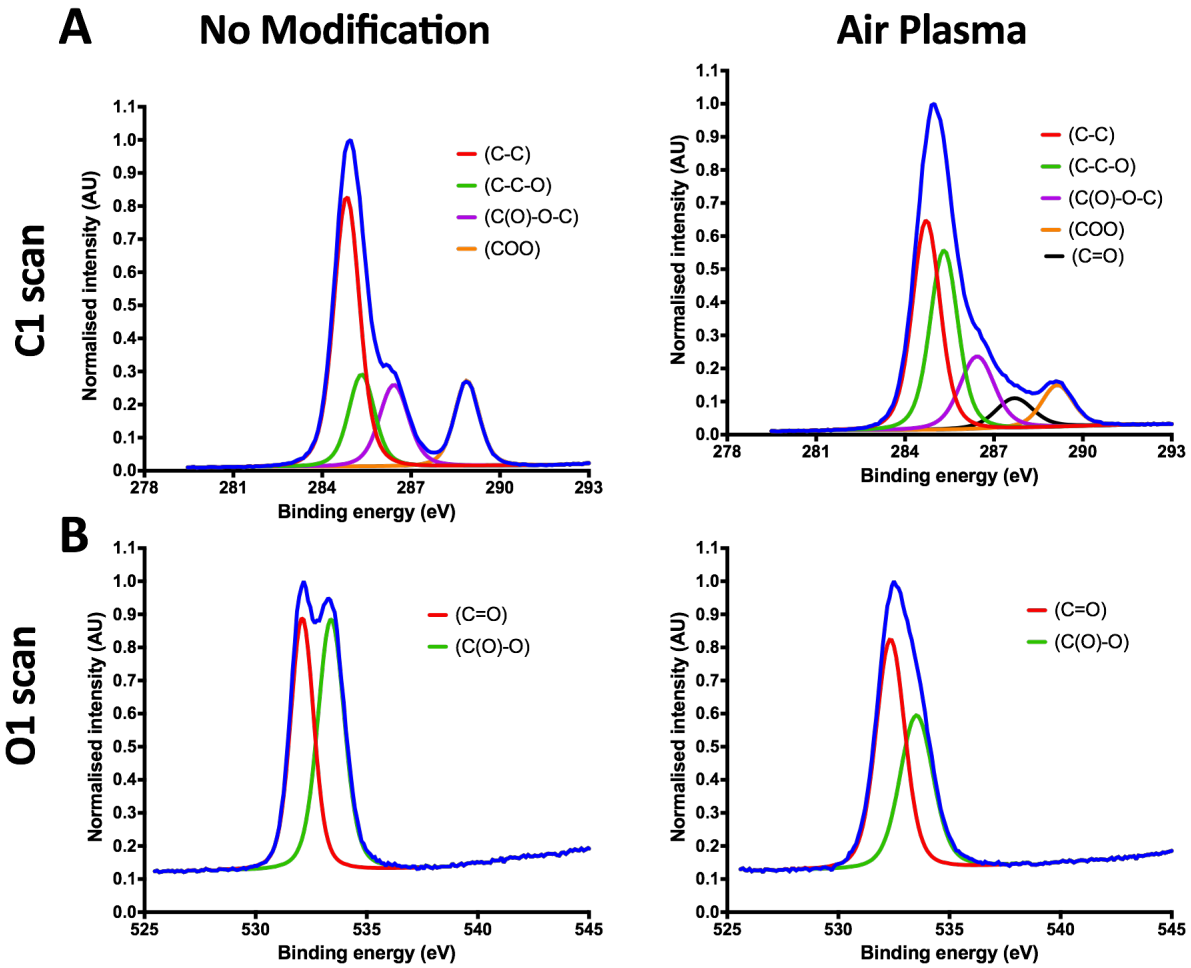

Figure 53 The effect of air plasma treatment on PCL films

Representative and normalised XPS spectra of unmodified PCL films ("No Modification") and air plasma-modified films ("Air Plasma") of the A) C1 and B) O1 region. Films were air plasma- modified for 60 s at 50 W and 0.4 mbar. XPS analysis was performed by the EPSRC National Facility for XPS at Cardiff University, UK. Analysis was conducted in the centre of two independently fabricated and air plasma- modified PCL films.

Table 7, Figure 54 and Figure 55 show the differences in elemental and chemical compositions between non-modified and plasma-deposited microfibres on three different positions on the fibre bundle. When comparing the results from Table 7, Figure 54 and Figure 55 with results from Table 6 and Figure 53, the same trend of changes in the C1s and O1s region can be seen. As shown in Table 7, the overall amount of carbon and oxygen remained unchanged when applying air plasma to microfibres. Carbon

accounted for 78 % elemental proportion on modified and non-modified fibre bundles, where proportions were similar at the ends and the middle of the bundles. On the contrary, total oxygen groups were reduced on plasma-modified microfibres, but consistent levels identified throughout the length of the fibre bundles. Microfibre controls contained around 20 % oxygen, where plasma-deposited bundles showed decreased levels of around 17 %. Similar to what was seen on PCL films, plasma-modified microfibres additionally contained nitrogen in quantities of about 1 % (Table 7)Changes in levels of C-C, C-C-O and COO bonds in the C1s region were as remarkable between control and plasma-deposited microfibres as described on PCL films. Spectra and percentage atomic levels are summarised in Table 7 and Figure 54.

Table 7 Wide and narrow scan analysis of the C1 and O1 region on air plasma-modified and unmodified PCL fibre bundles

Sample	Wide scan (%)			Narrow scan						
				C1s region (%)					O1s region (%)	
	C	O	N	C-C	C-C-O	C(O)-O-C	COO	C=O	C=O	C(O)-O
FB - #1	79.6	20.5	0	45.1	12.3	12.6	9.7	0	10.5	9.9
FB - #2	82.8	17.2	0	50.3	13.3	11.6	7.6	0	9.4	7.8
FB - #3	79.3	20.7	0	40.6	14.8	13.6	10.2	0	10.2	10.6
FB + #1	78.1	17.6	0.9	29.5	25.1	13.1	5.6	4.9	10.6	7.0
FB + #2	78.4	17.8	1.2	29.3	26.1	13.2	5.5	4.4	10.8	7.0
FB + #3	79.1	16.8	1.2	29.8	26.7	13.3	5.4	3.9	10.2	6.6

+ = Plasma
– = No Plasma
 # = Position on the sample (1 = top, 2 = middle, 3 = bottom)
FB = fibre bundle

A decrease in peak intensity at binding energies of around 284.5 eV and 289 eV for plasma-modified microfibres correlated with a loss of C-C and COO bonds in the plasma-modified samples. This decrease was identified for all three sample positions (Figure 54). Plasma deposition also caused a notable increase in C-C-O bonds and initiated the formation of a new C=O bond at around 287 eV (Figure 54). This change was observed on all three different fibre bundle positions (Figure 54 A – C). The arrangement of oxygen atoms in the O1s region of microfibre samples showed the same trend as on PCL films. A

slight increase in C=O bonds and a particular decrease in C(O)-O concentrations was observed on plasma-modified fibre bundles compared to non-modified samples throughout the length of the bundles (Table 7 and Figure 55). This decrease was also observed in a 20 % loss of peak intensity at binding energies of around 533 eV (Figure 55).

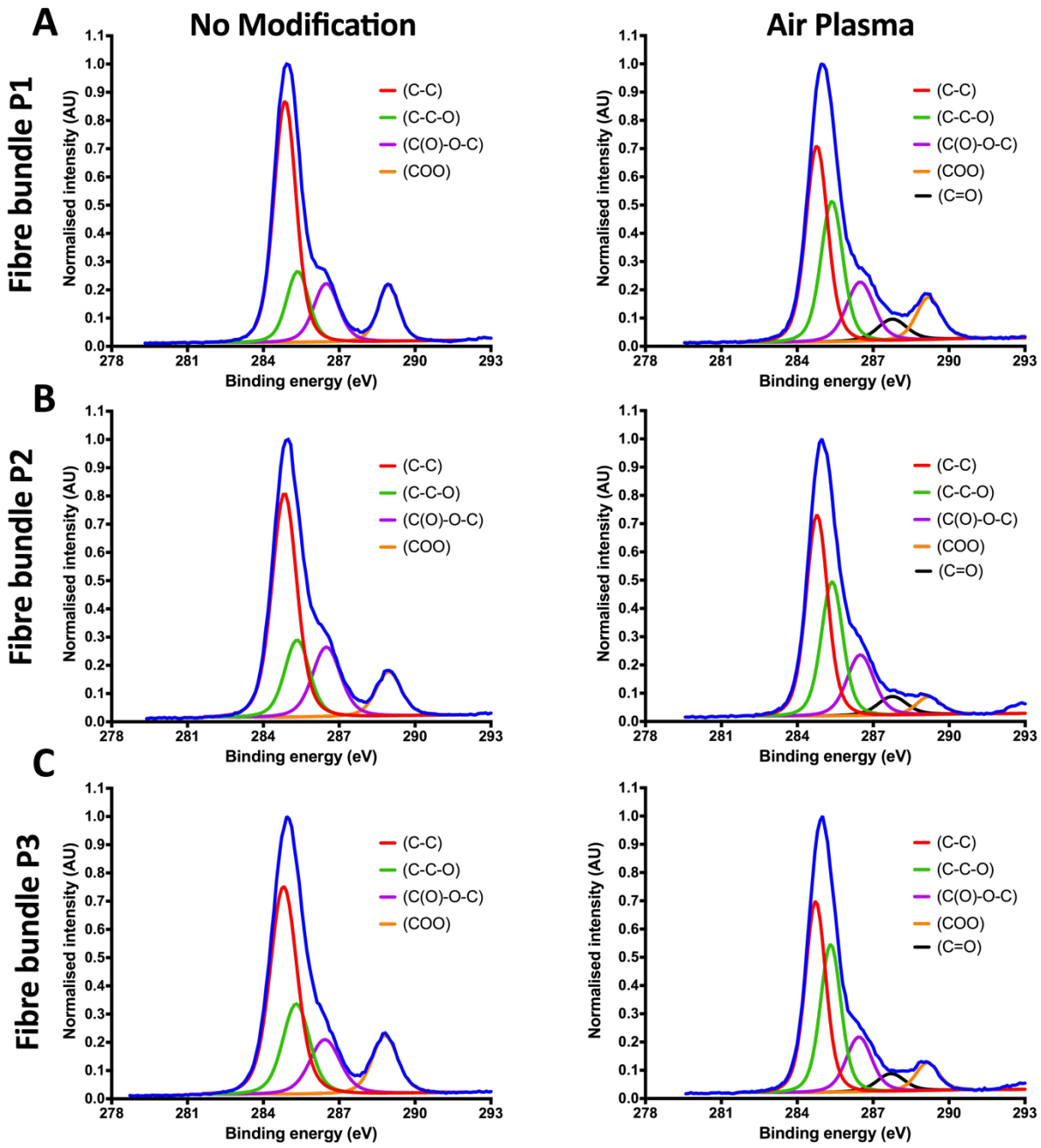

Figure 54 XPS analysis on PCL fibre scaffolds inside NGCs – C1 region

Representative and normalised XPS spectra of unmodified (left column) and modified air plasma-modified (right column) 10 µm fibre scaffolds after removal from PEG conduits (20 % fibre density). XPS analysis was performed at the A) top (P1), B) middle (P2) and C) end (P3) of the fibre bundle. Results were compared to unmodified fibre scaffolds inside conduits. XPS analysis was performed by the EPSRC National Facility for XPS at Cardiff University (UK) on two independently fabricated and air plasma modified fibre scaffolds.

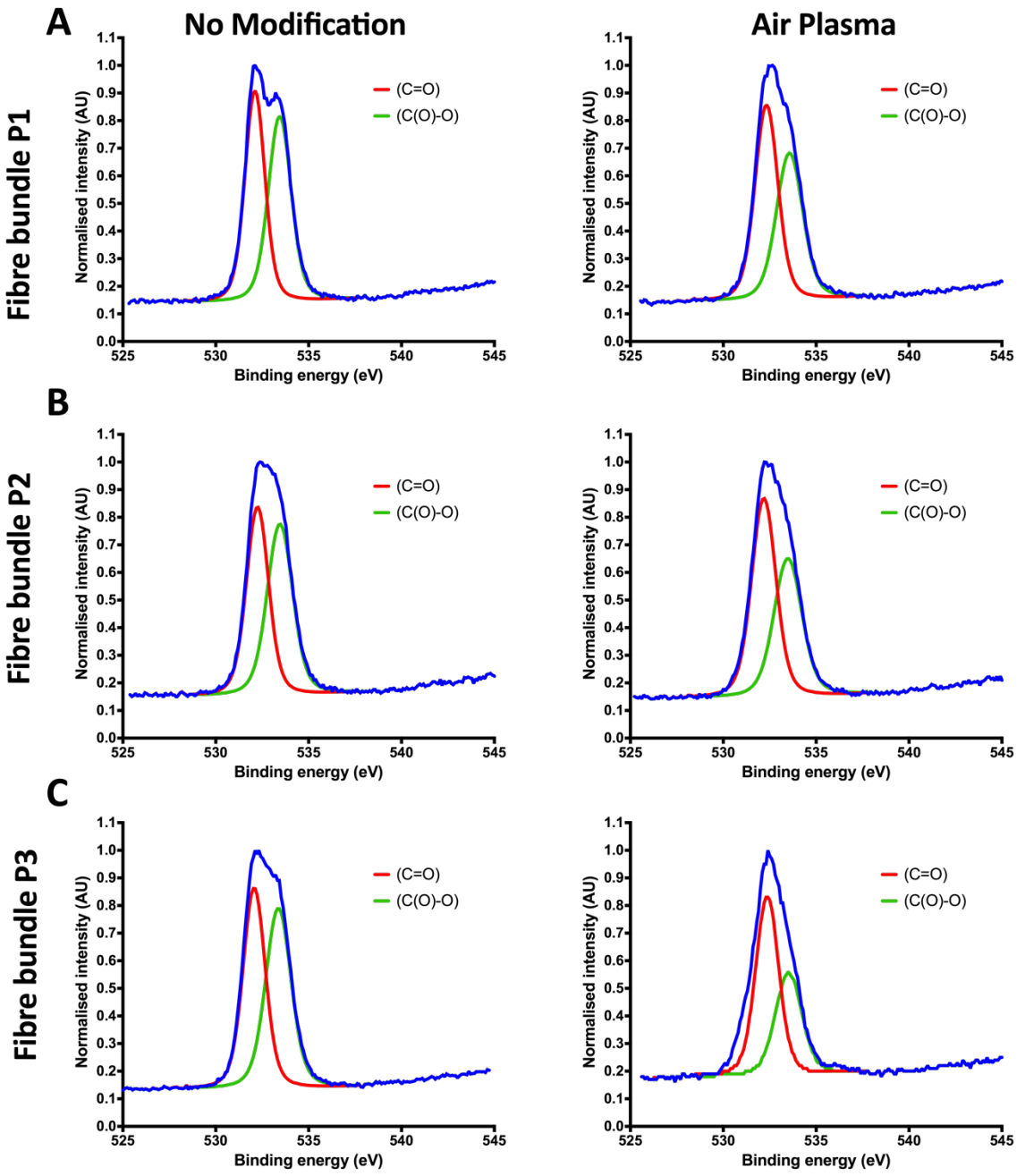

Figure 55 XPS analysis on PCL fibre scaffolds inside NGCs – O1 region

Representative and normalised XPS spectra of unmodified (left column) and modified air plasma-modified (right column) fibre scaffolds. 10 µm PCL fibres were inserted into PEG conduits with a filling density of about 20 %. Air plasma was applied for 60 s to the fibre-filled conduit. Fibre bundles were removed from conduits and XPS analysis performed at the A) top (P1), B) middle (P2) and C) end (P3) of the fibre bundle. Results were compared to unmodified fibre scaffolds inside conduits. XPS analysis was performed by the EPSRC National Facility for XPS at Cardiff University, UK on two independently fabricated and air plasma-modified fibre scaffolds.

5.4.3. The effect of air plasma treatment on neurite outgrowth *in vitro*

Furthermore, the effect of air plasma-modified PCL films on NG108-15 neuronal cells was analysed in regard to neurite incidence and outgrowth. The data was compared to neuronal cells which were cultured on un-modified PCL films and TCP. After 5 days in serum-free medium, axons were revealed by immunocytochemistry by labelling for the axon-specific protein βIII Tubulin. As shown in Figure 56 A, the number of neurons that formed neurites significantly increased from 17.9 ± 13.1 % on PCL films to 53.2 ± 10.3 % on air plasma-modified films. Neurite incidence on TCP measured 37.3 ± 0.9 %. Interestingly, there were no significant differences in numbers of neurons bearing neurites between TCP and unmodified films but between TCP and plasma-modified films, where modified films promoted a significant increase in neurite incidence (Figure 56 A). The differences in neurite lengths between air plasma-modified and unmodified films are highlighted in Figure 56 B. On unmodified PCL films, neurites measured on average 71.7 ± 34.4 µm and 134.2 ± 31.3 µm on air plasma-modified films. There was no statistical difference in neurite length between those two samples. Unmodified PCL films, however, formed significantly shorter neurites compared to TCP samples on which an average neurite length of 178.2 ± 33 µm was measured. Interestingly, there was no significant difference in neurite length between TCP and air plasma-modified samples (Figure 56 B).

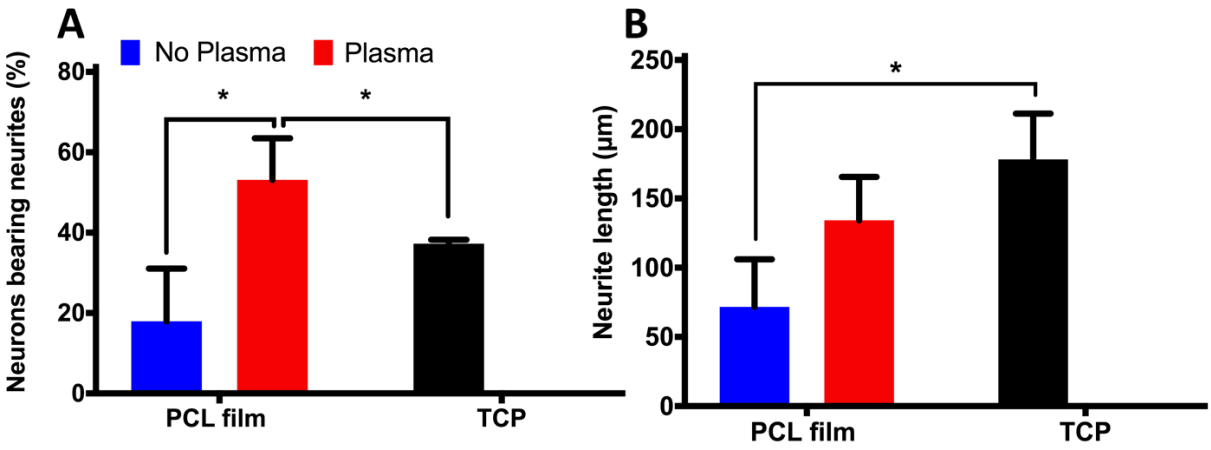

Figure 56 The influence of air plasma treatment on neurite incidence and length *in vitro*

NG108-15 neuronal cells were cultured under serum-free conditions on plasma-modified PCL films, unmodified PCL films and TCP for 5 days. A) Neurite incidence and B) neurite length were measured in Fiji based on confocal images which showed axons visualised with βIII Tubulin. Values are presented as mean + SD. Statistical differences were indicated as * $p<0.05$ (two-way ANOVA with Tukey's multiple comparisons test). Experiments were independently repeated three times and each experiment run in duplicate.

5.4.4. The effect of air plasma treatment on Schwann cell metabolic activity *in vitro*

The response of primary rat Schwann cells to air plasma-modified PCL films was further investigated in a metabolic activity study using resazurin reduction. The change in metabolic activity between unmodified PCL films, air plasma-modified PCL films and TCP was measured on day 1, 3 and 5 (Figure 57). A significant increase in metabolic activity between unmodified and air plasma-modified PCL films was measured at all three time points. The activity rates between unmodified PCL films and TCP measured comparably on day 1 and 3 but were significantly increased on TCP on day 5. On day 1 and 3, the measured metabolic activity on air plasma-modified films was significantly higher than on TCP but measured similar on day 5 (Figure 57).

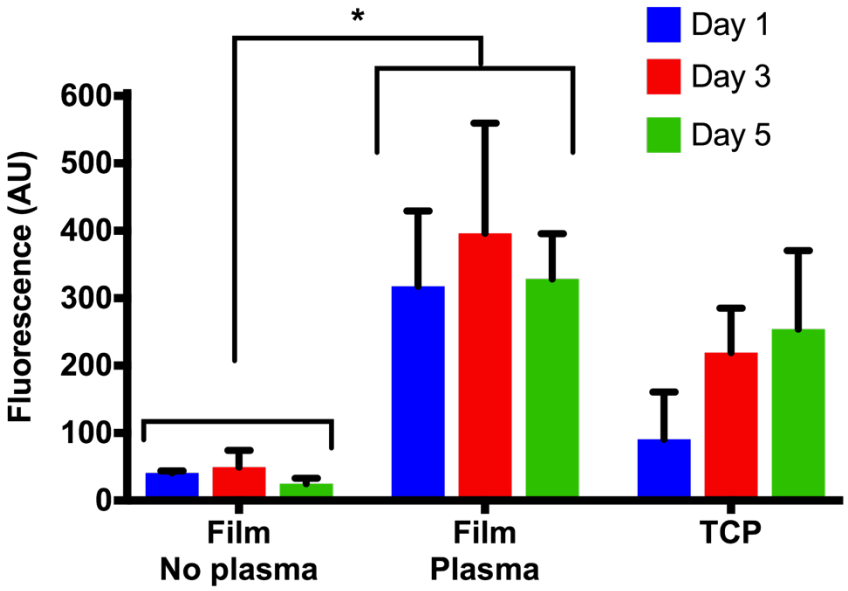

Figure 57 **The effect of air plasma treatment on Schwann cell metabolic activity *in vitro***

Resazurin reduction assays were performed on primary rat Schwann cells which were cultured on plasma-modified PCL films, unmodified PCL films and TCP to measure metabolic activity rates. Measurements were conducted on day 1, 3 and 5. Films were glued to 1 cm^2 stainless-steel rings using a silicone-based aquarium sealant. Statistical differences were indicated as * $p<0.05$ (two-way ANOVA with Tukey's multiple comparisons test). Values are presented as mean + SD of three independently performed experiments.

5.5. Discussion

This study set out with the aim of assessing the effect of air plasma treatment on PCL's surface and furthermore of studying the effect of change in surface functionality on primary Schwann cell and neuronal cell behaviour. On the question of chemical changes on the surface of PCL, this study found that air plasma treatment reduced the contact angle of PCL films from 117° to 78.8° which was similar to the contact angle of TCP. In accordance with the present results, previous studies have demonstrated that air plasma treatment is associated with an increase in PCL's wettability [331-333]. This is in further agreement with the findings of Surucu *et al.*, who reported a reduction in contact angle on PCL/chitosan/PCL layer-by-layer scaffolds from 126.5° down to 75.6° when air plasma was used [334].

On the question of surface composition, XPS was performed and revealed a decrease in ester groups and C-C bonds in the C1 and O1 regions on the surface of PCL films after the application of air plasma. Ester groups were identified through C(O)-O-C (286.4 – 286.6 eV), COO (288.8 – 289.2 eV) and C(O)-O (533.4 – 533.7 eV) components. This finding is in agreement with what has been found by Zander *et al.*, who showed a similar reduction in ester groups on the surface of PCL substrates using air plasma [335]. In this study, air plasma treatment was shown to increase the number of C-C-O (285.2 – 285.4 eV), C=O (287.6 – 287.8 eV) and C=O (532.1 – 532.6 eV) bonds and hence increased the number of hydroxyl and carbonyl groups on the surface of PCL. This increase in polar groups would therefore explain the measured reduction in contact angle on air plasma-modified PCL films. This is in agreement with other reports in the literature which showed an increase in material's wettability through an increase in polar groups on the material surface [336, 337]. In this study, nitrogen was additionally detected as a third element on plasma-modified samples. Previous studies have reported similar findings where air plasma treatment deposited nitrogen on PCL's surface [331, 335]. The appearance of nitrogen atoms on the surface of PCL, although not existing in PCL's chemical structure, might likely be explained with the high nitrogen content in atmospheric air. As nitrogen molecules split up to nitrogen atoms in the plasma, nitrogen molecules are stable and therefore it is difficult to create nitrogen atoms in the plasma process. This might explain the small amount of incorporated nitrogen on the surface of plasma-modified PCL.

Furthermore, this work found that chemical changes on PCL's surface were similar between fibres and films. The plasma process of 60 s was efficient enough to cause a chemical surface change throughout the fibre scaffold inside PEG conduits. Although not demonstrated by other studies, the finding of Barry *et al.* agrees with this finding indirectly. Barry *et al.* reported on an even presence of amine groups within a 3D porous PLA scaffold after introducing the sample to allylamine vapour prior to oxygen plasma activation. Without the activation step, amine groups were predominantly present on the scaffold edges and about four times lower in the scaffold middle [330]. The authors suggested that oxygen plasma was a key step to achieve an even allylamine penetration inside the scaffolds and hence Barry *et al.'s* finding supports what was found herein. This finding has furthermore important implications for developing nerve guides with internal fibre scaffolds on a commercial scale with this application being particularly advantageous regarding the short processing time. In comparison, Wan *et al.* reported on a treatment time of 30 min to ensure the penetration of ammonia plasma inside porous PLA scaffolds of 4 mm thickness [329]. Herein, a sufficient surface modification effect was achieved after 60 seconds penetrating a 5 mm long fibre-filled conduit. It is furthermore suggested that air plasma treatment of entire nerve guides could be conducted directly in the operation theatre prior to implantation.

Although the use of air plasma is a widely recognised surface functionalisation method for polymers, such modifications are not permanent [214, 338]. Herein, the stability of surface modification was investigated under different storage conditions. Initial contact angles on air plasma-modified PCL films increased over time until the degree of wettability was similar to non-modified PCL films. This effect was seen for samples stored in vacuum bags or on the laboratory bench. The process was observed to be quicker when samples were stored in vacuum bags. These results match those observed in earlier studies and confirm that the hydrophilic effect of air plasma is temporary. This may be due to a mechanism called "hydrophobic recovery", where polar groups on the polymer surface re-arrange depending on the environment they are exposed to. It has been reported in the past that functional groups on plasma-modified surfaces re-organise towards the bulk of the polymer, resulting in an increased water contact angle [211-213]. It seems therefore possible that these results are due to low humidity levels in the air and in particular in vacuum bags which might have caused the re-arrangement of

polar groups on plasma-modified PCL substrates towards their bulk. On the contrary, the storage of air plasma-modified samples in PBS showed the opposite effect, with the wettability increasing over time. This may be explained by the fact that PCL's polar groups orientated towards the polar PBS medium and presented an increased polarity on the surface. This observed effect correlates with what has been reported by Everaert *et al.* and Morra *et al.* who both observed that plasma-modified surfaces retained their contact angle when stored in water in comparison to samples stored in air on which an increase in contact angle was detected after 5 days [339, 340]. Murakami *et al.* gave additional insights on this matter that might be of use to further explain the observed increase or decrease in wettability on "aged" PCL films in different mediums over 21 days. The authors studied the effect of polydimethylsiloxane (PDMS) and polystyrene aging in water on the surface free energy. It has been highlighted that the way polymer surfaces orientated was dependant on the difference in surface free energy between the polymer and the surrounding medium, where polymer surfaces optimised towards a state of minimised surface free energy [216]. The relationship between the surface free energies of unmodified and plasma-modified polymer and the surrounding medium was described as follows: If the surface free energy of the surrounding medium (γ_M) was greater than the energy of the plasma-modified polymer (γ_T) and was in turn greater than the energy of the unmodified polymer (γ_P) ($\gamma_M > \gamma_T > \gamma_P$) then functional groups on the surface of the plasma-modified polymer will orientate towards the surface to minimise their surface free energy. Murakami and colleagues showed this effect with PDMS and polystyrene where surface free energies were measured to be 50 and 57 mJ/m^2 after oxygen plasma treatment which was lower than the surface free energy of water (72.8 mJ/m^2) in which samples were stored in. It was observed that the contact angle not only decreased over time but that both polymers measured a similar surface free energy as water after ageing was completed [216]. Furthermore, they made the assumption that if the surface free energy of the plasma-modified polymer is higher than the energy of unmodified polymers and which in turn is greater than the surface free energy of the surrounding medium ($\gamma_T > \gamma_P > \gamma_M$) then polar functional groups on the polymer surface orientated towards the bulk of the material [216]. This has been shown with phenol-formaldehyde resin where surface free energy measured > 100 mJ/m^2 after oxygen plasma treatment which was greater than the surface free energy of water. This

sample therefore showed the effect of hydrophobic recovery although stored in water like the other materials [216]. These findings can be used to explain the observed effects in this study. The surface free energy of unmodified PCL and PBS measures around 40 mJ/m^2 [341] and 72.2 mJ/m^2 [342], respectively. Although not tested, it is assumed that the surface free energy of PCL is increased after air plasma treatment but still lower than the surface free energy of PBS. The induced polar groups on PCL's surface therefore orientated towards the PBS medium in order to minimise the surface free energy on its surface. The same explanation can be used to explain the observed decrease in contact angle on non-modified PCL films over time as the surface free energy of unmodified PCL was lower than that of PBS. In this study, it has been noticed that this decrease in contact angle was delayed by 15 days in comparison to air plasma-modified PCL. It is assumed that this is due to the initially smaller amount of functional polar groups on unmodified PCL's surface. It is hence believed that those groups slowly started to orientate towards the PBS medium which did not initially have an effect on measurable wettability but which accumulated over time resulting in a detectable change.

The functional change on the surface of hydrophobic polymers caused by air plasma has previously been shown to have a significant positive effect on cell attachment and behaviour [221-224]. In this study, air plasma treatment was found to cause a significant increase in neurite formation in NG108-15 neuronal cells in comparison to unmodified samples and the TCP control. Furthermore, neurites measured similarly long between the TCP control and air plasma-modified PCL but were significantly shorter on unmodified samples. Additionally, air plasma-modified PCL films were shown to cause a significant increase in primary Schwann cell metabolic activity in comparison to unmodified samples and was furthermore significantly higher on day 1 and 3 than on TCP samples. Therefore, the positive effects of air plasma-modified PCL films on cells seen in this study align with findings of previously mentioned reports [221-224].

As the application of air plasma may alter surface chemistry, roughness, hydrophilicity and charge, it is difficult to determine which parameter is responsible the most for the detected changes on cellular level. It is, however, hypothesised that all those surface changes influenced the adsorption of proteins to the polymer surfaces and caused the observed changes in cell behaviour between air plasma-modified and unmodified PCL

films. This hypothesis is supported by the findings of Recek *et al.* who reported on a faster and increased protein adsorption from cell culture medium onto oxygen plasma-modified polyethylene terephthalate samples in comparison to the unmodified material [219]. Jaganjac *et al.* observed a similar effect on the same material, where an increased mass of adsorbed albumin protein and proteins from FBS were found on oxygen plasma-modified samples versus unmodified ones [218]. As herein presented, XPS analysis revealed a particular increase in hydroxyl groups on the surface of PCL after air plasma treatment which influence on protein adhesion is hence worth investigating. Lopis-Hernandez *et al.* identified that with increasing hydroxyl group content on a substrate surface there was an increase in vinculin and integrin expression. Additionally, they reported on more prominent F-actin fibres on hydrophilic hydroxyl samples in comparison to hydrophobic ones. Although the reported number of focal adhesion kinase (FAK) remained constant on all samples, the number of phosphorylated FAKs increased with increasing hydroxyl groups [343]. It is therefore likely that the herein detected increase in neurite formation and length on air plasma-modified PCL was caused by an enhanced expression of cell adhesion molecules. This is further highlighted by Lee *et al.*'s findings which indicated that an upregulation of integrin receptors and FAK had a significant effect on prolonged neurite outgrowth [344]. Furthermore, integrin and FAK influence general cell behaviour such as cell adherence, migration, survival and proliferation. It is therefore likely that an upregulation of adhesion molecules on the cell surface together with an increase in available protein binding domains on the material surface would favour the attachment of cells. This could explain the detected significant changes in Schwann cell metabolic activity as it is likely that the observed changes on day 1 were due to a difference in attached cell numbers. The findings further showed that metabolic activity values of Schwann cells on air plasma-modified and unmodified PCL remained unchanged over a period of 5 days. This finding could likely be explained by a potential difference in initial cell numbers on the two different substrates, where cell densities were so high on plasma-modified PCL films that cells reached confluence and stopped dividing. This phenomenon of high cell densities inhibiting cell proliferation has been described before including the hypothesis that an increase in cell secreted factors allows cells to sense their confluence and conversely inhibits growth [345]. On the other hand, it is assumed that too few cells attached to unmodified PCL films which slowed

down its growth rate. This might further correlate with earlier findings, where low cell numbers induced apoptosis in the cells [346].

Furthermore, it has been indicated that the change in surface roughness due to air plasma treatment might change cellular behaviour. Bunetti *et al.* reported on a comprehensive study of neuronal SH-SY5Y cells on smooth materials and materials with nano-roughness. Interestingly, the authors documented a reduced neurite outgrowth and increased cell apoptosis when cultured on rough surfaces [347]. However, those findings did not correlate with what has been demonstrated in this study and with what has been highlighted in the review of Vasita *et al.* [197]. It is therefore likely that the observed changes in neuronal and Schwann cell behaviour herein were also due to differences in surface roughness on plasma-modified and unmodified samples. However, SEM or AFM analysis need to be conducted on the substrate surfaces in order to confirm this statement.

Taken together, these results are meaningful in several ways. First, the reported significant increase in wettability on air plasma-modified PCL gives informative insights for the development of an optimal internal PCL fibre scaffold to improve hollow nerve guides. The application of air plasma to such PCL fibre scaffolds would not just increase the wettability of PCL but would further decrease its contact angle over time *in vivo.* This might be a critical point for enhancing the nerve regeneration outcome which is still limited to small nerve gaps. If directly implanted after air plasma treatment, the gradual increase in material wettability might act as a gradient over time that could enhance axon and Schwann cell outgrowth deep inside the enclosed conduit. Second, further information could be gathered on potential nerve guide storage after air plasma has been applied. The current study suggests a storage in physiological fluid such as PBS or saline. Third, the significant increase in Schwann cell metabolic activity seen on air plasma-modified PCL might suggest an increase in Schwann cell number inside the nerve gap. Since Schwann cells secrete neurotrophic factors this increase in number would also increase the soluble concentration of secreted neurotrophic factors in the conduit which may in turn enhance the regeneration outcome. Last and finally, the significant increase in neurite incidence on plasma-modified PCL films is likely to result in an increased outgrowth of axons along plasma-modified PCL guidance scaffolds *in vivo*. Air plasma

treatment might hence be a critical factor to increase the number of surviving axons in the nerve gap and support their regeneration. In the future, the biological response of air plasma-modified microfibres inside conduits needs to be further investigated in order to provide more meaningful and physiological relevant data. This could, for example, be accomplished by using primary co-cultures of Schwann cells and neurons like available in DRGs.

5.6. Conclusion

This chapter has discussed the introduction of polar functional groups on the surface of PCL films and PCL microfibres inside PEG conduits by air plasma and furthermore presented a positive effect of such treatment on neurite incidence, length and Schwann cell metabolic activity. The present work provides additional evidence with respect to air plasma penetration inside 3D constructs and the storage of air plasma-modified nerve guides. The evidence from this study suggests that air plasma treatment might play a significant role in enhancing the regeneration support of PCL microfibres in peripheral nerve repair. Further experimental investigations are highlighted in the next chapter evaluating the performance of air plasma-modified PCL microfibres of different diameter and densities in the reported DRG model.

The following was concluded in detail:

- Air plasma treatment enabled the quick and simple chemical modification of PCL surfaces
- The contact angle of PCL was significantly reduced after applying air plasma
- Air plasma treatment caused an increase in polar hydroxyl and carbonyl groups on the surface of PCL while reducing the C-C bonds on its surface
- Air plasma penetrated inside 5 mm nerve guides and caused a similar chemical change on PCL fibres than on plasma-modified PCL films
- Air plasma-modified PCL recovered its hydrophobicity when stored in air or vacuum bags
- PCL and air plasma-modified PCL increased its wettability over time when stored in PBS. This effect occurred quicker on plasma-modified samples.
- Neuronal cells formed significantly more neurites on air plasma-modified PCL films vs. the unmodified control and TCP

- Neurite lengths were measured to be similar on air plasma-modified PCL and TCP but were significantly shorter on unmodified PCL vs. TCP
- Metabolic activity rates of primary Schwann cells on PCL films were significantly elevated after air plasma treatment

Chapter 6 Analysis of NGC scaffold variables in a 3D *ex vivo* model

6.1. Introduction

In this thesis, I have highlighted and discussed limitations of hollow nerve guidance conduits (NGCs) and the need to improve these structures, and current regeneration outcomes by incorporating internal aligned guidance scaffolds. Chapter 3 – 5 report on electrospun PCL fibres with potential to support aligned nerve regeneration *in vivo* and draw attention to the need for reliable and physiological relevant 3D models to test NGC scaffolds *in vitro*. This chapter combines several lines of evidence and data to accomplish the overall aim for developing a 3D *ex vivo* peripheral nerve regeneration model for assessing and selecting appropriate NGC scaffolds prior to *in vivo* implantation.

Chapter 4 presented a 3D *in vitro* and *ex vivo* culturing model that enabled the evaluation of fibre scaffolds inside nerve guides. Due to the co-existence of neurons and Schwann cells, dorsal root ganglia (DRGs) demonstrated useful properties for studying peripheral nerve regeneration. However, the high rate of outgrowth failure of rat DRGs resulted in a small number of experimental replicates that compromised data analysis and hence the reliability of results. Therefore, improvements on DRG outgrowth were needed to increase accuracy of the model, yield and reliability. This was addressed herein by using DRGs from embryonic development day (EDD) 12 chick embryos. On EDD 12, nervous system development in chicks is not fully completed [348] and hence it was hypothesised that the active growth of nerves might increase the chance of cell outgrowth from DRGs. A softer collagen membrane surrounding both neurons and Schwann cells was believed to further enhance this response.

A major focus of the work in this chapter was imaging the model using light-sheet fluorescence microscopy (LSM) instead of confocal microscopy. The first fluorescence based LSM systems was developed in 1993 by Voie *et al.* [349] but the use of LSM was limited by its resolution. With further development of this method improving the resolution limitations, commercial availability of light-sheet microscopes increased opening up new avenues of complex sample imaging that allows capture of an entire

scaffold surface in 360°. LSM has the advantage that it separates fluorescence excitation and detection into two separate light paths which means that only the fluorescence from the in-focus plane of the sample is detected which eliminates the need for a pinhole as required in confocal microscopy. Fluorescent signals are collected on a camera-based detector and not pixel-by-pixel like in other microscope techniques, (e.g. confocal microscopy) which results in significantly faster image acquisition and significantly reduces sample light exposure. However, in comparison to other imaging approaches, there are surprisingly few studies that reported on LSM which predominantly focus on the study of morphogenesis, embryogenesis and organogenesis using model organisms like zebrafish and Drosophila melanogaster [350, 351]. LSM was furthermore used for imaging 3D cultures in form of spheroids and cysts [352]. However, to the author's knowledge no study has been published on using LSM for imaging polymer scaffolds. It was therefore hypothesised that NGC PCL fibre scaffolds in organotypic cultures can be imaged by LSM and which approach would further increase the accuracy of results herein, as all aspects of the scaffold can be analysed.

The importance of fibre diameter for designing internal NGC fibre scaffolds was highlighted and discussed in detail in Chapter 3. The diameter of PCL fibres influenced axon and Schwann cell orientation and furthermore controlled important nerve regeneration responses such as Schwann cell proliferation and axon outgrowth. So far this has only been studied on PCL fibre mats. Chapter 5 then demonstrated the advantage of air plasma treatment that improved axon and Schwann cell growth on PCL films. Both studies were carried out on 2D substrates which was beneficial at the time to identify underlying cell response mechanisms. This chapter then combined the findings of Chapter 3 – 5 and assessed fibre diameter and air plasma treatment inside NGCs using the developed 3D model with embryonic chick DRGs. This work further aimed to examine the effect of different PCL fibre densities on DRG outgrowth as it has been shown that fibre density influences nerve regeneration [145, 153]. Yoshii *et al.* reported on an increase in myelinated axon number with an increase in incorporated fibres in NGCs [145]. Ngo *et al.* found similar, where the number of regenerated axons improved after fibre densities were stepwise increased from 3.75 % up to 30 % [153]. Apart from Yoshii *et al.* and Ngo *et al.*, there is a general lack of research on assessing the effects of fibre

density inside nerve guides. Furthermore, no currently existing study has assessed different densities of PCL fibres.

Although this work focused on the assessment of PCL fibre scaffolds as a candidate for internal NGC scaffolds, this study further sought to ascertain that the reported model can be used for evaluating other fibre scaffold materials. Through a collaboration with Professor Ipsita Roy and Dr. Pooja Basnett from the University of Westminster (UK), this study assessed poly-3-hydroxybutyrate (P3HB) and blends of P3HB and poly-3-hydroxyoctanoate-*co*-3-hydroxydecanoate (P3HO-*co*-3HD) fibre scaffolds in the reported model. Both materials are polyhydroxyalkanoates (PHAs), a family of polyester which are produced by a number of bacteria as a result of high carbon availability and nutrient deficiency, (e.g. nitrogen, oxygen or potassium) [353]. PHAs are being used in biomedical applications such as nerve repair, thanks to their non-toxic and biodegradable properties [354]. Professor Roy's group has a track record of fabricating PHAs for tissue engineering and medical device applications [354-357] which provided the motivation to evaluate the PHA materials proposed by Roy as NGC guidance scaffolds for peripheral nerve regeneration.

Not only are guidance scaffolds currently being explored for enhancing peripheral nerve regeneration, but also are drugs and growth factors being considered [358]. However, particular attention has been paid to the delivery of autologous or allogenic Schwann cells for nerve lesions [359] [360, 361]. The delivered cells secrete trophic molecules such as laminin and neurotrophic factors that promote axon growth and therefore are hypothesised to influence a regenerative effect within the nerve lesion [359]. Although Schwann cells have been delivered through nerve guides into a nerve gap [362] [360, 361], it was noted that no study examined the effect of cell delivery on nerve regeneration inside NGCs *in vitro*. This study therefore sought to address the latter by evaluating the outgrowth of chick DRGs on PCL fibre scaffolds in NGCs which were seeded with primary chick Schwann cells prior to DRG culture. This experiment further aimed to explore the general applicability of the reported model for use in evaluating regenerative medicine approaches for nerve repair in the future.

6.2. Aims & Objectives

It was hypothesised that the developed 3D DRG model can be used to assess and compare different fibre scaffolds with each other for use as guidance in peripheral nerve repair. So far, nothing exists that enables a comprehensive assessment of NGC guidance scaffolds directly inside nerve guides *in vitro*. This work attempted to refine the existing DRG model, to improve its reliability, functionality, as well as accuracy, and evaluate and compare the regenerative support of PCL fibre scaffolds in regard to different fibre diameters, density and with versus without air plasma-modified surfaces. This data should lead to an informed choice for optimal PCL guidance scaffolds for peripheral nerve regeneration prior to future analysis *in vivo*.

The objectives were as follows:

- To assess changes in neurite outgrowth and Schwann cell metabolic activity between unmodified and air plasma-modified PCL fibres
- To investigate differences in embryonic chick DRG outgrowth between conduits with unmodified and air plasma-modified 10 µm PCL fibre scaffolds
- To study the effect of conduits with air plasma-modified PCL fibre scaffolds of different diameters on embryonic chick DRG outgrowth
- To compare the DRG outgrowth distances of scaffolds measured based on confocal or light-sheet microscopy images
- To analyse the impact of different fibre densities in conduits on DRG outgrowth
- To section fibre scaffolds of different density for evaluation of DRG outgrowth into the scaffold cores
- To evaluate the performance of conduits with selected fibre scaffolds in extended 21 day DRG cultures
- To isolate and purify chick Schwann cells from sciatic nerves of chick embryos

- To investigate whether allogeneic Schwann cells can be delivered to a nerve gap inside NGCs with selected PCL fibre scaffolds
- To test the compatibility of the reported model for evaluating fibre scaffolds of materials different to PCL

6.3. Materials & Methods

6.3.1. Cell culture on air plasma-modified samples

Cells were cultured on 1 and 10 µm PCL microfibres (see 2.2 for fabrication details) and PCL films (see 2.7 for fabrication details) which were either air plasma-modified (see 2.8 for more information) or left unmodified. TCP was used as a control surface. Microfibres and PCL films were mounted to 1 cm^2 stainless-steel rings and sterilised as outlined in 2.3. Fibres and films were both left to air dry in a sterile cabinet prior to cell seeding.

6.3.2. Neurite outgrowth on air plasma-modified samples

NG108-15 neuronal cells were trypsinised and counted as described in 2.9.3 and 2.9.4, respectively. In numbers of 2×10^4, cells were seeded inside 1 cm^2 stainless-steel rings in volumes of 500 µL using growth medium. Cells were left to attach at 37 °C in a CO_2 incubator overnight and growth medium replaced with serum-free growth medium the day after to encourage the formation of neurites. Neurons were fixed and prepared for immunocytochemical labelling as described in 2.12 after 5 days of culture in serum-free medium. Labelling was performed with the primary mouse anti-βIII Tubulin antibody (G7121, Promega) at a concentration of 2.5 µL/mL (1:400) for 48 h. As a secondary antibody, donkey anti-mouse FITC antibody (A24501, Life Technologies) was used at a concentration of 0.6 mg/mL for 3 h. Cell nuclei were labelled with DAPI as described in 2.12. Samples were imaged using z-stack confocal microscopy as described in 2.17 and neurite length and incidence measured and analysed as defined in 2.10.1. All samples were prepared in duplicate and experiments repeated three times.

6.3.3. Schwann cell metabolic activity analysis on air plasma-modified samples

Primary rat Schwann cells were trypsinised and counted as mentioned in sections 2.9.3 and 2.9.4. Cells were seeded in 1 cm^2 stainless-steel rings in concentrations of 2×10^4 cells per 500 µL growth medium. On day 1, 3 and 5, the metabolic activity of primary Schwann cells was measured using a resazurin reduction assay as described in 2.15. Microfibres attached to rings were transferred to customised PDMS moulds prior to resazurin application (see 2.15.1 for details). Each experiment was conducted in duplicate and repeated three times.

6.3.4. Preparation of NGCs with PCL fibre scaffolds for culture

PCL microfibres were electrospun using the parameters described in 2.2 to result in diameters ranging from 1 to 13 µm. Aligned fibres were incorporated in 5 mm long PEG conduits as described in 2.4. All PCL fibre scaffolds filled the PEG conduit to 20 % except for the study on different fibre density, where fibres made up either 10, 20 or 40 % of the tube. Fibre packing was conducted according to the reported method based on fibre weight as mentioned in 2.5. Selected samples were air plasma-modified using the parameters described in 2.8. Air plasma treatment was applied to the entire conduit containing internal fibre scaffolds.

6.3.5. Isolation of DRGs from chick embryos

Fertilised brown leghorn chicken eggs (*Gallus gallus domesticus*, Henry Stewart Co. Ltd., UK) was cleaned of pathogens using 20 % industrial methylated spirit (in H_2O, Fisher Scientific) and cultured at 37.5 °C in a humidified Rcom Suro 20 incubator, with a 45° rotation each way every hour, for 3 days. Afterwards, eggs were carefully transferred to a 37.5 °C incubator (no CO_2) without rotation. The care of chick embryos was guided strictly by the Home Office (UK) guidelines, where chick embryos were sacrificed at the latest on embryo development day (EDD) 14. For experimental work, embryos were used on EDD 12. Eggs were cracked into sterile Petri dishes in a sterile cabinet. Embryos were sacrificed by decapitation and the chick body transferred to a sterile Petri dish. Using forceps, all internal organs were removed while ventral side was facing up. Tissue was rinsed with PBS containing 100 units/mL penicillin and 100 µg/mL streptomycin (Sigma-Aldrich) and kept hydrated with the same solution in a Petri dish. Using forceps, DRGs were removed and placed in PBS with penicillin/streptomycin (Figure 58), where attached nerve roots were trimmed from DRG bodies using a scalpel. Throughout the dissection procedure, a Wild M3Z Heerbrugg Switzerland dissection microscope was used.

Figure 58 Dorsal root ganglion body with nerve root

Light microscope image of a dorsal root ganglion (indicated by *) dissected from a EDD 12 chick embryo submerged in PBS. The DRG body still has the nerve roots attached (indicated by arrows) which will be trimmed close to the DRG body before culture. Scale bar = 500 µm.

6.3.6. Chick embryo DRG culture and analysis

Aligned fibre scaffolds were incorporated to different densities (see Table 8 for details) inside 5 mm long PEG conduits as described in 2.4 and prepared for culture using the reported culture insert (see 2.6 for details). Dissected DRGs were placed on top of conduits and the well plates carrying both scaffolds and tissue transferred to a 37 °C CO_2 incubator for 30 min. Afterwards, DRGs were covered with growth medium and transferred back to the incubator. Certain experiments were performed with fibres modified with air plasma or were pre-seeded with primary chick Schwann cells. For details, please see section 2.8 and 6.3.9 accordingly. After culture times had passed (depending on experiments as listed in Table 8), fibre scaffolds were carefully removed from conduits using forceps, fixed and immunocytochemically labelled as outlined in 2.12. Immunocytochemistry revealed axons and Schwann cells by using mouse monoclonal anti-βIII Tubulin antibody (1 µg/mL (1:1000), ab78078, Abcam, incubated for 24 h at 4 °C) and rabbit anti-S100β antibody (10 µg/mL (1:400), Z5116, Dako, incubated for 24 h at 4 °C) as primary antibodies and donkey anti-mouse FITC (0.6 mg/mL, A24501,

Life Technologies, incubated for 3 h at room temperature) and goat anti-rabbit Alexa 546 (0.8 mg/mL, A11010, Life Technologies, incubated for 3 h at room temperature) as secondary antibodies, respectively. Nuclei were visualised with 300 nM DAPI as described in 2.12. Fibre scaffolds were imaged with LSM and samples prepared, imaged and processed according to the description in 2.18. Each DRG experiment was conducted in quadruplicate and repeated three times.

Table 8 Overview of fibre scaffolds and experimental specifications for chick DRG cultures

Scaffolds (inside 5 mm long PEG conduits)	Fibre density (%)	Specifications	DRG culture time (days)
10 µm PCL fibres	20	Air plasma vs. no plasma	7
1 – 13 µm PCL fibres	20	Air plasma	7
10 µm PCL fibres	10, 20 or 40	Air plasma vs. no plasma	7
10 µm PCL fibres	20	Air plasma vs. no plasma	21
10 µm PCL fibres	20	Air plasma, Pre-seeded with primary chick Schwann cells	7
P3HB or **P3HB/P3HO-*co*-3HD 80:20 blend fibres**	20	NA	7

6.3.7. Analysis of DRG attachment and outgrowth

The success of DRG attachment to fibre scaffolds was expressed as a percentage of the number of DRGs that showed an attached DRG body to the scaffold with the overall number of DRGs that were placed on the conduits (Equation 9).

$$\%\ Attachment = \frac{Number\ of\ attached\ DRGs}{Number\ of\ DRGs\ placed\ on\ scaffolds} \times 100 \qquad \textbf{Equation 9}$$

The percentage of DRGs that showed an outgrowth of axons or/and Schwann cells was calculated as demonstrated in Equation 10. Cell outgrowth was defined as any cell-

specific fluorescent signal that was detected distal to the DRG body along the fibre scaffold.

$$\%\ DRG\ outgrowth = \frac{Number\ of\ DRGs\ with\ cell\ outgrowth}{Number\ of\ attached\ DRGs} \times 100 \qquad \textbf{Equation 10}$$

Each axon or axon bundle (accumulation of axons that appeared as one big strand) and each Schwann cell "band" (aligned arrangement of Schwann cells that grew along the same fibre) were measured as the length between DRG body and the distal axon tip or the last Schwann cell of the Schwann cell "band" most distal to the DRG body. Measurements were conducted in Fiji using the "segmented-line" tool. The maximum outgrowth distance was defined as the longest outgrowth measured for one sample which was either based on one image when using confocal microscope images or based on four images representing each a different sample rotation when using LSM images. For the average outgrowth distance, all axons/axon bundles and Schwann cell "bands" were measured per sample and averaged. All measurements were averaged over the whole sample population and were reported as either "maximum outgrowth" or "average outgrowth".

6.3.8. Isolation and purification of chick primary Schwann cells

The isolation process of Schwann cells from EDD 12 chick embryo sciatic nerves was adapted from Kaewkhaw *et al.* [285] Schwann cell extraction protocol from adult rat sciatic nerves. Fertilised chick eggs were incubated and embryos sacrificed on EDD 12 as described in section 6.3.5. In order to localise the sciatic nerve in chick legs, the leg was gently pulled at the chick's foot to separate the connective tissue of the leg from the tissue of the spine and main body. The revealing nerve strand was traced back and dissected along the leg towards the foot. Four sciatic nerve strands were placed in 5 mL of 0.15 % sterile-filtered collagenase (from *Clostridium histolyticum*, Sigma-Aldrich) solution using serum-free growth medium. Nerves were incubated at 37 °C in a CO_2 incubator for 30 min. The cell suspension was homogenised with a sterile plastic Pasteur pipette and passed through a 40 µm cell strainer (Falcon, Corning Incorporated). Cells were centrifuged at room temperature at 400 g for 6 min. The supernatant was discarded and the cell pellet resuspended in 1 mL of Schwann cell purification medium (DMEM D-valine with supplements, see 2.11.1 for details). Cells were transferred to a 75

cm^2 culture flask with 15 mL of the same medium. Cells were passaged 1:4 when confluence was reached and further seeded into wells of a 6-well plate for purity analysis at passage 2. For this, cells were fixed and permeabilised as described in 2.12 after 70 % confluence was reached. Three wells were respectively used for visualising S100β and glial fibrillary acidic protein (GFAP) in Schwann cells, where all cells were visualised with DAPI. All nuclei and cells that were not co-localised with the S100β and GFAP protein were seen as impurities in the culture. Either anti-S100β primary rabbit antibody (1:400 or 10 µg/mL in 1 % vol/vol BSA, Dako, Z5116) or anti-GFAP primary rabbit antibody (1:200 in 1 % vol/vol BSA, Abcam, ab16997) were added to the samples for 48 h at 4 °C, followed by three washes in PBS. Goat anti-rabbit Alexa 546 antibody (0.8 mg/mL in 1 % BSA; Life Technologies, A11010) was used to visualise the S100β and GFAP protein. Both secondary antibodies were incubated for 120 min at room temperature. After two PBS washes, cell nuclei were labelled with 300 nM DAPI (Sigma-Aldrich) for 30 min at room temperature. Before imaging, samples were washed, then resubmerged in PBS. Cells were imaged with a Nikon Eclipse Ti microscope with a Nikon intensilight HGFI illuminator (Nikon Instruments Europe B.V.) and a neo sCOMS camera (Andor Technology Ltd., UK). Samples were imaged under both fluorescence and brightfield. Schwann cell purity was calculated as mentioned in 2.11.2.

6.3.9. Culture of chick primary Schwann cells for DRG culture

Primary chick Schwann cells (pcSCs) were isolated and purified as outlined in 6.3.8. pcSCs were usually used at passage 2 when cultures were 100 % pure and only contained Schwann cells. 5 mm long PEG conduits were fabricated as mentioned in section 2.1 and filled with 20 % aligned 10 µm PCL fibres according to the descriptions in 2.4 and 2.5. Four PEG conduits per experimental condition were secured in stainless-steel metal grids and prepared for culture as mentioned in 2.6. The same seeding technique as in section 4.3.7 was used as this showed to result in an even distribution of cells inside the conduits (see Figure 47 and Figure 48 for more details). 5×10^4 and 15×10^4 pcSCs were seeded in 10 µL growth medium in PEG conduits by pipetting the cell suspension into one side of the conduit. Well plates with conduits were transferred to a CO_2 incubator operating at 37 °C for 20 min. Afterwards, conduits were covered in growth medium and further incubated for 4 days. On day 4, two conduits with both pcSC concentrations were fixed in

order to assess the distribution of cells inside the scaffolds. On the same day of culture, DRGs were dissected from EDD 12 chick embryos and placed on top of pre-seeded conduits after the surrounding medium was removed. DRGs were left to attach at 37 °C in a CO_2 incubator for 20 min before DRGs were covered in growth medium and further incubated for 7 days. Conduits without pcSCs were additionally cultured for 4 days and DRGs added thereafter to act as the control. On day 7, fibre scaffolds were carefully removed from conduits using forceps, fixed and immunocytochemically labelled for βIII Tubulin and S100β as outlined in section 6.3.6. Scaffolds were imaged by LSM and images processed as described in 2.18.

6.3.10. Cryosectioning and imaging of fibre scaffolds

Aligned and air plasma-modified 10 µm PCL fibre scaffolds of different densities (10, 20 or 40 %) that were already immunocytochemically labelled, imaged by LSM and analysed were further sectioned using a cryostat (Leica Microsystems Ltd., model: CM1860 UV). For this, agarose gel, remaining from light-sheet imaging, was carefully removed with filter paper and sample basket filled with tissue freezing medium (Leica Microsystems Ltd.). Fibre scaffolds were placed in the middle of the sample baskets, gently pushed down to its bottom and centred using a thin needle. Air bubbles in the gel were removed with a thin needle. Fibre scaffolds in tissue freezing medium were placed on the designated chilled sample holder surface in the cryostat until completely frozen (about 1 – 2 h). Frozen blocks were adhered to metal stubs using tissue freezing medium and placed in the designated chilled sample holders inside the cryostat to solidify the gel. Samples were mounted and subsequently longitudinally sectioned with a blade in thicknesses of 30 µm. Sections were adhered to glass microscope slides (Polysine™ adhesion slides, Thermo Scientific) and left to dry in the dark. The surrounded tissue freezing medium, however, was not removed in order to remain the sample's integrity. From the first section carrying a part of the fibre scaffold, sections were sequentially numbered in order to correlate sample features with their location in the scaffold. Selected sections that represented the uppermost and lowermost scaffold exterior and core were imaged using a Nikon Eclipse Ti microscope with a Nikon intensilight HGFI illuminator (Nikon Instruments Europe B.V.) and a neo sCOMS camera (Andor Technology Ltd., UK). The sample uppermost exterior, core and lowermost exterior for fibre scaffolds

with a density of 20 or 40 % were defined as the first 120 – 150 µm sections, 400 – 450 µm and 800 – 900 µm sections, respectively. Scaffolds from fibres with a density of 10 % were thinner (due to fibre clumping in the conduit centre) so that the uppermost exterior, core and lowermost exterior of the scaffold were defined as the first 30 µm section, 300 µm and 500 µm, respectively. All scaffolds were imaged under brightfield and fluorescence in order to visualise the sectioned fibres and the pre-stained axon- and Schwann cell-specific features of βIII Tubulin and S100β, respectively. Scaffolds of two experimental repeats in quadruplicate were sectioned.

6.3.11. P3HB and P3HB/P3HO-*co*-3HD scaffold fabrication

Aligned fibre scaffolds of P3HB and P3HB/P3HO-*co*-3HD 80:20 were fabricated by Dr. Pooja Basnett from the University of Westminster (UK). In short, both PHA polymers were produced by bacterial fermentation using either a colony of *Bacillus subtilis* OK2 or *Pseudomonas mendocina* CH50 for the production of P3HB and P3HO-*co*-3HD, respectively. Bacteria broths were maintained at 30 °C in a bioreactor and the pH controlled at 6.8 and 7.0 for P3HB and P3HO-*co*-3HD production, respectively. The two polymers were extracted and purified with a two-stage Soxhlet method using methanol first, followed by chloroform. Fibres were fabricated through a pressurised gyration process inside a cylindrical aluminium vessel of 60 mm in diameter. For P3HB fibres, 7.4 % polymer was dissolved in chloroform, where blend fibres were fabricated by mixing 7.4 % P3HB and P3HO-*co*-3HD in an 80:20 ratio. Fibre production was carried out at 36,000 rpm and 0.1 MPa. The diameter of fibres was measured by Dr. Basnett and accounted 6.9 ± 1.9 µm for P3HB fibres and 9.1 ± 3.7 µm for P3HB/P3HO-*co*-3HD 80:20 blend fibres. DRG cultures on P3HB and fibre scaffold blends were carried out as described in section 6.3.6 and analysed as mentioned in section 6.3.7.

6.4. Results

6.4.1. The effect of air plasma treatment on neurite outgrowth *in vitro*

This study assessed the difference in neurite incidence and outgrowth of NG108-15 neuronal cells to air plasma-modified 1 and 10 µm PCL microfibres in comparison to unmodified samples. PCL films and TCP were used as control surfaces. After 5 days of culture in serum-free medium that initiated the outgrowth of neurites, neurons were visualised with the axon-specific protein βIII Tubulin as demonstrated in Figure 59. A similar difference in neurite incidence and outgrowth between the different unmodified substrates of fibres and films was found as described in Figure 31 in Chapter 3. Figure 59 (left row) clearly shows that neurite outgrowth and incidence was more prominent on 10 µm PCL fibres than on 1 µm ones or PCL films. After the application of air plasma, a remarkable increase in neurite length, incidence as well as cell number was identified for both fibre samples as well as on PCL films (Figure 59, right row). An additional difference in neurite orientation was observed between the air plasma-modified samples. An increased aligned directionality of axons with fibre direction was seen on 10 µm fibres in comparison to 1 µm ones (Figure 59 A and B, right row). Neurites on PCL films, on the other hand, appeared unorganised and extended in different directions (Figure 59 C, right row).

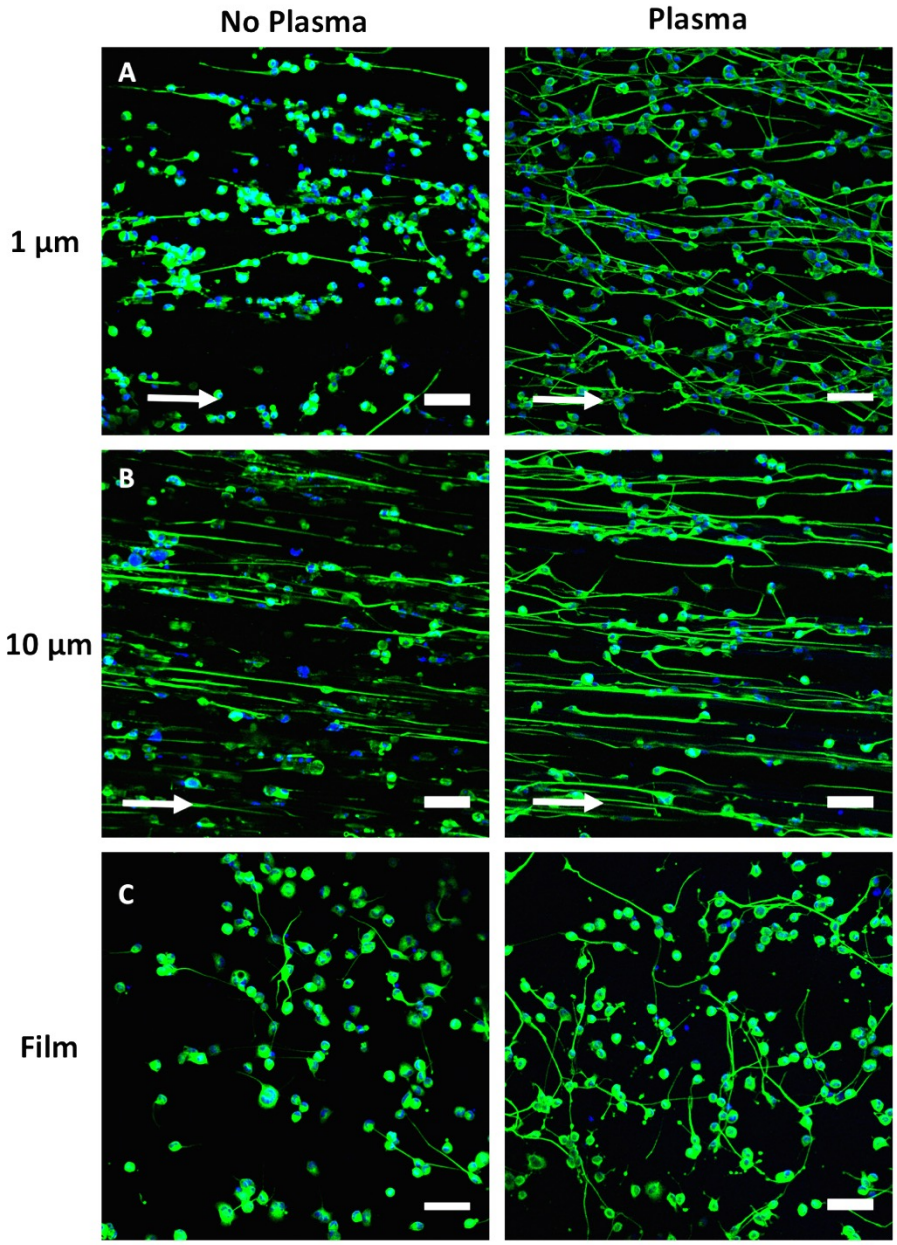

Figure 59 Neurite outgrowth on air plasma-modified PCL microfibres

Confocal micrographs of NG108-15 neuronal cells on unmodified (left column) and air plasma-modified (right column) A) 1 and B) 10 µm PCL fibres and C) PCL films. Cells were cultured for five days under serum-deprived conditions and fixed afterwards. Axons were labelled for βIII Tubulin (green) and nuclei labelled with DAPI (blue). Imaging was conducted in z-stacks. Arrows indicate the direction of fibre alignment. Scale bar = 100 µm. Representative images are shown of three independently repeated experiments.

Neurite incidence and length were further quantified and data is presented in Figure 60 A and Figure 60 B, respectively. The differences seen in neurite incidence between

unmodified 1 µm, 10 µm fibres and PCL films (Figure 59) were confirmed statistically, where neuronal cells formed significantly more neurites on unmodified 10 µm fibres (37.4 ± 15.5 %) compared to 1 µm unmodified fibres (20.2 ± 11.7 %) and PCL films (17.9 ± 13.1 %) (Figure 60 A). After air plasma treatment, the average neurite incidence measured 39.5 ± 6 %, 51.9 ± 13 % and 53.2 ± 10.3 % on 1 µm fibres, 10 µm fibres and PCL films, respectively (Figure 60 A). Interestingly, this change was significant between unmodified and air plasma-modified 1 µm fibres and PCL films but was not significantly different for 10 µm fibres. Neurons, however, formed significantly more neurites on 10 µm fibres and PCL films after air plasma treatment in comparison to cells cultured on TCP, which was 14 % greater (Figure 60 A). In contrast, there was no significant difference between neurite incidence on air plasma-modified 1 µm fibres and TCP (Figure 60 A).

The treatment of PCL substrates with air plasma affected neurite outgrowth, as illustrated in Figure 60 B. Neurons formed significantly longer neurites on unmodified 10 µm PCL fibres (measured 141.3 ± 34.2 µm) compared to unmodified 1 µm fibres and PCL films on which neurites measured on average 75.2 ± 30.3 µm and 71.7 ± 34.4 µm, respectively (Figure 60 B). This finding was similar to what has been found in Figure 31 (Chapter 3). Axons on TCP measured on average 178.2 ± 33 µm which was significantly longer than measured on unmodified 1 µm fibres and PCL films, but this was not significant compared to 10 µm fibres (Figure 60 B). After air plasma treatment, the average neurite length measured was 120.9 ± 19.5 µm on 1 µm fibres, 159 ± 43.8 µm on 10 µm fibres and 134.2 ± 31.3 on PCL films. Although there was a difference in average neurite length between unmodified and air plasma-modified PCL substrates, changes were not significant (Figure 60 B). However, there was a difference in neurite length between air plasma-modified PCL substrates and the TCP control. Neurites on air plasma-modified 1 µm fibres measured significantly shorter than on TCP but were similarly long on modified 10 µm fibres, PCL films and TCP (Figure 60 B).

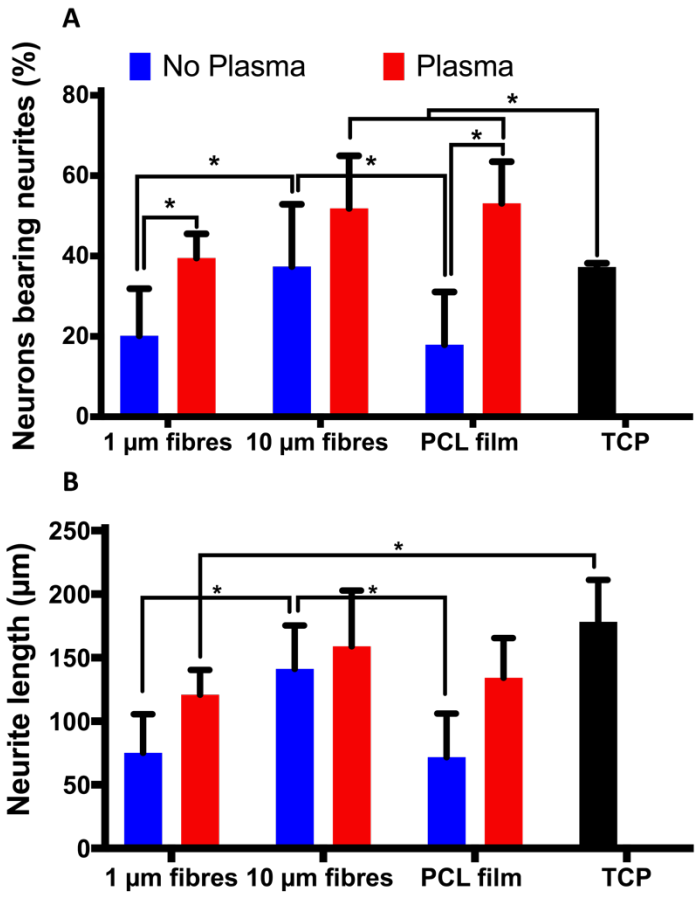

Figure 60 Quantified neurite outgrowth on air plasma-modified PCL microfibres

NG108-15 neuronal cells were cultured on unmodified (blue bars) and air plasma-modified (red bars) 1 and 10 µm PCL fibres and PCL films. TCP was used as the control substrate (black bars). Cells were cultured for five days under serum-deprived conditions and fixed afterwards. Immunocytochemistry revealed the axon-specific protein βIII Tubulin, where neurites were analysed on A) the percentage of neuronal cells that formed neurites and B) neurite length. Analysis was conducted using Fiji. Statistical differences were indicated as * $p<0.05$ (two-way ANOVA with Tukey's multiple comparisons test). Values presented as mean + SD. Experiments were performed in duplicate with three independent repeats.

6.4.2. The effect of air plasma treatment on Schwann cell metabolic activity *in vitro*

The response of primary rat Schwann cells to air plasma-modified 1 and 10 µm PCL fibres and PCL films was investigated in regard to changes in metabolic activity. Figure 37 in Chapter 3 already indicated that 10 µm fibres support a significant increase in metabolic activity of primary Schwann cells in comparison to 1 µm fibres. In this regard, resazurin reduction assays were performed on day 1, 3 and 5 in order to investigate whether the

treatment of PCL fibres with air plasma had an effect on Schwann cell metabolic activity and whether air plasma-modified 10 µm fibres would better support this effect versus plasma-modified 1 µm fibres. A summary of the results is presented in Figure 61. Interestingly, no significant increase in Schwann cell metabolic activity was detected grown on unmodified or air plasma-modified 1 and 10 µm fibres. It was however observed that with or without air plasma treatment metabolic activity on 1 µm fibres was unchanged over time. On the contrary, there was a significant increase in Schwann cell metabolic activity when grown on air plasma-modified 10 µm fibres between days 1 and 5 (Figure 61). As has already been shown in Figure 57 in Chapter 5, the modification of PCL films with air plasma significantly increased the metabolic activity of Schwann cells. Although there was no significant difference in metabolic activity between air plasma-modified 1 and 10 µm fibres, the responses of both differed when compared to air plasma-modified PCL films (Figure 61). On day 5, modified 1 µm fibres showed significantly lower cell metabolic activity rates compared to modified PCL films. Between modified 10 µm fibres and modified PCL films, on the other hand, activity rates were comparable and measured similar to reported activities on TCP (Figure 61).

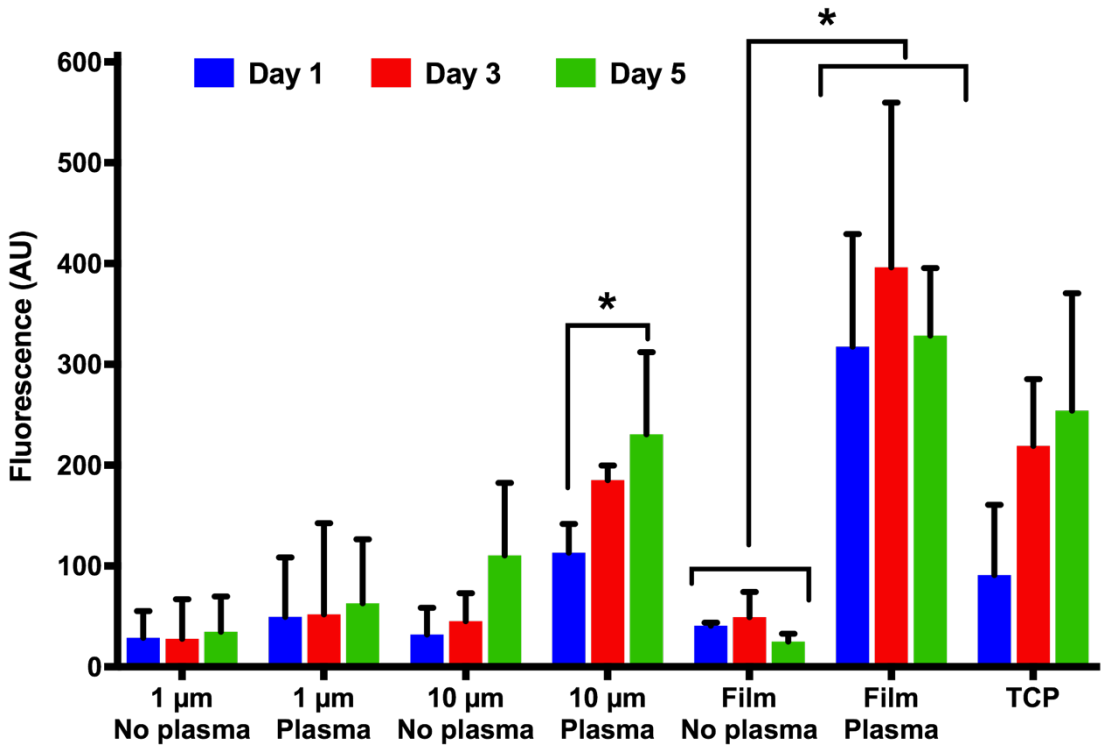

Figure 61 **Changes in Schwann cell metabolic activity on air plasma-modified PCL substrates**

Primary rat Schwann cells were cultured on unmodified or air plasma-modified 1 and 10 µm PCL fibres and PCL films. TCP was used as a control surface. Resazurin reduction assays were performed after days 1, 3 and 5 of culture as repeated measures. Fibres were mounted to stainless-steel rings and cells seeded inside the rings which were transferred into customised PDMS moulds for resazurin reduction analysis. Statistical differences were indicated as * $p<0.05$ (two-way ANOVA with Tukey's multiple comparisons test). Values presented as mean + SD. Experiments were performed in duplicate and repeated three times.

6.4.3. DRG outgrowth on PCL fibre scaffolds inside conduits with and without air plasma treatment

Next, 10 µm fibres were chosen to evaluate the effect of air plasma on the outgrowth of Schwann cells and axons in a more complex *ex vivo* co-culture arrangement. For this, the reported 3D culture model (Chapter 4) was used, where 5 mm long PEG conduits were filled with either 20 % air plasma-modified or unmodified aligned 10 µm PCL fibres. DRGs from EDD 12 chick embryos were dissected and placed on top of the conduits. After 7

days of culture, the outgrowth of axons and Schwann cells from the DRG body along the microfibre scaffolds towards the tube end was visualised by immunocytochemistry. As shown in Figure 62, axons and Schwann cells were visualised in green and red, respectively by staining for axon- and glial-specific βIII Tubulin and S100β, respectively. Samples were imaged using LSM and rotated every 90° to capture a 360° view of the samples.

Differences in DRG outgrowth on plasma-deposited 10 µm fibres versus those without modification are highlighted in Figure 62 A and B. It can be seen from Figure 62 A that the attached DRG body to the unmodified microfibre scaffold showed a minimal outgrowth of axons and Schwann cells. No outgrowth could be detected at the initial position of 0° and at a rotation of 90°. By further rotation of the sample to 180° and 270°, a minimal outgrowth of axons and Schwann cells was visible distal to the DRG body. Additionally, the number of outgrown Schwann cells and axons was poor with only a few cells present distal to the DRG body. In contrary, Figure 62 B demonstrates the outgrowth on air plasma-modified fibres which was more prominent and longer which was clearly visible as both cell types reached a more distal position in the conduit compared to in Figure 62 A. Furthermore, Figure 62 B showed that axons and Schwann cells extended out from a larger DRG area that faced the conduit opening, visible throughout the entire scaffold width, which was covered with both axons and Schwann cells. Additionally, it can be seen in Figure 62 B that Schwann cells and axons aligned with fibre direction and were in close physical position to each other. Where axons were barely present on unmodified microfibres (Figure 62 A), they arranged to form axonal bundles on plasma-modified fibres (Figure 62 B). A magnified section of Figure 62 B is presented in Figure 62 C which shows the arrangement of axons and Schwann cells on the fibre scaffold in detail. From this figure, it was apparent that axons co-localised with Schwann cells and that each axon branch accompanied several aligned Schwann cells. However, it was noted that Schwann cells appeared to be physically isolated if no axons were detected with them (Figure 62 C).

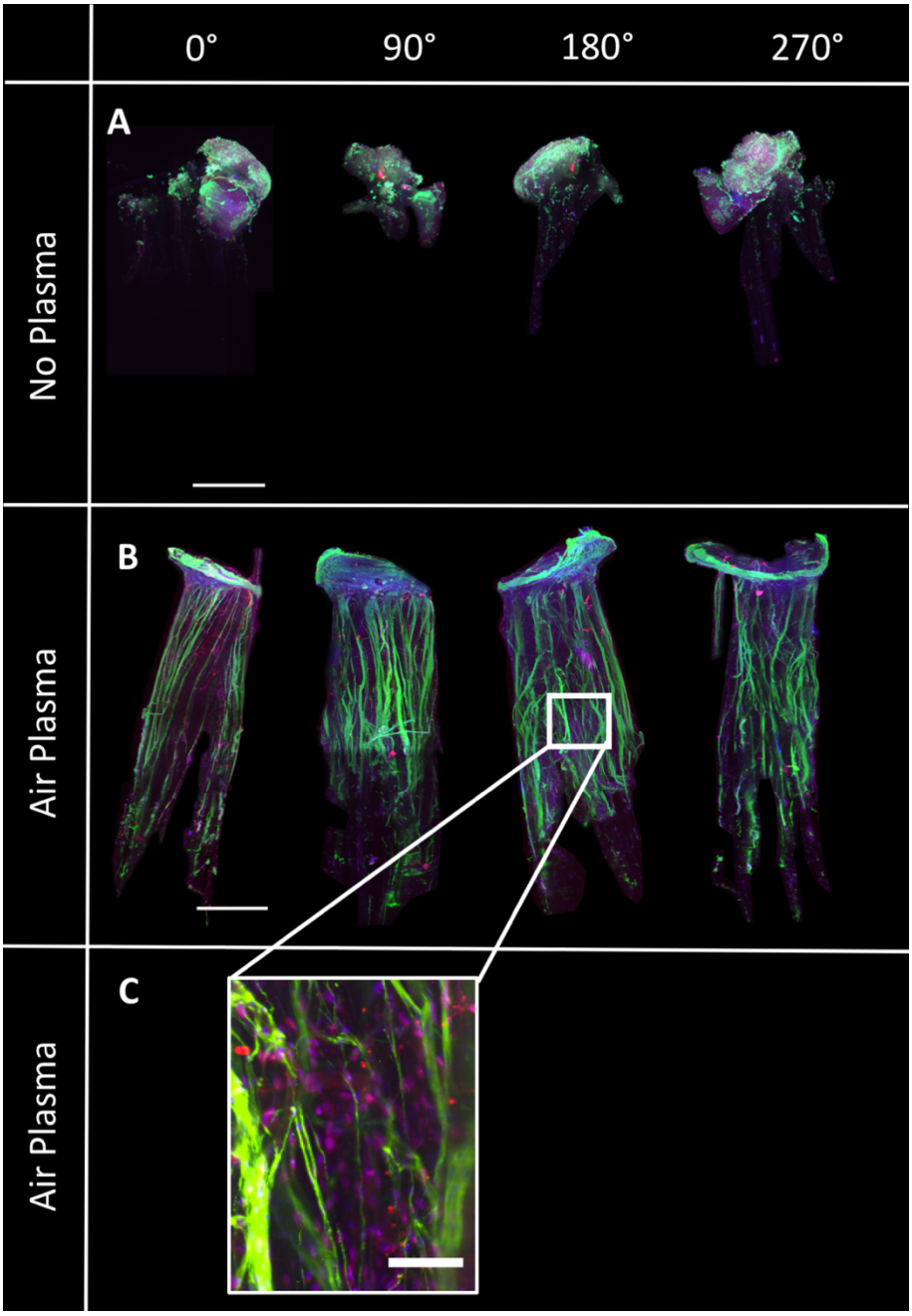

Figure 62 Chick DRG outgrowth on air plasma-modified 10 µm PCL fibres

LSM images of EDD 12 chick embryo DRG outgrowth along A) unmodified and B) air plasma-modified 10 µm PCL fibres inside PEG conduits (20 % fibre density). After 7 days of culture, Schwann cells and axons were labelled for S100β (red) and βIII Tubulin (green), respectively, using immunocytochemistry. Nuclei were labelled with DAPI (blue). Imaging was performed in multiple views in z-stacks, images stitched and presented as maximum intensity projections. Samples were rotated every 90° to capture a 360° sample view (0, 90, 180 and 270° from left to right). Scale bar = 0.5 mm. Representative images are shown from three experimental repeats. C) Magnified section of B) presenting the arrangement of axons (green) and Schwann cells (red) with nuclei (blue) on the fibre scaffold. Scale bar = 100 µm.

Further examination was conducted to examine the relationship between air plasma-modified and unmodified fibre scaffolds on DRG attachment and cell outgrowth from DRG bodies. Interestingly, it was found that irrespective of air plasma treatment, DRG attachment rate was similar between the two sample groups, where 82.1 ± 20.6 % of DRGs attached to unmodified fibre scaffolds and 85.6 ± 18.1 % to plasma-modified samples (N=3) (Figure 63 A). However, DRGs attached significantly better to fibre scaffolds inside conduits in comparison to flat TCP substrates to which 36.4 ± 9.1 % of DRGs attached (Figure 63 A). Furthermore, there was a significant difference in likelihood of DRG outgrowth that was measured by the presence or absence of any cell-specific signal distal to the DRG body. The chance of axon and/or Schwann cell outgrowth from DRG bodies was 55.8 ± 20.1 % (Figure 63 B). In contrast, air plasma modified PCL fibres and TCP showed a significant increase in DRG outgrowth, where 85 ± 11.8 % and 91.7 ± 14.4 % of all dissected DRGs grew out, respectively in comparison to unmodified PCL fibres (Figure 63 B).

The migration distance of axon and Schwann cell outgrowth from the DRG body along microfibres and towards the distal tube end was measured and compared between plasma-modified and unmodified samples. The average outgrowth distance was identified by way of four aspect positions for each sample and results presented in Figure 63 C. There was a significant difference between the average outgrowth of axons and Schwann cells between unmodified and plasma-modified fibre scaffolds. On unmodified samples, both axons and Schwann cells regenerated on average 0.38 ± 0.1 mm along the fibre scaffold. In comparison, the average cell outgrowth on plasma-modified scaffolds was about three times greater and measured 1.17 ± 0.3 mm for Schwann cells and 1.16 ± 0.36 mm for axons (Figure 63 C). Figure 63 D shows the maximum outgrowth distances in which a clear trend of increasing outgrowth on plasma-modified samples versus control samples is evident. The longest axon and Schwann cell outgrowth on unmodified scaffolds was identified with 0.54 ± 0.29 mm and 0.5 ± 0.23 mm, respectively (Figure 63 D). A significant increase in maximum outgrowth length was seen on plasma-modified PCL fibre scaffolds which measured 2.52 ± 0.36 mm and 2.46 ± 0.37 mm for axons and Schwann cells, respectively (Figure 63 D). In general, there was no significant difference in outgrowth between axons and Schwann cells on any of the PCL scaffolds (Figure 63 C and D).

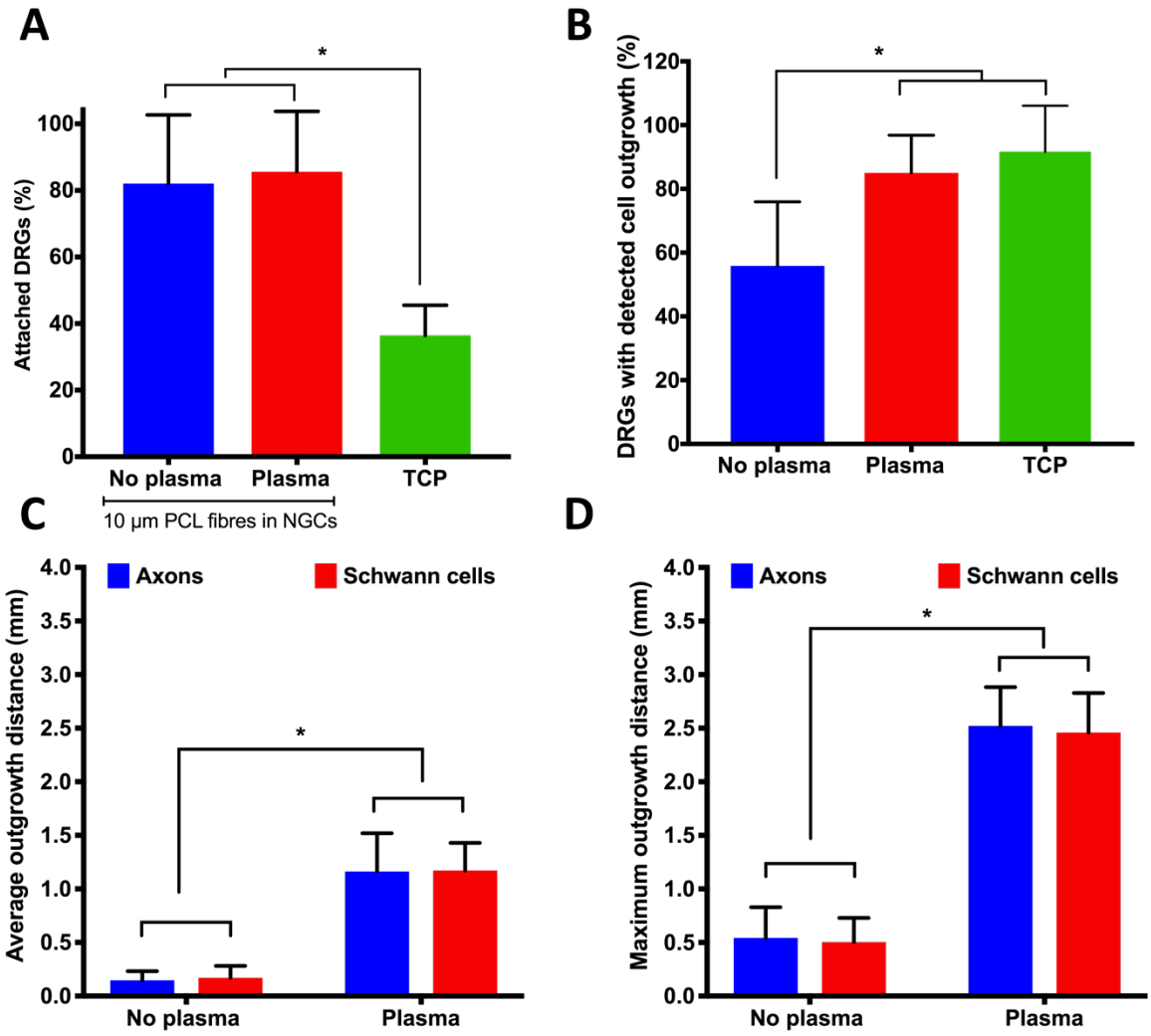

Figure 63 Quantified DRG outgrowth on air plasma-modified PCL fibre scaffolds

Comparative analysis of DRG outgrowth from EDD 12 chick embryos grown on unmodified versus air plasma-modified PCL fibre scaffolds. DRGs were cultured on 5 mm long PEG conduits containing 20 % of 10 µm PCL fibres or on TCP for 7 days. Analysis was based on LSM images as shown in Figure 62 and presented as A) the percentage DRGs attached to fibre scaffolds, B) the percentage of cell outgrowth from DRG bodies, C) the average outgrowth distance of axons and Schwann cells and D) the maximum outgrowth distance of both cell types. Values were presented as mean + SD and repeated three times in quadruplicate. Statistical differences were indicated as * $p<0.05$ using either a one-way ANOVA or two-way ANOVA with Tukey's multiple comparisons test.

6.4.4. Differences in DRG outgrowth on fibre scaffolds of different diameter

As shown in section 6.4.3, air plasma treatment had a significantly positive impact on DRG outgrowth. Thereafter, five different PCL diameters (1 – 13 µm) were investigated

inside PEG conduits with a density of 20 % and modified with air plasma. The performance of the different fibre diameters was then evaluated using the reported 3D culture model. After 7 days of culture, Schwann cells and axons from EDD 12 chick DRGs were visualised by immunocytochemistry.

Light-sheet microscopy images in Figure 64 and Figure 65 illustrate the outgrowth of both axons and Schwann cells from DRG bodies along the PCL fibre scaffold which was imaged every 90° to capture the entire scaffold architecture. Looking at any diameter, it was apparent that the extent of axon and Schwann cell outgrowth differed according to the position the sample was imaged in. The outgrowth of cells on plasma-modified 1 µm fibres, for example, measured about the same length in positions of 0°, 90° and 180° but a longer outgrowth was visible at a rotation position of 270° (Figure 64 A). It was furthermore noted that some scaffolds supported a more prominent outgrowth of both axons and Schwann cells on one half of the scaffolds in comparison to the other (Figure 64 and Figure 65 B). However, this observation was not seen on 10 µm fibres which supported an even outgrowth of axons and Schwann cells over the scaffold width as well as over the entire scaffold circumference (Figure 65 A). Looking at the localisation of axons and Schwann cells in Figure 64 and Figure 65, two main findings were observed. First, the presence of axons distal to the DRG body always co-localised with Schwann cells, but Schwann cells were also found in isolation. Second, Schwann cells were occasionally detected further distally than axons. This was predominantly seen on fibre scaffolds of 5, 8 and 13 µm (Figure 64 B – C, Figure 65 B). In addition, the migration distance of these cells was dependent on fibre diameter. The shortest outgrowth distance observed for axons and Schwann cells was on 1 µm fibres (Figure 64 A), where the greatest outgrowth distances were detected on 10 µm fibres (Figure 65 A). Finally, comparing the orientation of cell outgrowth on all fibre scaffolds it was evident that all five fibre diameter scaffolds supported the aligned outgrowth of cells consistent with fibre direction (Figure 64, Figure 65).

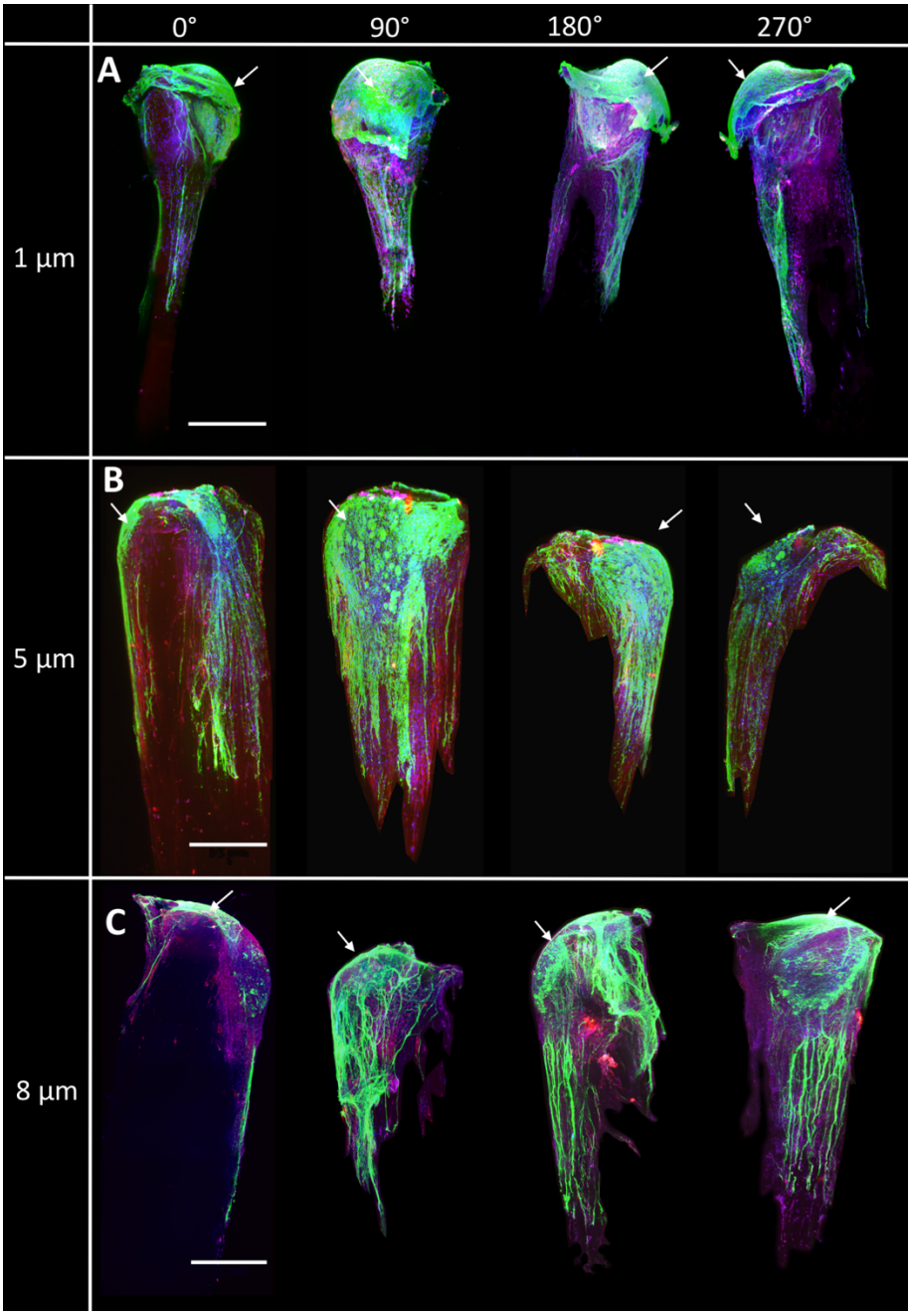

Figure 64 **DRG outgrowth on 1, 5 and 8 µm fibre scaffolds inside conduits after air plasma treatment**

Maximum projections of LSM images of EDD 12 chick DRG outgrowth along A) 1 µm, B) 5 µm and C) 8 µm air plasma-modified PCL fibres inside 5 mm long PEG conduits. Fibre density accounted for 20 %. DRGs were cultured for 7 days and Schwann cells and axons labelled for S100β (red) and βIII Tubulin (green), respectively. Nuclei were labelled with DAPI (blue). Samples were imaged in whole every 90° rotation (0, 90, 180 and 270° from left to right). Arrows indicate the location of DRG bodies. Scale bar = 0.5 mm. Representative images are shown of three experimental repeats.

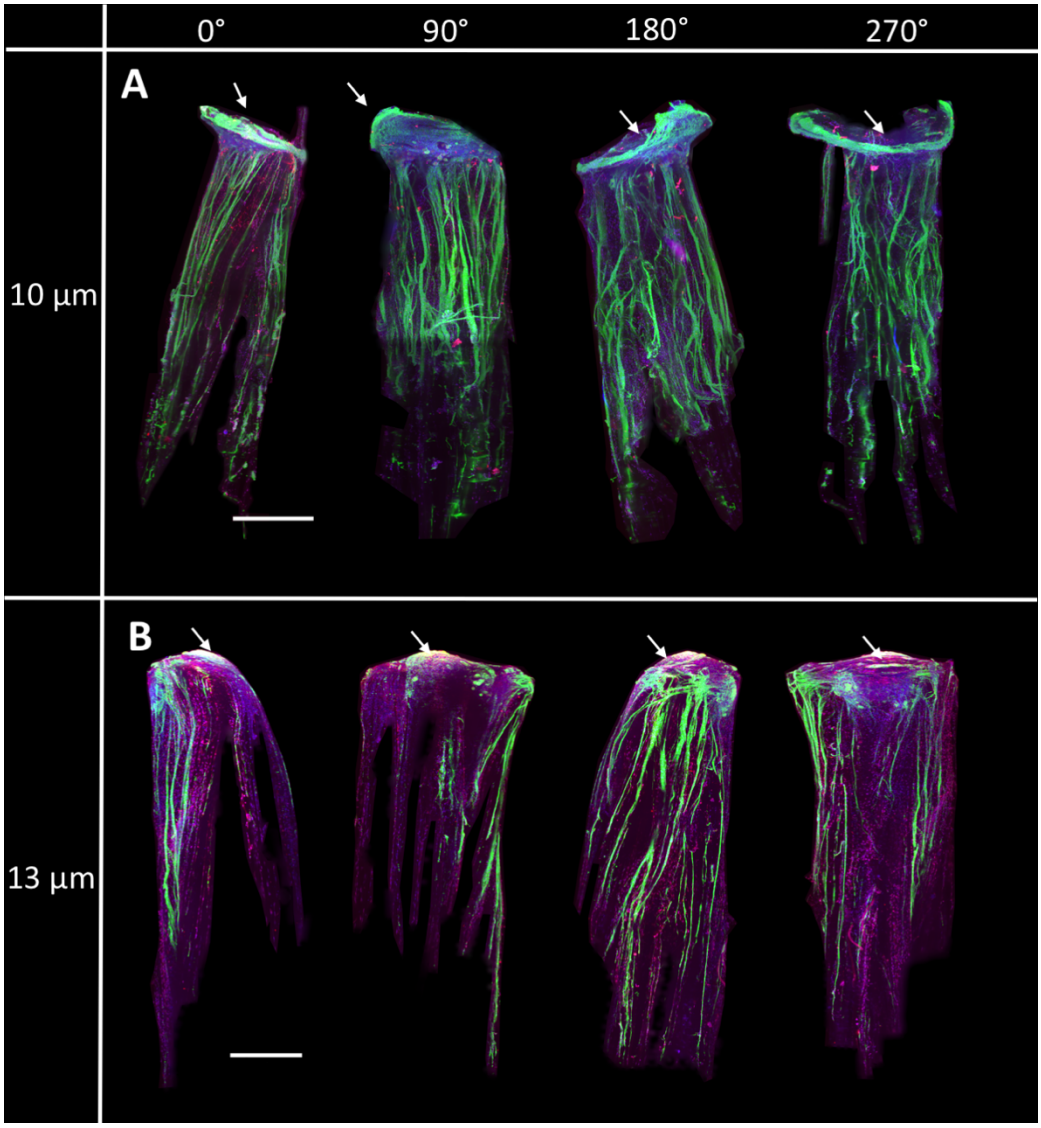

Figure 65 DRG outgrowth on 10 and 13 µm fibre scaffolds inside conduits after air plasma treatment

Maximum projections of LSM images of EDD 12 chick DRG outgrowth along A) 10 µm and B) 13 µm air plasma-modified PCL fibres inside 5 mm long PEG conduits. Fibre density accounted for 20 %. DRGs were cultured for 7 days and Schwann cells and axons labelled for S100β (red) and βIII Tubulin (green), respectively. Nuclei were labelled with DAPI (blue). Samples were imaged in whole every 90° rotation (0, 90, 180 and 270° from left to right). Arrows indicate the location of DRG bodies. Scale bar = 0.5 mm. Representative images are shown of three experimental repeats.

Further analysis was conducted in regard to the likelihood of DRG outgrowth when cultured on plasma-modified fibre scaffolds of different diameters. From all dissected DRGs, around 85 % attached to the fibre scaffolds. Detailed data is not presented herein as no significant differences were found between the different scaffolds. Figure 66 A

summarises those findings, where DRG outgrowth incidence was similar between 5, 8, 10 and 13 µm fibres which accounted for 76.6 ± 25.2 %, 83.3 ± 28.9 %, 85.6 ±18.1 % and 83.3 ± 14.4 %, respectively. On air plasma-modified 1 µm fibres, on the other hand, significantly less DRGs grew out (27.6 ± 25.4 %) in comparison to 8 – 13 µm fibres (Figure 66 A).

Figure 66 B presents experimental data on average cell outgrowth distances from DRG bodies based on LSM images. It was noted that the outgrowth distance measured was similar between different fibre diameter scaffolds. The smallest average outgrowth was detected on plasma-modified 1 µm fibres, where Schwann cells and axons grew 0.43 ±0.15 mm and 0.4 ±0.14 mm, respectively. 5 and 8 µm fibre scaffolds supported an average outgrowth of Schwann cells and axons with 0.55 ± 0.1 mm or 0.45 ± 0.13 mm and 0.48 ± 0.1 mm or 0.45 ± 0.12 mm measured, respectively. The longest average outgrowth was seen on 10 µm fibre scaffolds with 0.65 ± 0.3 mm for Schwann cells and 0.67 ± 0.27 mm for axons. This was closely followed by axon and Schwann cell outgrowth distances of 0.57 ± 0.16 mm and 0.58 ± 0.2 mm, respectively on 13 µm fibre scaffolds. Overall, the diameter did not affect the average cell outgrowth differently in these measures.

The maximum outgrowth distance of axons and Schwann cells from DRG bodies was further quantified based on either confocal microscopy or LSM images (Figure 66 C and D). The average maximum cell outgrowth based on confocal images is presented in Figure 66 C and based on images from one sample position. It can be seen from the data that outgrowth length for both axons and Schwann cells was similar between all fibre diameters. The smallest maximum outgrowth was detected with 2.06 ± 0.4 mm on 1 µm fibres for both cell types. The longest outgrowth was identified on plasma-modified 10 µm fibres with an axon and Schwann cell length of 2.84 ± 0.45 mm and 3.17 ± 0.84 mm, respectively. However, there was no statistical difference in maximum outgrowth length between the five different fibre diameters. Figure 66 D, on the other hand, presents the analysis of maximum DRG outgrowth based on LSM images chosen based on of four different positions imaged per scaffold. Overall, a similar maximum outgrowth trend was identified between the different fibre diameters herein, and that reported in Figure 66 C. It was noted that maximum lengths were overall shorter when based on LSM images

(Figure 66 D) in comparison when based on confocal images (Figure 66 C). The shortest maximum outgrowth was observed on 1 µm fibre scaffolds with 1.25 ± 0.06 mm and 1.34 ± 0.29 mm for axons and Schwann cell, respectively. The longest maximum outgrowth was measured on 10 µm fibres with an axon and Schwann cell length of 2.52 ± 0.36 mm and 2.46 ± 0.37 mm, respectively. What is interesting in this data is that 10 µm fibres supported a significantly better maximum outgrowth of both axons and Schwann cells, in comparison to 1 µm fibres. Furthermore, it was found that axons and Schwann cells showed similar outgrowth lengths in Figure 66 B, C and D, and were not statistically different from each other.

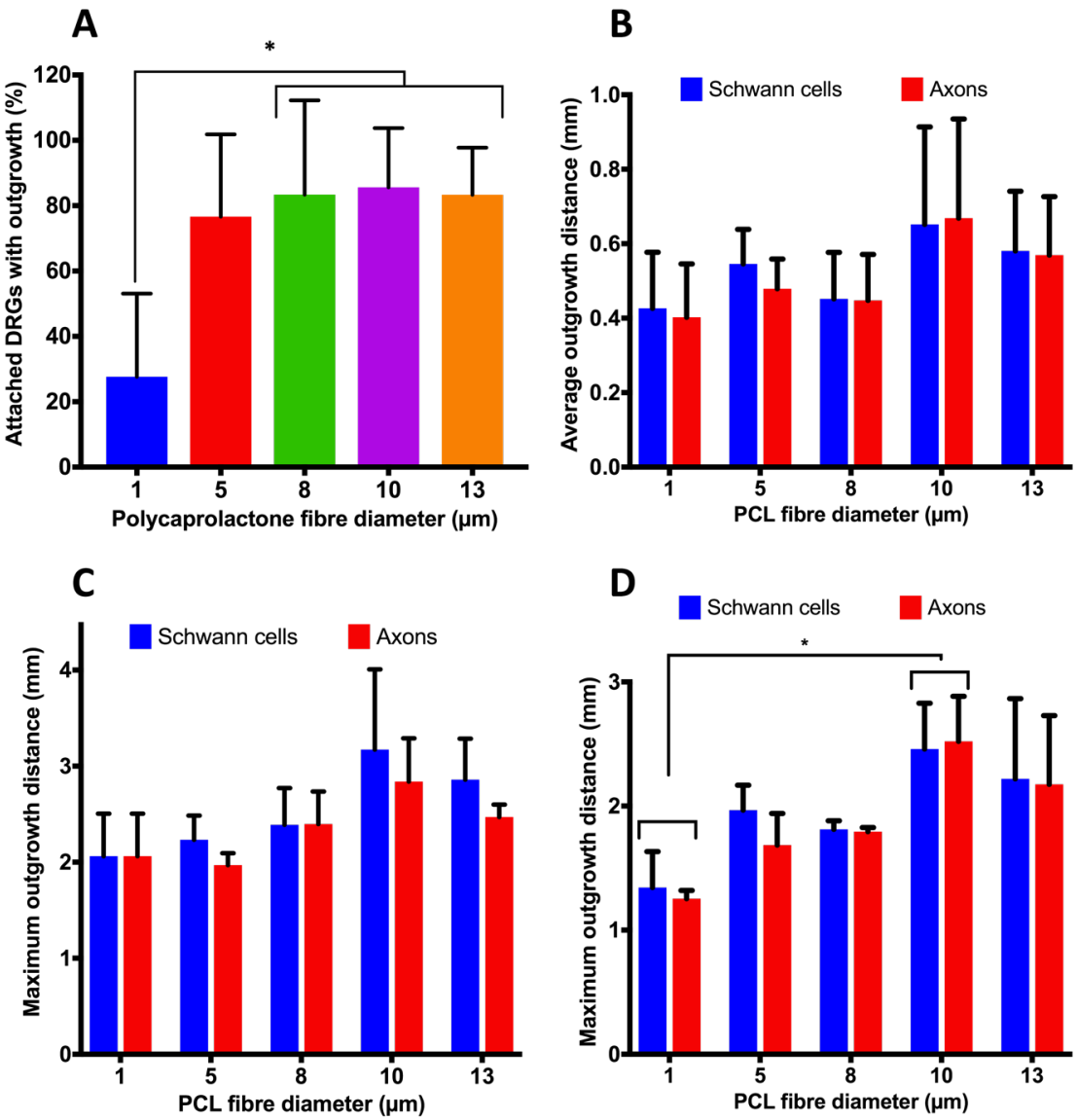

Figure 66 DRG outgrowth analysis on different diameters of 3D PCL fibre scaffolds

Analysis of DRG outgrowth regarding A) the attachment of DRGs to PCL fibre scaffolds of diameters 1, 5, 8, 10 and 13 µm, B) the average axon and Schwann cell outgrowth based on four sample positions imaged (0, 90, 180 and 270°) with LSM and the average maximum cell outgrowth identified based on C) confocal or D) light-sheet micrographs. Aligned PCL fibres filled 5 mm long PEG conduits to 20 %. DRGs were dissected from EDD 12 chick embryos and placed on top of the conduits. After 7 days of culture, scaffolds were fixed and immunocytochemically stained for S100β and βIII Tubulin to reveal Schwann cells and axons, respectively. Values are presented as mean + SD and experiments repeated three times in quadruplicate. Statistical differences were indicated as * $p<0.05$ by either one-way ANOVA (A) or two-way ANOVA (B – D) with Tukey's multiple comparisons test.

6.4.5. DRG outgrowth in NGCs with different fibre densities

This section investigated the effect of fibre density on axon and Schwann cell outgrowth from chick embryo DRG bodies. For this, plasma-modified 10 µm PCL fibres were used as demonstrated in section 6.4.4 to be the most supportive in regard to axon and Schwann cell outgrowth. Results were further compared to unmodified 10 µm PCL fibres of different densities. PEG conduits of 5 mm in length were filled with either 10, 20 or 40 % fibres and cultured with EDD 12 chick DRGs for 7 days. Fibre scaffolds were removed from conduits and immunocytochemically labelled for βIII Tubulin and S100β to reveal axons and Schwann cells, respectively. For LSM, fibre scaffolds of different densities were subsequently embedded in agarose gel and loaded into glass capillary tubes as illustrated in Figure 67 A – C. The thickness of fibre bundle increased with increasing fibre number used (Figure 67 A – C). The differences between axon and Schwann cell outgrowth from DRGs on either unmodified or air plasma-modified 10 µm fibres and different fibre densities are summarised in Figure 67 D – I. A clear difference between unmodified control and plasma-modified fibre bundles was found, where the outgrowth of axons and Schwann cells from DRGs was visibly shorter on unmodified PCL fibre scaffolds (Figure 67 D – F) in comparison to air plasma-modified scaffolds (Figure 67 G – I). Furthermore, it appeared that fibre scaffolds of 20 and 40 % density (Figure 67 E and F) showed longer cell outgrowth lengths with a greater number of outgrown axons in comparison to 10 % fibre-filled conduits (Figure 67 D). In contrast, air plasma-modified fibre scaffolds showed an even, more dominant and longer outgrowth of axons and Schwann cells. The degree to which this was true depended on the density of fibres (Figure 67 G – I). The longest DRG outgrowth was seen in conduits filled with 20 % of fibres (Figure 67 H). A greater ratio of Schwann cells to axons was furthermore observed on air plasma-modified fibre scaffolds and was particularly prominent o 10 and 20 % fibre scaffolds as can be seen in Figure 67 G and H. Axons were always seen together with Schwann cells but Schwann cells were also found alone without the close presence of axons (Figure 67 G – I).

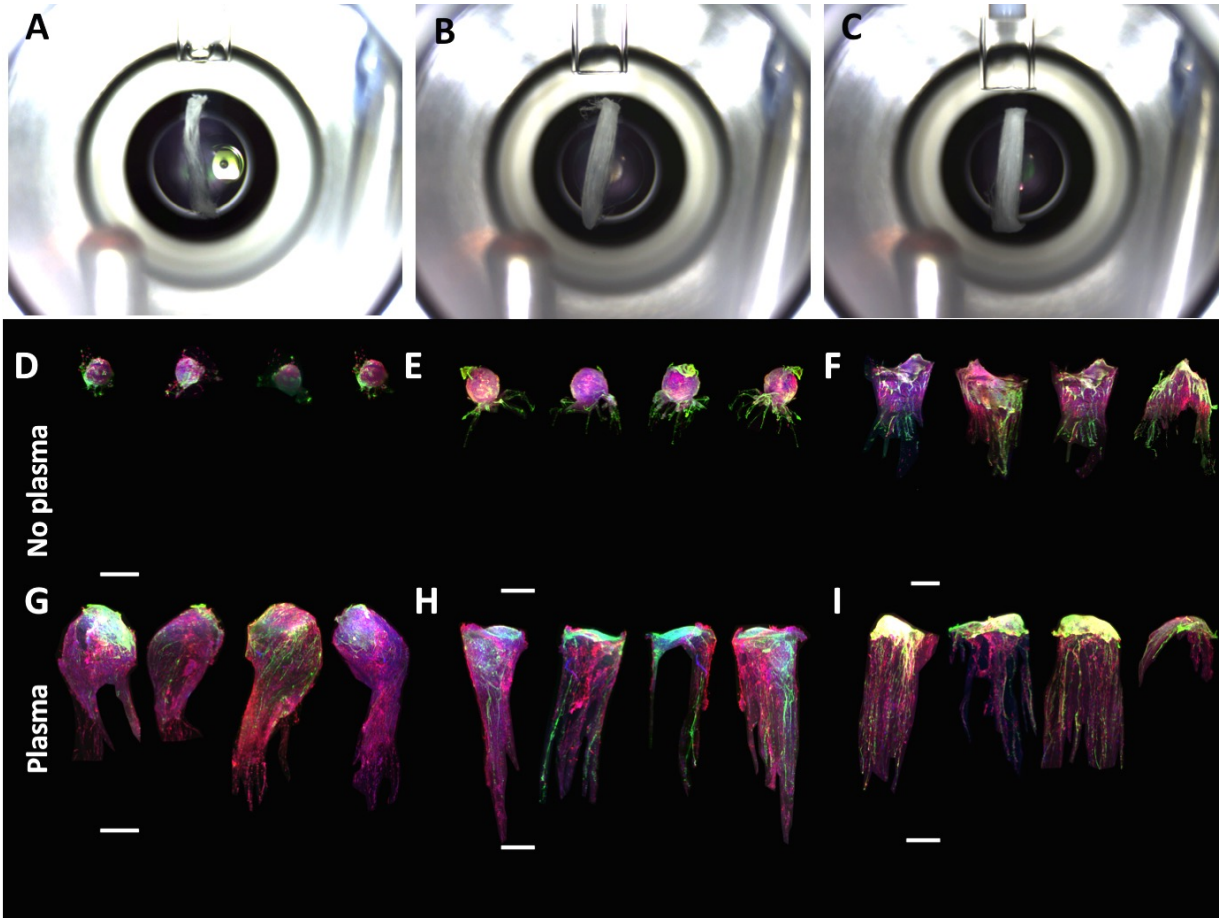

Figure 67 DRG outgrowth on conduits with internal fibre scaffolds of different densities

DRGs from EDD 12 chick embryos were cultured on 5 mm long PEG conduits filled with either 10, 20 or 40 % of 10 µm PCL fibres. After 7 days of culture, scaffolds were removed from conduits, fixed and immunocytochemically labelled for Schwann cell-specific S100β (red) and axon-specific βIII Tubulin protein (green). Nuclei were labelled with DAPI (blue). Fibre scaffolds that filled conduits to A) 10 %, B) 20 % and C) 40 % were embedded in agarose gel and mounted in glass capillaries for light-sheet imaging. Scaffolds were imaged in full using z-stacks to capture sample depth and sample rotations of 0, 90, 180 and 270° (from left to right in images D – I) to visualise the entire sample body. Air plasma-modified scaffolds with G) 10 %, H) 20 % and I) 40 % fibre fillings were compared to unmodified PCL fibre scaffolds that filled conduits to D) 10 %, E) 20 % and F) 40 %. Scale bar = 0.5 mm. Representative images are shown of three experimental repeats.

The images in Figure 67 were further quantified in regard to average and maximum outgrowth of axons from DRG bodies on PEG conduits filled with either air plasma-modified or unmodified 10, 20 or 40 % 10 µm fibres. The outgrowth of Schwann cells was not presented herein for clarity and because Schwann cell outgrowth distances did not

significantly differ from axon outgrowth distance under any circumstances. As can be seen from Figure 68 A, air plasma-modified PCL fibre scaffolds supported on average a significantly longer outgrowth of axons, compared to unmodified fibre scaffolds, which were not affected by fibre density. Outgrowth distance was similarly low between unmodified fibre scaffolds that filled conduits to 10, 20 and 40 % and measured in average 0.49 ± 0.43 mm, 0.62 ± 0.19 mm and 0.56 ± 0.16 mm, respectively (Figure 68 A). Conversely, air plasma-modified conduits with 20 % of fibres showed a significantly longer axon outgrowth in comparison to conduits filled with 40 % of fibres which accounted for 1.87 ± 0.68 and 1.17 ± 0.52 mm, respectively (Figure 68 A).

Similar to data reported in Figure 68 A was observed in Figure 68 B when studying maximum outgrowth distance of axons along fibre scaffolds. Between unmodified fibre scaffolds of different densities there was no significant difference in maximum axon outgrowth, where axonal outgrowth on small (10 %), medium (20 %) and large (40 %) fibre scaffolds measured 1.17 ± 1.0, 1.26 ± 0.6 and 1.15 ± 0.26 mm, respectively. There was however a significant increase in axon length when fibre scaffolds were air plasma-modified prior to DRG culture (Figure 68 B). Conduits filled with 20 % air plasma-modified fibres supported maximum axon outgrowth of 3.32 ± 0.68 mm, significantly longer than conduits with 40 % air plasma-modified fibres (2.4 ± 1.18 mm) (Figure 68 B). There was also increased variability in maximum axon outgrowth in both 10 and 40 % densities in comparison to 20 % density scaffolds (Figure 68 B).

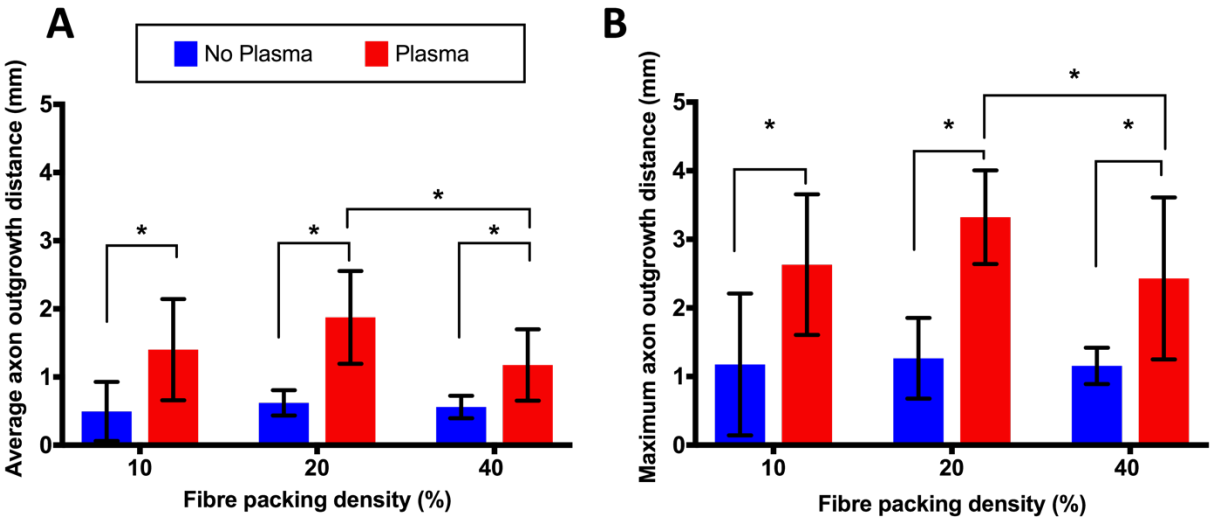

Figure 68 **Quantitative analysis of DRG outgrowth on conduits with fibre scaffolds of different densities**

Quantitative analysis of chick embryo (EDD 12) DRG outgrowth based on light-sheet microscope images shown in Figure 67 regarding A) the average and B) the maximum axon outgrowth after 7 days of culture. PEG conduits of 5 mm in length were either filled with air plasma-modified or unmodified 10 µm PCL fibres which accounted for 10, 20 or 40 % of the conduit. Values are presented as mean ± SD of three experimental repeats. Statistical differences were indicated as * $p<0.05$ and conducted using a two-way ANOVA with Tukey's multiple comparisons test.

6.4.6. DRG outgrowth in the middle of fibre scaffolds with different fibre density

Section 6.4.5 presented the DRG outgrowth inside NGCs with internal PCL fibre scaffolds of different densities imaged by LSM. Afterwards, air plasma-modified scaffolds were sectioned with a cryostat (data is presented in Figure 69). It is of note that the scaffold sections cannot be used to gather information regarding cell outgrowth distance, but instead could provide information regarding cell outgrowth within the core of fibre scaffolds as it was not possible by LSM to examine this core region. As seen in Figure 69, fibre scaffolds were successfully sectioned and the alignment of fibres were predominantly maintained. There was a difference in fibre scaffold thickness which increased with increasing fibre density in the conduits (Figure 69 top to bottom row). Irrespective of the fibre density, axons and Schwann cells were in close proximity to each

other as could be seen through co-localisation of axon- and Schwann cell-specific fluorescent signals (Figure 69). Analysis of sections furthermore demonstrated that both axons and Schwann cells grew along fibres on the scaffold exterior as well as in the centre or core. However, in the core of 20 and 40 % density scaffolds there was a greater degree of axon and Schwann cell growth (Figure 69, middle and bottom row) in comparison to the 10 % density scaffolds (Figure 69, top row).

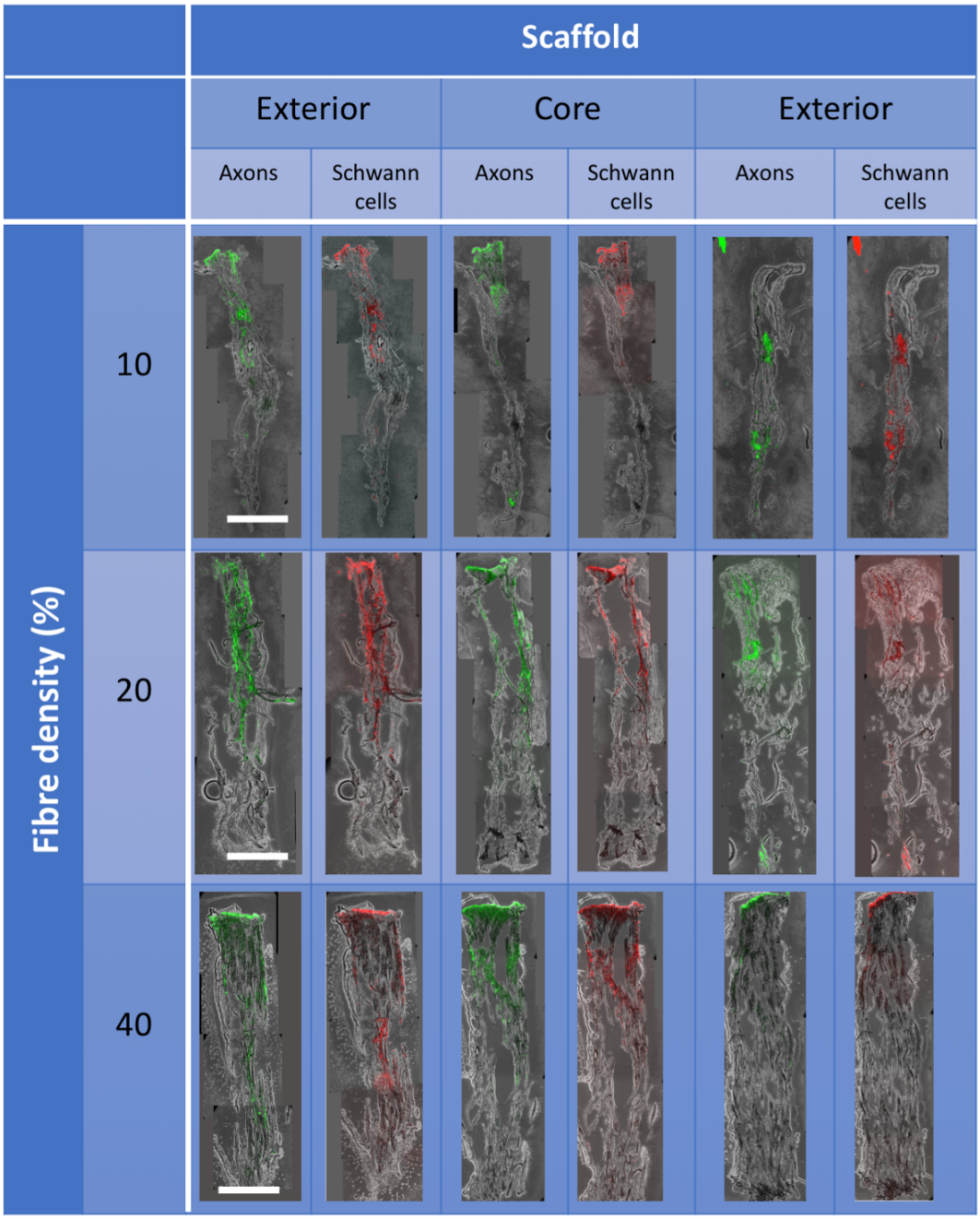

Figure 69 Sections of fibre scaffolds with different densities

Cryosections (30 µm thick) of air plasma-modified 10 µm fibre scaffolds that filled 5 mm long PEG conduits to 10, 20 and 40 % and were immunocytochemically labelled and imaged by LSM prior to sectioning (Figure 67). The outgrowth of axons and Schwann cells is visualised in green (βIII Tubulin) and in red (S100β), respectively. The fibre scaffold was visualised under brightfield (grey). Scaffolds were presented as the scaffold exteriors and core (also see 6.3.10). The top of sections represents the scaffold top which carried DRGs for culture. Representative images are shown from sections of scaffolds of two experimental repeats. Scale bar = 1 mm (applies to all images of the same row).

6.4.7. Response of DRG outgrowth to 10 µm fibre scaffolds in extended cultures

Based on the findings in sections 6.4.4 and 6.4.5, this section investigated the performance of PEG conduits filled to 20 % density with aligned and air plasma-modified 10 µm fibres in extended DRG cultures for 21 days. The outgrowth of axons and Schwann cells was compared between unmodified and air plasma-modified fibre scaffolds on day 7 and 21. Figure 70 shows LSM micrographs of axon and Schwann cell outgrowth from DRG bodies, immunocytochemically labelled for βIII Tubulin and S100β, respectively. There was a clear difference in axon and Schwann cell outgrowth lengths between unmodified and air plasma-modified fibre scaffolds on day 7 (Figure 70 A and B). After 21 days, both unmodified control and plasma-modified scaffolds showed longer outgrowth distances in comparison to day 7 (Figure 70 C and D). However, greater axon and Schwann cell outgrowth lengths were seen on air plasma-modified scaffolds in comparison to control samples (Figure 70 C and D). Interestingly, after 7 days, air plasma-modified scaffolds supported longer outgrowth distance in comparison to unmodified PCL scaffolds on day 21 (Figure 70 B and C).

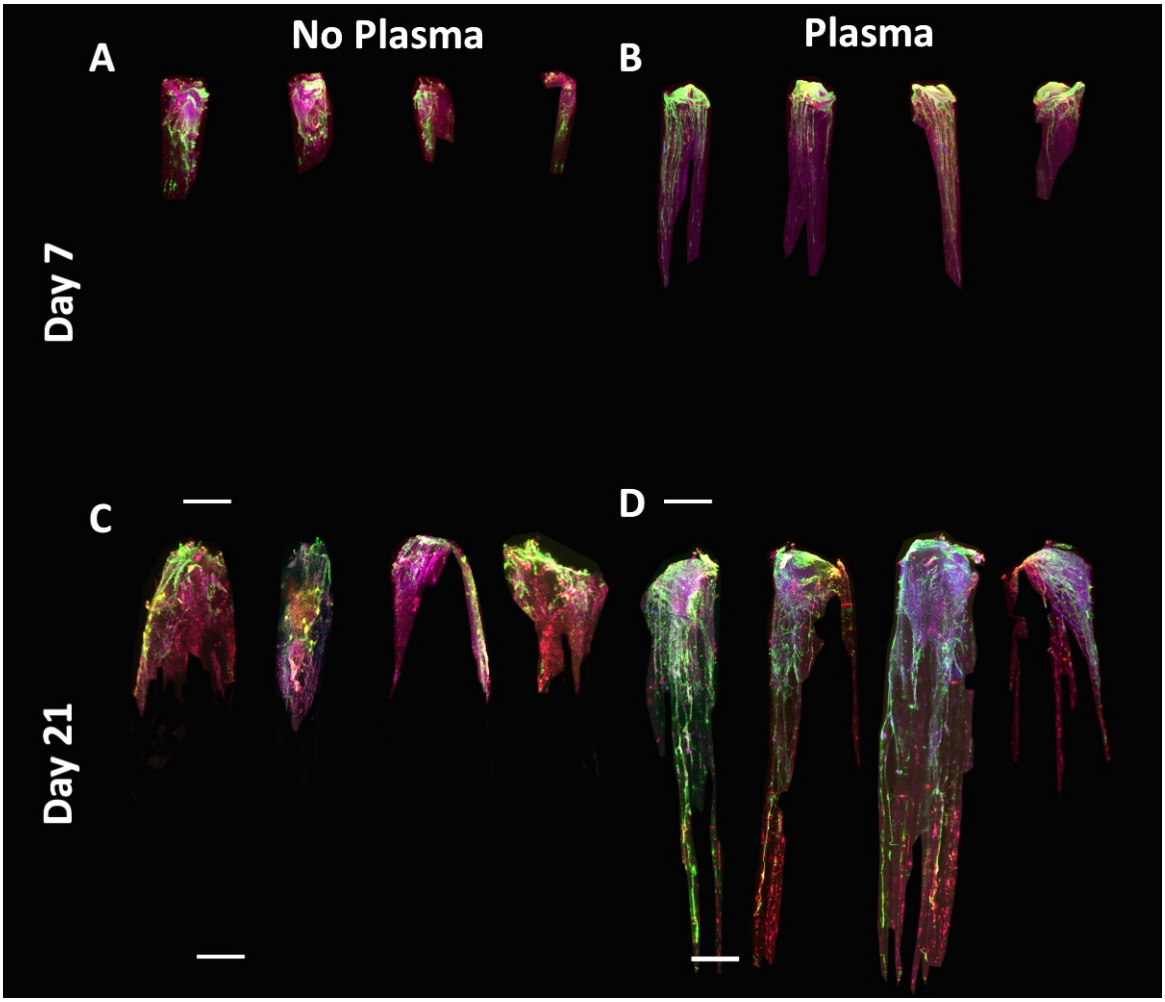

Figure 70 Extended DRG culture on fibre scaffolds inside NGCs

LSM images showing outgrowth of EDD 12 chick embryo DRGs on 10 µm PCL fibre scaffolds that filled 5 mm long PEG conduits to 20 %. Axons and Schwann cells were visualised by immunocytochemistry for βIII Tubulin (green) and S100β (red), respectively. Data was compared between A) unmodified and B) air plasma-modified conduits on day 7 and (C, D) day 21. Imaging was conducted in z-stacks and scaffolds rotated every 90° (0, 90, 180 and 270° from left to right) to capture the entire scaffold structure. Scale bar = 0.5 mm. Representative images are shown of three experimental repeats.

Quantification was conducted for average and maximum outgrowth distance of axons and Schwann cells which data is summarised in Figure 71. Significantly greater axon and Schwann cell outgrowth distances were measured on air plasma-modified scaffolds in comparison to unmodified samples on both day 7 and day 21. This applied to the average and maximum outgrowth assessed. On day 7, the average and maximum axon outgrowth lengths were 0.15 ± 0.1 mm and 0.54 ± 0.29 mm, respectively for unmodified scaffolds and were significantly longer on air plasma-modified samples with lengths of 0.94 ± 0.4

mm and 2.52 ± 0.36 mm, respectively measured. On day 21, unmodified fibre scaffolds supported an average and maximum axon outgrowth of 0.46 ± 0.32 mm and 1.15 ± 0.71 mm, respectively (Figure 71). In comparison, air plasma-modified scaffolds supported the average and maximum outgrowth of axons significantly better with 1.73 ± 0.24 mm and 4.26 ± 0.91 mm measured regeneration in the 5 mm long conduit. All samples supported a similarly long outgrowth of axons and Schwann cells with the exception of air plasma-modified scaffolds on which Schwann cells showed on average significant greater outgrowth distance than axons on day 21 (Figure 71 A). Interestingly, there were also differences in axon and Schwann cell outgrowth on the different samples between day 7 and 21. No significant increase in average and maximum axon and Schwann cell outgrowth was seen on unmodified fibre scaffolds between day 7 and 21 (Figure 71). However, a significantly longer cell outgrowth was detected on air plasma-modified scaffolds on day 21 in comparison to day 7 (Figure 71).

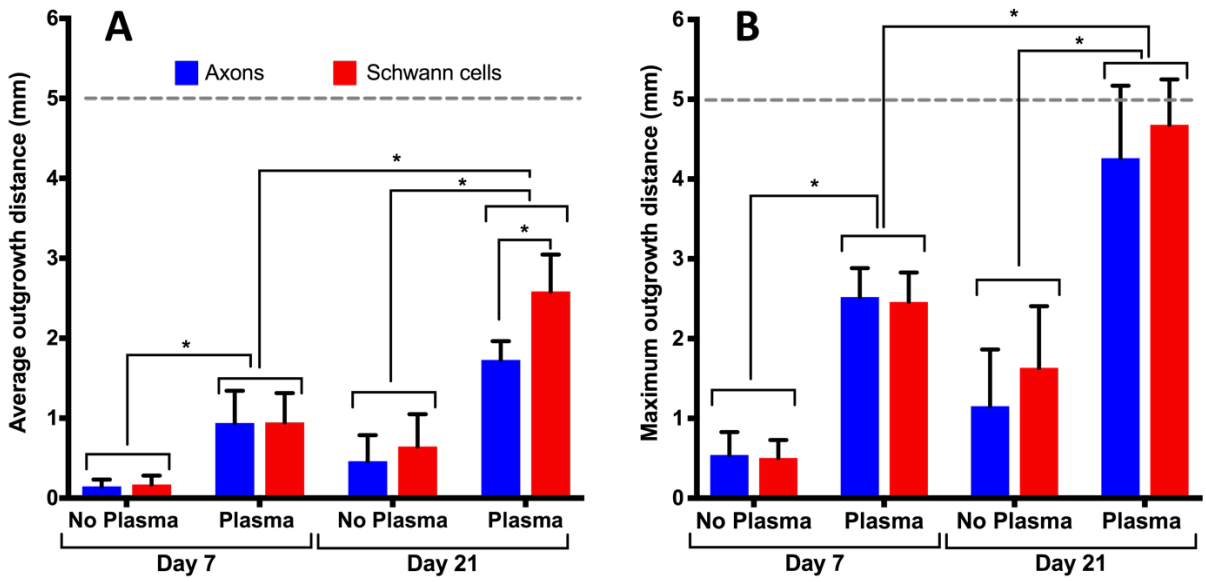

Figure 71 DRG outgrowth analysis on fibre scaffolds after 21 days

Quantitative analysis of LSM images from Figure 70 regarding A) the average and B) the maximum outgrowth of axons and Schwann cells from DRG bodies after 7 and 21 days. DRG bodies from EDD 12 chick embryos were cultured on top of 5 mm long PEG conduits which were filled with 20 % of either unmodified or air plasma-modified 10 µm PCL fibres. Values presented as mean + SD of three experimental repeats. Dotted lines indicate the conduit length of 5 mm. Two-way ANOVA with Tukey's multiple comparisons test was used to test for statistical differences which were indicated with * $p<0.05$.

6.4.8. Isolation of primary Schwann cells from chick embryos

The culture of primary chick Schwann cells on fibre scaffolds inside NGCs prior to the introduction of chick DRG cultures required the isolation and purification of Schwann cells from peripheral nerves in the chick embryo. Herein, Schwann cells isolated from the sciatic nerve of EDD 12 chick embryos. The purification of Schwann cells from fibroblasts followed the basic principle as shown by Kaewkhaw *et al.* [285] using a medium of DMEM-D-Valine. It was assumed that embryonic chick Schwann cells expressed D-amino acid oxidase (DAAO) which converts the non-essential amino acid D-Valine into L-Valine, essential for cell growth and survival. It was assumed that the expression of DAAO was absent in chick embryo fibroblasts which would result in cell death due to the depletion of essential L-Valine amino acids over time. After the isolation of Schwann cells, the morphology of cells was examined under a light microscope and results are shown in Figure 72 A. From this figure, it is apparent that the number of cells increased over time, reaching confluence by day 7. On day 1, there was a mix between cells of elongated bi- or tripolar shape and dying cells which showed a round morphology. The number of dying round-shaped cells decreased on day 3 and was absent on day 7. With increasing cell number a change in cell orientation was observed which was particularly apparent on days 5 and 7, where cells orientated to aligned and mostly parallel swirl-like formations (Figure 72 A). Figure 72 B shows isolated cells at passage 2, immunocytochemically labelled for the typical Schwann cell phenotype markers GFAP and S100β. All cells stained positively for both markers which were present in the cell cytoplasm in red with nuclei showing in blue. No fibroblasts were identified in these cultures as no cells were identified which were just positive for cell nuclei marker without the presence of Schwann cell markers (Figure 72 B).

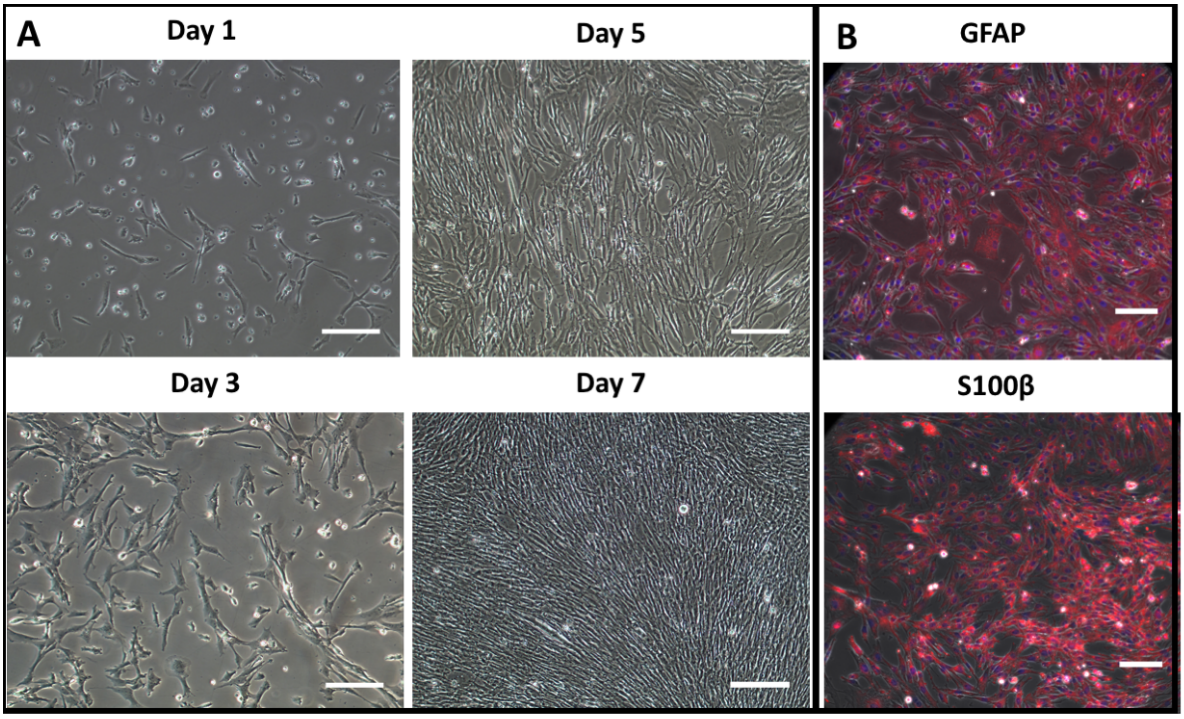

Figure 72 Primary Schwann cells from chick embryos

Primary Schwann cells were isolated from EDD 12 chick embryo sciatic nerves and cultured in DMEM-D-Valine to purify cultures from fibroblasts. Cell growth and morphology were documented in A) light microscope images on day 1, 3, 5 and 7. Scale bar = 200 µm B) At passage 2, cells were immunocytochemically labelled for the Schwann cell markers GFAP (red, top image) and S100β (red, bottom image) and nuclei subsequently labelled with DAPI (blue). Imaging was conducted under fluorescence and brightfield. Scale bar = 200 µm. Representative images are shown of two experimental repeats.

6.4.9. DRG outgrowth on fibre scaffolds pre-seeded with chick Schwann cells

In order to analyse the effect of different numbers of primary chick Schwann cells on the outgrowth of axons from DRG bodies along fibre scaffolds, 5 mm long PEG conduits were filled to 20 % with air plasma-modified 10 µm fibres. Isolated pcSCs were seeded in numbers of either 5×10^4 and 15×10^4 cells inside conduits. After 4 days, EDD 12 chick embryo DRGs were cultured on top of conduits with and without pre-seeded pcSCs for another 7 days. Figure 73 shows variations in axon outgrowth along those scaffolds. Differences in pcSC distribution can be clearly seen, where Schwann cells in Figure 73 A originate from the DRG body alone, Figure 73 B – D demonstrate fibre scaffolds completely covered in Schwann cells which originated both from DRG bodies and the pre-seeding process. Figure 73 D shows an even distribution of pcSCs seeded inside

conduits prior to DRG culture. The most prominent axon outgrowth was found on fibre scaffolds without pre-seeded Schwann cells which extended along the scaffold fibres (Figure 73 A). Furthermore, fibre scaffolds with a smaller number of pre-seeded pcSCs (5 $\times$ 10^4 cells) showed more and longer axons (Figure 73 B) in comparison to scaffolds with three times more Schwann cells (15 $\times$ 10^4 cells) (Figure 73 C).

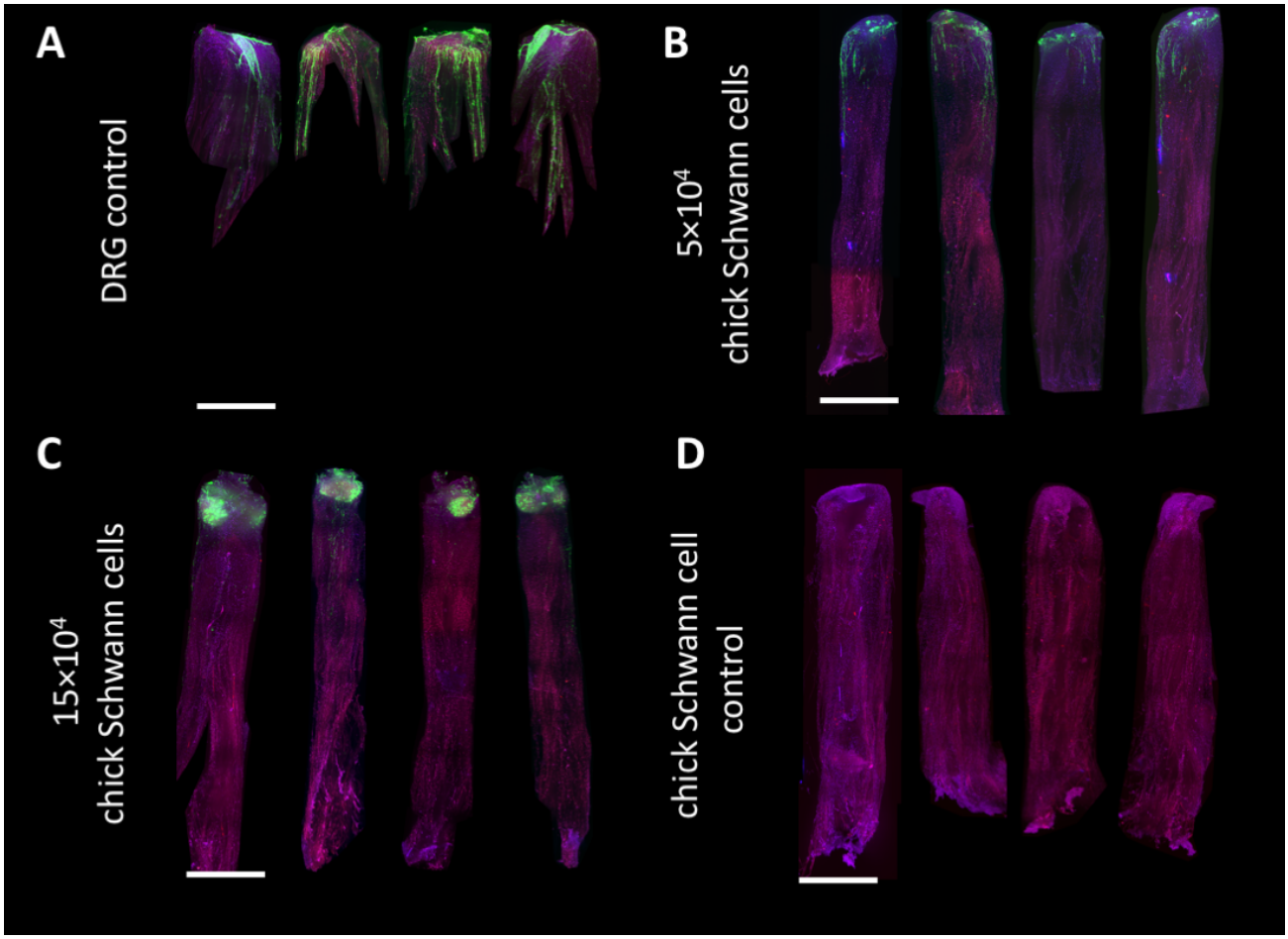

Figure 73 Differences in DRG outgrowth on fibre scaffolds with pre-seeded Schwann cells

LSM images of axon outgrowth from DRG bodies inside 5 mm long PEG conduits filled to 20 % with air plasma-modified 10 µm PCL fibres. EDD 12 chick DRGs were cultured on A) fibre scaffolds alone or fibre scaffolds which were pre-seeded with primary chick Schwann cells in numbers of B) 5×10^4 or C) 15×10^4 cells per conduit. Chick Schwann cell cultures in conduits were maintained for 4 days prior to DRG culture which lasted another 7 days. D) fibre scaffolds with 5×10^4 chick Schwann cells alone cultured for 4 days. Axons (green) and Schwann cells (red) were visualised through βIII Tubulin and S100β, respectively. Nuclei were labelled with DAPI (blue). LSM was performed in z-stacks (maximum intensity projections) and scaffolds presented at 0, 90, 180 and 270° (from left to right). Scale bar = 1 mm. Representative images are shown of three experimental repeats.

Images in Figure 73 were further quantified and the average and maximum outgrowth distance of axons measured. On average, axons from DRG bodies measured 0.93 ± 0.46 mm, 1.07 ± 0.27 mm and 0.7 ± 0.22 mm on fibre scaffolds alone and on scaffolds with either 5×10^4 or 15×10^4 pcSCs, respectively (Figure 74 A). There was no statistical

difference in average axon outgrowth between samples. However, there was a difference in maximum axon outgrowth (Figure 74 B). Axons grew significantly greater distances on fibre scaffolds that were pre-cultured with 5×10^4 pcSCs (2.69 ± 0.29 mm) in comparison to fibre scaffolds with a greater number of pcSCs (1.7 ± 0.5 mm) (Figure 74 B). However, there was no significant difference in maximum axon lengths between fibre scaffolds alone and the same scaffolds pre-seeded with pcSCs. It was additionally noted that data points for measured maximum axon lengths showed a greater variation on fibre scaffolds alone with a standard deviation of 1 mm. In comparison, standard deviations on scaffolds with 5×10^4 and 15×10^4 pcSCs accounted for 0.29 mm and 0.5 mm, respectively (Figure 74 B).

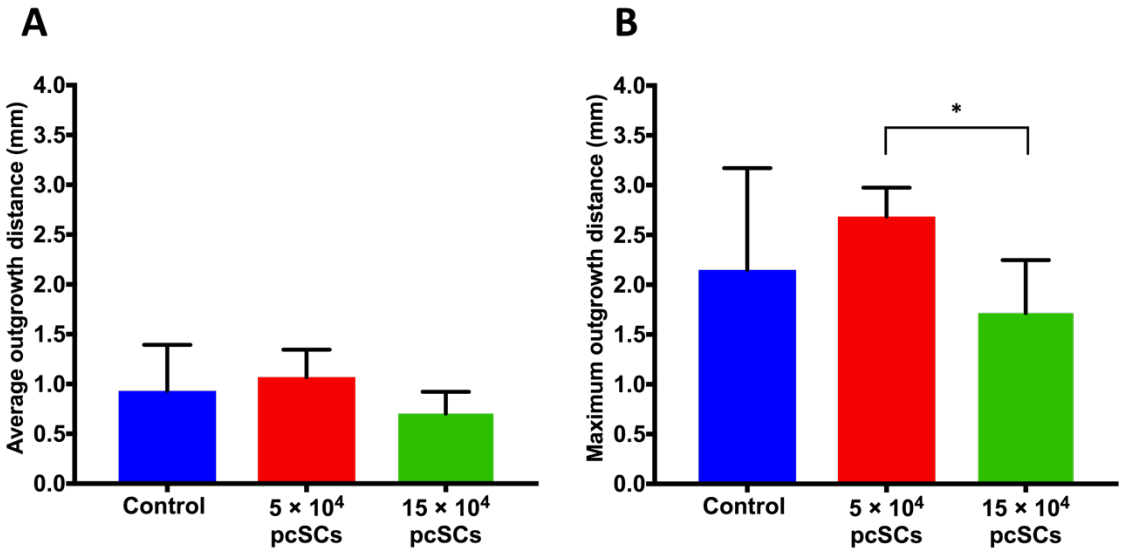

Figure 74 Analysis of DRG outgrowth on fibre scaffolds pre-seeded with Schwann cells

Quantitative analysis of LSM images (Figure 73) on A) average and B) maximum axon outgrowth from DRGs in 5 mm long PEG conduits filled with 20 % air plasma-modified 10 µm PCL fibres alone or pre-seeded with Schwann cells prior to DRG culture. Schwann cells were isolated and purified from EDD 12 chick embryo sciatic nerves and seeded on conduits with fibre scaffolds in numbers of either 5×10^4 or 15×10^4 cells per conduit. After 4 days of pcSC culture, conduits were cultured with EDD 12 chick embryo DRGs for 7 days. Values are presented as mean + SD of three experimental repeats. One-way ANOVA with Tukey's multiple comparisons test was performed to test for statistical differences which were indicated as * $p<0.05$.

6.4.10. DRG outgrowth on P3HB fibre scaffolds

In this section, the performance of gyrated aligned PHA fibres were assessed for use as internal NGC scaffolds for peripheral nerve repair. This work was conducted in collaboration with Dr. Pooja Basnett and Professor Ipsita Roy from Westminster University (UK). Professor Roy and Dr. Basnett have a track record in the fabrication of PHAs and processing into microfibres by gyrospinning. There was a specific interest in using the herein described 3D DRG culture model to assess the performance of P3HB and P3HB/P3HO-*co*-3HD 80:20 blend fibres directly inside NGCs. This demonstrated an opportunity to validate the applicability of the model developed using embryonic chick DRGs and LSM for testing the regenerative performance of other fibre scaffold designs and materials.

Both P3HB and P3HB/P3HO-*co*-3HD 80:20 blend fibres were incorporated inside PEG conduits with a filling density of 20 %. After 7 days of EDD 12 chick embryo DRG cultures, cells were immunocytochemically labelled and imaged with LSM which results are summarised in Figure 75. Both P3HB and P3HB/P3HO-*co*-3HD 80:20 blend fibres supported the outgrowth of axons and Schwann cells from the DRG body along the fibre scaffolds towards the conduit end as shown in Figure 75 A and B. A dense outgrowth of Schwann cells was observed on both fibre scaffolds which populated the entire scaffold width. Axons were found in co-localisation to Schwann cells but Schwann cells were also detected without the presence of axons (Figure 75 A and B). However, the outgrowth of Schwann cells appeared longer on P3HB fibre scaffolds (Figure 75 A) in comparison to P3HB blend fibres (Figure 75 B).

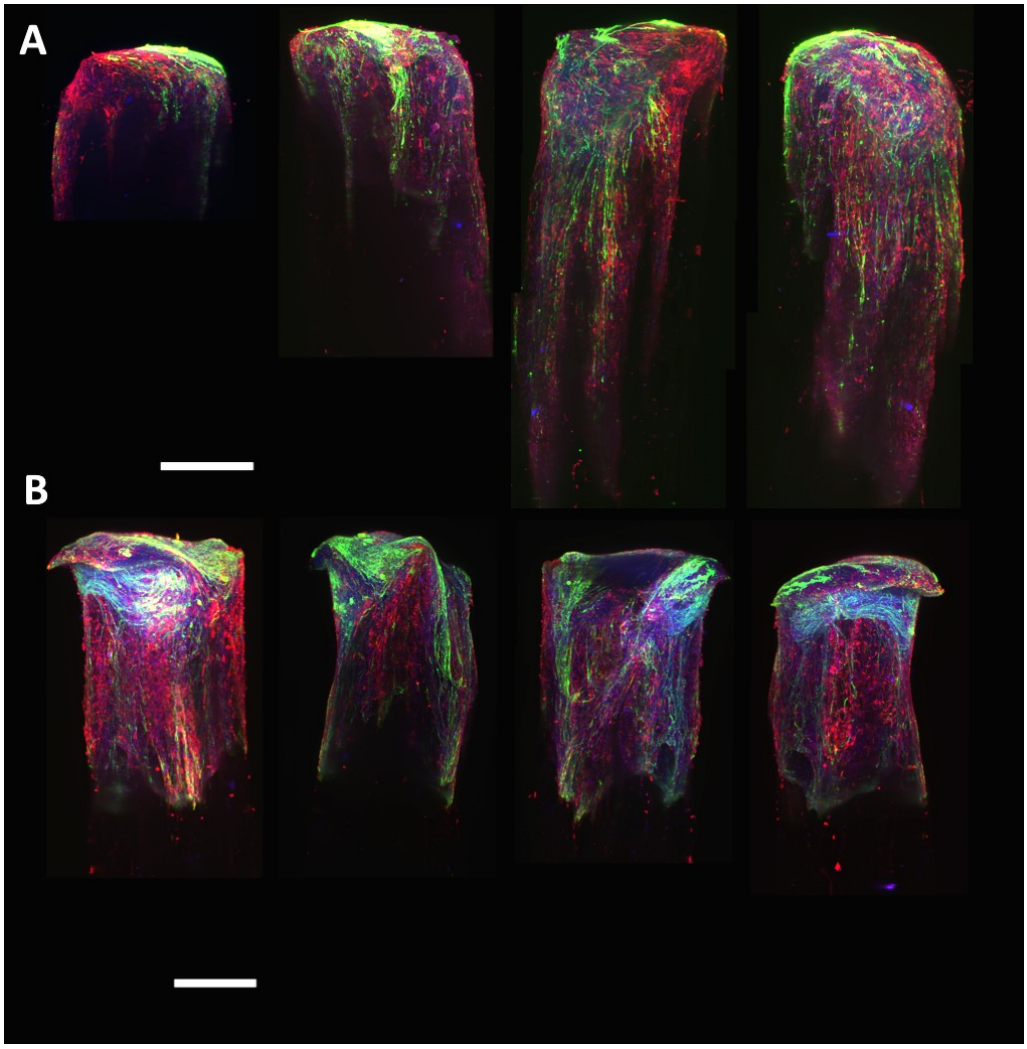

Figure 75 DRG outgrowth on P3HB fibre scaffolds

LSM images showing the outgrowth of axons (green) and Schwann cells (red) from DRG bodies along aligned A) P3HB fibres and B) P3HB/P3HO-*co*-3HD 80:20 blend fibre scaffolds. Polymer was fabricated and gyrospun to fibres by Dr. Pooja Basnett (University of Westminster). Fibres accounted for 20 % of the lumen of 5 mm long PEG conduits. DRGs were dissected from EDD 12 chick embryos and cultured on top of conduits for 7 days. Scaffolds were fixed and axons and Schwann cells visualised through βIII Tubulin (green) and S100β (red), respectively using immunocytochemistry. Nuclei were labelled with DAPI (blue). LSM was performed in z-stacks and scaffolds shown in angles of 0°, 90°, 180° and 270° (left to right). Scale bar = 0.5 mm. Representative images are shown of three experimental repeats.

Further quantifications showed that both fibre scaffolds performed equally well in supporting axon and Schwann cell outgrowth. The average axon and Schwann cell outgrowth on P3HB fibres measured 0.59 ± 0.16 mm and 0.75 ± 0.2 mm, respectively

(Figure 76 A). Similar outgrowth distances were detected on P3HB/P3HO-*co*-3HD 80:20 blend fibres with 0.49 ± 0.19 mm and 0.52 ± 0.17 mm for axons and Schwann cells, respectively (Figure 76 A). On average, the longest axon and Schwann cell outgrowth was detected on P3HB fibres with a maximum outgrowth of 1.39 ± 0.41 mm and 1.45 ± 0.42 mm, respectively (Figure 76 B). In comparison, the average maximum outgrowth measured 1.23 ± 0.41 mm for axons and 1.26 ± 0.39 mm for Schwann cells on the P3HB/P3HO-*co*-3HD 80:20 blend fibres (Figure 76 B). Although Schwann cells appeared to grow out further on P3HB fibres than on P3HB/P3HO-*co*-3HD 80:20 blend fibres, no significant differences could be detected. Overall, statistics confirmed that no differences existed in cell outgrowth between the two fibre groups.

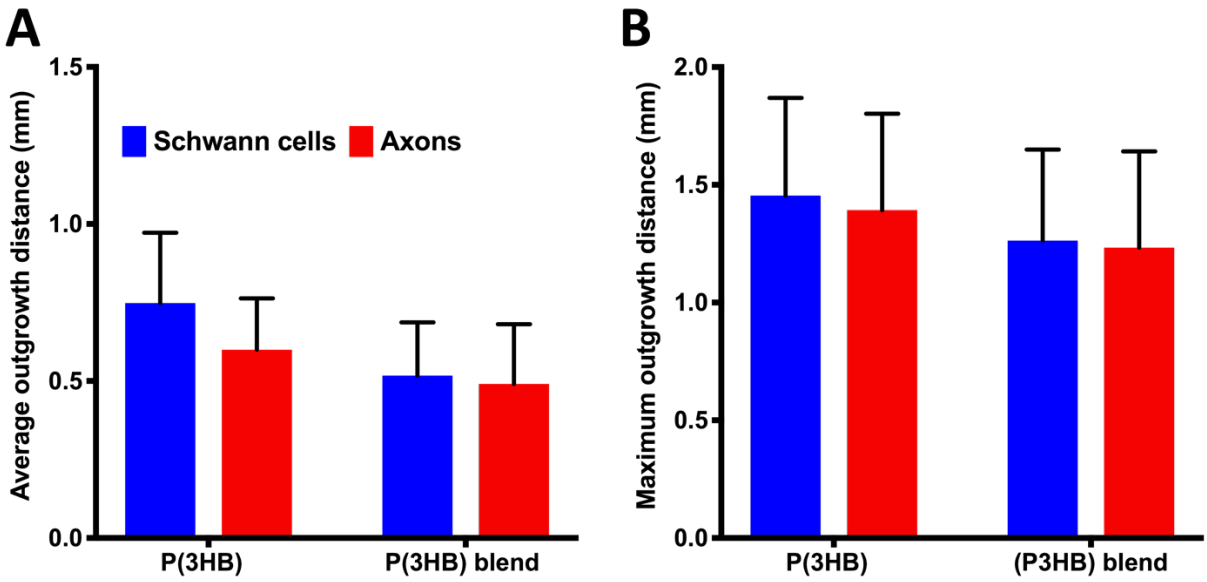

Figure 76 DRG outgrowth analysis on P3HB fibre scaffolds

Quantification analysis of light-sheet images as presented in Figure 75 regarding the A) average and B) maximum outgrowth of axons and Schwann cells from EDD 12 chick DRGs after 7 days of culture. Cultures were performed on P3HB on P3HB/P3HO-*co*-3HD 80:20 blend fibre scaffolds inside 5 mm long PEG conduits with a fibre density of 20 %. Values are presented as mean + SD of three experimental repeats. Unpaired Student t-test was performed to test for statistical differences.

6.5. Discussion

6.5.1. 3D model refinements and chick DRG outgrowth

The aim of this chapter was to refine the reported DRG model which initially showed major limitations in DRG outgrowth. It was of particular note that only half of all dissected adult rat DRGs attached to NGCs and furthermore showed poor outgrowth, where 8 dissected DRGs failed to grow from a starting sample of 10. This resulted in a small number of experimental replicates which compromised the reliable interpretation of data. Despite this, when DRGs fully attached and grew out, the model showed promising results in supporting axon and Schwann cell outgrowth. However, refinements were needed to make the reported model a more attractive tool for assessing internal NGC scaffolds by developing a more reliable 3D DRG model in terms of DRG attachment and outgrowth. This would result in a decrease in the number of animals needed and further improve its ethical acceptance.

Herein, refinements were made by using chick embryo DRGs instead of adult rat DRGs. DRGs were dissected from EDD 12 chick embryos which at this time point classified fall outside the Animals Scientific Procedures Act 1986 [282]. This method is a valid animal replacement technique [363] and therefore enhances the previous model with regard to ethical acceptance. The use of chick embryo DRGs additionally showed successful outcomes on unmodified scaffolds, where 82 % of DRGs attached and outgrowth rates doubled, accounting for 55 %. Interestingly, air plasma modification of fibre scaffolds did not influence the attachment of DRGs as there was no significant difference in numbers of attached DRGs between unmodified control and plasma-modified conduits but there was a significant reduction in attached DRGs on TCP. However, both TCP and air plasma-modified scaffolds significantly enhanced outgrowth incidence in comparison to unmodified fibres. This indicated that the use of embryonic chick DRGs alone, irrespective of surface modification, enhanced DRG attachment and incidence versus adult rat DRGs. As the majority of studies chose embryonic versus adult DRGs, (e.g. [271, 274]), it is likely that other authors noticed similar findings to the ones herein, but there are still no reports that mention or explain such differences. Herein an attempt was made to explain these findings. It seemed possible that observed variations in DRG softness during the dissection process of adult rats and chick embryos was related to

differences observed in attachment, where it was noted that chick embryo DRGs were softer than adult rats. This may be explained with the findings of Duband *et al.* who reported increased integrin, laminin and collagen IV expression in the DRGs of chick embryos but which numbers were significantly reduced after hatching [364]. Assuming this reduction can be translated to adult rat DRGs, it may thus be suggested that 1) the increase in collagen content within embryonic chick DRGs had increased adherent potential, favouring the adhesion of DRG bodies to NGCs and 2) that the increased integrin expression in embryonic chick DRGs might have furthermore enhanced cell attachment to scaffolds through integrin binding to, e.g. RGD binding domains.

Of particular interest was the observed difference in DRG attachment between NGCs with fibre scaffolds and flat TCP surfaces. This finding indicated that 1) DRG adhesion was dependent on structure, where NGCs supported DRG attachment significantly better than TCP and 2) that chemical surface composition did not affect the attachment of DRGs as initially assumed. This might be explained with the three-dimensional structure of conduits which presented a greater number of potential attachment points for DRGs in comparison with a two-dimensional flat TCP surface. Furthermore, it is likely that the conduit structure presented some kind of protection for DRGs, e.g. through the conduit walls, from culture medium that was added shortly after DRGs were placed on the substrates. Due to this missing protection, DRGs on TCP were more likely to be washed away.

Although air plasma modification did not affect DRG attachment, it had a significant influence on DRG outgrowth incidence which increased from 55 % to 85 % after plasma treatment. Furthermore, the growth distance of axons and Schwann cells was more than five times as long on air plasma scaffolds in comparison with unmodified controls. These findings support previous research in this thesis which identified similar positive correlations between air plasma-modified PCL films and axon incidence and outgrowth (Figure 56, Chapter 5). This effect is discussed in detail in Chapter 5, where the given explanations may further be applied to this chapter. In brief, it seems likely that the increase in surface polarity through air plasma treatment increased the affinity of protein binding (adsorption) to plasma-modified fibre scaffolds in comparison to the control. This, in general terms, is a basis for an increase in available RGD domains on the

surface of air plasma-modified fibre scaffolds favouring the outgrowth of axons and Schwann cells along the scaffold inside the conduits. This would further explain the similar DRG outgrowth incidences between NGCs with air-plasma modified fibre scaffolds and TCP as both surfaces exhibited surface modifications. This hypothesis is supported by findings of Recek *et al.* who report that proteins from cell culture medium adsorb faster and to a greater extent on surfaces modified by oxygen plasma in comparison to unmodified samples [219]. The findings of Lopis-Hernandez *et al.* might give additional explanation to what has been found herein, where the authors showed that increasing hydroxyl groups on substrate surfaces increased the expression of vinculin and integrin in the cell, and furthermore showed greater numbers of phosphorylated focal adhesion kinase (FAK) [343]. Together with Lee *et al.*'s findings who reported that an upregulation of FAK and integrin significantly enhanced neurite outgrowth [344], it is likely that a potential upregulation of cell adhesion molecules arises in cells grown on air plasma-modified fibre scaffolds resulting in increased DRG outgrowth, compared to control. Taken together, these findings convincingly showed the positive effects of air plasma treatment on DRG outgrowth and hence contribute to understanding and better designing optimal 3D models for peripheral nerve.

The reported model was originally proposed to either be used as a fundamental model of peripheral nerve to, e.g. study disease, (e.g. neuropathies), develop and test drugs, or as a model of peripheral nerve regeneration for evaluating and comparing internal NGC guidance scaffolds to aid nerve injuries. Although the reported model already showed useful applications, these findings could further significantly enhance its applicability and impact. This concerns the development of a reliable peripheral nerve model with robust cell outgrowth and limited chance of outgrowth failure. Furthermore, data indicated that air plasma-modified PCL fibre scaffolds would perform significantly better as internal NGC scaffolds than PCL scaffolds without surface modifications. This finding supports previous research which showed that air plasma modification enhanced the regenerative performance of hollow PLA conduits in a 10 mm rat sciatic nerve gap [220].

Of particular note was the observed increase in DRG outgrowth incidence after air plasma treatment (around 80 %). I would therefore hypothesise this increase in outgrowth seen *ex vivo* due to air plasma treatment would also result in improved axonal

regeneration *in* vivo. This is of particular importance in order to decrease the chance of potential NGC failure in patients. It is additionally believed that success rates might further increase *in vivo* due to the naturally occurring immune response after injury which among others drives nerve regeneration [57] but could not yet be represented in this model.

A significant difference in neurite incidence and length was found in Chapter 3 between 1 and 10 µm PCL fibres. This chapter therefore investigated whether the application of air plasma-modified 1 and 10 µm fibres showed similar outcomes to what has been found on unmodified fibres. First this study confirmed previous findings, where neurite length and incidence were significantly increased on unmodified 10 µm fibres in comparison to 1 µm ones (Figure 31, Chapter 3). Interestingly, however, there was no significant difference in neurite outgrowth between the two fibre groups after air plasma treatment nor a significant difference between unmodified and air plasma-modified fibres. This finding was rather surprising as Chapter 5 showed that air plasma-modified PCL films significantly increased neurite incidence in comparison to unmodified films. Although, there might have however been an indirect difference in neurite outgrowth between plasma-modified 1 and 10 µm fibres when comparing results to the TCP control. This showed a significant increase in neurite incidence on modified 10 µm fibres in comparison to TCP but where modified 1 µm fibres and TCP showed similar incidence values. Furthermore, neurites were significantly shorter on modified 1 µm fibres than on TCP but neurons on TCP and modified 10 µm fibres showed similar outgrowth lengths. This suggests that the material surface characteristics have a much greater effect on neurite outgrowth than fibre diameter. Where the beneficial effects of air plasma treatment act in such a way that they negate any negative effects from the fibre diameter.

This finding is supported by the observation that TCP had unlimited space available for neurites to extend on which led to the conclusion that the measured neurite lengths on TCP represented the maximum outgrowth that could be reached, as no physical barriers might have restricted outgrowth capacity. On the contrary, outgrowth space on fibres was physically restricted as the maximum theoretical outgrowth distance was defined by the length between two neurons on a fibre. It is highlighted in Chapter 3 that a

difference in axon directionality to fibre alignment between 1 and 10 µm fibres existed, which showed that axons on 10 µm aligned with fibre direction, where 1 µm fibres showed a large number of axons that extended across several fibres (see Figure 29). This therefore revealed differences in the available growth space between 10 and 1 µm fibres. Hence, one might hypothesise that neurites on plasma-modified 10 µm fibres might have been longer if more space was available on the fibre. However, it is suggested that neurite lengths on modified 1 µm fibres were already maximum, as space was not as restricted as on 10 µm fibres and hence neurite lengths were likely to be limited by small fibre diameter than by limited available space.

6.5.2. *Ex vivo* evaluations of fibre diameters inside conduits

Although there were no direct differences in neurite outgrowth on air plasma-modified 1 µm versus 10 µm fibres in 2D culture, there was a significant difference when tested in 3D. This study found that air plasma-modified 10 µm fibre scaffolds inside NGCs supported a significantly longer maximum outgrowth of axons and Schwann cells from chick DRGs in comparison to 1 µm fibre scaffolds. Interestingly, fibre diameter did not influence DRG attachment to NGCs but influenced the outgrowth of cells from DRGs inside the conduits. This finding supports the hypothesis made earlier which indicated that DRG attachment was better supported by the structure of the NGC than its internal air plasma-modified scaffolds. In this experiment, chick embryo DRGs attached equally well to NGCs of different fibre scaffolds. This finding was however surprising as earlier findings indicated that bigger fibre diameters significantly increased cell attachment in comparison to 1 µm fibres due to the suggested increase in available RGD domains on the surface of bigger fibre diameters through an increase in surface roughness as a result of longer and deeper surface topographies. It was hence assumed that attachment of DRGs would also be influenced by fibre diameter. As this wasn't confirmed, it might therefore be likely that chick embryo DRG attachment was due predominantly to 'sticky collagen membranes' that physically held DRG bodies on to the substrate.

There was however a difference in DRG outgrowth incidence and length on the different fibre diameters. Outgrowth incidence was significantly reduced on air plasma-modified 1 µm fibres which was similarly poor as when adult rat DRGs were used. Maximum outgrowth lengths of axons and Schwann cells were furthermore significantly shorter on

modified 1 µm fibres in comparison to 10 µm ones. These results match those observed in Chapter 3 which showed significantly shorter neurites and reduced Schwann cell metabolic activity on 1 µm fibres in comparison to 10 µm fibres (see Figure 31 and Figure 37). There are several possible explanations for these results. Firstly, it is assumed that the in Chapter 3 differences in fibre structure between different fibre diameters influenced the likelihood of DRG outgrowth as well as cell outgrowth length. To summarise discussion in Chapter 3, it seems possible that the increased length, area and depth of grooves on the surface of 5 – 13 µm fibres was associated with increased protein adsorption from the culture medium due to increased surface area and roughness which in turn favoured cell adhesion. This is in agreement with other studies which reported an increase in protein and cell adhesion to fibres with increased surface roughness [172, 304, 305]. It was therefore suggested that axon and Schwann cell adhesion was favoured on air plasma-modified 10 µm fibres in comparison to 1 µm fibres. This enhanced adhesion might further explain the increase in outgrowth length as it has been shown that axon growth cone elongation is strongly depending on a sufficient anchoring of its protrusions to matrix [306, 365]. Yang *et al.* highlighted this in particular, where it was shown that fibres with increased topographical features favoured neuronal cell anchoring through filopodia and pseudopodia which in turn led to an extension of microtubules and elongated axons [170].

Findings might be further related to the increase in Schwann cell metabolic activity seen on both unmodified and plasma-modified 10 µm fibres in comparison to 1 µm ones which were reported in Chapter 3 and Chapter 6. It is therefore likely that the metabolic activity of Schwann cells was also increased on air plasma-modified 10 µm fibre scaffolds in NGCs. As Schwann cells secrete trophic molecules such as laminin and neurotrophic factors that are beneficial for axon growth [366], it is believed that increased Schwann cell activities resulted in an increase in trophic molecules and neurotrophic factors in the conduits which hence promoted a better axon growth. This hypothesis agrees with a conclusion made by Janssen *et al.* who mentioned that increased metabolic activity rates in Schwann cells provide an increased neurotrophic factor support within the nerve [367].

Furthermore, this data confirmed that different fibre scaffold parameters, e.g. diameter can be evaluated and compared in the reported model in regard to their regenerative impact in nerve injury. This is the first study that compared fibre scaffolds of different diameters directly inside NGCs in an *ex vivo* model and used this comparison to identify a fibre scaffold that would support nerve regeneration the best. In here, air plasma-modified 10 µm PCL fibre scaffolds were selected as scaffolds supported axon and Schwann cell outgrowth the best among the other diameters tested. In 7 days of culture, up to 2.5 mm of the 5 mm long conduit were populated by axons and Schwann cells. Other studies also measured DRG outgrowth lengths on different guidance substrates, however, differences in culture parameters and setups, e.g. the use of embryonic vs. adult DRGs, embryonic DRGs taken from different development stages, the addition or absence of growth factors and 2D vs. 3D culture setups, make it very difficult to compare results.

Huval *et al.* and Rangappa *et al.*, for example, reported that axons extended up to 3 mm and 5.8 mm on hydrogel channels and PLA microfilaments, respectively, from embryonic rat DRG bodies in 7 and 8 days of culture, respectively [271, 274]. The most relevant publication to the findings herein was however presented by Wen and Tresco, who cultured rat pup DRGs on 5 µm thick polypropylene filaments and measured an axon and Schwann cell outgrowth of around 6 mm after 7 days of culture [150]. Although all studies cultured embryonic DRGs, outgrowth distances were much longer than herein measured. It was however noted that all authors added nerve growth factor (NGF) to DRG culture media which would explain the observed differences in outgrowth length as NGF promotes axon survival and growth [368]. This further points out the current limitations in comparing NGC scaffolds which were developed by different authors. The presented model hence made a noteworthy contribution to this area by enabling the precise and consistent testing of different NGC scaffold designs in one experimental setup, where results can then be accurately compared. Additionally, it is worth mentioning that in contrast to other studies reported, work herein cultured DRGs without addition of NGF or other growth factors. This is of particular benefit as it reduces experimental costs of the model. The absence of NGF, represented a closer *in vivo*-like condition, where axon promoting growth factors originated from Schwann cells. On the contrary, the addition of NGF showed a rather unrepresentative environment as Huval *et*

al.'s results demonstrated. The authors used NGF with their DRG cultures which resulted in a strong axon outgrowth but where Schwann cells showed little regeneration [271]. This suggests that axon outgrowth was mainly promoted by NGF addition and not through neurotrophic factors secreted by Schwann cells how it occurs *in vivo* in response to nerve injury.

Maximum outgrowth distances of axons and Schwann cells from DRGs were evaluated, which were analysed by confocal microscopy or LSM. It was of particular note that although the same samples were imaged, analysis resulted in different outgrowth values depending on the microscopy technique used. Longer axon and Schwann cell outgrowth distances were reported when the analysis was based using confocal microscopy and data was not significant between different fibre diameter scaffolds. On the other hand, significant differences in maximum axon and Schwann cell outgrowth between 1 and 10 µm fibres was found when data was obtained by LSM. This result can be explained according to differences in the image capture between confocal and LSM. With confocal microscopy, scaffolds were placed horizontally in a well plate or Petri dish and images taken from one side of the fibre scaffold, where precise position could not be controlled. Although fibre bundles could in theory be moved manually to image a different scaffold side, there was no controlled method or approach to do so. On the contrary for LSM, scaffolds were embedded in a clear agarose gel and mounted in a glass capillary. Sample positioning could be precisely controlled in X, Y and Z directions as well as sample rotation. Scaffolds were imaged every 90° allowing capture of a full 360° view of samples. This means that LSM enabled the capture of scaffold features "hidden" and not accessible by confocal microscopy. It could hence be said that LSM presented a robust imaging technique for analysing cell outgrowth that represented the entire fibre scaffold. Using LSM improved imaging throughput which enabled quick sample analysis and evaluation. Such benefits were reviewed by a number of researchers in the past which consistently highlight the accuracy and fast acquisition speeds of LSM [369, 370].

6.5.3. *Ex vivo* evaluations of fibre densities inside conduits

Taking into account the large number of studies that report on fibres for scaffolds in nerve regeneration, (e.g. [142, 146, 147]), it is surprising that little research has been carried out on evaluating fibre density although previously shown to influence

regeneration outcomes [145, 153]. The assessment of fibre density needs to be conducted inside NGCs which constrains researchers to use animal models [145, 153] as no suitable *in vitro* alternative has been described so far. The lack of adequate 3D *in vitro* models and fibre density studies presented an ideal opportunity to test a selected range of fibre densities (10, 20 and 40 %) in the present 3D *ex vivo* model. Based on previous results, evaluation was conducted with air plasma-modified 10 µm PCL fibre scaffolds inside PEG NGCs. At first, this study found that air plasma resulted in significantly increased axon outgrowth along fibre scaffolds of all tested densities, which confirmed earlier findings herein. Interestingly, there was no significant difference in axon outgrowth between unmodified scaffolds with different fibre density but with the application of air plasma treatment, a significant increase in average and maximum axon outgrowth was detected on 20 % density scaffolds in comparison to 40 % density scaffolds. It was of note that fibre scaffolds below 10 % were not suitable as they did not remain confined in the conduits when submerged in growth medium. Fibre densities of 40 %, on the other hand, demonstrated a maximum number of fibres that could physically be incorporated inside NGCs without physical device failure. From this, it was concluded that a fibre density of 20 % was the most suitable for air plasma-modified PCL fibre guidance scaffolds in nerve repair.

From all fibre densities tested, only 20 % air plasma-modified fibres when inside NGCs supported axon outgrowth significantly better than a 40 % density. There was no significant difference in axon outgrowth between 10 % fibres and the other scaffolds tested. Furthermore, 10 % fibres provided limited support of axon and Schwann cell outgrowth in the scaffolds, where 20 and 40 % density supported sufficient cell outgrowth in the scaffold interior. The observed accumulation of fibres that filled 10 % of conduits to thin scaffolds in the centre of conduits might have something to do with this. A similar observation was made by Ngo *et al.* who observed that small filament numbers clumped together in the NGC centre and failed to provide enough guidance support *in vivo* [153]. This observation might hence explain the poor cell ingrowth into the scaffold cores of 10 % density fibre scaffolds as the limited space between clumped fibres has likely inhibited cell infiltration.

Ngo *et al.* and Yoshii *et al.* proposed that a greater number of incorporated filaments inside NGCs enhances the regeneration area in conduits [145, 153]. This was confirmed *in vivo*, where an increased number of filaments increased the number of myelinated axons on distal injury site [145, 153]. This was observed in fibre densities up to 30 % [153] or with filament numbers up to 4000, where no percentage of fibre density was reported [145]. In comparison, this study further increased the investigated fibre density up to 40 % which inhibited axon outgrowth in comparison to 20 % densities. This study made hence a noteworthy contribution to the existing findings by identifying that too many fibres will inhibit nerve regeneration. There are a couple of possible explanations for this result. First, it might be possible that axon and Schwann cell outgrowth was physically inhibited through the large number of fibres. This hypothesis is in broader agreement with what has been reported by Yoshii *et al.* who suggested that the restricted space between fibres with large densities caused the observed changes in myelin sheath thickness around axons [145]. Second, it seemed possible that a fibre density of 40 % physically impeded the diffusuion of growth medium and nutrients in the scaffold centre, and hence would explain reduced axon growth. Such a concentration gradient of oxygen and nutrients high at the scaffold surface and low at its core has been reported by a number of researchers previously who observed limited cell growth into the scaffold centres [260, 371, 372]. This might even explain why there were no changes in axon growth between unmodified fibre scaffolds of different densities, as axons did not grow into the scaffold centre and hence growth might not have been affected by the suggested nutrient deficiency in the middle of NGCs with 40 % of fibres. A potentially restricted medium infiltration into scaffolds with high densities would additionally be of particular concern *in vivo* as high fibre density may impede blood and wound fluid penetration into scaffolds and possibly impede fibrin cable formation. Furthermore, it was noticed that maximum axon outgrowth distance varied on 40 % fibre scaffolds which made them unsuited as guidance scaffolds *in vivo,* as regeneration outcomes would logically vary between patients.

6.5.4. Prolonged culture of finalised PCL guidance scaffolds

Summarising the previous findings herein, it was concluded that from the parameters tested, 10 µm fibres with a fibre density of 20 % supported optimal axon and Schwann

cell outgrowth. However, long-term regenerative support of this scaffold was still needed before making a recommendation to test this scaffold in future animal studies. It is of note that other studies reporting on filaments and other guidance scaffolds for nerve repair limit DRG growth assessment to culture times of around 7 days [271, 274, 373]. Thus, culture times were extended to 21 days. The results of this study underpin previous findings that highlight the significant effect of air plasma treatment on PCL scaffold performance. Unmodified fibre scaffolds showed poor support on axon and Schwann cell outgrowth which did not reach the centre of NGCs after 21 days of culture. It was noted that outgrowth arrested after 7 days of culture as no significant differences were detected between day 7 and day 21. Conversely, air plasma-modified scaffolds promoted the growth of cells deep into conduits, where axons and Schwann cells nearly reached the conduit end after 21 days. This shows that only PCL scaffolds with air plasma treatment supported the necessary regeneration of axons and Schwann cells to bridge a potential nerve gap. In summary, these findings indicate that prolonged culture experiments can be performed in the reported model and more importantly provided further evidence on the significant impact of air plasma on PCL fibre scaffold performance. The prolonged culture of DRGs further revealed that Schwann cells were detected ahead of axons on air plasma-modified fibre scaffolds after 21 days of culture. Interestingly, axon and Schwann cell outgrowth measured similar distances on unmodified scaffolds. This finding agrees with that observed in an earlier study by Daud *et al.*, who also reported no significant difference between axon and Schwann cell outgrowth from DRGs on unmodified PCL fibre scaffolds [152]. It is therefore likely that Schwann cells on air plasma-modified scaffolds presented additional guidance cues to axons in a similar manner to *in vivo* events after nerve injury, where Schwann cells infiltrate the nerve lesion first and guide axons through the nerve gap [61]. These results hence provide further support for the hypothesis that air plasma-modified 10 µm PCL fibre scaffolds are ideal candidates for improving hollow NGCs and thus the nerve regeneration outcome.

6.5.5. Allogenic Schwann cell delivery inside conduits

As mentioned in the introduction, the addition of neurotrophic factors, drugs or autologous/allogenic Schwann cells to internal NGC guidance scaffolds or embedded in

the conduit walls has been discussed as a method to further enhance regeneration outcome [358, 360-362]. No study, has to date reported on a comprehensive 3D *in vitro* model for evaluating these factors directly in NGCs. Especially research on Schwann cell delivery approaches directly assessed conduits *in vivo* without conducting prior *in vitro* tests [360, 361, 374]. This is the first time that NGCs have been used to explore the effect of Schwann cell delivery on fibre scaffolds in a 3D *in vitro* model. The results of this study indicate that Schwann cells can be isolated from embryonic chick sciatic nerves and delivered on fibre scaffolds inside conduits for nerve repair. This is furthermore the first study that reports on the harvest and purification of Schwann cells from chick embryos using a selective DMEM D-Valine method. The protocol for Schwann cell isolation was adapted from Kaewkhaw *et al.* [285] who described the isolation and purification of adult rat sciatic Schwann cells. It was of particular note that Schwann cells from chick embryos reached confluence and purity significantly quicker compared to adult rat Schwann cells. From the same number of nerves, it took a minimum of 20 days for adult rat Schwann cells to become confluent in an area of 1.4 cm^2 (4 $\times$ 35 mm^2 Petri dishes) [285], where in comparison embryonic chick Schwann cells reached confluence in a minimum of 8 days and in much larger areas of 75 cm^2. The rapid growth of embryonic chick Schwann cells might be explained with the still ongoing cell proliferation during embryonic development in comparison to differentiated adult Schwann cells [16]. This is further highlighted by Stewart *et al.'s* findings on DNA synthesis in sciatic nerves which showed that DNA synthesis was high in rat embryos but which rapidly declined after birth [375].

Isolated Schwann cells are commonly contaminated with fibroblasts [285], however, Schwann cell purity was achieved quicker if isolated from chick embryos than from adult rats. This quick growth rate is in agreement with Brockes *et al*.'s findings who published one of the first protocols on Schwann cell isolation and purification. The authors purified Schwann cells from neonatal rats and observed cell confluence after 7 days of culture and 99.5 % purity in the second passage [376]. Although it was confirmed that fibroblasts are also present in peripheral nerves of chick embryos [377], there are no reports that compare between fibroblast contents of adult and embryonic specimens. It was however speculated that peripheral nerves in EDD 12 chick embryos might contain lower numbers of fibroblasts at this time point of development than adult chicks or rats. It is of additional note that the isolation and purification of embryonic chick Schwann cells

herein was conducted without the addition of forskolin, bovine purity extract or N2 supplement, as recommended for the isolation of adult rat Schwann cells [285]. Furthermore, Schwann cells adhered and proliferated in culture flasks without the application of poly-L-lysine and laminin. This was particularly beneficial as experimental costs could be significantly reduced.

This study then investigated the effect of a low and high Schwann cell number on axon outgrowth from EDD 12 chick DRGs on 10 µm fibre scaffolds in NGCs. Interestingly, there was no difference in average axon outgrowth between the control and conduits with pre-seeded Schwann cells. The maximum axon outgrowth, however, differed between conduits with low and high Schwann cell numbers but was not different to the control. It was surprising that no increase in axon outgrowth was noted with the addition of Schwann cells in the conduits as it has already been demonstrated that the delivery of Schwann cells significantly enhanced axon regeneration *in vivo* [361, 374]. It was additionally reported that also postnatal and embryonic Schwann cells expressed NGF after axotomy [378]. It could hence be ruled out that the findings herein were associated with an insufficient expression of neurotrophic factors. It was furthermore noted that other authors added Schwann cells to conduits directly before implantation [361, 374] and not 4 days earlier as conducted here.

It was however unlikely that the potential accumulation of metabolic products within the conduits had something to do with the effect observed herein. This was concluded from results in Chapter 4, where neuronal cells were cultured in considerably higher numbers which did not compromise cell viability in the scaffolds (see Figure 49). A possible explanation for this might however be that initially seeded Schwann cells and those outgrowing from DRG bodies reduced the free space in the conduit to an extent that impeded axon outgrowth. This would hence explain why higher Schwann cell numbers showed a significant reduction in axon outgrowth in comparison to lower cell numbers. This theory would further match the hypothesis made earlier where axon outgrowth was significantly reduced on 40 % fibre scaffold density, in comparison to a 20 % density due to the suggested decrease in available growth space. Although other authors embedded a significantly higher number of Schwann cells in conduits prior to implantation [361, 362, 374], there was also a difference in available regeneration space within the devices,

where hollow conduits were only filled with implanted Schwann cells, where in comparison, NGCs herein contained 20 % fibres and further supplemented with Schwann cells. It is hence believed that a further reduction in seeded Schwann cell number in the future might cause the expected stimulation of axon growth. However, so far, it can be noted that the reported model is suitable for investigating Schwann cell therapy approaches in conduits.

6.5.6. 3D *ex vivo* evaluation of other fibre scaffolds inside NGCs

As mentioned in the introduction, the presented 3D *ex vivo* model was developed to help identifying an ideal NGC guidance scaffold by evaluating and comparing scaffolds in one experimental setup before moving to *in vivo* device assessments. It has been shown herein that different scaffold variables such as fibre diameters, density and scaffolds with air plasma modifications could be analysed and compared using the presented 3D DRG model. An initial objective of this project was to further identify whether the 3D model can also be used to assess fibre scaffolds of materials other than PCL and that were fabricated differently to electrospinning. In this study, gyrospun P3HB and P3HB/P3HO-*co*-3HD 80:20 blend fibre scaffolds were assessed in collaboration with Professor Ipsita Roy and Dr. Pooja Basnett (University of Westminster, UK). Both fibre scaffolds were successfully assessed within the model and supported the outgrowth of axons and Schwann cells from DRGs equally well. This was not surprising as PHB demonstrated promising performance as hollow nerve guides in nerve repair before [361, 379] but however has not yet been considered in fibre form as internal NGC scaffolds.

It is worth noting that the scaffolds herein mainly differed in their material composition and showed similar fibre diameters and surface topographies (information provided by Dr. Basnett). Interestingly, this result indicated that the difference in material properties, where P3HB fibres are harder and stiffer than P3HB blend fibres ([354], personal communication with Dr. Basnett), did not affect axon or Schwann cell outgrowth.

Comparing the results herein with data obtained from unmodified and air plasma-modified 10 µm fibres, both PHA fibre scaffolds supported axon outgrowth significantly better than unmodified PCL scaffolds. Although, the average axon outgrowth length was not significantly different between plasma-modified PCL fibres and PHA scaffolds,

maximum axon lengths measured significantly longer on 10 µm PCL fibres. These results therefore suggest that both PHA scaffolds would be better NGC guidance scaffolds than unmodified 10 µm PCL fibre scaffolds but that air plasma-modified 10 µm PCL fibre scaffolds still achieved the best regeneration outcomes. Although this conclusion could be made, it was difficult to say whether the changes were caused by the different scaffold materials. This therefore points out that comparisons between fibre variables can only be reliably conducted if other parameters stay constant. Herein, for example, PHA and PCL fibre scaffolds showed further differences in nanotopographical features on the fibre surface which might have additionally influenced axon outgrowth. Surfaces of PHA fibres were covered in round-shaped pores (personal communication with Dr. Basnett), where 10 µm PCL fibres showed an elongated groove structure on its surface which might have likely favoured a longer axon outgrowth as discussed in Chapter 3. Furthermore, it is of note that there was no difference in surface hydrophilicity between air plasma-modified PCL scaffolds and those of PHA, where water contact angles on air plasma-modified PCL accounted around 78° (Figure 52) and around 70° on P3HB surfaces [356].

In summary, it can be said that air plasma-modified 10 µm PCL fibre scaffolds and both PHA fibre scaffolds mainly differed in the presented surface topography and material properties. As both PHA scaffolds mainly differed in their material stiffness which did not affect axon and Schwann cell outgrowth, it is hence hypothesised that nanotopographical features on the fibres played a major role in directing and accelerating axon and Schwann cell growth. Furthermore, this work confirmed that also other fibre scaffold materials can be evaluated and compared in the reported 3D *ex vivo* model. Additionally, and most importantly, the performance of air plasma-modified PCL fibre scaffolds could be compared to a scaffold of different material which furthermore indicated that 10 µm air plasma-modified fibre scaffolds supported the best axon and Schwann cell regeneration *in vitro* among all other factors tested.

6.6. Conclusion

This study has shown that replacing adult rat DRGs and confocal microscopy for fibre scaffold imaging, with embryonic chick DRGs and light-sheet microscopy, could significantly enhance experimental analysis, accuracy, reliability and time in the reported model and further increase its ethical acceptance. The refined 3D *ex vivo* model presented a platform for assessing and comparing the effect of internal NGC fibre scaffold variables like diameters, density and surface modification on axon and Schwann cell outgrowth. Finally, an optimised PCL fibre scaffold could be identified which comprised of 10 µm air plasma-modified PCL fibres which filled 20 % of the conduit lumen. The 3D *ex vivo* model showed further applications in evaluating cell therapy approaches for enhancing conduits in peripheral nerve repair as well as assessing fibre scaffolds of different materials and designs.

The following conclusions can be drawn from the present study:

- Over time, Schwann cell metabolic activity increased on 10 µm PCL fibres after air plasma modification, in comparison to unmodified 10 µm fibres and both modified and unmodified 1 µm fibres in 2D cultures
- Neurite length and incidence was similar between air plasma-modified 1 and 10 µm PCL fibres in 2D
- Air plasma modification did not influence the attachment of chick embryo DRGs
- Air plasma modification significantly enhanced the chance of DRG outgrowth
- Axon and Schwann cell outgrowth from DRGs was significantly enhanced on air plasma-modified PCL fibres
- Axons and Schwann cells from DRGs grew longer distances on modified 10 µm fibre scaffolds versus 1 µm fibre scaffolds
- DRG outgrowth was significantly reduced on air plasma-modified 1 µm fibres

- DRG outgrowth analysis based on light-sheet microscopy images was more accurate and robust than confocal microscopy
- Conduits with fibre densities of 10, 20 and 40 % had no influence on axon outgrowth on unmodified PCL fibres
- Conduits filled with 20 % air plasma-modified PCL fibres supported longer axon outgrowth than 40 % density
- PCL fibres that filled 10 % of conduits clumped together in the conduit when wet and prevented the growth of axons and Schwann cells to the scaffold centre
- After 21 days, axons regenerated on average in more than 85 % of conduits filled with 20 % air plasma-modified 10 µm fibre scaffolds
- Schwann cells were isolated and purified from sciatic nerves of chick embryos using a D-Valine selective method, supporting differential DAAO expression in the chick nervous system
- Allogenic Schwann cells can be seeded onto fibre scaffolds in NGCs and axon growth stimulation by allogenic Schwann cells assessed
- Different fibre scaffold materials can be assessed in the reported 3D *ex vivo* model
- Conduits with 20 % P3HB and P3HB/P3HO-co-3HD 80:20 blend fibre scaffolds supported axon and Schwann cell growth from DRGs equally well
- Conduits with 20 % air plasma-modified 10 µm PCL fibres supported axon and Schwann cell outgrowth significantly better than PHA scaffolds

Chapter 7 Conclusions & Future Work

The purpose of this thesis was to develop a 3D *ex vivo* model of peripheral nerve regeneration for evaluating and comparing different internal NGC scaffold design variables directly in the three-dimensional architecture of nerve guides, and use this to identify an ideal PCL fibre scaffold to improve regeneration outcomes with NGCs.

The study revealed that a 3D model of peripheral nerve regeneration can be built from NGCs with internal fibre scaffolds. The model used polystyrene adapters and metal grids to secure conduits in an upright position for culture. Both parts could be easily sterilised by autoclaving or ethanol/methanol treatment and were reusable. The setup was simple and showed particular advantages in comparison to the study of Vyas *et al.* [272], who developed an *ex vivo* model of motor nerve repair which had a rather complicated setup and consumed much time. This study further developed a reproducible technique to incorporate fibre scaffolds inside conduits by providing a detailed documentation of the fibre threading process. The fibre density was precisely controlled by choosing a fibre weight approach, determined, based on arithmetic calculation. This is the first study reporting on a detailed method that enables the user to fill conduits with a large number of single microfibres which maintain alignment inside the conduits. So far, only one study has validated fibre density inside a conduit, determined by conduit cross-section after fibre incorporation [153]. However, fibre density could not yet be predicted prior to fibre filling. Hence, this work made a noteworthy contribution by determining fibre density inside conduits prior to fibre incorporation and furthermore developed a micro-CT method for validation.

The method may therefore be applied to other laboratories to help control the fibre incorporation process which can easily be translated to different fibre materials, diameters and conduit dimensions. This method only requires a standard laboratory with no expensive or specialised items of equipment, making it easy to translate to other laboratories. In Chapter 4 it was shown that the predicted fibre density (determined by calculation) correlated with actual fibre density in the conduits, as validated by micro-CT. This suggests that the method is reproducible and does not necessarily require further validation by micro-CT. Translating the study from different fibre densities to *in vivo*

experiments, it might however be valuable to conduct a validation test on a series of randomly selected samples to confirm fibre density before implantation. Micro-CT is then of particular value as samples can still be considered for implantation after imaging.

The second major finding was that the model, consisting of NGCs and internal fibre scaffolds, could be used as a model of peripheral nerve regeneration as well as a general model of peripheral nerve itself. Although the main findings of this thesis were based on DRG cell outgrowth inside conduits, the research more broadly has shown that cell behaviour can also be studied *in vitro* by seeding cells directly inside nerve guides. No other study has reported on the direct culturing of neuronal or glial cells inside three-dimensional nerve guides before. Herein, neuronal cells were studied for axon orientation, outgrowth as well as viability. It would therefore be interesting to assess cellular behaviour of Schwann cells in this model by exploring migration, metabolic activity and proliferation of the seeded cell component within the NGC. This research might therefore serve as a base for future studies to evaluate neuron and Schwann cell behaviour in a more nerve-like environment where cells are organised into aligned orientation on multiple levels inside conduits, instead of relying on cultures predominantly conducted in primitive and unrepresentative monolayers.

Dorsal root ganglia when placed physically on top of conduits mimicked the proximal nerve stump after a nerve injury, with the outgrowth of axons and Schwann cells proceeding along the internal NGC scaffold from the DRG body. As such, this approach models the basic process for peripheral nerve regeneration, and therefore can be suggested as an *ex vivo* model, by proxy. The outgrowth of cells and neurites formed a close arrangement of axons and Schwann cells within the conduits, where both cell types were in close proximity and co-localised to each other. This finding has important implications for studying myelin formation or myelin degeneration, as it has been shown that direct physical contact between axons and Schwann cells is essential for the formation of myelin in Schwann cells controlled via neuregulin-1 and Necl4 [316, 317]. Therefore, in the future, both the regeneration of axons and the myelination process could be studied in this model. A comprehensive healthy and diseased myelination model within a nerve-like environment would help to study mechanisms that trigger neuropathies, (e.g. Guillain-Barré syndrome or Charcot-Marie-tooth disease) and help to

discover new therapeutics for neuroprotection or for general drug development. Such model would be of particular importance as current neuropathy treatments generally focus on symptom management since the cause of the disease is still poorly understood [318].

By using DRGs from chick embryos, a robust and reliable model was built with a high likelihood of DRG outgrowth. The latter is of particular importance in order to reduce the number of sacrificed animals, experimental cost and time. More importantly, the use of chick embryo DRGs addressed in part an ethical basis of animal sacrifice for medical research. Here, EDD 12 chick embryos were used, and are not classified as being developed sufficiently to be categorised as an animal according to the current Animals (Scientific Procedures) Act 1986. The *ex vivo* nerve regeneration model therefore not only replaced the use of animals within the model but could in future further reduce the number of animals for *in vivo* studies by implanting only NGCs which showed promising performance in the *ex vivo* model. In regard to technology development, this is the first study that has demonstrated the potential value of light-sheet microscopy for imaging internal NGC fibre scaffolds. Through capturing axon and Schwann cell outgrowth in 360°on the scaffolds, the reliability and accuracy of cell outgrowth was increased significantly, and hence substantiated a major aim of developing a 3D model that enables the reliable and accurate testing of NGC scaffolds.

A question posed at the beginning of this study was the identification of an ideal PCL fibre guidance scaffold for incorporation into NGCs. It was noted that although fibres supported neurite and Schwann cell growth in 2D on flat fibre mats, outgrowth from chick DRGs using the model was initially rather poor. This adds to a growing body of literature that continually reports on more representative three-dimensional culture models with closer-to-*in vivo* relevance. This led to the introduction of an air plasma discharge method to improve cell outgrowth on PCL fibre scaffolds. It was found that DRG outgrowth incidence increased significantly on air plasma-modified PCL fibre scaffolds, and furthermore increased axon and Schwann cell outgrowth lengths by more than fivefold. This was a major discovery and supports the use of air plasma surface modification on PCL fibre scaffolds for future nerve repair applications, without needing to change the bulk properties/chemistry of PCL. The reported improvement in DRG

outgrowth incidence is of particular importance as this might support a similar improvement *in vivo* on nerve regeneration success. The significant increase in axon and Schwann cell outgrowth distance on air plasma-modified PCL scaffolds supports an a priori basis that such scaffolds could promote peripheral nerve regeneration significantly better than unmodified scaffolds, and hence be a more suitable modified scaffold material for promoting peripheral nerve repair *in vivo*. It is therefore suggested that the positive results found for air plasma are investigated on other polymers suitable for nerve repair in the future, as this technique might substantially enhance regenerative performance.

XPS analysis was used to confirm that the entire fibre scaffold inside an NGC could be modified by air plasma within 60 seconds. Due to the quick processing time, easy handling and non-toxicity, the application of air plasma might be directly applied in the operation theatre prior implantation. This would additionally overcome the question of sample storage after air plasma treatment as it has been shown that hydrophobic recovery of PCL surfaces is an issue when stored in vacuum bags or on the work bench but where storage in physiological fluid increased the material's wettability. However, in the future, it may be worth investigating whether inert gas such as nitrogen is suitable for preserving the hydrophilic properties on air plasma-modified PCL scaffolds. In this regard, NGCs might be prepared in sterile conditions, sealed under appropriate conditions and delivered in, e.g. blister packs to the theatre.

In order to enhance our understanding on how nerve regeneration might be affected by a changing surface wettability of guidance scaffolds *in vivo*, it would be interesting to investigate the effect of air plasma-modified and unmodified PCL scaffolds that have been stored in PBS on axon and Schwann cell outgrowth in the *ex vivo* model. Future trials should additionally assess the impact of different air plasma exposure times and powers on the wettability of PCL surfaces in order to determine whether nerve regeneration on plasma-modified surfaces could be further enhanced.

This study explained the positive effect of air plasma on DRG cell outgrowth with an increased affinity of proteins to attach to plasma-modified surfaces that presented an increased surface polarity as validated by XPS and were hypothesised to show increased surface roughness. This hypothesis needs to be addressed in the future by studying

differences in protein adsorption between air plasma and unmodified surfaces to help establish a better understanding of the biological effects of air plasma treatment on peripheral nerve repair. More investigations have to be done on the proposed changes in surface roughness through air plasma by using, for example SEM and AFM analysis on PCL film surfaces before and after air plasma treatment.

Earlier research has indicated that peripheral nerve regeneration is influenced by fibre diameters [150-152], but a specific fibre diameter range that supports best nerve regeneration could yet not be identified. This study has shown that PCL could be precisely and reproducibly manufactured to microfibres using electrospinning. The diameters and surface topographies of electrospun PCL fibres influenced axon and Schwann cell orientation, as well as supporting important nerve regeneration properties such as Schwann cell activity and axon outgrowth. Differences in topographical structures were found between 1 µm fibres which displayed shallow and round-shaped dimples, versus 5 – 13 µm fibres which displayed elongated, long and deep grooves. It was found that PCL fibres with a diameter of 10 µm supported axon and Schwann cell outgrowth optimally among the tested fibre diameter range of 1 – 13 µm in both 2D monolayer cultures as well as in the 3D *ex vivo* model. This is the first study that addressed differences in electrospun fibre topographies between different fibre diameters and that provided detailed and quantified information about their morphology. It was hypothesised that large, elongated and deep grooves on 5 – 13 µm fibres increased fibre area and surface roughness which likely favoured optimal protein adsorption and hence cell attachment. However, this hypothesis needs to be confirmed in the future by measuring the difference in fibre surface roughness between the different fibre diameter and surface topographies using for example AFM. Additional validation would be required to confirm whether fibre surface topographies influenced protein adhesion.

It was also shown that fibre diameter and topographic surface features influenced axon orientation and guidance. It would hence be interesting to investigate to what extent surface topography influences axon orientation and elongation by changing surface topography, while maintaining the same fibre diameter. This information would aid the design of an ideal fibre guide scaffold for peripheral nerve repair. The performance of air

plasma-modified 10 µm fibres was further examined showing high metabolic activity of Schwann cells (Chapter 3 and 5). Increased metabolic activity was hypothesised to be caused by increased cell proliferation. A larger number of cells would therefore cause an increase in neurotrophic factors secreted by Schwann cells, which may have enhanced axon outgrowth. However, there is only limited data available on the characterisation of Schwann cells from embryonic chicks and hence it is not entirely clear whether or to what extent those Schwann cells secrete neurotrophic factors and trophic molecules. Further research could focus on general neurotrophic factor secretion from embryonic chick Schwann cells and could further investigate differences in factor secretion when cultured on different fibre diameter scaffolds, for example by conducting enzyme-linked immunosorbent assays. This information would help to understand outcomes observed herein when isolated chick Schwann cells were cultured on fibre scaffolds inside conduits prior to DRG culture, but did not cause an expected positive effect on axon outgrowth through neurotrophic factor secretion from pre-seeded Schwann cells. Additionally, this information would contribute to our understanding of changes in axon outgrowth when grown on different fibre diameters. This is furthermore the first study that reported on the isolation and purification of Schwann cells from chick embryo sciatic nerves. This might serve as a base for future studies to evaluate NGC scaffold candidates with primary chick Schwann cells instead of rat Schwann cells to achieve more comparable results between cell and chick DRG cultures.

It is additionally recommended to compare gene expression profiles of embryonic chick DRG cells with those of adult rat DRGs in order to enhance our understanding of potential differences between species and development stages. This information could further be used to identify whether Schwann cells from chick embryos have the potential to myelinate axons in culture, as there have been only a few studies reporting on myelin formation in embryonic rat or mouse Schwann cells [380, 381], but not in chick. In the future, myelination may hence be induced in the reported model that already provided the essential requirements for myelination through physical interactions of axons and Schwann cells [316, 382]. This might further help to answer questions regarding the myelination process of axons adhering to fibre scaffolds within NGCs, like for example whether Schwann cells wrap around axons alone or enclose the entire polymer fibre. An *ex vivo* model of myelination has yet not been demonstrated before.

This study has demonstrated, for the first time, that different fibre densities can be directly evaluated inside NGCs *in vitro*. There are only two studies that previously evaluated fibre density [145, 153] conducted *in vivo*, and to a maximum density of 30 %. The present work demonstrated that a 40 % fibre density impeded the outgrowth of DRG axons and Schwann cells, in comparison to a 20 % density. This points out that fibre density is of importance when designing an ideal fibre scaffold for nerve regeneration, as fibres within conduits at too high a density might inhibit axon regeneration. Conversely, if the density is too low fibre clumping in the centre of conduits limits an ability to physically support along the conduit lumen length, and hence result in a regenerated but thin nerve cable. Whilst this study did not analyse fibre densities between 20 and 40 %, this would be interesting to further investigate. Additional research might explore whether optimal fibre densities are similar between different scaffold materials and designs, as this would contribute to the refinement of an optimal internal NGC scaffold.

Further work could be done on developing a "hollow" NGC control within the model by filling the empty conduit lumen with gels, (e.g. collagen). Complete empty conduits are not suitable as no regeneration support exists as it is currently not possible to replicate the guiding fibrin cable formation that occurs *in vivo*, *in vitro*. "Hollow" NGC controls would help for comparing the guidance support of NGC scaffolds and in making conclusions of whether tested guidance scaffolds show improved nerve regeneration in comparison to current hollow NGCs.

Finally, an aim stated at the beginning of the study was confirmed, as the developed *ex vivo* model enabled the assessment of different fibre diameters and densities of PCL scaffolds as well as scaffolds with surface modifications. The model can further be used to evaluate fibre scaffolds over prolonged culture periods, to assess and compare other fibre scaffold materials and designs as well as to evaluate potential Schwann cell therapy approaches in the future. It could hence be concluded that from the parameters tested and extended DRG culture times, that conduits containing a 20 % density of air plasma-surface modified fibres of 10 µm diameter performed optimally in supporting nerve regeneration *ex vivo* overall.

The next logical step will be to evaluate the performance of this identified fibre scaffold in a critical nerve gap. This should firstly be evaluated in a longer NGC *ex vivo*, e.g. using

NGCs with lengths of 1.5 cm to mirror a critical nerve gap in rats, to then move forwards and assess regeneration performance *in vivo*. If the *in vivo* regeneration proves successful, this would form a basis for an internal NGC scaffold that supports regeneration across a critical nerve gap injury. In the future, it is also recommended to validate the 3D *ex vivo* model *in vivo* by asking the question of whether results obtained *ex vivo* on optimally performing NGC scaffolds is comparable with *in vivo* outcomes. In case validation is successful, the reported model would be able to make reliable predictions of best performing NGC scaffolds for *in vivo* use.

In the future, the 3D *ex vivo* model of peripheral nerve regeneration can be used as a platform to cross-compare different NGC scaffold designs which will help identify promising scaffold candidates. A selected list of candidates may then be implanted *in vivo* for further device evaluation. This therefore would make a significant contribution to the 3Rs by reducing the number of test animals needed for implantation.

References

[1] L. Squire, D. Berg, F. Bloom, S. d. Lac, A. Ghosh, and N. Spitzer, *Fundamental Neuroscience* 3ed.: Elsevier, 2008.

[2] K. Lam, A. J. Sefton, and M. R. Bennett, "Loss of axons from the optic nerve of the rat during early postnatal development," *Brain Res,* vol. 255, pp. 487-91, Mar 1982.

[3] M. X. Repka and H. A. Quigley, "The effect of age on normal human optic nerve fiber number and diameter," *Ophthalmology,* vol. 96, pp. 26-32, Jan 1989.

[4] K. S. Topp and B. S. Boyd, "Structure and biomechanics of peripheral nerves: nerve responses to physical stresses and implications for physical therapist practice," *Phys Ther,* vol. 86, pp. 92-109, Jan 2006.

[5] R. S. Tubbs, E. Rizk, M. M. Shoja, M. Loukas, N. Barbaro, and R. J. Spinner, "Microscopic Morphology and Ultrastructure of Human Peripheral Nerves," in *Nerves and Nerve Injuries*. vol. 1, ed: Elsevier Ltd, 2015.

[6] Magee, Zachazewski, and Quillen, "Peripheral Nerve: Structure, Function, and Physiology " in *Scientific Foundations and Principles of Practice in Musculoskeletal Rehabilitation*, ed: Saunders Elsevier Ltd, 2007.

[7] Nag, "Detection of Blood-Nerve Barrier Permeability by Magnetic Resonance Imaging," in *The Blood-Brain and Other Neural Barriers*, ed: Human Press Springer, 2011.

[8] R. K. Clark, "Your neurons and Their Electrical Activity," in *Anatomy and Physiology: Understanding the Human Body*, ed: Jones and Bartlett Publishers, 2005.

[9] K. Herrup and Y. Yang, "Cell cycle regulation in the postmitotic neuron: oxymoron or new biology?," *Nat Rev Neurosci,* vol. 8, pp. 368-78, May 2007.

[10] K. C. VanMeter and R. J. Hubert, "Nervous System Disorders," in *Gould's Pathophysiology for the Health Professions*, ed: Elsevier, 2014, p. 335.

[11] D. Chiras, "The Nervous system," in *Human Biology*, 8 ed: Jones & Bartlett Learning, 2015, pp. 228-235.

[12] W. T. Norton and W. Cammer, "Isolation and Characterization of Myelin," in *Myelin*, ed: Springer US, 1984, pp. 147-195.

[13] J. S. O'Brien, E. L. Sampson, and M. B. Stern, "Lipid composition of myelin from the peripheral nervous system. Intradural spinal roots," *J Neurochem,* vol. 14, pp. 357-65, Mar 1967.

[14] W. M. Campana, "Schwann cells: activated peripheral glia and their role in neuropathic pain," *Brain Behav Immun,* vol. 21, pp. 522-7, Jul 2007.

[15] M. Pavelka and J. Roth, "Node of Ranvier " in *Functional Ultrastructure: Atlas of Tissue Biology and Pathology*, 3 ed: Springer, 2015, p. 368.

[16] K. Bhatheja and J. Field, "Schwann cells: origins and role in axonal maintenance and regeneration," *Int J Biochem Cell Biol,* vol. 38, pp. 1995-9, 2006.

[17] K. Susuki, "Myelin: A Specialized Membrane for Cell Communication," *Nature Education,* vol. 3, p. 59, 2010.

[18] R. Quarles, W. Macklin, and P. Morell, "Myelin formation, structure and biochemistry," in *Basic Neurochemistry: Molecular, Cellular and Medical Aspects*, 7 ed: Elsevier, 2006, pp. 51-71.

[19] B. Garbay, A. M. Heape, F. Sargueil, and C. Cassagne, "Myelin synthesis in the peripheral nervous system," *Prog Neurobiol,* vol. 61, pp. 267-304, Jun 2000.

[20] R. P. Bunge, "Expanding roles for the Schwann cell: ensheathment, myelination, trophism and regeneration," *Curr Opin Neurobiol,* vol. 3, pp. 805-9, Oct 1993.

[21] J. Noble, C. A. Munro, V. S. Prasad, and R. Midha, "Analysis of upper and lower extremity peripheral nerve injuries in a population of patients with multiple injuries," *J Trauma,* vol. 45, pp. 116-22, Jul 1998.

[22] S. D. Hannah, "Psychosocial Issues after a Traumatic Hand Injury: Facilitating Adjustment," *Journal of Hand Therapy,* vol. 24, pp. 95-102, Apr-Jun 2011.

[23] C. Miller, A. L. Peek, D. Power, and N. R. Heneghan, "Psychological consequences of traumatic upper limb peripheral nerve injury: A systematic review," *Hand Therapy,* vol. 22, pp. 35-45, Mar 2017.
[24] H. E. Rosberg, K. S. Carlsson, R. I. Cederlund, E. Ramel, and L. B. Dahlin, "Costs and outcome for serious hand and arm injuries during the first year after trauma - a prospective study," *BMC Public Health,* vol. 13, p. 501, May 24 2013.
[25] A. N. Afsoun Seddighi, Amir Saied Seddighi, Ali Reza Zali, Seyed Mahmood Tabatabaei, Ali Reza Sheykhi, Fatemeh Yourdkhani, Shoayb Naeimian, "Peripheral Nerve Injury: A Review Article," *International Clinical Neuroscience Journal,* vol. 3, 2016.
[26] J. A. Kouyoumdjian, "Peripheral nerve injuries: a retrospective survey of 456 cases," *Muscle Nerve,* vol. 34, pp. 785-8, Dec 2006.
[27] J. C. Rivera, G. P. Glebus, and M. S. Cho, "Disability following combat-sustained nerve injury of the upper limb," *Bone Joint J,* vol. 96-B, pp. 254-8, Feb 2014.
[28] S. Razaq, R. Yasmeen, A. W. Butt, N. Akhtar, and S. N. Mansoor, "The pattern of peripheral nerve injuries among Pakistani soldiers in the war against terror," *J Coll Physicians Surg Pak,* vol. 25, pp. 363-6, May 2015.
[29] J. Haftek, "Stretch injury of peripheral nerve. Acute effects of stretching on rabbit nerve," *J Bone Joint Surg Br,* vol. 52, pp. 354-65, May 1970.
[30] B. L. Rydevik, M. K. Kwan, R. R. Myers, R. A. Brown, K. J. Triggs, S. L. Woo*, et al.*, "An in vitro mechanical and histological study of acute stretching on rabbit tibial nerve," *J Orthop Res,* vol. 8, pp. 694-701, Sep 1990.
[31] L. A. University of California. (2016, 10.12.2018). *Peripheral nerve injury*. Available: http://neurosurgery.ucla.edu/peripheral-nerve-injury
[32] S. L. Washington University. (2016, 10.12.2018). *Disorders and treatments*. Available: http://nerve.wustl.edu/nd_compression.php?np=nerve_disorders
[33] Johns Hopkins Medicine. (2016, 10.12.2018). *Neurology and Neurosurgery*. Available: http://www.hopkinsmedicine.org/neurology_neurosurgery/centers_clinics/peripheral_nerve_surgery/conditions/nerve_injury.html
[34] H. Assmus, G. Antoniadis, and C. Bischoff, "Carpal and cubital tunnel and other, rarer nerve compression syndromes," *Dtsch Arztebl Int,* vol. 112, pp. 14-25; quiz 26, Jan 5 2015.
[35] A. M. Dendooven, M. Lissens, F. Bruyninckx, and J. Vanhecke, "Electrical injuries to peripheral nerves," *Acta Belg Med Phys,* vol. 13, pp. 161-5, Oct-Dec 1990.
[36] M. H. Mankani, G. S. Abramov, A. Boddie, and R. C. Lee, "Detection of peripheral nerve injury in electrical shock patients," *Ann N Y Acad Sci,* vol. 720, pp. 206-12, May 31 1994.
[37] K. Webster. (2012) Peripheral nerve injuries and positioning for general anaesthesia *World federation of societies of anaesthesiologists* [Tutorial]. 8.
[38] S. J. Farber, M. Saheb-Al-Zamani, L. Zieske, O. Laurido-Soto, A. Bery, D. Hunter*, et al.*, "Peripheral nerve injury after local anesthetic injection," *Anesth Analg,* vol. 117, pp. 731-9, Sep 2013.
[39] G. Melli and A. Hoke, "Dorsal root ganglia sensory neuronal cultures: a tool for drug discovery for peripheral neuropathies," *Expert Opinion on Drug Discovery,* vol. 4, pp. 1035-1045, Oct 2009.
[40] G. M. Leinninger, J. L. Edwards, M. J. Lipshaw, and E. L. Feldman, "Mechanisms of disease: mitochondria as new therapeutic targets in diabetic neuropathy," *Nat Clin Pract Neurol,* vol. 2, pp. 620-8, Nov 2006.
[41] L. Estanislao, K. Carter, J. McArthur, R. Olney, D. Simpson, and H. I. V. N. G. Lidoderm, "A randomized controlled trial of 5% lidocaine gel for HIV-associated distal symmetric polyneuropathy," *J Acquir Immune Defic Syndr,* vol. 37, pp. 1584-6, Dec 15 2004.
[42] A. J. Windebank and W. Grisold, "Chemotherapy-induced neuropathy," *J Peripher Nerv Syst,* vol. 13, pp. 27-46, Mar 2008.
[43] H. J. Willison, B. C. Jacobs, and P. A. van Doorn, "Guillain-Barre syndrome," *Lancet,* vol. 388, pp. 717-27, Aug 13 2016.
[44] N. Mendez, M. Oviedo-Pastrana, S. Mattar, I. Caicedo-Castro, and G. Arrieta, "Zika virus disease, microcephaly and Guillain-Barre syndrome in Colombia: epidemiological

situation during 21 months of the Zika virus outbreak, 2015-2017," *Arch Public Health,* vol. 75, p. 65, 2017.

[45] P. Zis and G. Varrassi, "Painful Peripheral Neuropathy and Cancer," *Pain and Therapy,* vol. 6, pp. 115-116, Dec 2017.

[46] A. Waller, "Experiments on the Section of the Glossopharyngeal and Hypoglossal Nerves of the Frog, and Observations of the Alterations Produced Thereby in the Structure of Their Primitive Fibres," *Philosophical Transactions Royal Society London,* vol. 140, p. 9, 1 January 1850 1850.

[47] L. Lubinska, "Early course of Wallerian degeneration in myelinated fibres of the rat phrenic nerve," *Brain Res,* vol. 130, pp. 47-63, Jul 8 1977.

[48] V. Chaudhry and D. R. Cornblath, "Wallerian degeneration in human nerves: serial electrophysiological studies," *Muscle Nerve,* vol. 15, pp. 687-93, Jun 1992.

[49] M. S. Wang, A. A. Davis, D. G. Culver, Q. Wang, J. C. Powers, and J. D. Glass, "Calpain inhibition protects against Taxol-induced sensory neuropathy," *Brain,* vol. 127, pp. 671-9, Mar 2004.

[50] R. G. Pellegrino, M. J. Politis, J. M. Ritchie, and P. S. Spencer, "Events in degenerating cat peripheral nerve: induction of Schwann cell S phase and its relation to nerve fibre degeneration," *J Neurocytol,* vol. 15, pp. 17-28, Feb 1986.

[51] W. G. Bradley and A. K. Asbury, "Duration of synthesis phase in neuilemma cells in mouse sciatic nerve during degeneration," *Exp Neurol,* vol. 26, pp. 275-82, Feb 1970.

[52] P. J. Arthur-Farraj, M. Latouche, D. K. Wilton, S. Quintes, E. Chabrol, A. Banerjee*, et al.*, "c-Jun reprograms Schwann cells of injured nerves to generate a repair cell essential for regeneration," *Neuron,* vol. 75, pp. 633-47, Aug 23 2012.

[53] D. B. Parkinson, A. Bhaskaran, A. Droggiti, S. Dickinson, M. D'Antonio, R. Mirsky*, et al.*, "Krox-20 inhibits Jun-NH2-terminal kinase/c-Jun to control Schwann cell proliferation and death," *J Cell Biol,* vol. 164, pp. 385-94, Feb 2 2004.

[54] C. De Felipe and C. Belmonte, "c-Jun expression after axotomy of corneal trigeminal ganglion neurons is dependent on the site of injury," *Eur J Neurosci,* vol. 11, pp. 899-906, Mar 1999.

[55] C. De Felipe and S. P. Hunt, "The differential control of c-jun expression in regenerating sensory neurons and their associated glial cells," *J Neurosci,* vol. 14, pp. 2911-23, May 1994.

[56] K. R. Jessen and R. Mirsky, "The repair Schwann cell and its function in regenerating nerves," *J Physiol,* vol. 594, pp. 3521-31, Jul 1 2016.

[57] S. Rotshenker, "Wallerian degeneration: the innate-immune response to traumatic nerve injury," *Journal of Neuroinflammation,* vol. 8, p. 109, Aug 30 2011.

[58] P. Dubovy, R. Jancalek, and T. Kubek, "Role of inflammation and cytokines in peripheral nerve regeneration," *Int Rev Neurobiol,* vol. 108, pp. 173-206, 2013.

[59] J. W. Griffin and W. J. Thompson, "Biology and pathology of nonmyelinating Schwann cells," *Glia,* vol. 56, pp. 1518-31, Nov 1 2008.

[60] R. Deumens, A. Bozkurt, M. F. Meek, M. A. Marcus, E. A. Joosten, J. Weis*, et al.*, "Repairing injured peripheral nerves: Bridging the gap," *Progress in Neurobiology,* vol. 92, pp. 245-76, Nov 2010.

[61] J. L. Salzer and R. P. Bunge, "Studies of Schwann cell proliferation. I. An analysis in tissue culture of proliferation during development, Wallerian degeneration, and direct injury," *J Cell Biol,* vol. 84, pp. 739-52, Mar 1980.

[62] W. Daly, L. Yao, D. Zeugolis, A. Windebank, and A. Pandit, "A biomaterials approach to peripheral nerve regeneration: bridging the peripheral nerve gap and enhancing functional recovery," *Journal of The Royal Society Interface,* vol. 9, pp. 202-21, Feb 7 2012.

[63] J. Du, J. Liu, S. Yao, H. Mao, J. Peng, X. Sun*, et al.*, "Prompt peripheral nerve regeneration induced by a hierarchically aligned fibrin nanofiber hydrogel," *Acta Biomater,* vol. 55, pp. 296-309, Jun 2017.

[64] A. D. Gaudet, P. G. Popovich, and M. S. Ramer, "Wallerian degeneration: gaining perspective on inflammatory events after peripheral nerve injury," *Journal of Neuroinflammation,* vol. 8, p. 110, 2011.

[65] A. L. Cattin, J. J. Burden, L. Van Emmenis, F. E. Mackenzie, J. J. Hoving, N. Garcia Calavia*, et al.*, "Macrophage-Induced Blood Vessels Guide Schwann Cell-Mediated Regeneration of Peripheral Nerves," *Cell,* vol. 162, pp. 1127-39, Aug 27 2015.

[66] H. Colognato, C. ffrench-Constant, and M. L. Feltri, "Human diseases reveal novel roles for neural laminins," *Trends in Neurosciences,* vol. 28, pp. 480-486, Sep 2005.

[67] N. J. Gardiner, P. Fernyhough, D. R. Tomlinson, U. Mayer, H. von der Mark, and C. H. Streuli, "alpha 7 integrin mediates neurite outgrowth of distinct populations of adult sensory neurons," *Molecular and Cellular Neuroscience,* vol. 28, pp. 229-240, Feb 2005.

[68] A. Nodari, S. C. Previtali, G. Dati, S. Occhi, F. A. Court, C. Colombelli*, et al.*, "alpha 6 beta 4 integrin and dystroglycan cooperate to stabilize the myelin sheath," *Journal of Neuroscience,* vol. 28, pp. 6714-6719, Jun 25 2008.

[69] F. Fregnan, L. Muratori, A. R. Simoes, M. G. Giacobini-Robecchi, and S. Raimondo, "Role of inflammatory cytokines in peripheral nerve injury," *Neural Regeneration Research,* vol. 7, pp. 2259-2266, Oct 15 2012.

[70] A. Markus, T. D. Patel, and W. D. Snider, "Neurotrophic factors and axonall growth," *Current Opinion in Neurobiology,* vol. 12, pp. 523-531, Oct 2002.

[71] B. J. Dowsing, W. A. Morrison, N. A. Nicola, G. P. Starkey, T. Bucci, and T. J. Kilpatrick, "Leukemia inhibitory factor is an autocrine survival factor for Schwann cells," *Journal of Neurochemistry,* vol. 73, pp. 96-104, Jul 1999.

[72] A. P. Mizisin and A. Weerasuriya, "Homeostatic regulation of the endoneurial microenvironment during development, aging and in response to trauma, disease and toxic insult," *Acta Neuropathol,* vol. 121, pp. 291-312, Mar 2011.

[73] H. W. Luk, L. J. Noble, and Z. Werb, "Macrophages contribute to the maintenance of stable regenerating neurites following peripheral nerve injury," *J Neurosci Res,* vol. 73, pp. 644-58, Sep 1 2003.

[74] S. Shamash, F. Reichert, and S. Rotshenker, "The cytokine network of Wallerian degeneration: tumor necrosis factor-alpha, interleukin-1 alpha, and interleukin-1 beta," *Journal of Neuroscience,* vol. 22, pp. 3052-3060, Apr 15 2002.

[75] H. J. Seddon, "A Classification of Nerve Injuries," *Br Med J,* vol. 2, pp. 237-9, Aug 29 1942.

[76] S. Sunderland, "A classification of peripheral nerve injuries producing loss of function," *Brain,* vol. 74, pp. 491-516, Dec 1951.

[77] D. Grinsell and C. P. Keating, "Peripheral nerve reconstruction after injury: a review of clinical and experimental therapies," *Biomed Research International,* vol. 2014, p. 698256, 2014.

[78] W. Z. Ray and S. E. Mackinnon, "Management of nerve gaps: autografts, allografts, nerve transfers, and end-to-side neurorrhaphy," *Exp Neurol,* vol. 223, pp. 77-85, May 2010.

[79] F. G. M, M. M, H. S, and W. S. Khan, "Peripheral nerve injury: principles for repair and regeneration," *Open Orthop J,* vol. 8, pp. 199-203, 2014.

[80] H. Millesi, G. Meissl, and A. Berger, "The interfascicular nerve-grafting of the median and ulnar nerves," *Journal of Bone and Joint Surgery,* vol. 54, pp. 727-50, Jun 1972.

[81] W. L. Clark, T. E. Trumble, M. F. Swiontkowski, and A. F. Tencer, "Nerve tension and blood flow in a rat model of immediate and delayed repairs," *Journal of Hand Surgery,* vol. 17, pp. 677-87, Jul 1992.

[82] S. Y. Fu and T. Gordon, "Contributing Factors to Poor Functional Recovery after Delayed Nerve Repair - Prolonged Denervation," *Journal of Neuroscience,* vol. 15, pp. 3886-3895, May 1995.

[83] S. Y. Fu and T. Gordon, "Contributing Factors to Poor Functional Recovery after Delayed Nerve Repair - Prolonged Axotomy," *Journal of Neuroscience,* vol. 15, pp. 3876-3885, May 1995.

[84] B. Rosen, G. Lundborg, L. B. Dahlin, J. Holmberg, and B. Karlson, "Nerve Repair - Correlation of Restitution of Functional Sensibility with Specific Cognitive Capacities," *Journal of Hand Surgery-British and European Volume,* vol. 19b, pp. 452-458, Aug 1994.

[85] U. Kovacic, J. Sketelj, and F. F. Bajrovic, "Age-Related Differences in the Reinnervation after Peripheral Nerve Injury," *Essays on Peripheral Nerve Repair and Regeneration,* vol. 87, pp. 465-482, 2009.

[86] E. S. Dellon and A. L. Dellon, "The first nerve graft, Vulpian, and the nineteenth century neural regeneration controversy," *J Hand Surg Am,* vol. 18, pp. 369-72, Mar 1993.
[87] A. Hallgren, A. Bjorkman, A. Chemnitz, and L. B. Dahlin, "Subjective outcome related to donor site morbidity after sural nerve graft harvesting: a survey in 41 patients," *BMC Surgery,* vol. 13, p. 39, 2013.
[88] K. L. Colen, M. Choi, and D. T. Chiu, "Nerve grafts and conduits," *Plast Reconstr Surg,* vol. 124, pp. e386-94, Dec 2009.
[89] J. K. Terzis and V. K. Kostopoulos, "Vascularized nerve grafts and vascularized fascia for upper extremity nerve reconstruction," *Hand (N Y),* vol. 5, pp. 19-30, Mar 2010.
[90] M. Griffin, M. Malahias, and S. Hindocha, "Peripheral Nerve Injury: Principles for Repair and Regeneration," *The Open Orthpaedics Journal,* p. 5, 2014.
[91] P. Mafi, S. Hindocha, M. Dhital, and M. Saleh, "Advances of peripheral nerve repair techniques to improve hand function: a systematic review of literature," *Open Orthop J,* vol. 6, pp. 60-8, 2012.
[92] G. M. Hoben, X. Ee, L. Schellhardt, Y. Yan, D. A. Hunter, A. M. Moore*, et al.*, "Increasing Nerve Autograft Length Increases Senescence and Reduces Regeneration," *Plast Reconstr Surg,* vol. 142, pp. 952-961, Oct 2018.
[93] S. K. Lee and S. W. Wolfe, "Peripheral nerve injury and repair," *J Am Acad Orthop Surg,* vol. 8, pp. 243-52, Jul-Aug 2000.
[94] Adam Osbourne, "Peripheral Nerve Injury and Repair " *Trinity College Dublin,* vol. 7, p. 5, 2007.
[95] R. J. Li, Z. G. Liu, Y. M. Pan, L. Chen, Z. X. Zhang, and L. J. Lu, "Peripheral Nerve Injuries Treatment: a Systematic Review," *Cell Biochemistry and Biophysics,* vol. 68, pp. 449-454, Apr 2014.
[96] M. J. Brenner, J. R. Hess, T. M. Myckatyn, A. Hayashi, D. A. Hunter, and S. E. Mackinnon, "Repair of motor nerve gaps with sensory nerve inhibits regeneration in rats," *Laryngoscope,* vol. 116, pp. 1685-1692, Sep 2006.
[97] A. Hoke, R. Redett, H. Hameed, R. Jari, C. Zhou, Z. B. Li*, et al.*, "Schwann cells express motor and sensory phenotypes that regulate axon regeneration," *Journal of Neuroscience,* vol. 26, pp. 9646-9655, Sep 20 2006.
[98] P. J. Johnson, M. D. Wood, A. M. Moore, and S. E. Mackinnon, "Tissue engineered constructs for peripheral nerve surgery," *European Surgery-Acta Chirurgica Austriaca,* vol. 45, pp. 122-135, Jun 2013.
[99] A. M. Moore, R. Kasukurthi, C. K. Magill, H. F. Farhadi, G. H. Borschel, and S. E. Mackinnon, "Limitations of conduits in peripheral nerve repairs," *Hand (N Y),* vol. 4, pp. 180-6, Jun 2009.
[100] B. J. Pfister, T. Gordon, J. R. Loverde, A. S. Kochar, S. E. Mackinnon, and D. K. Cullen, "Biomedical engineering strategies for peripheral nerve repair: surgical applications, state of the art, and future challenges," *Crit Rev Biomed Eng,* vol. 39, pp. 81-124, 2011.
[101] H. M. Kaplan, P. Mishra, and J. Kohn, "The overwhelming use of rat models in nerve regeneration research may compromise designs of nerve guidance conduits for humans," *J Mater Sci Mater Med,* vol. 26, p. 226, Aug 2015.
[102] J. S. Belkas, M. S. Shoichett, and R. Midha, "Peripheral nerve regeneration through guidance tubes," *Neurological Research,* vol. 26, pp. 151-160, Mar 2004.
[103] G. Lundborg, "A 25-year perspective of peripheral nerve surgery: Evolving neuroscientific concepts and clinical significance," *Journal of Hand Surgery-American Volume,* vol. 25a, pp. 391-414, May 2000.
[104] M. Sarker, S. Naghieh, A. D. McInnes, D. J. Schreyer, and X. B. Chen, "Strategic Design and Fabrication of Nerve Guidance Conduits for Peripheral Nerve Regeneration," *Biotechnology Journal,* vol. 13, Jul 2018.
[105] C. J. Pateman, A. J. Harding, A. Glen, C. S. Taylor, C. R. Christmas, P. P. Robinson*, et al.*, "Nerve guides manufactured from photocurable polymers to aid peripheral nerve repair," *Biomaterials,* vol. 49, pp. 77-89, May 2015.

[106] X. Jiang, R. F. Mi, A. Hoke, and S. Y. Chew, "Nanofibrous nerve conduit-enhanced peripheral nerve regeneration," *Journal of Tissue Engineering and Regenerative Medicine,* vol. 8, pp. 377-385, May 2014.
[107] A. Muheremu and Q. Ao, "Past, Present, and Future of Nerve Conduits in the Treatment of Peripheral Nerve Injury," *Biomed Res Int,* vol. 2015, p. 237507, 2015.
[108] Integra Life Sciences Corporation. (2016, 10.12.2018). *Integra NeuraGen Nerve Guide*. Available: https://www.integralife.com/neuragen-nerve-guide/product/nerve-tendon-neuragen-nerve-guide
[109] C. A. Heath and G. E. Rutkowski, "The development of bioartificial nerve grafts for peripheral-nerve regeneration," *Trends in Biotechnology,* vol. 16, pp. 163-168, Apr 1998.
[110] F. Stang, G. Keilhoff, and H. Fansa, "Biocompatibility of Different Nerve Tubes," *Materials,* vol. 2, pp. 1480-1507, Dec 2009.
[111] J. Braga-Silva, "The use of silicone tubing in the late repair of the median and ulnar nerves in the forearm," *J Hand Surg Br,* vol. 24, pp. 703-6, Dec 1999.
[112] G. Lundborg, L. B. Dahlin, and N. Danielsen, "Ulnar nerve repair by the silicone chamber technique. Case report," *Scand J Plast Reconstr Surg Hand Surg,* vol. 25, pp. 79-82, 1991.
[113] X. Jiang, S. H. Lim, H. Q. Mao, and S. Y. Chew, "Current applications and future perspectives of artificial nerve conduits," *Experimental Neurology,* vol. 223, pp. 86-101, May 2010.
[114] S. Kehoe, X. F. Zhang, and D. Boyd, "FDA approved guidance conduits and wraps for peripheral nerve injury: a review of materials and efficacy," *Injury,* vol. 43, pp. 553-72, May 2012.
[115] Stryker. (2007, 10.12.18). *Stryker Neuroflex*. Available: http://www.stryker.com/en-us/GSDAMRetirement/index.htmstellent/groups/public/documents/web_prod/056518.pdf
[116] B. Schlosshauer, L. Dreesmann, H. E. Schaller, and N. Sinis, "Synthetic nerve guide implants in humans: a comprehensive survey," *Neurosurgery,* vol. 59, pp. 740-7; discussion 747-8, Oct 2006.
[117] S. J. Archibald, J. Shefner, C. Krarup, and R. D. Madison, "Monkey Median Nerve Repaired by Nerve Graft or Collagen Nerve Guide Tube," *Journal of Neuroscience,* vol. 15, pp. 4109-4123, May 1995.
[118] Axogen Inc. (2013, 10.12.18). *Annual report - Securities and Exchange Commission*. Available: http://ir.axogeninc.com/annual-reports/content/0001104659-14-017051/a14-5254_110k.htm
[119] Polyganics. (2016, 07.12.2018). *Neurolac*. Available: http://www.polyganics.com/products/pnr-and-neurosurgery-products-portfolio/neurolac
[120] W. W. Ashley, Jr., T. Weatherly, and T. S. Park, "Collagen nerve guides for surgical repair of brachial plexus birth injury," *J Neurosurg,* vol. 105, pp. 452-6, Dec 2006.
[121] B. D. Bushnell, A. D. McWilliams, G. B. Whitener, and T. M. Messer, "Early clinical experience with collagen nerve tubes in digital nerve repair," *J Hand Surg Am,* vol. 33, pp. 1081-7, Sep 2008.
[122] A. Farole and B. T. Jamal, "A bioabsorbable collagen nerve cuff (NeuraGen) for repair of lingual and inferior alveolar nerve injuries: a case series," *J Oral Maxillofac Surg,* vol. 66, pp. 2058-62, Oct 2008.
[123] J. A. Lohmeyer, F. Siemers, H. G. Machens, and P. Mailander, "The clinical use of artificial nerve conduits for digital nerve repair: a prospective cohort study and literature review," *J Reconstr Microsurg,* vol. 25, pp. 55-61, Jan 2009.
[124] K. J. Wangensteen and L. K. Kalliainen, "Collagen tube conduits in peripheral nerve repair: a retrospective analysis," *Hand (N Y),* vol. 5, pp. 273-7, Sep 2010.
[125] K. S. Straley, C. W. P. Foo, and S. C. Heilshorn, "Biomaterial Design Strategies for the Treatment of Spinal Cord Injuries," *Journal of Neurotrauma,* vol. 27, pp. 1-19, Jan 2010.
[126] AxoGen Inc. (2016, 10.12.2018). *AxoGuard Nerve Connector*. Available: http://www.axogeninc.com/products/4124/axoguard-nerve-connector

[127] G. D. Rosson, E. H. Williams, and A. L. Dellon, "Motor nerve regeneration across a conduit," *Microsurgery,* vol. 29, pp. 107-14, 2009.
[128] R. A. Weber, W. C. Breidenbach, R. E. Brown, M. E. Jabaley, and D. P. Mass, "A randomized prospective study of polyglycolic acid conduits for digital nerve reconstruction in humans," *Plastic and Reconstructive Surgery,* vol. 106, pp. 1036-1045, Oct 2000.
[129] P. B. Maurus and C. C. Kaeding, "Bioabsorbable implant material review," *Operative Techniques in Sports Medicine,* vol. 12, pp. 158-160, Jul 2004.
[130] Polyganics. (2016, 10.12.18). *Neurolac product leaflet*. Available: http://www.polyganics.com/products/pnr-and-neurosurgery-products-portfolio/neurolac
[131] M. F. Meek and K. Jansen, "Two years after in vivo implantation of poly(DL-lactide-epsilon-caprolactone) nerve guides: has the material finally resorbed?," *J Biomed Mater Res A,* vol. 89, pp. 734-8, Jun 2009.
[132] M. J. Bertleff, M. F. Meek, and J. P. Nicolai, "A prospective clinical evaluation of biodegradable neurolac nerve guides for sensory nerve repair in the hand," *J Hand Surg Am,* vol. 30, pp. 513-8, May 2005.
[133] M. F. Meek and W. F. A. Den Dunnen, "Porosity of the Wall of a Neurolac (R) Nerve Conduit Hampers Nerve Regeneration," *Microsurgery,* vol. 29, pp. 473-478, 2009.
[134] R. Gaudin, C. Knipfer, A. Henningsen, R. Smeets, M. Heiland, and T. Hadlock, "Approaches to Peripheral Nerve Repair: Generations of Biomaterial Conduits Yielding to Replacing Autologous Nerve Grafts in Craniomaxillofacial Surgery," *Biomed Research International,* 2016.
[135] W. T. Daly, L. Yao, M. T. Abu-rub, C. O'Connell, D. I. Zeugolis, A. J. Windebank*, et al.*, "The effect of intraluminal contact mediated guidance signals on axonal mismatch during peripheral nerve repair," *Biomaterials,* vol. 33, pp. 6660-71, Oct 2012.
[136] G. C. de Ruiter, M. J. Malessy, M. J. Yaszemski, A. J. Windebank, and R. J. Spinner, "Designing ideal conduits for peripheral nerve repair," *Neurosurg Focus,* vol. 26, p. E5, Feb 2009.
[137] A. Bozkurt, R. Deumens, C. Beckmann, L. O. Damink, F. Schugner, I. Heschel*, et al.*, "In vitro cell alignment obtained with a Schwann cell enriched microstructured nerve guide with longitudinal guidance channels," *Biomaterials,* vol. 30, pp. 169-179, Jan 2009.
[138] X. Y. Hu, J. H. Huang, Z. X. Ye, L. Xia, M. Li, B. C. Lv*, et al.*, "A Novel Scaffold with Longitudinally Oriented Microchannels Promotes Peripheral Nerve Regeneration," *Tissue Engineering Part A,* vol. 15, pp. 3297-3308, Nov 2009.
[139] G. E. Rutkowski, C. A. Miller, S. Jeftinija, and S. K. Mallapragada, "Synergistic effects of micropatterned biodegradable conduits and Schwann cells on sciatic nerve regeneration," *Journal of Neural Engineering,* vol. 1, pp. 151-157, Sep 2004.
[140] E. Verdu, R. O. Labrador, F. J. Rodriguez, D. Ceballos, J. Fores, and X. Navarro, "Alignment of collagen and laminin-containing gels improve nerve regeneration within silicone tubes," *Restor Neurol Neurosci,* vol. 20, pp. 169-79, 2002.
[141] Y. T. Kim, V. K. Haftel, S. Kumar, and R. V. Bellamkonda, "The role of aligned polymer fiber-based constructs in the bridging of long peripheral nerve gaps," *Biomaterials,* vol. 29, pp. 3117-27, Jul 2008.
[142] R. A. Neal, S. S. Tholpady, P. L. Foley, N. Swami, R. C. Ogle, and E. A. Botchwey, "Alignment and composition of laminin-polycaprolactone nanofiber blends enhance peripheral nerve regeneration," *Journal of Biomedical Materials Research Part A,* vol. 100a, pp. 406-423, Feb 2012.
[143] A. Faroni, S. A. Mobasseri, P. J. Kingham, and A. J. Reid, "Peripheral nerve regeneration: experimental strategies and future perspectives," *Adv Drug Deliv Rev,* vol. 82-83, pp. 160-7, Mar 2015.
[144] G. Lundborg, L. Dahlin, D. Dohi, M. Kanje, and N. Terada, "A new type of "bioartificial" nerve graft for bridging extended defects in nerves," *J Hand Surg Br,* vol. 22, pp. 299-303, Jun 1997.
[145] S. Yoshii, M. Oka, M. Shima, A. Taniguchi, and M. Akagi, "Bridging a 30-mm nerve defect using collagen filaments," *J Biomed Mater Res A,* vol. 67, pp. 467-74, Nov 1 2003.

[146] K. Matsumoto, K. Ohnishi, T. Kiyotani, T. Sekine, H. Ueda, T. Nakamura*, et al.*, "Peripheral nerve regeneration across an 80-mm gap bridged by a polyglycolic acid (PGA)-collagen tube filled with laminin-coated collagen fibers: a histological and electrophysiological evaluation of regenerated nerves," *Brain Research,* vol. 868, pp. 315-28, Jun 23 2000.
[147] J. Cai, X. Peng, K. D. Nelson, R. Eberhart, and G. M. Smith, "Permeable guidance channels containing microfilament scaffolds enhance axon growth and maturation," *J Biomed Mater Res A,* vol. 75, pp. 374-86, Nov 1 2005.
[148] H. S. Koh, T. Yong, W. E. Teo, C. K. Chan, M. E. Puhaindran, T. C. Tan*, et al.*, "In vivo study of novel nanofibrous intra-luminal guidance channels to promote nerve regeneration," *Journal of Neural Engineering,* vol. 7, p. 046003, Aug 2010.
[149] C. Radtke, C. Allmeling, K. H. Waldmann, K. Reimers, K. Thies, H. C. Schenk*, et al.*, "Spider silk constructs enhance axonal regeneration and remyelination in long nerve defects in sheep," *PLoS One,* vol. 6, p. e16990, 2011.
[150] X. J. Wen and P. A. Tresco, "Effect of filament diameter and extracellular matrix molecule precoating on neurite outgrowth and Schwann cell behavior on multifilament entubulation bridging device in vitro," *Journal of Biomedical Materials Research Part A,* vol. 76a, pp. 626-637, Mar 1 2006.
[151] H. B. Wang, M. E. Mullins, J. M. Cregg, C. W. McCarthy, and R. J. Gilbert, "Varying the diameter of aligned electrospun fibers alters neurite outgrowth and Schwann cell migration," *Acta Biomater,* vol. 6, pp. 2970-8, Aug 2010.
[152] M. F. Daud, K. C. Pawar, F. Claeyssens, A. J. Ryan, and J. W. Haycock, "An aligned 3D neuronal-glial co-culture model for peripheral nerve studies," *Biomaterials,* vol. 33, pp. 5901-13, Sep 2012.
[153] T. T. Ngo, P. J. Waggoner, A. A. Romero, K. D. Nelson, R. C. Eberhart, and G. M. Smith, "Poly(L-Lactide) microfilaments enhance peripheral nerve regeneration across extended nerve lesions," *J Neurosci Res,* vol. 72, pp. 227-38, Apr 15 2003.
[154] C. V. Boys, "On the production, properties, and some suggested uses of the finest threads," *Proceedings of the Physical Society of London,* vol. 9, pp. 8-19, 1887.
[155] A. Formhals, "Process and apparatus for preparing artificial threads," US Patent, 1934.
[156] M. Bognitzki, W. Czado, T. Frese, A. Schaper, M. Hellwig, M. Steinhart*, et al.*, "Nanostructured fibers via electrospinning," *Advanced Materials,* vol. 13, pp. 70-+, Jan 5 2001.
[157] Y. M. Shin, M. M. Hohman, M. P. Brenner, and G. C. Rutledge, "Experimental characterization of electrospinning: the electrically forced jet and instabilities," *Polymer,* vol. 42, pp. 9955-9967, Dec 2001.
[158] T. J. Sill and H. A. von Recum, "Electro spinning: Applications in drug delivery and tissue engineering," *Biomaterials,* vol. 29, pp. 1989-2006, May 2008.
[159] H. Q. Liu and Y. L. Hsieh, "Ultrafine fibrous cellulose membranes from electrospinning of cellulose acetate," *Journal of Polymer Science Part B-Polymer Physics,* vol. 40, pp. 2119-2129, Sep 15 2002.
[160] S. Megelski, J. S. Stephens, D. B. Chase, and J. F. Rabolt, "Micro- and nanostructured surface morphology on electrospun polymer fibers," *Macromolecules,* vol. 35, pp. 8456-8466, Oct 22 2002.
[161] X. P. Tang, N. Si, L. Xu, and H. Y. Liu, "Effect of Flow Rate on Diameter of Electrospun Nanoporous Fibers," *Thermal Science,* vol. 18, pp. 1447-1449, 2014.
[162] J. Doshi and D. H. Reneker, "Electrospinning Process and Applications of Electrospun Fibers," *Journal of Electrostatics,* vol. 35, pp. 151-160, Aug 1995.
[163] S. Haider, Y. Al-Zeghayer, F. A. A. Ali, A. Haider, A. Mahmood, W. A. Al-Masry*, et al.*, "Highly aligned narrow diameter chitosan electrospun nanofibers," *Journal of Polymer Research,* vol. 20, Apr 2013.
[164] J. M. Deitzel, J. Kleinmeyer, D. Harris, and N. C. B. Tan, "The effect of processing variables on the morphology of electrospun nanofibers and textiles," *Polymer,* vol. 42, pp. 261-272, Jan 2001.

[165] H. Lian and Z. Meng, "Melt electrospinning vs. solution electrospinning: A comparative study of drug-loaded poly (epsilon-caprolactone) fibres," *Mater Sci Eng C Mater Biol Appl,* vol. 74, pp. 117-123, May 1 2017.

[166] N. Nikmaram, S. Roohinejad, S. Hashemi, M. Koubaa, F. J. Barba, A. Abbaspourrad*, et al.*, "Emulsion-based systems for fabrication of electrospun nanofibers: food, pharmaceutical and biomedical applications," *Rsc Advances,* vol. 7, pp. 28951-28964, 2017.

[167] P. McClellan and W. J. Landis, "Recent Applications of Coaxial and Emulsion Electrospinning Methods in the Field of Tissue Engineering," *Bioresearch Open Access,* vol. 5, pp. 212-227, Aug 2016.

[168] N. J. Schaub, T. Britton, R. Rajachar, and R. J. Gilbert, "Engineered nanotopography on electrospun PLLA microfibers modifies RAW 264.7 cell response," *ACS Appl Mater Interfaces,* vol. 5, pp. 10173-84, Oct 23 2013.

[169] C. L. Casper, J. S. Stephens, N. G. Tassi, D. B. Chase, and J. F. Rabolt, "Controlling surface morphology of electrospun polystyrene fibers: Effect of humidity and molecular weight in the electrospinning process," *Macromolecules,* vol. 37, pp. 573-578, Jan 27 2004.

[170] A. N. Yang, Z. B. Huang, G. F. Yin, and X. M. Pu, "Fabrication of aligned, porous and conductive fibers and their effects on cell adhesion and guidance," *Colloids and Surfaces B-Biointerfaces,* vol. 134, pp. 469-474, Oct 1 2015.

[171] L. Moroni, R. Licht, J. de Boer, J. R. de Wijn, and C. A. van Blitterswijk, "Fiber diameter and texture of electrospun PEOT/PBT scaffolds influence human mesenchymal stem cell proliferation and morphology, and the release of incorporated compounds," *Biomaterials,* vol. 27, pp. 4911-22, Oct 2006.

[172] M. F. Leong, K. S. Chian, P. S. Mhaisalkar, W. F. Ong, and B. D. Ratner, "Effect of electrospun poly(D,L-lactide) fibrous scaffold with nanoporous surface on attachment of porcine esophageal epithelial cells and protein adsorption," *J Biomed Mater Res A,* vol. 89, pp. 1040-8, Jun 15 2009.

[173] M. B. Taskin, D. Xia, F. Besenbacher, M. Dong, and M. Chen, "Nanotopography featured polycaprolactone/polyethyleneoxide microfibers modulate endothelial cell response," *Nanoscale,* vol. 9, pp. 9218-9229, Jul 6 2017.

[174] P. Dayal, J. Liu, S. Kumar, and T. Kyu, "Experimental and theoretical investigations of porous structure formation in electrospun fibers," *Macromolecules,* vol. 40, pp. 7689-7694, Oct 16 2007.

[175] Q. Z. Yu, Z. W. Dai, and P. Lan, "Fabrication of high conductivity dual multi-porous poly (L-lactic acid)/polypyrrole composite micro/nanofiber film," *Materials Science and Engineering B-Advanced Functional Solid-State Materials,* vol. 176, pp. 913-920, Jul 25 2011.

[176] M. A. Woodruff and D. W. Hutmacher, "The return of a forgotten polymer-Polycaprolactone in the 21st century," *Progress in Polymer Science,* vol. 35, pp. 1217-1256, Oct 2010.

[177] B. N. Saxena, "Phase-Ii - Clinical-Trial with Biodegradable Subdermal Contraceptive Implant Capronor (4.0-Cm Single Implant)," *Contraception,* vol. 44, pp. 409-417, Oct 1991.

[178] Ethicon. (2016, 07.12.2018). *MONOCRYL® (poliglecaprone 25) Suture*. Available: http://www.ethicon.com/healthcare-professionals/products/wound-closure/absorbable-sutures/monocryl-poliglecaprone-25 - !description-and-specs

[179] A. Reid. (2016). *A Phase I Trial of a Novel Synthetic Polymer Nerve Conduit 'Polynerve' in Participants With Sensory Digital Nerve Injury (UMANC)*. Available: https://clinicaltrials.gov/ct2/show/NCT02970864

[180] S. Eshraghi and S. Das, "Mechanical and microstructural properties of polycaprolactone scaffolds with one-dimensional, two-dimensional, and three-dimensional orthogonally oriented porous architectures produced by selective laser sintering," *Acta Biomaterialia,* vol. 6, pp. 2467-2476, Jul 2010.

[181] L. Ghasemi-Mobarakeh, M. P. Prabhakaran, L. Tian, E. Shamirzaei-Jeshvaghani, L. Dehghani, and S. Ramakrishna, "Structural properties of scaffolds: Crucial parameters towards stem cells differentiation," *World J Stem Cells,* vol. 7, pp. 728-44, May 26 2015.

[182] B. W. Tuft, L. C. Zhang, L. J. Xu, A. Hangartner, B. Leigh, M. R. Hansen*, et al.*, "Material Stiffness Effects on Neurite Alignment to Photopolymerized Micropatterns," *Biomacromolecules,* vol. 15, pp. 3717-3727, Oct 2014.
[183] Y. Poitelon, C. Lopez-Anido, K. Catignas, C. Berti, M. Palmisano, C. Williamson*, et al.*, "YAP and TAZ control peripheral myelination and the expression of laminin receptors in Schwann cells," *Nat Neurosci,* vol. 19, pp. 879-87, Jul 2016.
[184] N. Lucas, C. Bienaime, C. Belloy, M. Queneudec, F. Silvestre, and J. E. Nava-Saucedo, "Polymer biodegradation: Mechanisms and estimation techniques," *Chemosphere,* vol. 73, pp. 429-442, Sep 2008.
[185] M. Vert, "Degradable and bioresorbable polymers in surgery and in pharmacology: beliefs and facts," *Journal of Materials Science-Materials in Medicine,* vol. 20, pp. 437-446, Feb 2009.
[186] C. G. Pitt, F. I. Chasalow, Y. M. Hibionada, D. M. Klimas, and A. Schindler, "Aliphatic Polyesters .1. The Degradation of Poly(Epsilon-Caprolactone) Invivo," *Journal of Applied Polymer Science,* vol. 26, pp. 3779-3787, 1981.
[187] H. F. Sun, L. Mei, C. X. Song, X. M. Cui, and P. Y. Wang, "The in vivo degradation, absorption and excretion of PCL-based implant," *Biomaterials,* vol. 27, pp. 1735-1740, Mar 2006.
[188] C. X. F. Lam, M. M. Savalani, S. H. Teoh, and D. W. Hutmacher, "Dynamics of in vitro polymer degradation of polycaprolactone-based scaffolds: accelerated versus simulated physiological conditions," *Biomedical Materials,* vol. 3, Sep 2008.
[189] N. Bolgen, Y. Z. Menceloglu, K. Acatay, I. Vargel, and E. Piskin, "In vitro and in vivo degradation of non-woven materials made of poly(epsilon-caprolactone) nanofibers prepared by electrospinning under different conditions," *Journal of Biomaterials Science-Polymer Edition,* vol. 16, pp. 1537-1555, 2005.
[190] S. C. Woodward, P. S. Brewer, F. Moatamed, A. Schindler, and C. G. Pitt, "The Intracellular Degradation of Poly(Epsilon-Caprolactone)," *Journal of Biomedical Materials Research,* vol. 19, pp. 437-444, 1985.
[191] K. Ceonzo, A. Gaynor, L. Shaffer, K. Kojima, C. A. Vacanti, and G. L. Stahl, "Polyglycolic acid-induced inflammation: Role of hydrolysis and resulting complement activation," *Tissue Engineering,* vol. 12, pp. 301-308, Feb 2006.
[192] Z. Zhang, O. Ortiz, R. Goyal, and J. Kohn, "Biodegradable Polymers," *Principles of Tissue Engineering, 4th Edition,* pp. 441-473, 2014.
[193] H. Kweon, M. K. Yoo, I. K. Park, T. H. Kim, H. C. Lee, H. S. Lee*, et al.*, "A novel degradable polycaprolactone networks for tissue engineering," *Biomaterials,* vol. 24, pp. 801-8, Feb 2003.
[194] E. Diaz, I. Sandonis, I. Puerto, and I. Ibanez, "In Vitro Degradation of PLLA/nHA Composite Scaffolds," *Polymer Engineering and Science,* vol. 54, pp. 2571-2578, Nov 2014.
[195] E. Ruoslahti and M. D. Pierschbacher, "New perspectives in cell adhesion: RGD and integrins," *Science,* vol. 238, pp. 491-7, Oct 23 1987.
[196] S. K. Akiyama, "Integrins in cell adhesion and signaling," *Hum Cell,* vol. 9, pp. 181-6, Sep 1996.
[197] R. Vasita, K. Shanmugam, and D. S. Katti, "Improved biomaterials for tissue engineering applications: Surface modification of polymers," *Current Topics in Medicinal Chemistry,* vol. 8, pp. 341-353, Mar 2008.
[198] A. A. Khalili and M. R. Ahmad, "A Review of Cell Adhesion Studies for Biomedical and Biological Applications," *Int J Mol Sci,* vol. 16, pp. 18149-84, Aug 5 2015.
[199] H. Sun and S. Onneby, "Facile polyester surface functionalization via hydrolysis and cell-recognizing peptide attachment," *Polymer International,* vol. 55, pp. 1336-1340, Nov 2006.
[200] B. Chuenjitkuntaworn, W. Inrung, D. Damrongsri, K. Mekaapiruk, P. Supaphol, and P. Pavasant, "Polycaprolactone/hydroxyapatite composite scaffolds: preparation, characterization, and in vitro and in vivo biological responses of human primary bone cells," *J Biomed Mater Res A,* vol. 94, pp. 241-51, Jul 2010.
[201] A. Crawford-Corrie, D. J. Buttle, and J. W. Haycock, "Medical Implant," UK Patent, 2017.

[202] C. Murray-Dunning, S. L. McArthur, T. Sun, R. McKean, A. J. Ryan, and J. W. Haycock, "Three-Dimensional Alignment of Schwann Cells Using Hydrolysable Microfiber Scaffolds: Strategies for Peripheral Nerve Repair," *3d Cell Culture: Methods and Protocols,* vol. 695, pp. 155-166, 2011.

[203] Z. L. Yang, Q. F. Tu, J. Wang, and N. Huang, "The role of heparin binding surfaces in the direction of endothelial and smooth muscle cell fate and re-endothelialization," *Biomaterials,* vol. 33, pp. 6615-6625, Oct 2012.

[204] T. Scientific. (2018). *Crosslinking Technical Handbook*. Available: https://tools.thermofisher.com/content/sfs/brochures/1602163-Crosslinking-Reagents-Handbook.pdf

[205] H. S. Koh, T. Yong, C. K. Chan, and S. Ramakrishna, "Enhancement of neurite outgrowth using nano-structured scaffolds coupled with laminin," *Biomaterials,* vol. 29, pp. 3574-82, Sep 2008.

[206] L. Sirghi, O. Kylian, D. Gilliland, G. Ceccone, and F. Rossi, "Cleaning and hydrophilization of atomic force microscopy silicon probes," *Journal of Physical Chemistry B,* vol. 110, pp. 25975-25981, Dec 28 2006.

[207] V. Weissig and M. Edeas, *Mitochondrial Medicine* vol. 1: Humana Press, 2015.

[208] K. S. Koh, J. Chin, J. Chia, and C. L. Chiang, "Quantitative Studies on PDMS-PDMS Interface Bonding with Piranha Solution and its Swelling Effect," *Micromachines,* vol. 3, pp. 427-441, Jun 2012.

[209] S. Al-Gharabli, J. Kujawa, M. O. Mavukkandy, and H. A. Arafat, "Functional groups docking on PVDF membranes: Novel Piranha approach," *European Polymer Journal,* vol. 96, pp. 414-428, Nov 2017.

[210] S. G. Wang, W. J. Cui, and J. Z. Bei, "Bulk and surface modifications of polylactide," *Analytical and Bioanalytical Chemistry,* vol. 381, pp. 547-556, Feb 2005.

[211] C. Arpagaus, A. Rossi, and P. R. von Rohr, "Short-time plasma surface modification of HDPE powder in a Plasma Downer Reactor - process, wettability improvement and ageing effects," *Applied Surface Science,* vol. 252, pp. 1581-1595, Dec 15 2005.

[212] D. Hegemann, H. Brunner, and C. Oehr, "Plasma treatment of polymers for surface and adhesion improvement," *Nuclear Instruments & Methods in Physics Research Section B-Beam Interactions with Materials and Atoms,* vol. 208, pp. 281-286, Aug 2003.

[213] T. Hirotsu, A. A. J. Ketelaars, and K. Nakayama, "Plasma surface treatment of PCL/PC blend sheets," *Polymer Engineering and Science,* vol. 40, pp. 2324-2331, Nov 2000.

[214] R. Morent, N. De Geyter, T. Desmet, P. Dubruel, and C. Leys, "Plasma Surface Modification of Biodegradable Polymers: A Review," *Plasma Processes and Polymers,* vol. 8, pp. 171-190, Mar 22 2011.

[215] M. R. Sanchis, O. Calvo, O. Fenollar, D. Garcia, and R. Balart, "Characterization of the surface changes and the aging effects of low-pressure nitrogen plasma treatment in a polyurethane film," *Polymer Testing,* vol. 27, pp. 75-83, Feb 2008.

[216] T. Murakami, S. Kuroda, and Z. Osawa, "Dynamics of polymeric solid surfaces treated with oxygen plasma: Effect of aging media after plasma treatment," *Journal of Colloid and Interface Science,* vol. 202, pp. 37-44, Jun 1 1998.

[217] E. C. Onyiriuka, L. S. Hersh, and W. Hertl, "Solubilization of Corona Discharge-Treated and Plasma-Treated Polystyrene," *Journal of Colloid and Interface Science,* vol. 144, pp. 98-102, Jun 1991.

[218] M. Jaganjac, A. Vesel, L. Milkovic, N. Recek, M. Kolar, N. Zarkovic*, et al.*, "Oxygen-rich coating promotes binding of proteins and endothelialization of polyethylene terephthalate polymers," *Journal of Biomedical Materials Research Part A,* vol. 102, pp. 2305-2314, Jul 2014.

[219] N. Recek, M. Jaganjac, M. Kolar, L. Milkovic, M. Mozetic, K. Stana-Kleinschek*, et al.*, "Protein Adsorption on Various Plasma-Treated Polyethylene Terephthalate Substrates," *Molecules,* vol. 18, pp. 12441-12463, Oct 2013.

[220] H. C. Ni, Z. Y. Lin, S. H. Hsu, and I. M. Chiu, "The use of air plasma in surface modification of peripheral nerve conduits," *Acta Biomaterialia,* vol. 6, pp. 2066-2076, Jun 2010.

[221] J. Wang, N. Chen, S. Ramakrishna, L. L. Tian, and X. M. Mo, "The Effect of Plasma Treated PLGA/MWCNTs-COOH Composite Nanofibers on Nerve Cell Behavior," *Polymers,* vol. 9, Dec 2017.
[222] N. Abbasi, S. Soudi, N. Hayati-Roodbari, M. Dodel, and M. Soleimani, "The Effects of Plasma Treated Electrospun Nanofibrous Poly (epsilon-caprolactone) Scaffolds with Different Orientations on Mouse Embryonic Stem Cell Proliferation," *Cell Journal,* vol. 16, pp. 245-254, Fal 2014.
[223] E. D. Yildirim, D. Pappas, S. Guceri, and W. Sun, "Enhanced Cellular Functions on Polycaprolactone Tissue Scaffolds by O-2 Plasma Surface Modification," *Plasma Processes and Polymers,* vol. 8, pp. 256-267, Mar 22 2011.
[224] N. Recek, M. Resnik, H. Motaln, T. Lah-Turnsek, R. Augustine, N. Kalarikkal*, et al.*, "Cell Adhesion on Polycaprolactone Modified by Plasma Treatment," *International Journal of Polymer Science,* 2016.
[225] D. Hetemi and J. Pinson, "Surface functionalisation of polymers," *Chem Soc Rev,* vol. 46, pp. 5701-5713, Oct 2 2017.
[226] J. I. Goldstein, D. E. Newbury, J. R. Michael, N. W. M. Ritchie, J. H. J. Scott, and D. C. Joy, "Electron Beam - Specimen Interactions: Interaction Volume," in *Scanning Electron Microscopy and X-Ray Microanalysis*. vol. 1, 4 ed: Springer, 2017, pp. 1-2.
[227] Y. F. Dufrene, T. Ando, R. Garcia, D. Alsteens, D. Martinez-Martin, A. Engel*, et al.*, "Imaging modes of atomic force microscopy for application in molecular and cell biology," *Nat Nanotechnol,* vol. 12, pp. 295-307, Apr 6 2017.
[228] J. D. Schuttlefield and V. H. Grassian, "ATR-FTIR spectroscopy in the undergraduate chemistry laboratory," *Journal of Chemical Education,* vol. 85, pp. 279-281, Feb 2008.
[229] C. Y. Y. Tang, Y. N. Kwon, and J. O. Leckie, "Effect of membrane chemistry and coating layer on physiochemical properties of thin film composite polyamide RO and NF membranes I. FTIR and XPS characterization of polyamide and coating layer chemistry," *Desalination,* vol. 242, pp. 149-167, Jun 2009.
[230] H. Hillborg, J. F. Ankner, U. W. Gedde, G. D. Smith, H. K. Yasuda, and K. Wikstrom, "Crosslinked polydimethylsiloxane exposed to oxygen plasma studied by neutron reflectometry and other surface specific techniques," *Polymer,* vol. 41, pp. 6851-6863, Aug 2000.
[231] Z. Ma, Z. Mao, and C. Gao, "Surface modification and property analysis of biomedical polymers used for tissue engineering," *Colloids Surf B Biointerfaces,* vol. 60, pp. 137-57, Nov 15 2007.
[232] W. E. Swartz, "X-Ray Photoelectron Spectroscopy," *Analytical Chemistry,* vol. 45, pp. A788-+, 1973.
[233] R. G. Harrison, "Observations on the living developing nerve fiber," *Proceedings of the Society for Experimental Biology and Medicine,* vol. 4, pp. 140-143, Aug 1907.
[234] C. F. Amstein and P. A. Hartman, "Adaptation of plastic surfaces for tissue culture by glow discharge," *J Clin Microbiol,* vol. 2, pp. 46-54, Jul 1975.
[235] M. J. Bissell, D. C. Radisky, A. Rizki, V. M. Weaver, and O. W. Petersen, "The organizing principle: microenvironmental influences in the normal and malignant breast," *Differentiation,* vol. 70, pp. 537-546, Dec 2002.
[236] F. Pampaloni, E. G. Reynaud, and E. H. Stelzer, "The third dimension bridges the gap between cell culture and live tissue," *Nature Review Molecular Cell Biology* vol. 8, pp. 839-45, Oct 2007.
[237] K. Vondermark, V. Gauss, H. Vondermark, and P. Muller, "Relationship between Cell-Shape and Type of Collagen Synthesized as Chondrocytes Lose Their Cartilage Phenotype in Culture," *Nature,* vol. 267, pp. 531-532, 1977.
[238] W. Russel and R. Burch. (1959, 4.12.16). *The Principles of Humane Experimental Technique*. Available: http://altweb.jhsph.edu/pubs/books/humane_exp/het-toc
[239] NC3Rs. (2004, 08/12/18). *National Centre for the Replacement, Refinement and Reduction of Animals in Research* Available: https://www.nc3rs.org.uk/
[240] T. Hartung, "Food for thought ... on animal tests," *Altex-Alternativen Zu Tierexperimenten,* vol. 25, pp. 3-9, 2008.

[241] FDA. (2004, 10.12.2018). *Innovation or Stagnation: Challenge and Opportunity on the Critical Path to New Medical Products*. Available: http://www.fda.gov/downloads/ScienceResearch/SpecialTopics/CriticalPathInitiative/CriticalPathOpportunitiesReports/UCM113411.pdf

[242] N. Bhogal and R. Combes, "TGN1412: Time to change the paradigm for the testing of new pharmaceuticals," *Atla-Alternatives to Laboratory Animals,* vol. 34, pp. 225-239, May 2006.

[243] E. Farrell, E. M. Byrne, J. Fischer, F. J. O'Brien, B. C. O'Connell, P. J. Prendergast*, et al.*, "A comparison of the osteogenic potential of adult rat mesenchymal stem cells cultured in 2-D and on 3-D collagen glycosaminoglycan scaffolds," *Technol Health Care,* vol. 15, pp. 19-31, 2007.

[244] H. Liu and K. Roy, "Biomimetic three-dimensional cultures significantly increase hematopoietic differentiation efficacy of embryonic stem cells," *Tissue Eng,* vol. 11, pp. 319-30, Jan-Feb 2005.

[245] D. N. Rockwood, E. S. Gil, S. H. Park, J. A. Kluge, W. Grayson, S. Bhumiratana*, et al.*, "Ingrowth of human mesenchymal stem cells into porous silk particle reinforced silk composite scaffolds: An in vitro study," *Acta Biomater,* vol. 7, pp. 144-51, Jan 2011.

[246] V. S. Nirmalanandhan, A. Duren, P. Hendricks, G. Vielhauer, and G. S. Sittampalam, "Activity of anticancer agents in a three-dimensional cell culture model," *Assay Drug Dev Technol,* vol. 8, pp. 581-90, Oct 2010.

[247] J. Yin, Q. Meng, G. Zhang, and Y. Sun, "Differential methotrexate hepatotoxicity on rat hepatocytes in 2-D monolayer culture and 3-D gel entrapment culture," *Chem Biol Interact,* vol. 180, pp. 368-75, Aug 14 2009.

[248] D. Loessner, K. S. Stok, M. P. Lutolf, D. W. Hutmacher, J. A. Clements, and S. C. Rizzi, "Bioengineered 3D platform to explore cell-ECM interactions and drug resistance of epithelial ovarian cancer cells," *Biomaterials,* vol. 31, pp. 8494-506, Nov 2010.

[249] H. Kobayashi, S. Man, C. H. Graham, S. J. Kapitain, B. A. Teicher, and R. S. Kerbel, "Acquired multicellular-mediated resistance to alkylating agents in cancer," *Proc Natl Acad Sci U S A,* vol. 90, pp. 3294-8, Apr 15 1993.

[250] F. Wang, V. M. Weaver, O. W. Petersen, C. A. Larabell, S. Dedhar, P. Briand*, et al.*, "Reciprocal interactions between beta1-integrin and epidermal growth factor receptor in three-dimensional basement membrane breast cultures: a different perspective in epithelial biology," *Proc Natl Acad Sci U S A,* vol. 95, pp. 14821-6, Dec 8 1998.

[251] A. S. Meshel, Q. Wei, R. S. Adelstein, and M. P. Sheetz, "Basic mechanism of three-dimensional collagen fibre transport by fibroblasts," *Nat Cell Biol,* vol. 7, pp. 157-64, Feb 2005.

[252] C. C. Park, H. Zhang, M. Pallavicini, J. W. Gray, F. Baehner, C. J. Park*, et al.*, "Beta1 integrin inhibitory antibody induces apoptosis of breast cancer cells, inhibits growth, and distinguishes malignant from normal phenotype in three dimensional cultures and in vivo," *Cancer Res,* vol. 66, pp. 1526-35, Feb 1 2006.

[253] G. Patel, M. Szczypka, S. Pettit, and C. Huang, "Microcarrier-based production of dengue virus in an optimized animal-free virus production medium," presented at the Vaccine Technology VI, Portugal, 2016.

[254] B. A. Justice, N. A. Badr, and R. A. Felder, "3D cell culture opens new dimensions in cell-based assays," *Drug Discovery Today,* vol. 14, pp. 102-107, Jan 2009.

[255] M. M. Ghosh, S. Boyce, C. Layton, E. Freedlander, and S. MacNeil, "A comparison of methodologies for the preparation of human epidermal-dermal composites," *Annals of Plastic Surgery,* vol. 39, pp. 390-404, Oct 1997.

[256] S. MacNeil, "Progress and opportunities for tissue-engineered skin," *Nature,* vol. 445, pp. 874-80, Feb 22 2007.

[257] M. Ravi, V. Paramesh, S. R. Kaviya, E. Anuradha, and F. D. Solomon, "3D cell culture systems: advantages and applications," *Journal of Cellular Physiology* vol. 230, pp. 16-26, Jan 2015.

[258] J. W. Haycock, "3D cell culture: a review of current approaches and techniques," *Methods Mol Biol,* vol. 695, pp. 1-15, 2011.

[259] L. G. Griffith and M. A. Swartz, "Capturing complex 3D tissue physiology in vitro," *Nat Rev Mol Cell Biol,* vol. 7, pp. 211-24, Mar 2006.
[260] K. Duval, H. Grover, L. H. Han, Y. Mou, A. F. Pegoraro, J. Fredberg*, et al.*, "Modeling Physiological Events in 2D vs. 3D Cell Culture," *Physiology,* vol. 32, pp. 266-277, Jul 2017.
[261] E. R. Kandel, J. H. Schwartz, and T. M. Jessel, *Principles of Neural Science*, 3 ed.: Harlow Books, New York, 1991.
[262] D. B. Edelman and E. W. Keefer, "A cultural renaissance: in vitro cell biology embraces three-dimensional context," *Experimental Neurology,* vol. 192, pp. 1-6, Mar 2005.
[263] S. Bosi, R. Rauti, J. Laishram, A. Turco, D. Lonardoni, T. Nieus*, et al.*, "From 2D to 3D: novel nanostructured scaffolds to investigate signalling in reconstructed neuronal networks," *Scientific Reports,* vol. 5, Apr 24 2015.
[264] M. Frega, M. Tedesco, P. Massobrio, M. Pesce, and S. Martinoia, "Network dynamics of 3D engineered neuronal cultures: a new experimental model for in-vitro electrophysiology," *Sci Rep,* vol. 4, p. 5489, 2014.
[265] D. Kraus, V. Boyle, N. Leibig, G. B. Stark, and V. Penna, "The Neuro-spheroid-A novel 3D in vitro model for peripheral nerve regeneration," *Journal of Neuroscience Methods,* vol. 246, pp. 97-105, May 15 2015.
[266] M. Gingras, M. M. Beaulieu, V. Gagnon, H. D. Durham, and F. Berthod, "In vitro study of axonal migration and myelination of motor neurons in a three-dimensional tissue-engineered model," *Glia,* vol. 56, pp. 354-364, Feb 2008.
[267] R. S. Nascimento, M. F. Santiago, S. A. Marques, S. Allodi, and A. M. B. Martinez, "Diversity among satellite glial cells in dorsal root ganglia of the rat," *Brazilian Journal of Medical and Biological Research,* vol. 41, pp. 1011-1017, Nov 2008.
[268] S. Geuna, S. Raimondo, F. Fregnan, K. Haastert-Talini, and C. Grothe, "In vitro models for peripheral nerve regeneration," *Eur J Neurosci,* vol. 43, pp. 287-96, Feb 2016.
[269] J. J. Fei, X. X. Wen, X. Lin, Saijilafu, W. H. Wang, O. Ren*, et al.*, "Biocompatibility and neurotoxicity of magnesium alloys potentially used for neural repairs," *Materials Science & Engineering C-Materials for Biological Applications,* vol. 78, pp. 1155-1163, Sep 1 2017.
[270] Y. Wang, W. Wang, Y. Wo, T. Gui, H. Zhu, X. Mo*, et al.*, "Orientated Guidance of Peripheral Nerve Regeneration Using Conduits with a Microtube Array Sheet (MTAS)," *ACS Appl Mater Interfaces,* vol. 7, pp. 8437-50, Apr 29 2015.
[271] R. M. Huval, O. H. Miller, J. L. Curley, Y. Fan, B. J. Hall, and M. J. Moore, "Microengineered peripheral nerve-on-a-chip for preclinical physiological testing," *Lab Chip,* vol. 15, pp. 2221-32, May 21 2015.
[272] A. Vyas, Z. B. Li, M. Aspalter, J. Feiner, A. Hoke, C. H. Zhou*, et al.*, "An in vitro model of adult mammalian nerve repair," *Experimental Neurology,* vol. 223, pp. 112-118, May 2010.
[273] A. Bozkurt, G. A. Brook, S. Moellers, F. Lassner, B. Sellhaus, J. Weis*, et al.*, "In vitro assessment of axonal growth using dorsal root ganglia explants in a novel three-dimensional collagen matrix," *Tissue Engineering,* vol. 13, pp. 2971-9, Dec 2007.
[274] N. Rangappa, A. Romero, K. D. Nelson, R. C. Eberhart, and G. M. Smith, "Laminin-coated poly(L-lactide) filaments induce robust neurite growth while providing directional orientation," *J Biomed Mater Res,* vol. 51, pp. 625-34, Sep 15 2000.
[275] T. H. Burkey, C. M. Hingtgen, and M. R. Vasko, "Isolation and culture of sensory neurons from the dorsal-root ganglia of embryonic or adult rats," *Methods Mol Med,* vol. 99, pp. 189-202, 2004.
[276] D. E. Owen and J. Egerton, "Culture of Dissociated Sensory Neurons from Dorsal Root Ganglia of Postnatal and Adult Rats," in *Neurotrophic Factors*, S. D. Skaper, Ed., ed: Methods in Molecular Biology 2012.
[277] B. S. Scott, "Adult Mouse Dorsal Root-Ganglia Neurons in Cell-Culture," *Journal of Neurobiology,* vol. 8, pp. 417-427, 1977.
[278] C. F. Vogelaar, N. M. Gervasi, L. F. Gumy, D. J. Story, R. Raha-Chowdhury, K. M. Leung*, et al.*, "Axonal mRNAs: Characterisation and role in the growth and regeneration of dorsal root ganglion axons and growth cones," *Molecular and Cellular Neuroscience,* vol. 42, pp. 102-115, Sep 2009.

[279] S. Matsuda, P. Baluk, D. Shimizu, and T. Fujiwara, "Dorsal root ganglion neuron development in chick and rat," *Anat Embryol (Berl),* vol. 193, pp. 475-80, May 1996.
[280] C. F. Ibanez, F. Hallbook, S. Soderstrom, T. Ebendal, and H. Persson, "Biological and immunological properties of recombinant human, rat, and chicken nerve growth factors: a comparative study," *J Neurochem,* vol. 57, pp. 1033-41, Sep 1991.
[281] W. D. Johnson and R. W. Storts, "Peripheral neuropathy associated with dietary riboflavin deficiency in the chicken. I. Light microscopic study," *Vet Pathol,* vol. 25, pp. 9-16, Jan 1988.
[282] D. Ribatti, "The chick embryo chorioallantoic membrane (CAM). A multifaceted experimental model," *Mechanisms of Development,* vol. 141, pp. 70-77, Aug 2016.
[283] A. G. Schwaid, A. Krasowka-Zoladek, A. Chi, and I. Cornella-Taracido, "Comparison of the Rat and Human Dorsal Root Ganglion Proteome," *Sci Rep,* vol. 8, p. 13469, Sep 7 2018.
[284] J. Schindelin, I. Arganda-Carreras, E. Frise, V. Kaynig, M. Longair, T. Pietzsch*, et al.*, "Fiji: an open-source platform for biological-image analysis," *Nat Methods,* vol. 9, pp. 676-82, Jun 28 2012.
[285] R. Kaewkhaw, A. M. Scutt, and J. W. Haycock, "Integrated culture and purification of rat Schwann cells from freshly isolated adult tissue," *Nat Protoc,* vol. 7, pp. 1996-2004, Nov 2012.
[286] S. Preibisch, S. Saalfeld, and P. Tomancak, "Globally optimal stitching of tiled 3D microscopic image acquisitions," *Bioinformatics,* vol. 25, pp. 1463-5, Jun 1 2009.
[287] M. Behbehani, A. Glen, C. Taylor, A. Schuhmacher, F. Claeyssens, and J. Haycock, "Pre-clinical evaluation of advanced nerve guide conduits using a novel 3D in vitro testing model," *International Journal of Bioprinting* vol. 4, 2018
[288] M. F. Meek and J. H. Coert, "US Food and Drug Administration /Conformit Europe-approved absorbable nerve conduits for clinical repair of peripheral and cranial nerves," *Annals of Plastic Surgery,* vol. 60, pp. 466-72, Apr 2008.
[289] E. M. Jeffries and Y. Wang, "Incorporation of parallel electrospun fibers for improved topographical guidance in 3D nerve guides," *Biofabrication,* vol. 5, p. 035015, Sep 2013.
[290] F. Ma, Z. Xiao, D. Meng, X. Hou, J. Zhu, J. Dai*, et al.*, "Use of natural neural scaffolds consisting of engineered vascular endothelial growth factor immobilized on ordered collagen fibers filled in a collagen tube for peripheral nerve regeneration in rats," *International Journal of Molecular Sciences,* vol. 15, pp. 18593-609, 2014.
[291] A. Faroni, S. A. Mobasseri, P. J. Kingham, and A. J. Reid, "Peripheral nerve regeneration: experimental strategies and future perspectives," *Advanced Drug Delivery Reviews,* vol. 82-83, pp. 160-7, Mar 2015.
[292] C. H. Jang, H. Lee, M. Kim, and G. Kim, "Effect of polycaprolactone/collagen/hUCS microfiber nerve conduit on facial nerve regeneration," *Int J Biol Macromol,* vol. 93, pp. 1575-1582, Dec 2016.
[293] C. J. Chang, "Effects of nerve growth factor from genipin-crosslinked gelatin in polycaprolactone conduit on peripheral nerve regeneration-in vitro and in vivo," *Journal of Biomedical Materials Research Part A,* vol. 91a, pp. 586-596, Nov 2009.
[294] S. C. Hsieh, C. M. Tang, W. T. Huang, L. L. Hsieh, C. M. Lu, C. J. Chang*, et al.*, "Comparison between two different methods of immobilizing NGF in poly(DL-lactic acid-co-glycolic acid) conduit for peripheral nerve regeneration by EDC/NHS/MES and genipin," *Journal of Biomedical Materials Research Part A,* vol. 99a, pp. 576-585, Dec 2011.
[295] C. D. Johnson, A. R. D'Amato, D. L. Puhl, D. M. Wich, A. Vesperman, and R. J. Gilbert, "Electrospun fiber surface nanotopography influences astrocyte-mediated neurite outgrowth," *Biomed Mater,* vol. 13, p. 054101, Jun 4 2018.
[296] H. Onoe, T. Okitsu, A. Itou, M. Kato-Negishi, R. Gojo, D. Kiriya*, et al.*, "Metre-long cell-laden microfibres exhibit tissue morphologies and functions," *Nat Mater,* vol. 12, pp. 584-90, Jun 2013.
[297] S. K. Vimal, N. Ahamad, and D. S. Katti, "A simple method for fabrication of electrospun fibers with controlled degree of alignment having potential for nerve regeneration applications," *Materials Science & Engineering C-Materials for Biological Applications,* vol. 63, pp. 616-627, Jun 1 2016.

[298] E. Verdu, R. O. Labrador, F. J. Rodriguez, D. Ceballos, J. Fores, and X. Navarro, "Alignment of collagen and laminin-containing gels improve nerve regeneration within silicone tubes," *Restorative Neurology and Neuroscience,* vol. 20, pp. 169-179, 2002.
[299] S. V. Fridrikh, J. H. Yu, M. P. Brenner, and G. C. Rutledge, "Controlling the fiber diameter during electrospinning," *Physical Review Letters,* vol. 90, Apr 11 2003.
[300] H. Fong, I. Chun, and D. H. Reneker, "Beaded nanofibers formed during electrospinning," *Polymer,* vol. 40, pp. 4585-4592, Jul 1999.
[301] A. V. Limaye, R. D. Narhe, A. M. Dhote, and S. B. Ogale, "Evidence for convective effects in breath figure formation on volatile fluid surfaces," *Phys Rev Lett,* vol. 76, pp. 3762-3765, May 13 1996.
[302] J. I. Kim, T. I. Hwang, L. E. Aguilar, C. H. Park, and C. S. Kim, "A Controlled Design of Aligned and Random Nanofibers for 3D Bi-functionalized Nerve Conduits Fabricated via a Novel Electrospinning Set-up," *Sci Rep,* vol. 6, p. 23761, Mar 29 2016.
[303] R. D. Cardwell, L. A. Dahlgren, and A. S. Goldstein, "Electrospun fibre diameter, not alignment, affects mesenchymal stem cell differentiation into the tendon/ligament lineage," *Journal of Tissue Engineering and Regenerative Medicine,* vol. 8, pp. 937-945, Dec 2014.
[304] H. H. Kim, M. J. Kim, S. J. Ryu, C. S. Ki, and Y. H. Park, "Effect of fiber diameter on surface morphology, mechanical property, and cell behavior of electrospun poly(epsilon-caprolactone) mat," *Fibers and Polymers,* vol. 17, pp. 1033-1042, Jul 2016.
[305] M. Chen, P. K. Patra, M. L. Lovett, D. L. Kaplan, and S. Bhowmick, "Role of electrospun fibre diameter and corresponding specific surface area (SSA) on cell attachment," *J Tissue Eng Regen Med,* vol. 3, pp. 269-79, Jun 2009.
[306] J. T. Parsons, A. R. Horwitz, and M. A. Schwartz, "Cell adhesion: integrating cytoskeletal dynamics and cellular tension," *Nat Rev Mol Cell Biol,* vol. 11, pp. 633-43, Sep 2010.
[307] S. Lee, M. K. Leach, S. A. Redmond, S. Y. Chong, S. H. Mellon, S. J. Tuck*, et al.*, "A culture system to study oligodendrocyte myelination processes using engineered nanofibers," *Nat Methods,* vol. 9, pp. 917-22, Sep 2012.
[308] C. Gerard and A. Goldbeter, "The balance between cell cycle arrest and cell proliferation: control by the extracellular matrix and by contact inhibition," *Interface Focus,* vol. 4, Jun 6 2014.
[309] J. W. Haycock, "3D cell culture: a review of current approaches and techniques," *Methods in Molecular Biology,* vol. 695, pp. 1-15, 2011.
[310] S. Sharma, R. W. Johnson, and T. A. Desai, "Evaluation of the stability of nonfouling ultrathin poly(ethylene glycol) films for silicon-based microdevices," *Langmuir,* vol. 20, pp. 348-356, Jan 20 2004.
[311] M. Behbehani, A. Glen, C. S. Taylor, A. Schuhmacher, F. Claeyssens, and J. W. Haycock, "Pre-clinical evaluation of advanced nerve guide conduits using a novel 3D in vitro testing model," *International Journal of Bioprinting,* vol. 4, 2018.
[312] L. Yan, Y. Guo, J. Qi, Q. Zhu, L. Gu, C. Zheng*, et al.*, "Iodine and freeze-drying enhanced high-resolution MicroCT imaging for reconstructing 3D intraneural topography of human peripheral nerve fascicles," *J Neurosci Methods,* vol. 287, pp. 58-67, Aug 1 2017.
[313] D. W. Li, X. Pan, B. B. Sun, T. Wu, W. M. Chen, C. Huang*, et al.*, "Nerve conduits constructed by electrospun P(LLA-CL) nanofibers and PLLA nanofiber yarns," *Journal of Materials Chemistry B,* vol. 3, pp. 8823-8831, 2015.
[314] M. Antman-Passig, S. Levy, C. Gartenberg, H. Schori, and O. Shefi, "Mechanically Oriented 3D Collagen Hydrogel for Directing Neurite Growth," *Tissue Eng Part A,* vol. 23, pp. 403-414, May 2017.
[315] E. S. Krames, "The dorsal root ganglion in chronic pain and as a target for neuromodulation: a review," *Neuromodulation,* vol. 18, pp. 24-32; discussion 32, Jan 2015.
[316] G. V. Michailov, M. W. Sereda, B. G. Brinkmann, T. M. Fischer, B. Haug, C. Birchmeier*, et al.*, "Axonal neuregulin-1 regulates myelin sheath thickness," *Science,* vol. 304, pp. 700-703, Apr 30 2004.

[317] I. Spiegel, K. Adamsky, Y. Eshed, R. Milo, H. Sabanay, O. Sarig-Nadir*, et al.*, "A central role for Necl4 (SynCAM4) in Schwann cell- axon interaction and myelination," *Nature Neuroscience,* vol. 10, pp. 861-869, Jul 2007.

[318] G. Melli and A. Hoke, "Dorsal Root Ganglia Sensory Neuronal Cultures: a tool for drug discovery for peripheral neuropathies," *Expert Opin Drug Discov,* vol. 4, pp. 1035-1045, Oct 1 2009.

[319] B. S. Jha, R. J. Colello, J. R. Bowman, S. A. Sell, K. D. Lee, J. W. Bigbee*, et al.*, "Two pole air gap electrospinning: Fabrication of highly aligned, three-dimensional scaffolds for nerve reconstruction," *Acta Biomater,* vol. 7, pp. 203-15, Jan 2011.

[320] F. Yang, R. Murugan, S. Wang, and S. Ramakrishna, "Electrospinning of nano/micro scale poly(L-lactic acid) aligned fibers and their potential in neural tissue engineering," *Biomaterials,* vol. 26, pp. 2603-10, May 2005.

[321] F. Stang, H. Fansa, G. Wolf, M. Reppin, and G. Keilhoff, "Structural parameters of collagen nerve grafts influence peripheral nerve regeneration," *Biomaterials,* vol. 26, pp. 3083-91, Jun 2005.

[322] L. Yao, G. C. de Ruiter, H. Wang, A. M. Knight, R. J. Spinner, M. J. Yaszemski*, et al.*, "Controlling dispersion of axonal regeneration using a multichannel collagen nerve conduit," *Biomaterials,* vol. 31, pp. 5789-97, Aug 2010.

[323] P. Thevenot, A. Nair, J. Dey, J. Yang, and L. P. Tang, "Method to Analyze Three-Dimensional Cell Distribution and Infiltration in Degradable Scaffolds," *Tissue Engineering Part C-Methods,* vol. 14, pp. 319-331, Dec 2008.

[324] T. Toba, T. Nakamura, Y. Shimizu, K. Matsumoto, K. Ohnishi, S. Fukuda*, et al.*, "Regeneration of canine peroneal nerve with the use of a polyglycolic acid-collagen tube filled with laminin-soaked collagen sponge: a comparative study of collagen sponge and collagen fibers as filling materials for nerve conduits," *J Biomed Mater Res,* vol. 58, pp. 622-30, 2001.

[325] X. Wang, W. Hu, Y. Cao, J. Yao, J. Wu, and X. Gu, "Dog sciatic nerve regeneration across a 30-mm defect bridged by a chitosan/PGA artificial nerve graft," *Brain,* vol. 128, pp. 1897-910, Aug 2005.

[326] S. J. Hollister and W. L. Murphy, "Scaffold Translation: Barriers Between Concept and Clinic," *Tissue Engineering Part B-Reviews,* vol. 17, pp. 459-474, Dec 2011.

[327] I. Armentano, G. Ciapetti, M. Pennacchi, M. Dottori, V. Devescovi, D. Granchi*, et al.*, "Role of PLLA Plasma Surface Modification in the Interaction with Human Marrow Stromal Cells," *Journal of Applied Polymer Science,* vol. 114, pp. 3602-3611, Dec 15 2009.

[328] H. Chim, J. L. Ong, J. T. Schantz, D. W. Hutmacher, and C. M. Agrawal, "Efficacy of glow discharge gas plasma treatment as a surface modification process for three-dimensional poly (D,L-lactide) scaffolds," *Journal of Biomedical Materials Research Part A,* vol. 65a, pp. 327-335, Jun 1 2003.

[329] Y. Q. Wan, C. F. Tu, J. A. Yang, J. Z. Bei, and S. G. Wang, "Influences of ammonia plasma treatment on modifying depth and degradation of poly(L-lactide) scaffolds," *Biomaterials,* vol. 27, pp. 2699-2704, May 2006.

[330] J. J. A. Barry, M. M. C. G. Silva, K. M. Shakesheff, S. M. Howdle, and M. R. Alexander, "Using plasma deposits to promote cell population of the porous interior of three-dimensional poly(D,L-lactic acid) tissue-engineering scaffolds," *Advanced Functional Materials,* vol. 15, pp. 1134-1140, Jul 2005.

[331] L. A. Can-Herrera, A. Avila-Ortega, S. de la Rosa-Garcia, A. I. Oliva, J. V. Cauich-Rodriguez, and J. M. Cervantes-Uc, "Surface modification of electrospun polycaprolactone microfibers by air plasma treatment: Effect of plasma power and treatment time," *European Polymer Journal,* vol. 84, pp. 502-513, Nov 2016.

[332] S. Shafei, J. Foroughi, Z. Q. Chen, C. S. Wong, and M. Naebe, "Short Oxygen Plasma Treatment Leading to Long-Term Hydrophilicity of Conductive PCL-PPy Nanofiber Scaffolds," *Polymers,* vol. 9, Nov 2017.

[333] T. Jacobs, N. De Geyter, R. Morent, T. Desmet, P. Dubruel, and C. Leys, "Plasma treatment of polycaprolactone at medium pressure," *Surface & Coatings Technology,* vol. 205, pp. S543-S547, Jul 25 2011.

[334] S. Surucu, K. Masur, H. T. Sasmazel, T. Von Woedtke, and K. D. Weltmann, "Atmospheric plasma surface modifications of electrospun PCL/chitosan/PCL hybrid scaffolds by nozzle type plasma jets for usage of cell cultivation," *Applied Surface Science,* vol. 385, pp. 400-409, Nov 1 2016.

[335] N. E. Zander, J. A. Orlicki, A. M. Rawlett, and T. P. Beebe, "Quantification of Protein Incorporated into Electrospun Polycaprolactone Tissue Engineering Scaffolds," *Acs Applied Materials & Interfaces,* vol. 4, pp. 2074-2081, Apr 2012.

[336] A. Nandakumar, Z. T. Birgani, D. Santos, A. Mentink, N. Auffermann, K. van der Werf*, et al.*, "Surface modification of electrospun fibre meshes by oxygen plasma for bone regeneration," *Biofabrication,* vol. 5, Mar 2013.

[337] N. Y. Cui and N. M. D. Brown, "Modification of the surface properties of a polypropylene (PP) film using an air dielectric barrier discharge plasma," *Applied Surface Science,* vol. 189, pp. 31-38, Apr 14 2002.

[338] M. R. Sanchis, V. Blanes, M. Blanes, D. Garcia, and R. Balart, "Surface modification of low density polyethylene (LDPE) film by low pressure O-2 plasma treatment," *European Polymer Journal,* vol. 42, pp. 1558-1568, Jul 2006.

[339] E. P. Everaert, H. C. VanderMei, and H. J. Busscher, "Hydrophobic recovery of repeatedly plasma-treated silicone rubber .2. A comparison of the hydrophobic recovery in air, water, or liquid nitrogen," *Journal of Adhesion Science and Technology,* vol. 10, pp. 351-359, 1996.

[340] M. Morra, E. Occhiello, R. Marola, F. Garbassi, P. Humphrey, and D. Johnson, "On the Aging of Oxygen Plasma-Treated Polydimethylsiloxane Surfaces," *Journal of Colloid and Interface Science,* vol. 137, pp. 11-24, Jun 1990.

[341] D. Cava, R. Gavara, J. M. Lagaron, and A. Voelkel, "Surface characterization of poly(lactic acid) and polycaprolactone by inverse gas chromatography," *Journal of Chromatography A,* vol. 1148, pp. 86-91, Apr 27 2007.

[342] H. Tavana, C. H. Kuo, Q. Y. Lee, B. Mosadegh, D. Huh, P. J. Christensen*, et al.*, "Dynamics of Liquid Plugs of Buffer and Surfactant Solutions in a Micro-Engineered.Pulmonary Airway Model," *Langmuir,* vol. 26, pp. 3744-3752, Mar 2 2010.

[343] V. Llopis-Hernandez, P. Rico, J. Ballester-Beltran, D. Moratal, and M. Salmeron-Sanchez, "Role of Surface Chemistry in Protein Remodeling at the Cell-Material Interface," *Plos One,* vol. 6, May 9 2011.

[344] J. H. Lee, H. Y. Lee, and H. W. Kim, "Adhesive proteins linked with focal adhesion kinase regulate neurite outgrowth of PC12 cells," *Acta Biomaterialia,* vol. 8, pp. 165-172, Jan 2012.

[345] L. Cheng, F. S. Esch, M. A. Marchionni, and A. W. Mudge, "Control of Schwann cell survival and proliferation: autocrine factors and neuregulins," *Mol Cell Neurosci,* vol. 12, pp. 141-56, Oct 1998.

[346] E. Berger, N. Vega, M. Weiss-Gayet, and A. Geloen, "Gene Network Analysis of Glucose Linked Signaling Pathways and Their Role in Human Hepatocellular Carcinoma Cell Growth and Survival in HuH7 and HepG2 Cell Lines," *Biomed Res Int,* vol. 2015, p. 821761, 2015.

[347] V. Brunetti, G. Maiorano, L. Rizzello, B. Sorce, S. Sabella, R. Cingolani*, et al.*, "Neurons sense nanoscale roughness with nanometer sensitivity," *Proceedings of the National Academy of Sciences of the United States of America,* vol. 107, pp. 6264-6269, Apr 6 2010.

[348] R. Bellairs, "The development of the nervous system in chick embryos, studied by electron microscopy," *J Embryol Exp Morphol,* vol. 7, pp. 94-115, Mar 1959.

[349] A. H. Voie, D. H. Burns, and F. A. Spelman, "Orthogonal-Plane Fluorescence Optical Sectioning - 3-Dimensional Imaging of Macroscopic Biological Specimens," *Journal of Microscopy,* vol. 170, pp. 229-236, Jun 1993.

[350] R. Tomer, K. Khairy, and P. J. Keller, "Shedding light on the system: Studying embryonic development with light sheet microscopy," *Current Opinion in Genetics & Development,* vol. 21, pp. 558-565, Oct 2011.

[351] B. Hockendorf, T. Thumberger, and J. Wittbrodt, "Quantitative Analysis of Embryogenesis: A Perspective for Light Sheet Microscopy," *Developmental Cell,* vol. 23, pp. 1111-1120, Dec 11 2012.
[352] F. Pampaloni, B. J. Chang, and E. H. K. Stelzer, "Light sheet-based fluorescence microscopy (LSFM) for the quantitative imaging of cells and tissues," *Cell and Tissue Research,* vol. 360, pp. 129-141, Apr 2015.
[353] S. Ray and V. C. Kalia, "Biomedical Applications of Polyhydroxyalkanoates," *Indian Journal of Microbiology,* vol. 57, pp. 261-269, Sep 2017.
[354] R. Rai, T. Keshavarz, J. A. Roether, A. R. Boccaccini, and I. Roy, "Medium chain length polyhydroxyalkanoates, promising new biomedical materials for the future," *Materials Science & Engineering R-Reports,* vol. 72, pp. 29-47, Apr 22 2011.
[355] S. P. Valappil, S. K. Misra, A. R. Boccaccini, and I. Roy, "Biomedical applications of polyhydroxyalkanoates, an overview of animal testing and in vivo responses," *Expert Review of Medical Devices,* vol. 3, pp. 853-868, Nov 2006.
[356] L. R. Lizarraga-Valderrama, R. Nigmatullin, C. Taylor, J. W. Haycock, F. Claeyssens, J. C. Knowles*, et al.*, "Nerve tissue engineering using blends of poly(3-hydroxyalkanoates) for peripheral nerve regeneration," *Engineering in Life Sciences,* vol. 15, pp. 612-621, Sep 2015.
[357] L. R. Lizarraga-Valderrama, R. Nigmatullin, C. Taylor, J. W. Haycock, F. Claeyssens, and I. Roy, "Peripheral Nerve Regeneration Using Blends of Polyhydroxyalkanoates," *Journal of the Peripheral Nervous System,* vol. 20, pp. 185-185, Jun 2015.
[358] P. Ramburrun, P. Kumar, Y. E. Choonara, D. Bijukumar, L. C. du Toit, and V. Pillay, "A Review of Bioactive Release from Nerve Conduits as a Neurotherapeutic Strategy for Neuronal Growth in Peripheral Nerve Injury," *Biomed Research International,* 2014.
[359] M. C. O. Rodrigues, A. A. Rodrigues, L. E. Glover, J. Voltarelli, and C. V. Borlongan, "Peripheral Nerve Repair with Cultured Schwann Cells: Getting Closer to the Clinics," *Scientific World Journal,* 2012.
[360] A. Mosahebi, B. Woodward, M. Wiberg, R. Martin, and G. Terenghi, "Retroviral labeling of Schwann cells: in vitro characterization and in vivo transplantation to improve peripheral nerve regeneration," *Glia,* vol. 34, pp. 8-17, Apr 1 2001.
[361] A. Mosahebi, P. Fuller, M. Wiberg, and G. Terenghi, "Effect of allogeneic Schwann cell transplantation on peripheral nerve regeneration," *Exp Neurol,* vol. 173, pp. 213-23, Feb 2002.
[362] M. Georgiou, S. C. J. Bunting, H. A. Davies, A. J. Loughlin, J. P. Golding, and J. B. Phillips, "Engineered neural tissue for peripheral nerve repair," *Biomaterials,* vol. 34, pp. 7335-7343, Oct 2013.
[363] NC3Rs. (2019, 09/01/2019). *Development of the chick embryo as a replacement for rodent models of tumour metastasis*. Available: https://www.nc3rs.org.uk/development-chick-embryo-replacement-rodent-models-tumour-metastasis
[364] J. L. Duband, A. M. Belkin, J. Syfrig, J. P. Thiery, and V. E. Koteliansky, "Expression of Alpha-1 Integrin, a Laminin-Collagen Receptor, during Myogenesis and Neurogenesis in the Avian Embryo," *Development,* vol. 116, pp. 585-600, Nov 1992.
[365] O. E. Bloom and J. R. Morgan, "Membrane trafficking events underlying axon repair, growth, and regeneration," *Mol Cell Neurosci,* vol. 48, pp. 339-48, Dec 2011.
[366] T. Gordon, "The role of neurotrophic factors in nerve regeneration," *Neurosurg Focus,* vol. 26, p. E3, Feb 2009.
[367] I. Janssen, K. Reimers, C. Allmeling, S. Matthes, P. M. Vogt, and C. Radtke, "Schwann cell metabolic activity in various short-term holding conditions: implications for improved nerve graft viability," *Int J Otolaryngol,* vol. 2012, p. 742183, 2012.
[368] S. G. Turney, M. Ahmed, I. Chandrasekar, R. B. Wysolmerski, Z. M. Goeckeler, R. M. Rioux*, et al.*, "Nerve growth factor stimulates axon outgrowth through negative regulation of growth cone actomyosin restraint of microtubule advance," *Mol Biol Cell,* vol. 27, pp. 500-17, Feb 1 2016.

[369] E. G. Reynaud, U. Krzic, K. Greger, and E. H. Stelzer, "Light sheet-based fluorescence microscopy: more dimensions, more photons, and less photodamage," *HFSP J,* vol. 2, pp. 266-75, Oct 2008.
[370] J. Colombelli and C. Lorenzo, "Light Sheet Fluorescence Microscopy Applications for Multicellular Systems," *Fluorescence Microscopy: Super-Resolution and Other Novel Techniques,* pp. 109-120, 2014.
[371] J. Malda, T. J. Klein, and Z. Upton, "The roles of hypoxia in the in vitro engineering of tissues," *Tissue Eng,* vol. 13, pp. 2153-62, Sep 2007.
[372] C. Bergemann, P. Elter, R. Lange, V. Weissmann, H. Hansmann, E. D. Klinkenberg*, et al.*, "Cellular Nutrition in Complex Three-Dimensional Scaffolds: A Comparison between Experiments and Computer Simulations," *Int J Biomater,* vol. 2015, p. 584362, 2015.
[373] X. Wen and P. A. Tresco, "Effect of filament diameter and extracellular matrix molecule precoating on neurite outgrowth and Schwann cell behavior on multifilament entubulation bridging device in vitro," *J Biomed Mater Res A,* vol. 76, pp. 626-37, Mar 01 2006.
[374] P. G. di Summa, P. J. Kingham, W. Raffoul, M. Wiberg, G. Terenghi, and D. F. Kalbermatten, "Adipose-derived stem cells enhance peripheral nerve regeneration," *J Plast Reconstr Aesthet Surg,* vol. 63, pp. 1544-52, Sep 2010.
[375] H. J. Stewart, L. Morgan, K. R. Jessen, and R. Mirsky, "Changes in DNA synthesis rate in the Schwann cell lineage in vivo are correlated with the precursor--Schwann cell transition and myelination," *Eur J Neurosci,* vol. 5, pp. 1136-44, Sep 1 1993.
[376] J. P. Brockes, K. L. Fields, and M. C. Raff, "Studies on cultured rat Schwann cells. I. Establishment of purified populations from cultures of peripheral nerve," *Brain Res,* vol. 165, pp. 105-18, Apr 6 1979.
[377] E. Linder, A. Vaheri, E. Ruoslahti, and J. Wartiovaara, "Distribution of fibroblast surface antigen in the developing chick embryo," *J Exp Med,* vol. 142, pp. 41-9, Jul 1 1975.
[378] P. S. DiStefano and E. M. Johnson, Jr., "Identification of a truncated form of the nerve growth factor receptor," *Proc Natl Acad Sci U S A,* vol. 85, pp. 270-4, Jan 1988.
[379] R. C. Young, M. Wiberg, and G. Terenghi, "Poly-3-hydroxybutyrate (PHB): a resorbable conduit for long-gap repair in peripheral nerves," *Br J Plast Surg,* vol. 55, pp. 235-40, Apr 2002.
[380] C. Demerens, B. Stankoff, M. Logak, P. Anglade, B. Allinquant, F. Couraud*, et al.*, "Induction of myelination in the central nervous system by electrical activity," *Proc Natl Acad Sci U S A,* vol. 93, pp. 9887-92, Sep 3 1996.
[381] C. F. Eldridge, M. B. Bunge, and R. P. Bunge, "Differentiation of axon-related Schwann cells in vitro: II. Control of myelin formation by basal lamina," *J Neurosci,* vol. 9, pp. 625-38, Feb 1989.
[382] I. Spiegel, K. Adamsky, Y. Eshed, R. Milo, H. Sabanay, O. Sarig-Nadir*, et al.*, "A central role for Necl4 (SynCAM4) in Schwann cell-axon interaction and myelination," *Nat Neurosci,* vol. 10, pp. 861-9, Jul 2007.